Università degli Studi di Milano-Bicocca
Facoltà di Scienze Matematiche, Fisiche e Naturali
Dipartimento di Scienza dei Materiali

Ph. D. School in Materials Science
XXIV cycle

Synthesis, characterization and modeling of *sp*-*sp*^{2} carbon systems

PACS codes : 63.22.-m, 68.65.-k, 78.30.-j, 81.07.Nb

Advisor: Prof. Giorgio Benedek
Dean of the Doctorate: Prof. Gian Paolo Brivio

Eugenio Cinquanta
Matricola n° 725140
A.A. 2010/2011

Contents

List of publications

Published articles

- L.Ravagnan, N. Manini, **E. Cinquanta**, G. Onida, D. Sangalli, C. Motta, M. Devetta, A. Bordoni, P. Piseri and P. Milani, "Effect of axial torsion on carbon atomic wires", Phys. Rev. Lett., **102**:245502, 2009;

- G. Onida, N. Manini, L. Ravagnan, **E. Cinquanta**, D. Sangalli and P. Milani, "Vibrational properties of sp carbon atomic wires in cluster- assembled carbon films", Phys. Stat. Sol. B, **247**:2017-2021, 2010;

- F. Cataldo, L. Ravagnan, **E. Cinquanta**, I. E. Castelli, N. Manini, G. Onida, and P. Milani, "Synthesis, characterization, and modeling of naphthyl-terminated *sp* carbon chains: Dinaphthylpolyynes", J. Phys. Chem. B, **102**:14834-14841, 2010

- **E. Cinquanta**, L. Ravagnan, I. E. Castelli, F. Cataldo, N. Manini, G. Onida, and P. Milani, "Vibrational characterization of dinaphthylpolyynes: A model system for the study of end-capped *sp* carbon chains", J. Chem. Phys, **135**:194501, 2011;

In preparation

- **E. Cinquanta**, L. Ravagnan, N. Manini, M. Bulla, L. Venema, G. Onida, P. Rudolf and P. Milani, "Infrared and resonant-Raman spectroscopy of *sp*-sp^2 pure carbon films", 2011.

Books

- G. Benedek, M. Bernasconi, **E. Cinquanta**, Luca D'Alessio and Marzio De Corato, "The Topological Background of Schwarzite Physics" in Mathematics and Topology of Fullerenes. Springer series on CARBON MATERIALS CHEMISTRY AND PHYSICS, Heidelberg, Berlin, 20010

Chapter 1

Introduction

1.1 Scientific background

In the last decade carbon based nano-materials have attracted the interest of scientist from many different fields, ranging from astrochemistry to solid state physics. Although carbon is one of the most studied element ever, it has never ceased to stupefy due to the large variety of materials it can form. Beyond the most famous 3D sp^3 diamond and sp^2 graphite, in the last 20 years have been discovered also the 1D and 0D pure sp^2 forms, nanotubes and fullerenes respectively [1, 2].

Recently, the discover by Novoselov and Geim [3] of graphene, the pure 2D sp^2 phase, put once again carbon on the world scientific stage. Its promising and fascinating physical properties and possible applications in growing fields as nano-electronic, hydrogen storage and sensoring, make graphene one of the most studied system, both from theoreticians and experimentalists.

Carbon can also give rise to an exotic "spongy" phase formed by sp^2 carbon atoms structures. Triply periodic minimal surfaces [4, 5] have been theoretically suggested as possible model structures for spongy carbon, which has since termed *schwarzite*, after the name of the mathematician Hermann Schwarz who first investigated that class of surfaces [6,7]. While fullerenes, nanotubes, graphite layers aggregate through comparatively weak van der Waals forces, spongy carbon constitutes a fully covalent highly-connected three-dimensional (3D) form of sp^2 carbon, which combines many valuable properties of fullerenes, nanotubes and graphene with a robust 3D architecture. For detailed description of this exotic form, see the review reported in the appendix A [8].

Beyond these mono-crystalline forms of carbon, in the recent past also mixed-phase carbon based materials have been studied; sp^2/sp^3 amorphous carbon films have been proposed as promising materials for technological applications. The mechanical and optical properties of such materials can be tuned by varying the ratio between the amount of sp^2 and sp^3 atoms, providing graphitic-like materials or diamond-like materials respectively [9]. These systems have been proposed as protective overcoat for magnetic storage disks [10], as component in filed emission devices [11] and as gas barriers [12].

In the framework of amorphous carbon materials, the possibility of the inclusion of the *sp* hybridized carbon phase is one of the most intriguing point for solid state physicist and chemists. *sp* carbon atoms give rise to linear carbon chains (*sp*CCs) known as carbyne. This exotic phase of carbon, expected to be highly unstable because of the

dangling bonds at chains extremes, can occur in two different forms, depending on the configuration of the molecular σ and π orbitals. Ideal infinite polyynes ($\text{-C}\equiv\text{C-}_\infty$) present an alternation of single (σ) and triple bonds (1 σ and 2 π) along the chain axis, that is they are dimerized. On the other hand, infinite cumulenes ($=\text{C}=\text{C}=_\infty$) are characterized by the alternation of double bonds (1 σ and 1 π) of equal length along the chain, making them un-dimerized molecules. Although the infinite cumulenic structure is proposed in the framework of infinite chains, it is not the energetically favored configuration indeed, due to Peierls distortion, the stable phase of the infinite chains is the polyynic (dimerized) one.

This scenario completely fails if finite carbon chains are considered. Let us consider the most simple and intuitive termination possible, that is hydrogen; if one hydrogen atom passivates the dangling bonds of the chains, the first carbon is already *sp* hybridized, and the remaining two p and one *sp* orbitals form the triple bond with the next carbon atom thus inducing the polyynic form. On contrary, with two hydrogen atoms, the first carbon atom is not *sp* hybridized, but sp^2, and the two hydrogens are bonded by π bonds with two of the three trigonal sp^2 orbitals. The carbon atom has then two un-bonded orbitals, a sp^2 and the non hybridized p, that can form a double bond with the next carbon atom, which is then *sp* hybridize thus giving rise to un-dimerized cumulenic chains also for quite long chains [13]. This demonstrates how the energetic considerations on the tendency of infinite *sp*CCs to be polyynes induced by Peierls-type distortion become meaningless when terminated chains are considered.

Remarkably *sp*CCs show electronic properties strongly correlated to the structure of their molecular orbitals. Weimer *et al.* [13] demonstrated how the HOMO-LUMO gap of chemical (H, F, CN, NO_2 NH_2) stabilized *sp*CCs linearly decreases as a function of the chains length. Polyynes have optical gap value systematically higher by $\sim$ 1eV than that of cumulenes with the same length. This observation will be crucial for the comprehension of the different resonant Raman behavior characterizing polyynes and cumulenes. Furthermore, while for the infinite cumulene a metallic behavior is expected due to the complete delocalization of π bonds along the chain axis, for infinite polyyne a finite gap persists due to the presence of the strong and localized σ bonds, thus leading to a semiconductive character. Nevertheless, for what concerns finite and stabilized *sp*CCs, a small gap is expected also for cumulenic structures: because the interaction between the chains and the termination, end-capped cumulenes are not expected to be complete un-dimerized, that is they show non-zero Bond Length Alternation (BLA) and thus a small finite HOMO-LUMO gap is present. As a consequence, as in the case of polyynes, stabilized cumulenic structures are characterized by a semiconductive behavior, thus paving the way for their potential application in nano-devices. It is now clear how important *sp*CCs terminations are: First Bond Length (FBL), i.e. the length of the bond between the first carbon atom of the chains and the termination, BLA, i.e. a measure of the chains dimerization, energy gap, magnetic state and conductivity of *sp*CCs strongly depend on the type of stabilizing end group, thus making the stabilization process the fundamental point for determining the *sp*CCs physical and chemical properties.

In the literature have been proposed many different techniques for the production of stabilized *sp*CCs. Chemists for instance were able to synthesize *sp*CCs stable in solution or even in the solid state phase, by terminating the chains with organic group through chemical reactions. These class of *sp*CCs, stabilized by different chemical end-group, have interesting and promising physical properties; they are characterized by a HOMO-LUMO gap strongly influenced by the number of carbon atoms constituting the *sp*CCs (i.e. the chains length) [13], then it has been reported that their third-order nonlinear

optical (NLO) and their non-resonant molecular second hyperpolarizabilites (α) increase as a function of the chains length [14]. Furthermore, it has been shown that the fluorescence, phosphorescence and absorption spectra of these molecules can be modulated by applying an external electric field [15]. Finally, unusual photophysical and spectroscopic properties have been reported and they are considered promising candidates as materials for the fabrication of semiconductive thin film transistor structures [16], as the active semiconductor material in light-emitting diodes in electroluminescent devices [17] and in organic solar cells [18].

The possibility of the production of stable *sp*CCs embedded in a pure carbon solid, opens new prospectives for nano-electronic [19,20] applications since they could be used as molecular conductors bridging graphene nano-gap devices. First potential applications have been already demonstrated for the realization of non-volatile memories, as their use in two-terminal atomic-scale switches [20]. Furthermore, *sp*CCs are expected to have interesting rectifying performances and to be effective as spin-filters and spin-valves. [21]. More recently, end-capped *sp*CCs stabilized by different terminations have also been proposed also as building blocks of hydrogen storage nanomaterials [22,23].

Beyond these applicative fields, *sp*CCs are very intriguing also for more speculative aspects. For instance, one of the most unsolved phenomena in astrophysics are the Diffusive Interstellar Bands (DIBs). These absorption bands are present in the visible-near IR region of the interstellar extinction curve and are formed in the interstellar clouds. Due to their width (FWHM c.ca $0.006 - 4$nm) and their large variety, DIBs can be made up by molecules and solid-state materials rather than atomic emission. In these framework organic compounds are the most promising candidates to be responsible of DIBs since only carbon atoms can form the wide zoology of structures which can be the carriers of these broad features [24]. By comparing laboratory infrared spectra with astrophysical observations of the Inter-Stellar Medium (ISM), it has been proposed that some of these DIBs lines can be generated by Polycyclic Aromatic Hydrocarbons (PAH), small hydrocarbons molecules (e.g. acetylene and cyanopolyyne), fullerenes and also not terminated *sp*CCs [25,26,27]. Cami et al. has recently demonstrated the presence of $C60$ and $C70$ neutral molecules in the young planetary nebulae Tc-1 [28] and, more generally, it is now accepted that *sp*CCs can act as intermediates in the formation of fullerenes and PAH in, respectively, hydrogen-poor and hydrogen-rich region [29].

Although many techniques have been developed for the synthesis of such materials, the characterization of the physical and chemical properties of pure carbon system containing *sp*CCs requires further experimental and theoretical efforts. Vibrational and optical spectroscopy can provide information about the physical and structural properties of end-capped *sp*CCs, but the identification of the spectroscopical signature of different chains families embedded in *sp*-sp^2-sp^3 materials remains challenging.

1.2 Scope

The core of this thesis is to provide an exhaustive identification of the vibrational properties of the cluster assembled *sp*-sp^2 pure carbon material. This system consists in an amorphous sp^2 matrix where *sp*CCs are embedded and stabilized by sp^2 fragments and it is synthesized by depositing, through the Supersonic Cluster Beam Deposition (*SCBD*) technique, *sp*-sp^2 pure carbon clusters produced in a Pulsed Microplasma Cluster Source (*PMCS*) [30]. Although this material has been continuously studied for long time mainly by Raman spectroscopy [31], its vibrational features are not clear yet.

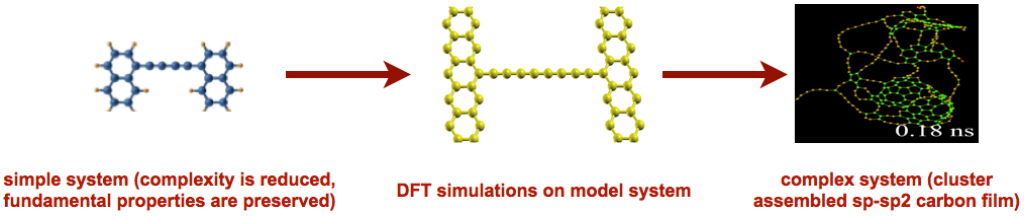

Figure 1.1: sketch of the approach adopted for the study of the vibrational properties of the *sp*-sp^2 carbon material: experiment and simulations are performed on a benchmark system→the results are used for the identification of suitable model system representing the complex one→experimental results obtained on the *sp*-sp^2 carbon system are interpreted by comparing them with simulations

In order obtain a better comprehension on the presence, structure (i.e. length, terminations) and stability of *sp*CCs in the *sp*-sp^2 pure carbon film, new experimental and theoretical efforts are required. In particular it is necessary to clearly and unambiguously identify chains with different lengths and terminations in order to obtain a clear description of the physical and chemical properties characterizing the *sp*-sp^2 material.

From one side, it is interesting to study the chemical properties of the *sp*-sp^2 thin film, both *in-situ* and during reactive gas exposure (O_2, N_2, H), from the other one would like to compare laboratory spectra with astrophysical observation in order to identify *sp*CCs in the ISM. By using infrared spectroscopy it is possible not only to detect species with different functional groups from their vibrational infrared-active signatures, but also to obtain quantitative analysis about the *sp* content and about the reaction products. Remarkably in the literature it is not present an Infrared spectrum of a *sp*-sp^2 pure carbon material, thus making this experiment trail-blazing and challenging.

Furthermore it is interesting to investigate the *sp*-sp^2 material by Raman spectroscopy using different laser wavelength in order to explore the resonance effects. This measurements are fascinating because can provide a clear identification of the presence of polyynic-like and cumulenic-like *sp*CCs with different length thanks to the activation of the Raman resonance as the incident photon energy matches the energy of actual electronic transition of the *sp*-sp^2 amorphous carbon solid.

For the comprehension of the vibrational (both Raman and infrared) spectra of such a complex system, it is then necessary to compare experimental data with theoretical calculations performed on a simplified system. As sketched in the scheme reported above, one can remove the complexity of the *sp*-sp^2 pure carbon clusters by modeling them with a simpler system which represents the actual cluster structure. By following this idea, an *sp* chains embedded in a pure sp^2 covalent bonded carbon cluster can be viewed as an *sp*CCs bridging two graphene nano-ribbons, thus preserving the fundamental properties of the sp^2 termination but removing the complexity induced by the amorphous carbon matrix. Furthermore, in order to be able to compare data provided by the simulations with experimental results, it is necessary to refer to a benchmark system, i.e., a system that can be both synthesized in the laboratory and modeled through theoretical calculations without the need to introduce further simplifications. For this reason in my Phd I propose the synthesis, characterization and modeling of *sp*CCs terminated by the simplest sp^2 termination, i.e. Naphthalene, which well approximates an sp^2 end-group present in the *sp*-sp^2 system (graphene nano-ribbons). The combined

experimental-theoretical study of the solution containing Naphthalene-terminated *sp*CCs (dinaphtylpolyynes) with different length (Ar-C_{2n}-Ar with n=2:8), performed through Infrared and Multi-Wavelength Resonant Raman spectroscopy combined with structural and vibrational *ab-initio* density-functional theory (DFT) simulations, leads to the deep comprehension of the vibrational properties of the dinaphtylpolyynes. The model provided for dinaphtylpolyynes can be then used for the interpretation of the intricate results obtained by performing Infrared and Multi-Wavelength Resonant Raman experiment on the complex *sp*-sp^2 pure carbon material.

1.3 Thesis frame

This work consists, apart of the Introduction, of three parts. The first one is dedicated to the description of the chemical and physical synthesis techniques used for the production of stabilized *sp*CCs. In the second part I briefly describe the computational framework used for the simulations and experimental methods used for the characterization of the *sp*CCs. In the last part I present all the results obtained, both published in referred journal (or in the preparation/submitted step) and unpublished. In particular in the first chapter of this part I present the result obtained about the synthesis, characterization and modeling of dinaphtylpolyynes. Then I report the results obtained about the *sp*-sp^2 by using the framework developed for dinaphtylpolyynes: MWWR and infrared spectroscopies combined with *ab-initio* DFT-LSDA calculations. The last chapter is dedicated to the final remarks, conclusions and prospectives.

notes:

- *Some parts of the results I obtained in my Phd have been already published or submitted to international journals. In writing this thesis I've tried to minimize superimpositions with the reprinted papers. Nevertheless some overlapping still remains.*

Part I

Synthesis of sp-sp^2 carbon system

Chapter 2

Chemical Synthesis

In the recent history, many different techniques have been proposed for the synthesis of chemically stabilized *sp*CCs. For instance Lucotti *et al.* showed how it is possible to produce H-terminated *sp*CCs in the polyynic configuration by electric arc discharge between two graphite electrodes in methanol [32,33]. This technique leads to the synthesis of stable H-C_{2n}-H with n=2:8. Another procedure is based on the Fritsch-Nuttenberg-Wiechell rearrangement, that is a chemical reaction between a 1,1-dyaril-2-bromo-alkene with a strong base (e.g. alkoxyde), which leads to the production of polyynic *sp*CCs stabilized by bulkier group as Adamantyle [34]. Alternatively, recently has been demonstrated the possibility of synthesize stabilized H-terminated *sp*CCs (polyynes and cumulenes) by ablating micormetric graphite particle in an organic [35,36,37] and even aqueos solvents [38] using the harmonics of a Nd:YAG laser.

Particularly interesting is the family of *sp*CCs end-capped by organic group. This class of molecules, often referred to as α,$\omega-$diarylpolyynes (DAPs), already synthesized in the 1960's and 1970's by the group of M. Nakagawa [39, 40, 41], represents a family of *sp*CCs stabilized by aromatic end-groups which are of high interest for several reasons: from one side, they are potentially useful in optoelectronical applications and are promising building blocks for the production of *sp*-sp^2 carbon systems for nano-electronic devices; from the other side, they constitute the simplest examples of *sp*CCs terminated by a PAH that could be identified in the interstellar medium.

As a result, naphthalene represents the ideal end-capping group from many points of view. First of all it is the simplest and most abundant PAH present in the ISM, furthermore it represents an ideal system that can be used for the modeling an sp^2 stabilizing sites as occur in the more complex case of graphitic terminations in the *sp*-sp^2 pure carbon films. For these reasons the possibility of easily synthesize Naphthalene-terminated *sp*CCs (in the following dinaphtylpolyynes) of different length is a crucial step both for the comprehension of the presence and stability of *sp*CCs embedded in the *sp*-sp^2 material and for the identification of the carriers of Diffusive Interstellar Bands (Dibs) and of the composition of the ISM.

In this section I present a new route for the synthesis of dinaphtylpolyynes which enables, by a remarkably simpler chemical approach than in [39, 40, 41], to produce at the same time a solution containing Ar-C_{2n}-Ar molecules with $2 \leq n \leq 6$.

2.1 Cadiot-Chodkiewicz coupling

The Cadiot-Chodkiewicz (C-C) cross-coupling in organic chemistry is a reaction between a terminal alkyne and a haloalkyne catalyzed by a copper(I) salt such as copper(I)bromide and an amine base [42, 43, 44]. This synthesis procedure is typically used for the production of symmetric and asymmetric polyacetylenic molecules stabilized by different chemical end-group. The reaction mechanism involves deprotonation by base of the acetylenic proton followed by formation of a copper(I) acetylide. A cycle of oxidative addition and reductive elimination on the copper center then creates a new carbon-carbon bond. The repetition of this procedure leads to the production of Ar-C_{2n}-Ar molecules composed by n acetylenic units. In fig.2.1 is reported a sketch representing an example of C-C reaction cycles.

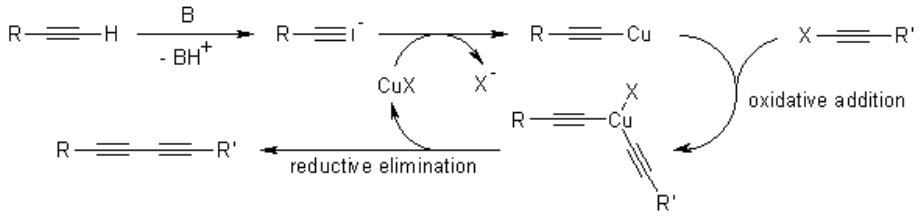

Figure 2.1: A complete cycle of a Cadiot-Chodkiewicz reaction providing polyacetylenic molecules

In the literature C-C reactions ha been used for the synthesis of many different *sp* molecules. J. Marino *et al.* proposed the production of bulky trialkylsilyl acetylenes under C-C coupling conditions by reacting 3-bromo-prop-2-yn-1-ol (8) and a trialkylsilyl acetylene catalyzed by CuCl and NH2oh·HCL in a 30% n-butylamine in water solvent [45]. Terminal-conjugated diynes were prepared by N.J. Matovic *et al.*by using C-C coupling sequence utilizing a protected bromoacetylene, and methyl-substituted diynes were made via a base-catalyzed rearrangement of terminal-skipped diynes [46]. In the framework of α,ω-diarylpolyynes F. Cataldo*et al.*demonstrated the possibility of easily synthesize Diphenylpolyynes, i.e. phenyl-terminated *sp*CCs terminated [47].

2.1.1 Synthesis of dinaphtylpolyynes

The procedure presented by F. Cataldo *et al.* in [47] was followed for the synthesis of *sp*CCs terminated with Naphtyl groups (dinaphtylpolyynes). In a first stage the copper salt of ethynylnaphthalene was synthesized by dissolving Cu(I) chloride (1.0 g) in 30ml of aqueous ammonia (30%) together with 0.5g of hydroxylamine hydrochloride (NH2OH·HCl). 1-Ethynylnaphthalene (1.5ml) was then added to this solution under stirring. We collected a dark yellow precipitate of copper(I) ethynylnaphthalide by filtration in considerable yield (1.8 g). After that about 6.0 g of $I - C \equiv C - I$ was dissolved/suspended in 90ml of decalin, it was transferred in a 500ml round bottomed flask and was stirred with 100ml of distilled water. Copper(I)-ethynylnaphthalide (1.8g) was then added to the reaction mixture together with 25ml of tetrahydrofuran, 50ml aqueous NH3 30% and 30ml of *N,N'*, *N*, *N'*-tetramethylethylenediamine (TMEDA). The mixture was stirred at room temperature for two days and after this process the decalin layer became deep orange. The reaction mixture was filtered with the aid of an aspirator to

separate the black residue formed. The filtered solution consisted of two layers. The organic layer was separated from the aqueous layer by means of a separatory funnel. The resulting crude solution contained dinaphthylpolyynes dissolved in decalin, together with a significant amount of free unreacted ethynylnaphthalene and other by-products. These latter were removed from the crude solution (as a dark red precipitate) by shaking the solution with 4.0g of CuCl dissolved in 100ml of aqueous NH3 30% together with 3.0g of NH2OH·HCl. The key innovation in this synthetic approach is the use of diiodoacety-

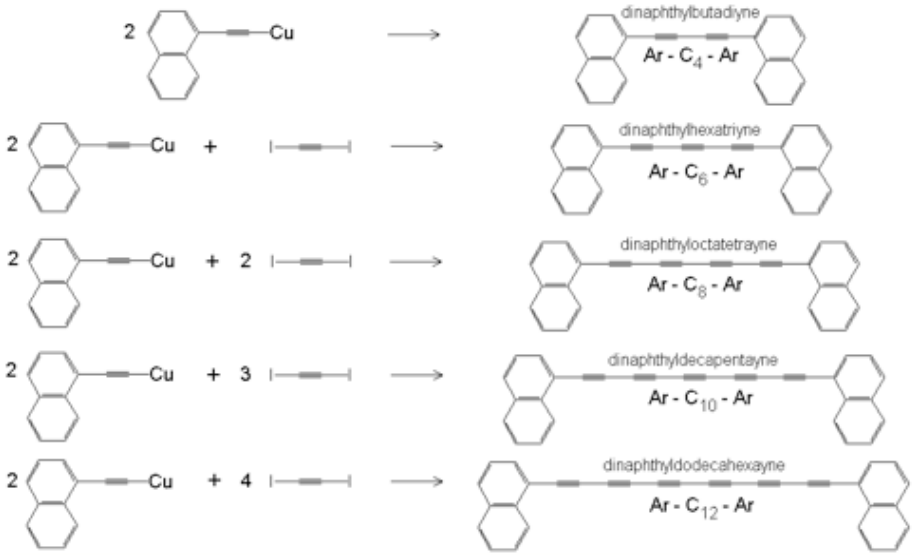

Figure 2.2: Sketch of the structure of the dinaphtylpolyynes (Ar-C_{2n}-Ar molecules with $2 \leq n \leq 6$) synthesized under an increasing number of Cadiot-Chodkiewicz cross coupling cycles

lene, which simplifies the synthetic route to long polyynes chains with taylor-made end caps, thus indicating its general applicability in the synthesis of α,ω-diarylpolyynes.

Chapter 3

Physical Synthesis

One of the most intriguing and challenging point for solid state physicists working on carbon-based materials, is the introduction of the *sp* hybridization in the phase diagram of carbon structures. Recent experimental observation by HR-TEM of *sp*CCs forming during the irradiation of graphene planes has strongly increased the interest for this field [48,49], opening the way for the production of *sp* carbon based nano-devices. W. Hu and co-workers proposed the fs-laser ablation of Highly Ordered Pyrolitic Graphite as a new route for the production of micrometric *sp*-patterned sp^2 pure carbon material [50, 51]. This technique represents an intriguing procedure: the formation of *sp*CCs is under many graphite layer due the focalization of the laser pulse just before the HOPG surface, as a consequence the graphitic "coating" prevents chains to react with reactive gases, thus leading to longer shelf-life for *sp*CCs. The carbon chains formation is strictly connected to the fs duration of the laser pulse, indeed it is the huge local warming in such a short pulse which sets the thermodynamics conditions suitable for the carbyne coalescence. If one would use laser pulses longer than tens of fs, just after their formation, metastable *sp*CCs suddenly relax in sp^2 structures due to thermal heating which provides enough energy for the activation of the graphitization process. With respect of the procedures mentioned in sec.2.1.1, which provide chemically mixed structures, these top-down approach lead to the synthesis of pure carbon system.

Furthermore, also Bottom-Up approach have been explored attempting to produce *sp*CCs stabilized by graphitic fragments; the basic idea is to assemble clusters in suitable thermodynamics conditions, under which it is energetically favored for the carbon atoms to arrange in linear chains terminated by pure carbon end-groups.

In this framework A.A. Shvartsburg *et al.* showed how it is possible, by producing carbon clusters through laser desorption of C60 films, the formation of *sp*CCs, with a length up to eight atoms, stabilized both by two fullerenes at their extremes [52,53] and inside a single fullerene (where *sp*CCs can arrange as "sticks" or as an "handles") [52]. They interpreted those structures as intermediate steps in the fullerene road, where small cages capture chains that will be eventually incorporated in the sp^2 network, leading to the growth of the fullerene. By rapidly quenching the plasma plume they were able to inhibit further evolution of those structures to fully sp^2 cages, and they then observed those intermediate structures by ion mobility. Those results provide a first indication on the feasibility of incorporating a stabilized carbon chain in a big cluster. It is interesting to notice that just a defect on a sp^2 cluster is sufficient to serve as stabilizing site, that can be either sp^2 or sp^3 hybridized carbon atoms.

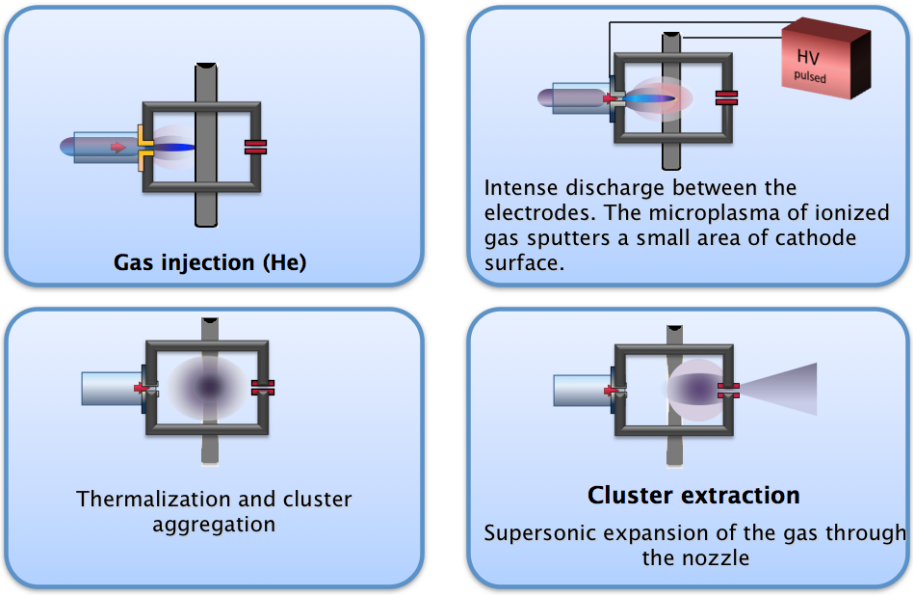

Figure 3.1: Structure and working principle of the *PMCS*

As a result, the most explored way for the synthesis of *sp*-sp^2 pure carbon materials, is the production of carbon aggregates by means of cluster sources whose working thermodynamics conditions allow the formation and survival of such metastable *sp*-sp^2 structures.

During the last years many different sources have been developed for the production of carbon clusters, as for instance laser vaporization [54] and arch discharge [55]. All these techniques are based on the extraction of carbon atoms by huge heating of bulk graphite through an highly focused laser bream or by igniting an electric arc respectively. Because the plasma generated by the intense laser flux used for the graphite vaporization is too hot, the thermodynamic conditions (T$\sim$ 10000K) typical for these kind of sources do not allow the production of metastable *sp*-sp^2 structures but only fullerenic sp^2 clusters composed by an even number of carbon atoms [56]. Such an high temperature promotes the formation of metastable aggregates but, without a rapid quenching, they immediately rearrange in more stable full sp^2 structures.

On the other hand, Ion sputtering techniques, based on the extraction of the carbon atoms from the target by momentum exchange between the impacting atoms and the target [57], are more promising candidates for the production of metastable *sp*CCs-rich clusters. This is actually not a direct process (the emission of the atoms is due to a recoil-like effect) but nevertheless the ejected atoms and molecules have kinetic energies far higher than those extracted by evaporation sources [57]and lower vibrational temperatures.

3.1 The Pulsed Microplasma Cluster Source

With the purpose of the exploration of the wide zoology of structures (*sp*CCs included) that carbon can form along the fullerene road, P. Milani *et al.*, form the LGM (Molecular

Beam Laboratory) group of the Department of Physics of the University of Milan and from *Cimaina* (Interdepartmental Center for Nanostructured Materials and Interfaces) have developed a cluster source based on ion sputtering, where the gas expansion inside the cavity is not just used to quench the aggregates, but also for the target ablation. This source is named *Pulsed Microplasma Cluster Source (PMCS)* [30] and it has been demonstrated how it is possible to use it for the synthesis of metastable sp-sp^2 pure carbon clusters [31]. The PMCS consists in a cylindrical cavity (1.8 cm^3) in which

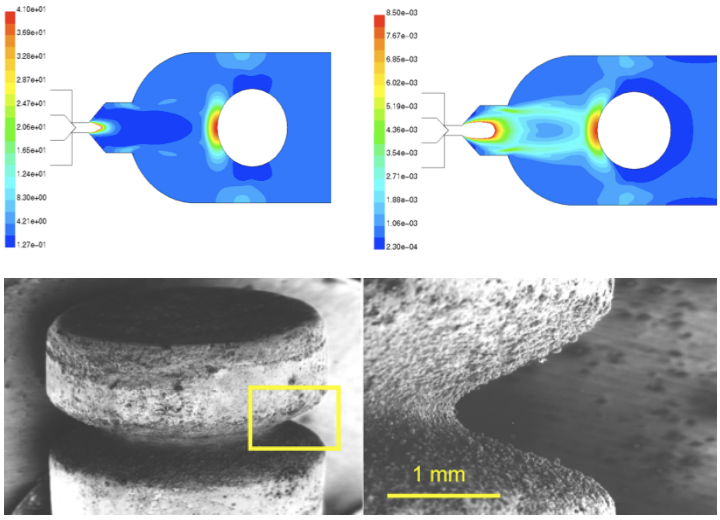

Figure 3.2: Density plot (top left) pressure plot (top right) of the gas inside the cavity source as reported by K. Wegner . (Bottom left) SEM image of the graphite cathode after the ablation, (bottom right) magnification of the ablated region.

a rotating solid target made of the sp^2 carbon (graphite) is vaporized by a localized discharge supported by a pulsed injection of an inert gas (He 6.0) at high pressure (30bars) through a solenoid valve (General Valve Corp., Series 9) linked to one extreme of the cavity (see fig. 3.1). The supersonic expansion of the inert gas, due to the high pressure difference [58], forms an high density and highly localized region near the cathode where occurs the ablation of the graphite rode [30]. Few μs after the valve opening, an intense discharge (1 KV) between the cathode (graphite rode) and a copper anode ionizes highly localized He atoms, thus producing the plasma responsible of the ablation of the graphite rode's surface (see fig.3.1). Because of the plasma confinement, also the ablation of the graphite rode is highly confined, as can be seen in fig.3.2.

The vaporized carbon atoms aggregate in the cavity at high temperature (2000 $\div$ 3500 K) and with a density of 1.8 $\div$ 2.5 g cm^{-3} [59], thermodynamics conditions which do not inhibit the formation of metastable carbon clusters where sp and the sp^2 hybridization can coexist. Thanks to the high atomic kinetic energy, the plasma expands rapidly and thus this aggregation stage results quite short (few ns). After this first "hot" step where the formation of metastable sp-sp^2 carbon clusters occurs, there is a second "cold" step where clusters atoms thermalize and are "frozen" at 100K due to the rapid adiabatic supersonic expansion of the non-ionized He([30]). In this stage a second aggregation process occurs: primary clusters aggregates to form bigger nanoparticles which are then driven out of the source cavity by the supersonic expansion of the inert gas through

a nozzle to a vacuum chamber (expansion chamber, at a pressure of about 10^{-6}mbar). Because of the high pressure difference between the source cavity and expansion chamber and the exploitation of aerodynamic focusing effects, the neutrally charged clusters exit from the source in the form of a highly collimated beam with a divergence lower than 1 degree and with the kinetic energy described in previous works [30].

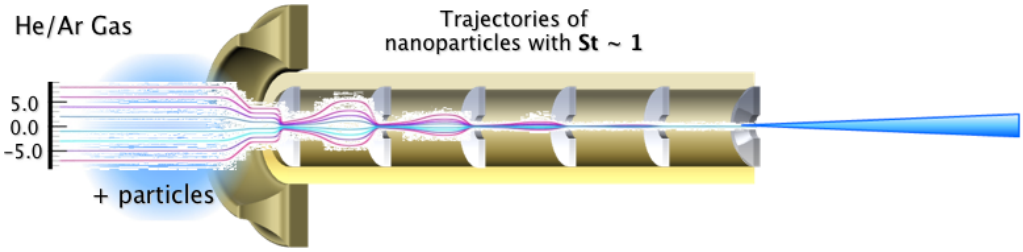

Figure 3.3: sketch of the aerodynamical focusing set-up and working principle

In fig.3.3 is reported a sketch of the focusing set-up: it consists in a sequence of aerodynamic lenses (disks with a hole of 2 mm in their centre) which provide successive axisymmetric contractions-enlargements of the aerosol flow passage. The working principle of this nozzle is based on simply aerodynamical considerations. The fundamental parameter which controls the focusing system is the nanoparticles Stoke number $s = \frac{\tau}{d}$, where τ is the relaxation time and d is the hole diameter (assuming for convenience spherical clusters). Nanoparticles with $s = \frac{\tau}{d} \ll 1$ follow fluid streamlines closely, i.e. they are not focused. On the other hand, nanoparticles with s$\gg$ 1 will escape from the gas streamlines where the flow decelerates and are stopped against the focuser's walls. As a consequence only clusters with s$\sim$ 1 are focused on the beam axis, thus, by using aerodynamical lenses with different hole diameter d, it is possible to select, just through aerodynamical consideration, the range of mass that can be focused [30].

3.1.1 Simulation of sp-sp^2 pure carbon clusters growth

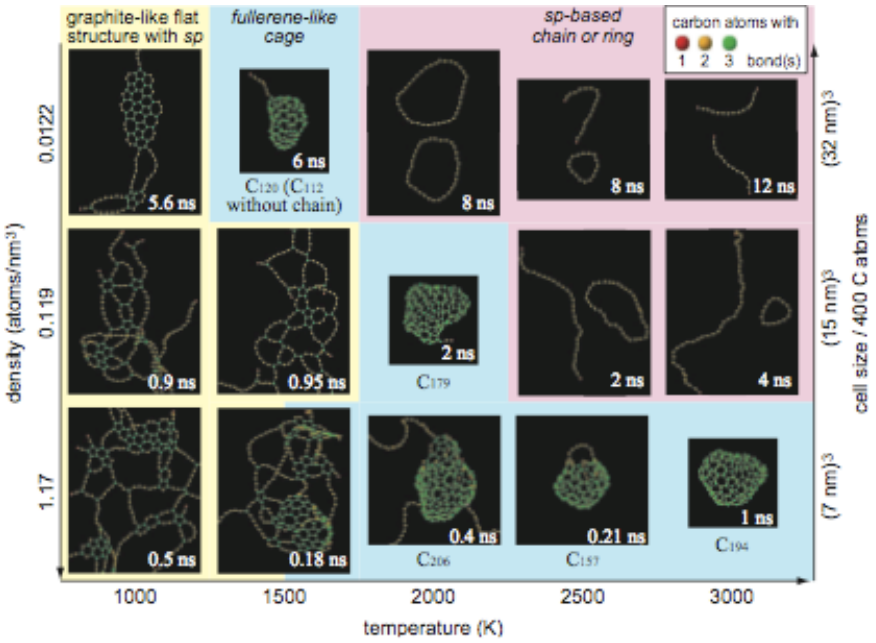

Figure 3.4: TBMD simulations of carbon clusters growth under different thermodynamics (temperature and density) conditions [60]

The possibility of synthesize carbon chains is thus tightly connected to the thermodynamic conditions that characterize the PMCS source, as spCCs are an exotic and evasive form of carbon extremely reactive with gases and unstable at high temperature. Therefore thermodynamics conditions (temperature and pressure) are the fundamental parameter that can be tuned in order to find the optimal conditions for the spCCs production and survival.

In the past have been carried out Molecular Dynamic simulation in order to better understand the pathway of the formation of big clusters produced with the PMCS source.

M. Bogana *et al.* showed how both even and odd clusters can be formed and that *sp* chain-like structures are embedded (i.e., stabilized) in cage-like clusters, thus providing a mixed *sp*-sp^2 hybridized system [59].

Furthermore Yamaguchi *et al.* performed Tight Binding Molecular Dynamic (*TBMD*) simulations arranged so as to mimic the cluster formation conditions typical of a *PMCS* source [60]. The formation of linear, ring-like and fullerene-like objects in the carbon plasma is found to proceed through a very long multistep process. Therefore, tight-binding simulations of unprecedented duration have been performed by exploiting the disconnected topology of the simulated carbon plasma. These simulations demonstrated how many different structures can be formed in experiments, depending on the plasma temperature and density. As it is reported in fig. [60], the possible aggregates can be divided in three main families. Isolated *sp*CCs or rings form with temperature of about 3000K and low density (pink quadrants), fullerene-like cages form with temperature range of $1500-2500$K and variable density (light blue quadrants) while *sp*CCs embedded in graphitic-like flat structures can be produced at low temperature, about 1000K, and over a wide range of carbon atoms densities.

This simulations demonstrate that the thermodynamics conditions inside the *PMCS* source are suitable for the growth of metastable *sp*-sp^2 carbon clusters. Furthermore, as discussed in the previous sections, it is necessary that this extremely evasive aggregates cool down after their formation, otherwise they undergo to relaxation towards more stable pure sp^2 structures. The supersonic expansion of the non-ionized carrier gas which occurs immediately after the coalescence process of primary clusters, provides this quenching and as a consequence*sp*-sp^2 carbon aggregates can survive and then used for the cluster assembly of pure carbon materials.

3.1.2 NEXAFS characterization of the cluster beam

As it has been demonstrated through Time of Flight-Mass Spectrometric measurement on clusters in the gas phase, the *PMCS* thermodynamics conditions favor the coalescence of pure carbon clusters with a large variety of structures quite far from the Most Stable Isomer (MSI). The typical mass spectra of carbon clusters produced by the *PMCS* and focused with aerodynamical lenses set-up is reported here [61]. The mass distribution is lognormal, as usually observed in gas phase grown particles [62, 63] and, despite of what occurs with other cluster sources (PACIS, PVLS), one can observe the presence of very large clusters, composed by both an even and odd number of carbon atoms [61]. In the recent past L. Ravagnan *et al.* demonstrated by gas-phase, i.e. as free nanoparticle prior the deposition, Near Edge X-ray Absorption Fine Structure (NEXAFS) experiments the presence of the *sp* phase in the cluster produced with the *PMCS* [64]. In NEXAFS a core electron is excited to an unoccupied molecular orbital and the resulting core hole filled through fluorescent decay or an Auger process. For carbon the latter is preponderant and by collecting the emitted electrons one obtains a peak in the spectrum each time the exciting photon energy matches the difference between the core level and an empty σ^* π^* orbital. NEXAFS is thus capable of identifying the chemical bonds present and, via a building block approach, quantify their abundance. The fraction of NEXAFS signal related to *sp* bond X_{sp} is defined as:

$$X_{sp} = 100 \times \frac{A[\pi^*_{C\equiv C}]}{A[\pi^*_{C\equiv C}] + A[\pi^*_{C=C}]} \tag{3.1}$$

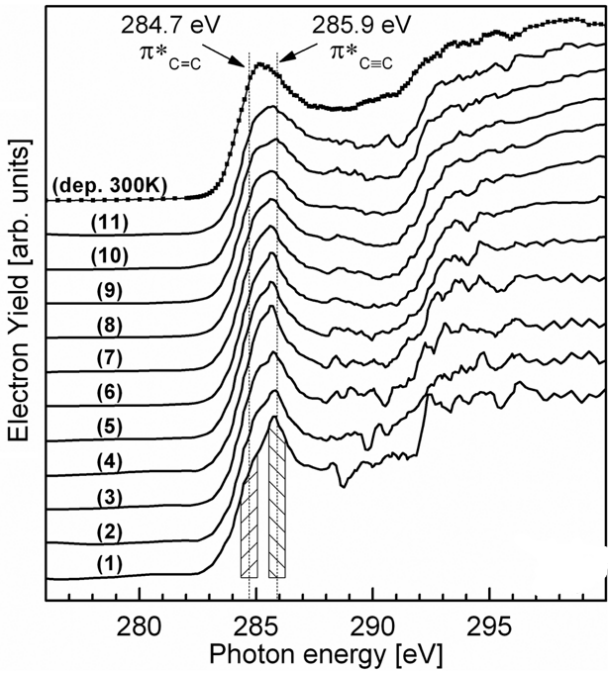

Figure 3.5: NEXAFS spectra of the free NPs acquired in the 11 delay time windows compared to the in situ NEXAFS spectrum of the NP assembled film deposited at RT (dep. 300 K). The acetylene and ethylene π^* resonances are indicated as dotted lines [64].

where $A[\pi^*_{C\equiv C}]$ and $A[\pi^*_{C=C}]$ are integral intensities from the spectra in fig. 3.5 in two 0.6 eV wide energy windows centered at 284.7 eV and 285.9 eV, respectively (shaded regions in fig. 3.5). Thanks to this definition X_{sp} is the percentage of the integrated intensity of the NEXAFS spectra in the energy region relative to the π^* resonance for *sp* hybridization, in respect to the integrated intensity in the regions relative to both sp^2 and *sp* hybridizations. As can be see in fig.3.5, which reports NEXAFS spectra acquired at different delays (the delay time is the residence time of the NPs in the cavity plus a small interval due to the time of flight from the source to the interaction region), free carbon clusters contain an amount of *sp* carbon atoms as a function of the residence time in the source. This is due to the aggregation of primary clusters, which remains longer in the source, that induces the graphitization of *sp* carbon atoms. As a consequence, the less a cluster stays inside the source, the more is the fraction of *sp* carbon atoms (see fig.3.6). The deposition process at room temperature further provides, due to the thermal energy released during the impact onto the substrate, the re-oganization of a large number of *sp*CCs in more stable sp^2 structures.

This NEXAFS measurements demonstrated the *sp* hybridization of free carbon clusters and clarified the evolution of their structure on a millisecond time scale under low temperature conditions in an inert atmosphere. These results confirm the prediction of the TBMD simulation carried out by Yamaguchi [60]about the growth of *sp*-sp^2 clusters in the *PMCS* and show that free carbon nanoparticles can have a complex structure with varying relative amounts of *sp* and sp^2 bonds.

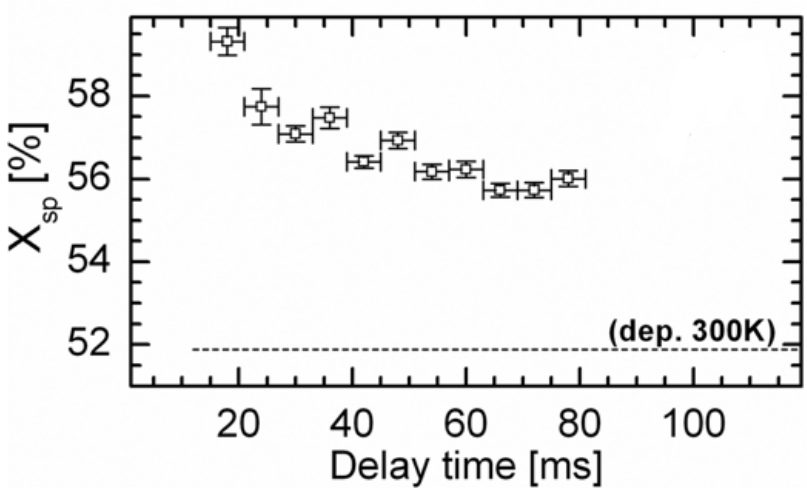

Figure 3.6: Evolution of the *sp* carbon atoms fraction with the delay time; for the deposited film is the *sp* fraction is indicated as a dashed line [64].

3.2 Synthesis of sp-sp^2 pure carbon films

3.2.1 Supersonic Cluster Beam Deposition

The crucial point for obtaining a cluster assembled sp-sp^2 pure carbon film, is that metastable clusters should not break during the deposition process. Thus it is necessary for the kinetic energy per atom to be smaller than the cohesive energy per atom of the cluster, otherwise during the deposition it would released enough energy for the graphitization of the metastable cluster [65]. As a consequences, the fundamental parameter that controls the deposition regime is the kinetic energy/atom of the cluster (k) compared to the cohesive energy/atom of the cluster (ϵ). The tendency of the clusters to preserve their structures or to fragment during the impact onto the substrate, their mobility on the substrates surface and the morphology of the deposited thin films strongly depend from these quantities. One should consider two limit cases:

- *LECBD*, Low Energy Cluster Beam Deposition: cluster deposit on the substrate with $k \ll \epsilon$. In this case deposited clusters preserve their original structure (memory effect, see fig.3.7). Cluster assembled film obtained in this regime are characterize by high porosity and half density with respect of bulk films.
- *HECBD*, High Energy Cluster Beam Deposition: In this case deposited clusters do not preserve their original structure, that is $k \gg \epsilon$. With such an high kinetic energy, during the impact with the substrate the clusters completely break, loosing their pristine structure. Cluster assembled film obtained in this regime are characterize by an high adhesion to the substrate and have the same density of the bulk films.

In order to obtain an sp-sp^2 pure carbon films it is necessary to deposit carbon cluster produced with the *PMCS* with a LECBD technique. Among LECBD techniques, Supersonic Cluster Beam Deposition (*SCBD*) attracted much interest in the last decade. The

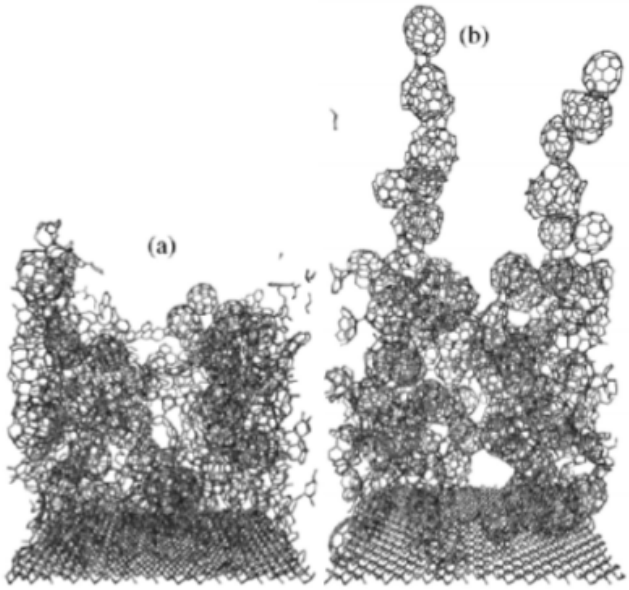

Figure 3.7: Tight Binding Molecular Dynamic simulation of low energy deposition of a carbon cluster beam characterized by a bi-modal mass distribution. Carbon aggregates are in form of chains and rings until 23 atoms and cages until 146 atoms. The ratio between the two modes is 5 : 1 in a) and 10 : 1 in b)

use of supersonic beams of clusters allows a stronger control of the cluster mass distribution and kinetic energy with the possibility to obtain very high deposition rates [66] and very collimated beams [67]. As described in the previous section, by exploiting simple aerodynamic effects, one can control the divergence of the supersonic beam and the mass distribution of the particles in it (this allows to tailor the properties of the produced films [68]).

By producing carbon clusters with the PMCS ($k \sim 0.3$eV/atom, $\epsilon \sim 7eV$/atom) and depositing them by using SCBD, it is then possible to obtain an high collimated cluster beam whose deposition leads to the synthesis of *sp*-sp^2 pure carbon films. D. Donadio *et al.* have demonstrated, through Tight Binding Molecular Dynamic (TBMD) simulations, that the structure of fullerenic precursors is preserved after the deposition in a SCBD regime (fig.3.7) [69]. Although in these simulations *sp* phase has not be taken into account, the results indicate that the sp^2 cages (which contains *sp*CCs) do not break during a deposition in the low kinetic energy regime, thus preserving their pristine structure (memory effect).

In fig.3.8 is reported the NEXAFS spectrum of a *sp*-sp^2 pure carbon film obtained by depositing by *SCBD* carbon cluster produced with the *PMCS* [64]. As can be clearly see a fraction of *sp*CCs survives after the impact onto the substrate at room temperature. A graphitization process can be induced by increasing the substrate temperature till 350K, thus providing another proof of the metastability of the *sp*CCs embedded in the sp^2 matrix [70, 71, 64].

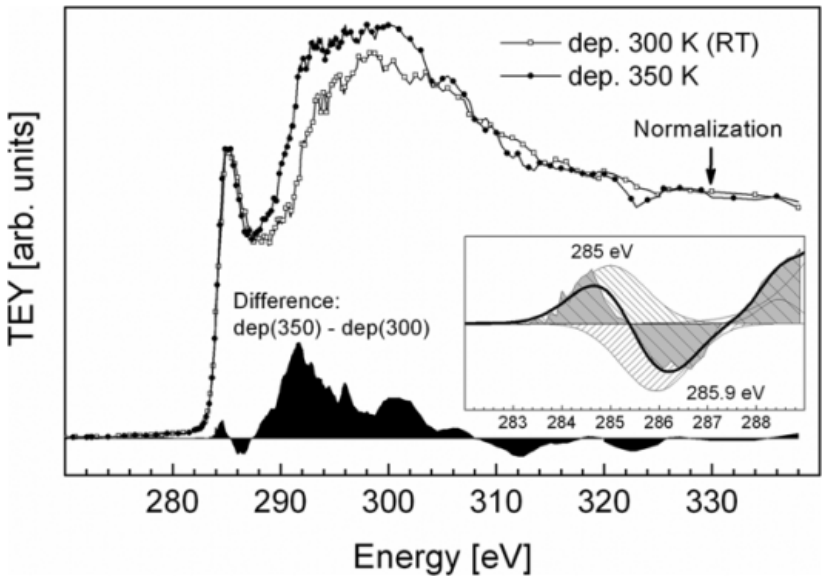

Figure 3.8: Total electron yield NEXAFS spectra (normalized to the post edge region as indicated by the arrow) of NP assembled films deposited at 300 K (RT) and at 350 K. The difference spectrum is indicated in black, and its Gaussian fit is shown in the inset [64]

Part II

Methods

Chapter 4

Multi-wavelength resonant-Raman spectroscopy

4.1 The Raman effect: classical description

The Raman effect is a scattering process where photons interacts with molecular or lattice vibrations of molecules and solids respectively. This effect can thus be exploited for the identification of species/materials form their vibrational features. Raman spectroscopy is based on the analysis of the spectrum resulting form the scattering between the incident radiation and the sample. The major part of the photons will emerge with the same energy and momentum, as they experienced elastic scattering process, while only few of them will suffer inelastic scattering, thus loosing or gaining some energy (i.e. slightly longer or shorter wavelength respectively).

For concision I'm going to present the classical description of the Raman effect of molecules, then it is possible to easily extend the findings to bulk systems.

Form a classical point of view the Raman effect can be described by considering that the polarizability $\vec{\alpha}$ of a molecule can vary due to normal modes vibrations $\vec{Q}$, and thus as a first approximation the polarizability can be written as expansion in powers of the normal modes vibrations:

$$\vec{\alpha}(\vec{\mathbf{k}}, \omega, \vec{Q}) = \vec{\alpha_0}(\vec{\mathbf{k}}, \omega) + \frac{\partial \vec{\alpha}}{\partial \vec{Q}}(\vec{\mathbf{k}}, \omega) \cdot \vec{Q} + \dots \tag{4.1}$$

where $\vec{\mathbf{k}}$ and ω are the wavevector and the frequency of an incident electric field:

$$\vec{E}(\vec{\mathbf{r}}, t) = \vec{E_0} \cos(\vec{\mathbf{k}} \cdot \vec{\mathbf{r}} - \omega_i t). \tag{4.2}$$

Then one can consider a normal mode represented by a cosinusoidal function

$$\vec{Q}(\vec{\mathbf{s}}, t) = \vec{Q_0} \cos(\vec{\mathbf{q}} \cdot \vec{\mathbf{s}} - \omega_0 t) \tag{4.3}$$

where $\vec{\mathbf{q}}$ and $\vec{\mathbf{s}}$ are the wavevector and the frequency of the normal mode, then by substituting eq. 4.2 and 4.3 and remembering the general equation of the electric dipole given by oscillating charges $P = \vec{\alpha} \cdot \vec{E}$, we obtain

$$\begin{aligned}\vec{P} = \vec{\alpha_0} \cdot \vec{E_0} \cos(\vec{\mathbf{k_i}} \cdot \vec{\mathbf{r}} - \omega_i t) + \\ + \frac{\partial \vec{\alpha}}{\partial \vec{Q}}(\vec{\mathbf{k}}, \omega) \cdot \vec{Q}(\vec{\mathbf{q}}, \omega_0) \cdot \vec{E_0} \cos[(\vec{\mathbf{k_i}} + \vec{\mathbf{q}}) \cdot \vec{\mathbf{r}} - (\omega_i + \omega_0)t] + \\ + \frac{\partial \vec{\alpha}}{\partial \vec{Q}}(\vec{\mathbf{k}}, \omega) \cdot \vec{Q}(\vec{\mathbf{q}}, \omega_0) \cdot \vec{E_0} \cos[(\vec{\mathbf{k_i}} - \vec{\mathbf{q}}) \cdot \vec{\mathbf{r}} - (\omega_i - \omega_0)t].\end{aligned} \tag{4.4}$$

The first term on the right hand of the equation above is the one describing the elastic scattering between the incident photons and the normal mode of the system (Reyleight scattering). Photons experiencing this kind of process are diffused with the same energy and momentum as before as the scattering occurs. The second term is related to process where a photons emerge with energy greater than the before the scattering (anti-Stokes process) due to phonon emission while the last term is the case where photons loose energy due to the phonons absorption (Stokes process). One should notice that Raman effect occurs if and only if state that:

$$\frac{\partial P}{\partial Q} \neq 0 \tag{4.5}$$

otherwise only elastic scattering is accessible.

Then by introducing a unit vector in direction $\hat{Q} = \frac{Q}{|Q|}$ of the lattice displacement, it is possible to define the Raman tensor as:

$$\vec{R} = (\frac{\partial \vec{\alpha}}{\partial \vec{Q}}) \cdot \hat{Q} \tag{4.6}$$

Assuming $\hat{e}_i$ and $\hat{e}_s$ to be the unit vectors of the polarization of the incoming and scattered light, respectively, the Raman scattering intensity I is proportional to $|\hat{e}_i \cdot \vec{R} \cdot \hat{e}_s|^2$ and consequently to the squared absolute value of the partial derivative of the polarization $\vec{\alpha}$ over the lattice vibrational patterns. In order to have Raman effect, it is thus necessary that $\frac{\partial \vec{\alpha}}{\partial \vec{Q}} \neq 0$ at the equilibrium vibrational position Q_0.

However this classical description is useful just to understand the origin of the Raman effect as inelastic scattering process, but it completely fails in describing the difference observed between experimental Stokes and anti-Stokes peak intensities and the strong enhancement of the Raman signal as the incident photon energy match an electronic transition.

4.2 The resonant Raman effect: quantum-mechanical description

As mentioned in previous section, the classical description of the Raman effect is not sufficient to understand all the features one can observe during Raman experiments. First of all the intensity of Stokes and anti-Stokes is not the same, in particular processes involving the phonon absorption (Stokes, initial state is the ground state) are more intense than the ones characterized by the emission of a phonon (anti-Stokes, the initial state is an excited vibrational state). This can be understand by considering the ratio between the vibrational ground state and the vibrational excited states at room temperature:

$$\frac{I_{anti-Stokes}}{I_{Stokes}} = \frac{N_1}{N_0} = \frac{g_1}{g_0} \exp^{-\frac{\Delta E_\nu}{K_b T}} . \tag{4.7}$$

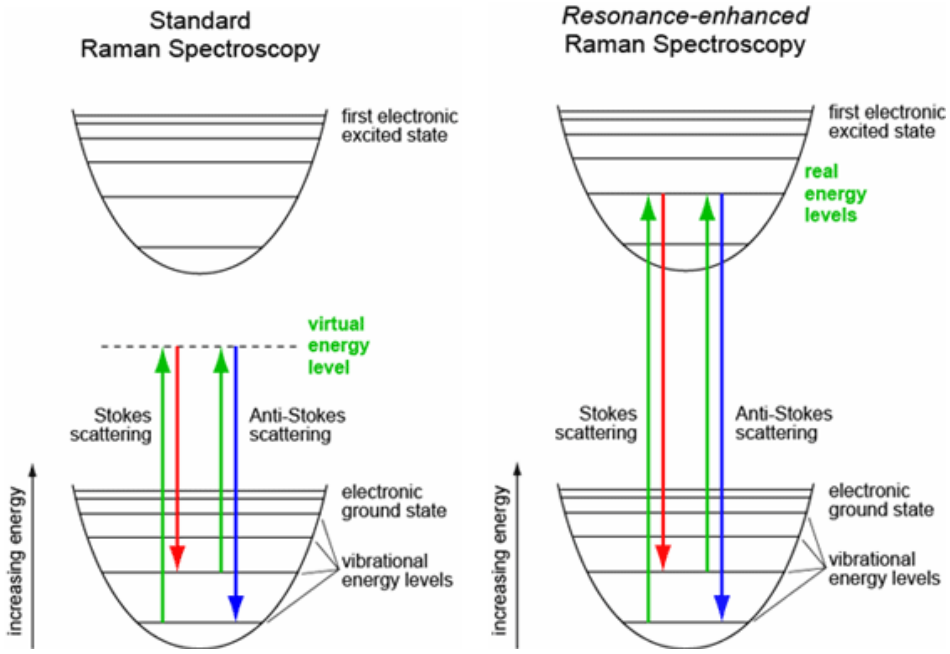

Figure 4.1: (a) scheme of non-resonant Raman scattering where the electronic transition are between virtual states;(b) the resonance Raman effect occurs when electronic transition are between actual electronic excited states

where N_0 and N_1 are the population of the vibrational ground state and the excited state respectively, g_0 g_1 the related degeneracy ΔE_ν is the energy difference between these two states. It is thus clear that as at room temperature $\Delta E_{e-m} \gg K_b T$, then the vibrational ground state is much more populated than any excited ones and therefore transitions involving the vibrational ground state as initial state have an higher probability to occur, i.e. they are more intense. In fig.4.2(a) the non resonant Stokes and anti-Stokes process are sketched.

A little bit more complex is the case of the activation of the resonance effect. For the comprehension of such an effect it is necessary to calculate, by using the perturbation theory, the Raman cross-section $\frac{d\sum}{d\Omega} \propto |\alpha_{nm}|^2_{\rho\sum}$ where:

$$|\alpha_{nm}|_{\rho\sigma} = \frac{1}{\hbar}\sum_{Rr}[\frac{\langle nG|\hat{M}_\rho|Rr\rangle\langle Rr|\hat{M}_\sigma|Gm\rangle}{\nu_{Rr} - \nu_k - \nu_0 + i\gamma_r} + \frac{\langle rR|\hat{M}_\sigma|Gm\rangle\langle nG|\hat{M}_\rho|Rr\rangle}{\nu_{Rr} - \nu_k + \nu_0 + i\gamma_r}] \tag{4.8}$$

where $\hat{M}_\rho(\hat{M}_\sigma)$ is the electronic transition dipole moment in terms of a molecule fixed coordinate system [72], ν_0 and ν_k are the frequency of the excitation radiation and the normal mode Q_k respectively, and the indices "R" and "r" are related to electronic and vibronic states (the damping factor γ_r is the correspondent lifetime). One should note that for the Raman transitions all vibronic states have to be considered and thus Raman intensity is given by the transition probabilities involving all states, even though those referred to the electronic ground state. If the exciting energy $h\nu_0$ is small compared to the energy of any vibrational transition $h\nu_{Rr}$ one can neglect the damping term and

determine the relative weights of the individual terms in the previous equation as given by the denominators. In these conditions, the contributions of the four electronic states to the scattering tensor are comparable. On contrary, if the incident photon energy approaches the energy of an electronic transition, then for this specific transition the term $(\nu_{Rr} - \nu_k - \nu_0)^{-1}$ dominates over all other terms in the sum. These are the conditions of the resonant Raman effect and eq.4.8 can be simplified as follows:

$$|\alpha_{nm}|_{\rho\sigma} = \frac{1}{\hbar} \sum_{Rr} [\frac{\langle nG|\hat{M}_\rho|Rr\rangle\langle Rr|\hat{M}_\sigma|Gm\rangle}{\nu_{Rr} - \nu_k - \nu_0 + i\gamma_r} \tag{4.9}$$

where summation is now restricted to the vibrational states r of the resonant electronically excited state. Then, by using the Born-Oppenheimer approximation it is possible to separate the ionic and the electronic coordinates, thus obtaining a further simplification of eq.4.9:

$$|\alpha_{nm}|_{\rho\sigma} \approx \frac{1}{\hbar} \sum_{r} [\frac{\langle nR\rangle\langle rm\rangle\hat{M}_{GR,\rho}\hat{M}_{GR,\sigma}}{\nu_{Rr} - \nu_k - \nu_0 + i\gamma_r}]. \tag{4.10}$$

The electronic transition dipole moment components $\hat{M}_{GR,\rho}$, related to the resonant electronic transition between the ground state G and the excited state R, can be expanded in Taylor series over the normal coordinates Q_k and, within the harmonic approximations by neglecting higher order terms, thus obtaining the scattering tensor as the sum of two terms, the AlbrechtÕs A- and B-terms [72].

$$|\alpha_{nm}|_{\rho\sigma} \approx A_{\rho\sigma} + B_{\rho\sigma}. \tag{4.11}$$

For the sake of brevity, it is now enough to remind that both the two terms represent different scattering mechanisms but the leading parameter for the two terms are the dominators which rapidly vanishes as the excitation energy approaches the frequency of an electronic transition. If $\hat{M}^0_{GR}$ term is large, then the A term which scales as $|\hat{M}^0_{GR}|^2$, increase more rapidly than the B term and thus it is the leading term. As a result the phonon intensity enhancement strictly depends on the factor $\langle nR\rangle\langle rm\rangle$ (Franc-Condon term) and therefore on the geometry of the excited state involved in the resonant transition.

On the other hand, also the B term can be responsible of the enhancement of the Raman intensity. For this kind of resonance, the crucial parameters is the derivative of the dipole moment with respect of the normal mode coordinate [72]. This term is the leading one for those modes that can effectively couple to an electronic transition and thus may gain Raman intensity even when the resonant electronic transition is relatively weak.

Beyond these formal treatment, one has to note that the border between non-resonant and resonant Raman effect is not sharp. Indeed it is not necessary that the incident photon energy exactly matches the energy of an electronic transition, but in order to obtain the enhancement of these modes it is enough that the exciting frequency is relatively close to the maximum of the electronic transition. It is possible to compare the non-resonant intensity with the resonant one (considering A term mechanism); for the latter it is possible to obtain a simplified version for Stokes scattering under pre-resonance conditions, that is by neglecting the damping factor (i.e., $\nu_r - \nu_0 \gg \gamma r$):

$$I_{nm,RR} \approx (\nu_0 - \nu_k)^4 \frac{(\nu_0 - \nu_k)^2(\nu_0^2 - \nu_R^2)}{(\nu_R^2 - \nu_0^2)^2}. \tag{4.12}$$

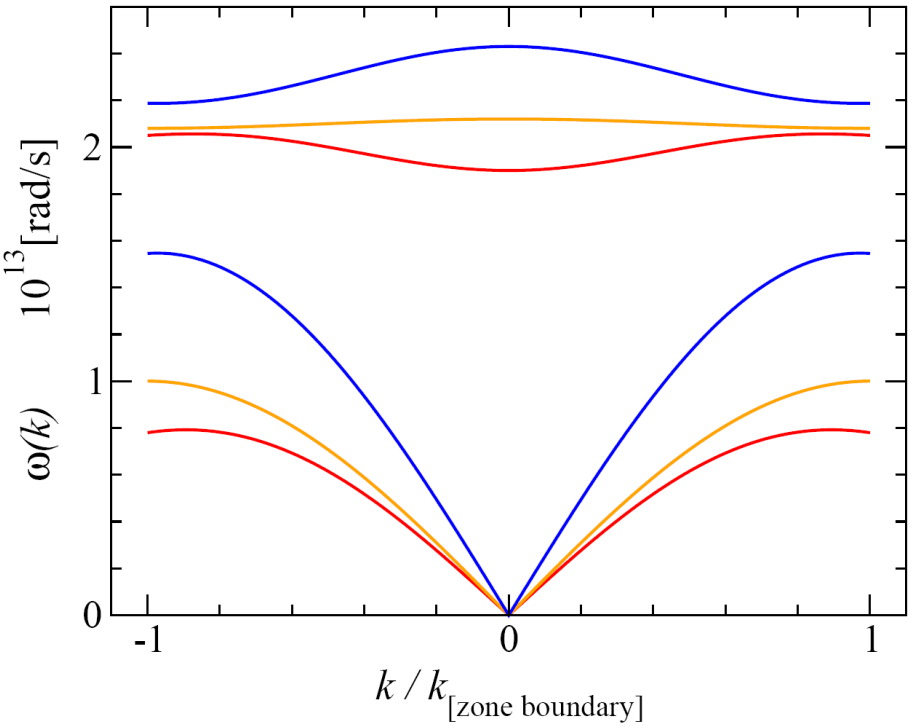

Figure 4.2:

Now one can evaluate non-resonant and resonant Raman intensity by considering the resonant transition RR and the non-resonant transition Ra and by considering the ratio:

$$\frac{I_{nm,RR}}{I_{nm,Ra}} \approx \frac{(\nu_0 - \nu_k)^2(\nu_0^2 - \nu_R^2)}{(\nu_R^2 - \nu_0^2)^2}. \tag{4.13}$$

which represents the resonance enhancement. This value can vary from 10^2 even to 10^6 for rigorous resonance conditions (for which eq.4.13 doesn't hold anymore) depending on the other quantities that control the scattering tensor, i.e., the Franck-Condon factor products, the square of the electronic transition dipole moment, and the damping constant. Generally speaking one can state that the intensity gain given by exploiting resonance effect scales with the square of the extinction coefficient of the electronic absorption band at the excitation line. As a consequence the Raman intensity increases thanks to the resonance effect and become comparable to that of UV-vis absorption spectroscopy.

For a complete and exhaustive quantum treatment of the resonant Raman effect, please look at here [72].

4.3 Resonant Raman spectroscopy

As briefly described before, Raman spectroscopy is a powerful technique for the study of the vibrational properties of molecules and solids. A typical Raman spectrum is

composed by the Reyleight component (elastic scattering) and Stokes features which are shifted from the elastic one by the energy related to the absorption of one phonon (Raman shift).

Let us now focus on what happens with solids where lattice vibrational modes are quantized (phonons) and thus they are propagating waves characterized by a dispersion relation $\omega|\mathbf{k}| = f(\mathbf{k})$. From the conservation of energy and linear momentum during the inelastic scattering process it follows that:

$$\mathbf{k}^{inc} = \mathbf{k}^{sc} + \sum_{i=1}^{N}(-1)^{\alpha_i}\mathbf{k}_i^{ph} \tag{4.14}$$

$$\hbar\omega_{inc} = \hbar\omega_{sc} + \sum_{i=1}^{N}(-1)^{\alpha_i}\hbar\omega_i(\mathbf{k}_i^{ph}) \tag{4.15}$$

where α is 1 is a photon is destroyed and 0 if it is created. By considering that the photon momentum is quite small with respect of the phonon one, equation 4.15 becomes:

$$\sum_{i=1}^{N}(-1)^{\alpha_i}\mathbf{k}_i^{ph} \approx 0 \tag{4.16}$$

and considering only the first order process eq.4.16 also provide Raman selection rules similar to those of bi-atomic molecule:

$$\begin{aligned} \mathbf{k}^{phonon} &\approx 0 \\ (|\hbar\omega_{inc} - \hbar\omega_{sc}|) &= \hbar\omega(\mathbf{k}^{ph}). \end{aligned} \tag{4.17}$$

As a consequence phonos produced by inelastic scattering are characterized by null momentum and energy given by the Raman shift. As reported in fig.4.2 only one phonon energy is detectable by first order Raman, corresponding to the crossing of the dispersion curve with the $k = 0$ axis, i.e. the Γ point of the first Brillouin zone. Typical energies for optical phonons are about few meV.

It is interesting to notice that in a solid the number of vibrational modes grows as $3N - 3$, where N is number of atoms in the unit cell, and their classification is based on the irreducible representation of the crystal structure. Remarkably with $N = 1$ optical modes are not present while they occur from $N > 1$ and only some of them are detected by Raman spectroscopy.

As described in the previous sections, Raman effect occur only if an anisotropic variation of the polarization is induced by the interaction between lattice vibrations and the incident electromagnetic field. By summarizing these observations, one can conclude that with Raman spectroscopy it is possible to detect phonons having $k = 0$ and whose lattice vibrational patterns provide $\frac{\partial\alpha}{\partial Q} \neq 0$ at the equilibrium position.

Although not all the vibrational modes of a system are Raman active, some of them can nevertheless absorb electromagnetic radiation. This is the case of infrared absorption where photons in the infrared range of the electromagnetic spectrum can be directly absorbed (this is not a scattering technique) by the material in order to create a phonon with the same energy. For what concerns the distinction of Raman and infrared active modes, it cannot be found a rule which holds for all the cases but, if the inversion is included in the group of symmetry of the crystal, then it holds that Raman and infrared active modes are complementary.

In the previous section I demonstrated how by changing the energy of the exciting photons it is possible to exploit the resonance effect. In case of mixed system made of molecules, it means that the strong enhancement will occur only for those Raman active vibrational modes whose electronic bonding state is resonant. By resonant Raman spectroscopy it is thus possible to "bond-selectively" study the vibrational states of molecules for which the bonding electrons have discrete energy level and thus resonance occurs for well defined photons energy. Regarding solid state systems, electronic transitions are responsible for the production of lattice phonons and involve states belonging to the valence band. Indeed, electrons in solids are not discretize as in molecules, but they occupy a continuum of states, i.e. energy bands $E(\mathbf{k})$, up to the Fermi energy. Both for low-gap semiconductors (E_F is between valence and conduction band), metals (E_F cross one or more bands) and semi-metals (conduction and valence band coincide at least in one k-point in the Brillouin zone), resonance effect occurs since there are electrons which can be promoted in an unoccupied state in the conduction band. In solids where are present mixed covalent bonds (i.e. solids where different hybridizations coexist), resonant Raman effect can cause the variation of the intensity ratio between different peaks if different excitation wavelength are used. Thus by performing multi-wavelength resonant Raman spectroscopy also the electronic structure (i.e. the optical gap) of the investigated system becomes accessible and it is also possible to distinguish between vibrational modes associated to different bonds having different resonant behavior.

In practice, the Raman effect has a very weak cross section, namely during Raman measurement of solid state samples one has for 1 photon elastically scattered only 10^{-7} Raman photons. This is way one should use monochromatic source, i.e. lasers, notch filters to remove Reyleight scattering as much as it is possible, a monochromator to well separate elastic and inelastic scattered photons and an efficient detector capable to identify also very weak signal, usually a CCD (charge coupled device).

Chapter 5

Infrared Spectroscopy

5.1 Infrared absorption

As briefly mentioned in the previous section, another powerful technique for the study of the vibrational properties of a system is infrared (IR in the following) spectroscopy. Despite Raman spectroscopy, IR is not a scattering based technique but rather an absorption technique and thus it is controlled by the electrical dipole moment operator $\hat{\mu}_q$ defined as:

$$\hat{\mu}_q = \sum_a \mathbf{e}_\alpha \mathbf{q}_\alpha \tag{5.1}$$

where $\mathbf{e}_\alpha$ is the effective charge at the atom a and $\mathbf{q}_\alpha$ is the distance to the centre of gravity of the molecule in Cartesian coordinates. As for the Raman effect, I present a rigorous treatment of the infrared absorption valid for molecules, then in can be extend to solids with some modifications. In order to have IR absorption for a certain transition $n \longrightarrow m$, it has to occur that the associated transition dipole moment $[\hat{\mu}_q]_{mn}$ is non-zero. In order to check if a vibrational mode is IR active, we can expand $\hat{\mu}_q$ in Taylor series with respect of normal coordinates Q_k and, within the harmonic approximation, and we can consider just the linear terms:

$$\hat{\mu}_q = \mu_q^0 + \sum_{k=1}^{3N-6} \hat{\mu}_q^k Q_k \tag{5.2}$$

where:

$$\hat{\mu}_q^k = \left(\frac{\partial \mu_q}{\partial Q_k}\right)_0 . \tag{5.3}$$

Now by evaluating the mean value of the transition dipole moment we obtain:

$$[\hat{\mu}_q^k] = \langle \psi_m^* | \hat{\mu}_q^k | \psi_n \rangle = \mu_q^0 \langle \psi_m^* \psi_n \rangle + \sum_{k=1}^{3N-6} \hat{\mu}_q^k \langle \psi_m^* | Q_k | \psi_n \rangle. \tag{5.4}$$

The first term on the right-hand side of eq.5.4 vanishes as ψ_m and ψ_n states are orthogonal. As a result, in order for a phonons to be IR active, two conditions have to hold: (i) the derivative of the dipole moment with respect to the normal coordinate Q_k in eq.5.4 must be non-zero, which requires that the normal mode is associated with a change in the dipole moment (ii) the integral $\langle \psi_m^* | Q_k | \psi_n \rangle$ must be non-zero, which is the situation when the vibrational quantum numbers n and m differ by one.

5.2 Fourier-Transform Infrared spectroscopy

Infrared absorption by molecules, liquids and solids can be measured by using two different spectrometric families: dispersing and interferometric spectrometers. Fourier-Transform infrared spectroscopy (FT-IR in the following) belong to the second families and is characterized by many advantages with respect of dispersing technique:

- *Fellget* advantage: FT-IR collects all resolution elements with a complete scan of the interferometer. Successive scans of the FT-IR instrument are co-added and averaged to enhance the signal-to-noise of the spectrum. When spectra are collected under identical conditions on dispersive and FT-IR spectrometers, the signal-to-noise ratio of the FT-IR spectrum will be greater than that of the dispersive IR spectrum by a factor of $\sqrt{M}$, where $\sqrt{M}$ is the number of resolution elements. For instance, a 2 cm^{-1} resolution $800 - 8000$ cm^{-1} spectrum measured in 30 minutes on a dispersive spectrometer, by using a FT-IR one it is possible to collect a spectrum, with the same S/N ratio, in just 1 second;

- *Connes* advantage : an FT-IR spectrometer uses a HeNe laser as an internal wavelength standard. The infrared wavelengths are calculated using the laser wavelength, itself a very precise and repeatable standard. As a consequence the assignment of the vibrational features present in the spectrum is very repeatable and reproducible;

- *Jacquinot* advantage: FT-IR uses a combination of circular apertures and interferometer travel to define resolution. To improve signal-to-noise, one simply collects more scans;

on the other hand, there are also some disadvantages:

- FT-IR collects interferograms, not spectra. In order to convert an interferogram into a spectrum a Fourier transform has to be used. The main issue is how the transformation is performed, since it can affect the spectrum itself, and thus care must be taken ;

- *Fellget* disadvantage : all regions of the spectrum are observed simultaneously and thus, if noise occurs in one part of the radiation from the infrared source, it will be spread throughout the spectrum in an FTIR system;

- FT-IR are single beam spectrometer. If the experiment takes long time, changes in the experiment conditions can affect the results;

It is interesting to notice that the intrinsic problems of FT-IR spectroscopy can be easily fixed by some observation. First of all at present day thanks to the dramatic increase of computers performances, performing Fourier transform is a quick and easy process. Secondly, by using detectors noise-limited (as in the Mid-IR case) then the Fellget advantage applies but not the Fellget disadvantage. For the last point, it is much safer, in order to preserve the experiment validity, to maintain the optical path in vacuum conditions (namely at least 10^{-1} mbar) or, if this it is not possible, to flux IR inactive gases, as for instance N_2, in order to clean the optical path form CO_2 and H_2O mostly.

5.2.1 Theory

In this section I briefly report the basic principle of the Fourier-Transform infrared spectroscopy theory. As previously mentioned FT-IR spectroscopy is an interferometric technique and thus the crucial part of such a spectrometer is represented by the Michelson interferometer (a scheme is reported in fig.5.1), whose working principle can be sketched as follows: a light beam passes through a beamsplitter and then the emerged beams are reflected at either the movable or fixed mirror and finally they recombine at the beamsplitter to proceed to the sample and then to the detector. Now, let us consider an incoming electromagnetic field incident on the beam splitter:

$$\vec{E} = E_m \cos(\vec{k}x - \omega t) \tag{5.5}$$

where E_m is the field amplitude, ω it frequency and $k = \frac{1}{\lambda_0}$ its wavenumber (λ_0 is the corresponding wavelength). Then, the beam reflected by the fixed mirror and just after the beam splitter can be written as:

$$\hat{E}_1 = CE_m[\vec{k}x - \omega t] \tag{5.6}$$

C is a constant depending on the optical properties of the beam splitter and on the polarization. For what concerns the beam reflected by the movable mirror, the related field can be written as:

$$\hat{E}_2 = CE_m \cos[(\vec{k}(x+y) - \omega t)] \tag{5.7}$$

where "y" is the path difference. Then, by summing the two fields, using prosthaphaeresis relation for sum of cosine functions, time averaging the results and considering the difference path, or retardation δ, one obtains the intensity of the beam at the detector, i.e. the interferogram is given by:

$$I^{'}(\delta) = \frac{1}{2} I_0 (1 + \cos 2\pi \frac{\delta}{\lambda_0}) \tag{5.8}$$

This expression can be divided in two terms, a constant term $\frac{1}{2}I_0$ plus a variable term $I(\delta) = \frac{1}{2} I_0 \cos 2\pi\delta\nu_0$, with $\nu_0 = \frac{1}{\lambda_0}$, which is a function of the retardation δ induced by the interferometer. Only the variable component $I(\delta)$ is important in interferometric spectrometry and, usually, is referred to as the *interferogram*. However this results holds for ideal detector having the same response at all wavelength, ideal beam splitter and amplifier characteristics. Nevertheless it is possible to group all these corrective factors, plus the intensity of the source at a given frequency in a coefficient $B(\nu_0)$, i.e. the single beam spectral intensity. This parameter gives the intensity of the source at the given wavenumber ν_0 as modified by the instrument characteristic. As a consequence eq.5.8 can be rewritten as follows:

$$S(\delta) = B(\nu_0) \cos 2\pi\delta\nu_0 \tag{5.9}$$

and mathematically now $S(\delta)$ is nothing but the cosine Fourier transform of $B(\nu_0)$. As the source is a continuum, $S(\delta)$ become an integral over the whole retardation δ:

$$S(\delta) = \int_{-\infty}^{+\infty} B(\tilde{\nu}) \cos 2\pi\delta\tilde{\nu} d\tilde{\nu} \tag{5.10}$$

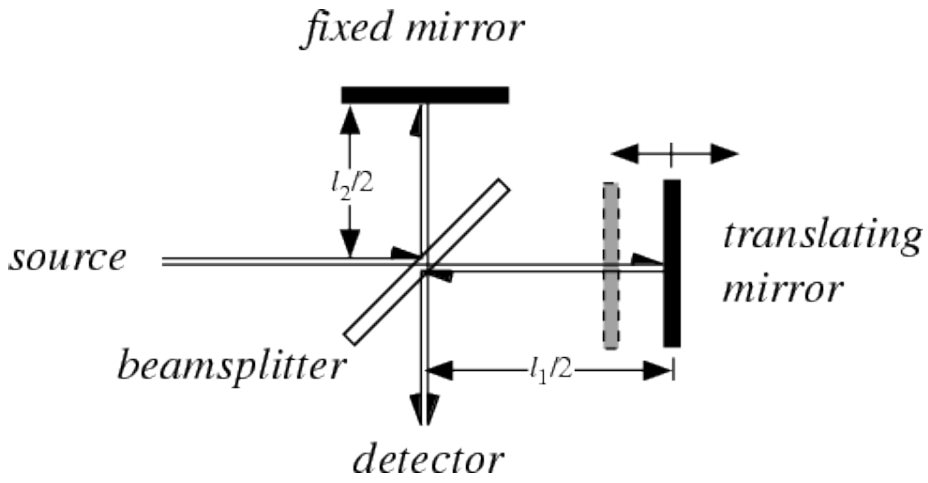

Figure 5.1:

and the inverse transform gives the response in the frequency domain:

$$B(\tilde{\nu}) = \int_{-\infty}^{+\infty} S(\delta) \cos 2\pi\delta\tilde{\nu} d\delta. \tag{5.11}$$

Finally we notice that the integrand is an even function, thus the integral in eq. 5.12 can start from 0 and furthermore that in actual measurement, it is not possible to explore all the retardation, as a consequence the upper limit of the integral cannot be ∞:

$$B(\tilde{\nu}) = \int_{0}^{\nu_M} S(\delta) \cos 2\pi\delta\tilde{\nu} d\delta. \tag{5.12}$$

As a result, this frequency limitation implies that the resulting spectrum will have a finite resolution. For a deep and detailed formal description about FT-IR, please look at here [73].

Chapter 6

Computational method

6.1 The Density Functional Theory

In condensed matter physics and chemistry one of the most important issue is the many-electron problem, that is how can be exactly found the ground state of a system where electron interacts with themselves, with ions and, in some case, with an external perturbation. The Density Functional Theory (DFT in the following) [74, 75]is a ground-state theory developed to approximate in the more precise way the ground state of many-electron wavefunction $\Psi_G(\vec{r}_1\sigma_1, \ldots, \vec{r}_n\sigma_n)$. DFT is based on the assumption that the relevant physical quantity is the ground-state one-body electron density, despite of the ground-state wavefunction. As a result DFT, by providing the solution of a one-electron Schrödinger equation with a local effective potential, finds the ground-state properties of the many-electron system. In this section I show the fundamental basis for the development of DFT, that is the two Hoenberg-Kohn theorems and the consequent Kohn-Sham equations which determine the exact electron density and energy of the ground state of the system.

T 1 First Hoenberg-Kohn Theorem *There is a one-to-one correspondence between the ground-state density of a N electron system and the external potential acting on it.*

In other words, given an interaction between electrons U_{ee}, the external potential $\mathrm{V}_{ext}(\mathrm{r})$, and thus the total energy, is a unique functional of the electron density $\rho(\mathrm{r})$. The ground-state properties is thus determined by the electron density and the total energy of the system can thus be written as:

$$E^{HK}[\rho(\mathbf{r})] = V_{ext}[\rho(\mathbf{r})] + T[\rho(\mathbf{r})] + U_{ee}[\rho(\mathbf{r})] + \int \rho(\mathbf{r}) V_{ext}(\mathbf{r}) d\mathbf{r} + F_{HK}[\rho(\mathbf{r})] \qquad (6.1)$$

where $T[\rho(\mathbf{r})]$ is the kinetic energy, $V[\rho(\mathbf{r})] = V_{ext}[\rho(\mathbf{r})] + U_{ee}[\rho(\mathbf{r})]$ is the potential energy. The H-K functional $\mathrm{F}_{HK}[\rho(\mathbf{r})]$ depends only on the electron density of the system.

T 2 Second Hoenberg-Kohn Theorem *The ground-state energy can be obtained by a variational approach: the density that minimizes the total energy is the exact ground-state density.*

As previously mentioned, DFT reduces the many-body problem to the determination of a functional $\rho(\mathbf{r})$ which minimizes $E[\rho(\mathbf{r})]$. This result is only apparently exact as

the functional which contains the exchange-correlation term $\mathrm{F}_{HK}[\rho(\mathbf{r})]$ is not exactly known. Although the H-K theorems are extremely powerful, they do not offer a way of computing the ground-state density of a system in practice.

Kohn and Sham devised a simple way to overcome this limit by preserving the exact nature of DFT. K-S equation are derived by minimizing $E^{HK}[\rho(\mathbf{r})]$ with respect of the density $\rho(\mathbf{r})$. The starting point is to imagine a fictitious system of non-interacting electrons, whose ground-state density $\rho_0(\mathbf{r})$ equals $\rho(\mathbf{r})$. Indeed the H-K theorem applies to any electron system, no matter if it is interacting or non-interacting and, for the non-interacting electrons it guarantees the existence and unicity of an external potential $v^0_{ext}(\mathbf{r})$ producing the ground-state density $n_0(\mathbf{r})$. The ground-state wavefunction of the non-interacting electrons is just the Slater determinant $A\{\phi_1\phi_2\dots\phi_N\}$ of the orbitals ϕ_i of the lowest energy of the system. The related ground state density is the defined as $\rho_0(\mathbf{r}) = \sum_i \phi_i^*(\mathbf{r})\phi_i(\mathbf{r})$. As $\rho_0(\mathbf{r})$ and $\rho(\mathbf{r})$ are equal the previous decomposition holds also for the interacting electrons provided that exact ground-state of an interacting system is not the Slater determinant formed with the orbitals contributing to $\rho(\mathbf{r})$.

Once extracted the Hartree and the kinetic term from the expression of the functional 6.1, then it can be written as:

$$E^{HK}[\rho(\mathbf{r}); V_{ext}(\mathbf{r})] = T_0[\rho] + V_H[\rho] + \int \rho(\mathbf{r})V_{ext}(\mathbf{r})d\mathbf{r} + E_{xc}[\rho] \tag{6.2}$$

where:

$$E_{xc}[\rho] = T[\rho] - T_0[\rho] + V_{ee}(\mathbf{r}) - V_H(\mathbf{r}). \tag{6.3}$$

By applying the variational procedure to the H-K functional, for the above terms one obtains the same result he will get within the Hartree-Fock framework. The novel part is the calculation of the variation of $\delta E_{xc}(\rho)$ which is defined as:

$$\delta E_{xc}[\rho] = \int V_{xc}(\mathbf{r})\delta n(\mathbf{r})d\mathbf{r} = \int V_{xc}(\mathbf{r})\delta \sum_i \phi_i^*(\mathbf{r})\phi_i(\mathbf{r})d\mathbf{r} \tag{6.4}$$

where:

$$V_{xc}(\mathbf{r}) = \frac{\delta E_{xc}[\rho]}{\delta n(\mathbf{r})} \tag{6.5}$$

is the functional derivative of $E_{xc}[\rho]$. Then, a straightforward variational calculation of the H-K functional, combined with the statement of eq.6.4 and 6.5, leads to the K-S equations:

$$\Big[\frac{\hbar^2\nabla^2}{2m} + V_{ext}(\mathbf{r}) + V_{coul}(\mathbf{r}) + V_{xc}(\mathbf{r})\Big]\phi_i(\mathbf{r}) = \varepsilon_i\phi_i(\mathbf{r}). \tag{6.6}$$

Once K-S orbitals and energies have been determined, then it is possible to get the ground-state total energy of the many-electron system:

$$E_0 = \sum_i \varepsilon_i - \frac{1}{2}\sum_{ij}\langle\phi_i\phi_j|\frac{e^2}{r_{ij}}|\phi_i\phi_j\rangle + E_{xc}[\rho] - \int V_{xc}(\mathbf{r})\rho(\mathbf{r})d\mathbf{r}) \tag{6.7}$$

and thus any difficulties in this calculation is shifted to the reasonable guess of the exchange-correlation functional $E_{xc}[\rho]$, which is not exactly known. Although K-S equation provide the exact ground-state electron density and energy of the electron system, the ε_i orbitals energy remain just Lagrange multipliers and their identification with one-electron energies is to be justified case by case. In practice, DFT calculations based on approximate forms of E_{xc} usually tend to underestimate the energy band gap in insulators and semiconductors.

6.1.1 The Local Density Approximation

With respect of Hartree-Fock equations, obtained by approximating the total electron wavefunction with a Slater determinant, K-S ones are a set of exact equations. However, are discussed in the previous section, in the K-S framework the $E_{xc}[\rho]$ functional is not known in principle and therefore it is necessary to adopt some approximations in order to solve the K-S equation. One of the most used approximation for the exchange-correlation potential is the Local Density Approximation (LDA) which is based on the assumption that $E_{xc}[\rho]$ can be replaced by a function of the local density:

$$E_{xc}^{LDA}[\rho] = \int \varepsilon_{xc}(\rho(\mathbf{r}))\rho(\mathbf{r})d\mathbf{r} \tag{6.8}$$

In eq.6.8 $\varepsilon_{xc}(\rho(\mathbf{r}))$ represent the many-body exchange-correlation energy per electron of a uniform gas of interacting electrons with density $\rho(\mathbf{r})$, which is particularly justified in system with reasonably slowly varying spatial density $\rho(\mathbf{r})$. Then the exchange-correlation potential becomes:

$$V_{xc}^{LDA}[\rho] = \varepsilon_{xc}(\rho(\mathbf{r})) + \rho(\mathbf{r})\frac{d\varepsilon_{xc}(\rho(\mathbf{r}))}{d\rho(\mathbf{r})}. \tag{6.9}$$

Within the LDA approximation the ground-state total energy becomes:

$$E_0^{LDA} = \sum_i \varepsilon_i - \frac{1}{2}\int \rho(\mathbf{r})\frac{e^2}{|\mathbf{r}-\bar{\mathbf{r}}|}\rho(\bar{\mathbf{r}})d\mathbf{r}d\bar{\mathbf{r}} - \int \rho(\mathbf{r})\frac{d\varepsilon_{xc}(\rho(\mathbf{r}))}{d\rho(\mathbf{r})}\rho(\mathbf{r})d\mathbf{r}. \tag{6.10}$$

Since the DFT in the LDA approximation has been adopted as one of the most successful tools for the calculation of ground-state physical and chemical properties of molecular and solid-state systems, many forms of ε_{xc} have been proposed by parametrizing numerical results.

For magnetic system, in order to get the total energy of the ground state, the electronic density is split into two parts polarized in opposite way, $\rho = \rho_\uparrow + \rho_\downarrow$ and the energy is a functional of both these components, $E = E(\rho_\uparrow, \rho_\downarrow)$. This procedure is known as Local Spin Density Approximation (LSDA), and in this framework the exchange-correlation potential can be written as:

$$V_{xc}^{LSDA} = \int \rho(\mathbf{r})\varepsilon_{xc}\rho[\rho_\uparrow(\mathbf{r}), \rho_\downarrow(\mathbf{r})]d\mathbf{r}. \tag{6.11}$$

where ε_{xc} is the exchange and correlation energy of the homogeneous electron gas at density $(\rho_\uparrow, \rho_\downarrow)$. The total magnetization can be defined as:

$$M = \rho_\uparrow + \rho_\downarrow. \tag{6.12}$$

Thus, if $M = 1$ the system is completely polarized while if $M = 0$ the system is non-magnetic.

DFT-LSDA scheme provides good results for solids, whose structural and vibrational properties are well described [76, 77] with errors within a few percent. This accuracy is considered satisfactory in condensed-matter system, but it is much less so in atomic and molecular physics, that is highly inhomogeneous systems for which an approximation based on the homogeneous electron gas would hardly be appropriate. For all systems LSDA overestimates (up to $\sim$ 20% and more) cohesive energies and bond strengths

[78, 79] and then, due to the failure of KS, it also significantly underestimates band gaps (up to 50%). As a consequence it fails in the accurate reproduction of both phonons frequencies and the true band/HOMO-LUMO gaps in solids/molecules respectively.

However, also considering these intrinsic failures of the DFT-LSDA framework, the *sp*-sp^2 system analyzed in this thesis is characterized by very large vibrational features (up to (100 cm^{-1})), thus making negligible errors of 1% or 2% (10-20 cm^{-1})) in phonons calculations. Also for what concerns HOMO-LUMO gap calculations of dinaphthylpolyynes, what is remarkable is the reproducibility of its trend as a function of the chains length, rather than the accurate matching with experimental values.

6.1.2 The Plane-Waves basis set and Pseudopotential

The K-S equation are usually solved by iterating self-consistent step until some convergence criteria are satisfied, and therefore it is necessary to identify a suitable guess density (i.e. K-S orbitals) to be used in the first self-consistent step. There are any different approaches but the choice of a plain-wave basis set show some advantages, the most relevant is that the Hilbert space span by the basis is independent of the atomic position.

The plane-waves basis set works fine in periodic system and it is less adapt to describe molecules and clusters but, if one uses it in a repeated-supercell geometry by putting enough vacuum around the finite object, then he can obtain fine results as well.

Bloch theorem states that independent electron states in a periodic context can be represented as the product of a period function times a plane wave, that is $\psi_k((\mathbf{r})) = e^{i\cdot\mathbf{k}\cdot\mathbf{r}}u_{\mathbf{k}}(\mathbf{r})$, where $u_{\mathbf{k}}(\mathbf{r}+\mathbf{R}) = u_{\mathbf{k}}(\mathbf{r})$ if $\mathbf{R}$ is a direct lattice vector. Now, if we consider the first Brillouin zone, then vector $\mathbf{k}$ can be can be confined to the closest $\mathbf{G}$ vector of the reciprocal lattice ($e^{i\mathbf{G}\cdot\mathbf{r}}$ has the lattice periodicity). By using the Bloch's ansatz, the K-S equation becomes:

$$\hat{H}_{KS}\psi_{\mathbf{k}}(\mathbf{r}) = \Big[\frac{\hbar^2\nabla^2}{2m} + V_{KS}(\mathbf{r})\Big]e^{i\cdot\mathbf{k}\cdot\mathbf{r}}u_{\mathbf{k}}(\mathbf{r}) = \varepsilon_{\mathbf{k}}e^{i\cdot\mathbf{k}\cdot\mathbf{r}}u_{\mathbf{k}}(\mathbf{r}). \tag{6.13}$$

now, by expanding $u_{\mathbf{k}}(\mathbf{r})$ on a set of plain-wave $\phi_{\mathbf{k}} = \frac{1}{\sqrt{\Omega}}e^{i\cdot\mathbf{G}\cdot\mathbf{r}}$, for which orthogonality holds ($\langle\phi_G|\phi'_G\rangle$) . As a result, wavefunction are now in the form:

$$\psi_{\mathbf{k}}(\mathbf{r}) = \frac{e^{i\cdot\mathbf{k}\cdot\mathbf{r}}}{\sqrt{\Omega}}\sum_{\mathbf{G}} c_{\mathbf{k},\mathbf{G}}e^{i\cdot\mathbf{G}\cdot\mathbf{r}} \tag{6.14}$$

and we can write the K-S equation in the following form:

$$\sum_{\mathbf{G}'}\Big[\frac{\hbar^2\nabla^2}{2m}|\mathbf{k}+\mathbf{G}|\delta_{\mathbf{G},\mathbf{G}'} + \tilde{V}_{KS}(\mathbf{G}-\mathbf{G}')\Big]c_{n\mathbf{k},\mathbf{G}'} = \varepsilon_{n\mathbf{k}}c_{n\mathbf{k}} \tag{6.15}$$

where $\tilde{V}_{KS}(\mathbf{G}-\mathbf{G}')$ is the Fourier transform of the potential $V_{KS}(\mathbf{r})$ and n is the band index. As calculation are carried out, one has to set a kinetic energy cut-off, i.e. one usually selects the G vectors according to $\mathbf{G}$: $\frac{\hbar^2\nabla^2}{2m}|\mathbf{k}+\mathbf{G}| \leq E_{cut}$.

Pseudopotentials (PP) are effective potentials used for the simplification of complex system. In the DFT framework PPs are constructed, in order to replace the singular all-electron potential, by replacing the complicated effects of the motion of the core states of an atom and its nucleus with an effective potential. In this way, the Schrödinger equation contains a modified effective potential term instead of the Coulomb potential

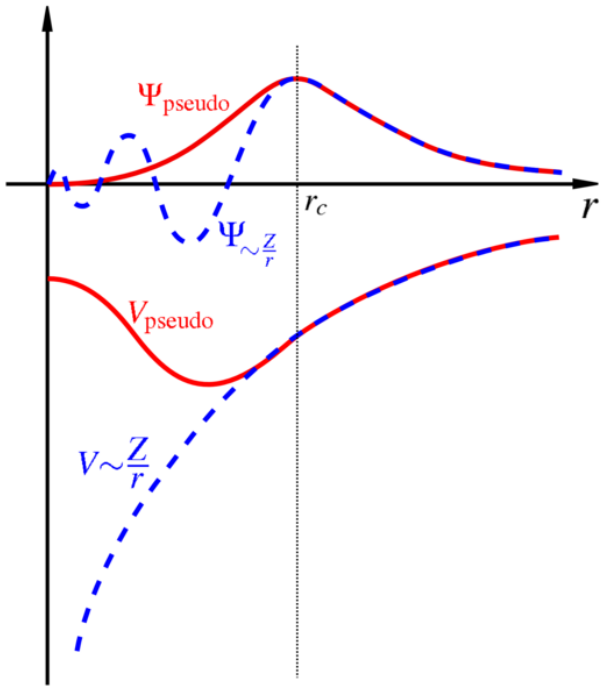

Figure 6.1: sketch representing the construction principle of a pseudopotential. Blue dotted lines are the atomic wavefunction, red ones refer to potential and pseudopotential

term for core electrons normally found in the Schrödinger equation. This is a "clean" way for reducing the complexity of the many-electron system because core states are not so relevant in determining physical and chemical properties of solids and molecules. As a result only valence electrons are taken into account as a PP is being developed, while core electrons are considered as frozen in their atomic state (a sketch is reported in fig.6.1) .

PPs are divided in two families, norm-conserving (NCPP) ones and ultrasoft (USPP) ones. NCPP has the following properties: (i) outside the core region the real and pseudo wavefunctions are identical so that both wavefunctions generate identical charge densities, (ii) all-electron and pseudo-wavefunctions must have the same energy, (iii) pseudo- and true-charge contained in the region $r < r_c$ must be the same.

USPP are derived by relaxing the constraint used for NCPP, thus providing greater flexibility in the construction of the pseudo-wavefunctions, and were developed by Vanderbilt in the early 1990s [80]. With respect of NCPP, USPP are based on smoother pseudo-wavefunctions and thus considerably fewer plane-waves are necessary for calculations of the same accuracy.

In general PP and all-electron calculations on the same systems yield almost indistinguishable results, except for those cases where core states are not sufficiently frozen.

6.2 Adopted DFT implementation

As mentioned in the Introduction, in my Thesis I study the vibrational properties of *sp*CCs terminated by both naphthyl-terminated and graphitic fragments. From the simulations point of view I perform all calculations within density-functional theory in the local spin density approximation, using a plane-wave basis as implemented in the ESPRESSO suite [81]. To depict the optimized structures I use the XCRYSDEN package [82].

Regarding the pure carbon structures I use ultrasoft pseudopotential with a wave-function/charge cutoff of 30/240 Ry, and relax all atomic positions until the largest residual force is $< 2 \times 10^{-4}$ Ry/a$_0$ (8 pN). Brillouin zone integration in these metallic systems are performed using 2×10^{-4} Ry (3 meV in the case of dinaphthylpolyynes) wide Gaussian smearing.

In the case of graphene NRs, we adopt supercells with three hexagonal units along the periodic direction and at least 7 Å of vacuum separating periodic images in the two other directions, optimizing the lattice constant until the stress tensor drops below 2×10^{-5} Ry/a$_0^3$. We sample the Brillouin zone with at least 13 k-points in each periodic direction and only $k = 0$ in non-periodic directions. Numerical details are similar to those validated and used, e.g., in ref. [83].

For what concerns calculations of dinaphthylpolyynes properties, I used the same receipt presented in the case of graphitic terminations but I consider only one k-point (Γ) for all the calculations.

Vibrational properties of both dinaphthylpolyynes and pure graphitic structure have been performed within density-functional perturbation theory (DFPT) by direct calculation of second-order derivatives of the energy with respect of the variational parameter λ. In crystals, normal modes are classified by a wave-vector $\mathbf{q}$, whose frequencies $\omega(\mathbf{q})$ and displacement patterns U$_s^\alpha$, for cartesian component α of atom s, at atomic position R$_s$, are determined by the secular equation:

$$\sum_{t,\beta} \left(\tilde{C}_{s,t}^{\alpha,\beta}(\mathbf{q}) - M_s(\mathbf{q})\omega^2 \delta_{st}\delta_{\alpha\beta} \right) U_t^\beta(\mathbf{q}) \tag{6.16}$$

where $\tilde{C}_{s,t}^{\alpha,\beta}$ is the matrix of inter-atomic force constants (IFC), i.e. second derivatives of the energy with respect to atomic positions. In the perturbation theory framework, if a perturbation $\mathbf{u}$ in the atomic position $\mathbf{R}_I = \mathbf{R}_l + \tau_s + \mathbf{u}_s(\mathbf{q})e^{i\mathbf{q}\cdot\mathbf{R}_l}$ is introduced, this induces a response having the same wave vector $\mathbf{q}$ (at linear order). Fourier transform of force constants at $\mathbf{q}$ are second derivatives of the energy with respect to such monochromatic perturbations:

$$\tilde{C}_{s,t}^{\alpha,\beta}(\mathbf{q}) \equiv \sum_{\mathbf{R}} e^{-i\mathbf{q}\cdot\mathbf{R}} C_{s,t}^{\alpha,\beta}(\mathbf{R}) = \frac{1}{N} \frac{\partial^2 E}{\partial u_s^{*\alpha}(\mathbf{q}) \partial u_t^\beta(\mathbf{q})} \tag{6.17}$$

This can be calculated from the knowledge of the linear response $\frac{\partial \rho(\mathbf{q})}{\partial u_s^\alpha(\mathbf{q})}$ and diagonalized to get phonon modes at $\mathbf{q}$.

Then, as the calculation of infrared cross sections, in the Q-E package, is implemented only for non-metallic system, I limit the calculation of non-resonant Raman intensities and infrared cross section to dinaphyhylpolyyne and H-terminated spCCs. Non-resonant Raman cross-sections are calculated following the Placzek [84] approximation, where

Raman intensity is proportional to the second derivative of the electric polarizability χ with respect of atomic displacement u along the mode ν $u^{(\nu)}$

$$I_{stokes}(\nu) \propto \frac{(\omega_L - \omega_\nu)^4}{\omega_\nu} \Big| \frac{\partial \chi_{\alpha\beta}}{\partial u(\nu)} \Big|^2 \tag{6.18}$$

where the Raman tensor $r_{\alpha\beta} = \frac{\partial \chi_{\alpha\beta}}{\partial u^(\nu)}$ is a third-order derivative of the energy that can be calculated by DFPT plus second order response to electric filed (as implemented in the Q-E package).

For what concerns infrared intensities, they are proportional to the square of the dipole induced by the phonon that is excited by the IR radiation:

$$I_{IR}(\nu) = \sum_\alpha \Big| \sum_{I\beta} Z_I^{*\alpha\beta} U_I^\beta(\nu) \Big|^2 \tag{6.19}$$

where $Z_s^{*\alpha\beta} = \Omega \frac{\partial P_\alpha}{\partial u_s^\beta(\mathbf{q}=0)}$ are the effective charges (Ω is the solid angle, u_s^β is a normal mode displacement and P is the polarization) which are calculated from (mixed) second derivatives of the energy.

In order to compute infrared cross-section I had to switch to norm-conserving PP (60/240 wavefunction/density cut-off) as the Q-E implementation for ultrasoft PP is still missing.

Part III

Results

Chapter 7

Dinaphtylpolyynes

This chapter is devoted to the presentation of the results obtained about the characterization and modeling of *sp*CCs stabilized by napthyl group (dinaphthylpolyynes). As anticipated in the introduction, this kind of molecules is interesting from two point of view: first of all *sp*CCs stabilized by aromatic group are supposed to be one of the constituent of the diffuse interstellar medium, where they act both as intermediates during PAHs photodegradation and as building blocks of more complex structures [24, 25, 26, 27, 28, 29, 85]. Furthermore, always in the astrophysical contest, both terminated and non terminated *sp*CCs are supposed to be the carrier of the DIBs.

From the other side, dinaphthylpolyynes represent an ideal-actual system that can be used for modeling the vibrational properties of *sp*CCs embedded in the *sp*-sp^2 pure carbon material. Indeed, *sp*CCs are stabilized in the pure carbon system by anchoring to sp^2 and sp^3 sites of the covalent fullerenic pure sp^2 clusters. Therefore naphtyl group represents a suitable simplification for such a complex system, preserving the fundamental properties of a graphene nanoribbon, which in turn represents a modelization of the carbon cluster as well.

In the first paper I show the synthesis procedure used for the production of dinaphthylpolyynes, the analysis of the reaction yield and the molar concentration of the chains with different length present in the solution. Then the optical characterization of the dinaphthylpolyyne-containing solution is reported in combination with *ab-initio* DFT-LSDA calculation of the structural and electronic properties of the isolated molecules.

In the second paper I present the vibrational characterization and modeling of the dinaphthylpolyynes obtained by performing MWRR and infrared spectroscopy. Then the experimental spectra are compared with simulated ones obtained by calculating normal modes frequencies and weighting the measured molar concentration to the calculated non-resonant Raman and infrared cross sections.

This combined study allows to provide a precise picture for the vibrational properties of end-capped *sp*CCs, thus opening the possibility of clearly describe the presence of linear carbon chains in more complex system, as for instance the *sp*-sp^2 pure carbon material.

7.1 Synthesis of dinaphthylpolyynes via Cadiot-Chodkiewicz reaction

First of all I present the results obtained by using the Cadiot-Chodkiewicz (C-C in the following) reaction described in sec. 2.1.1. In the following paper I show the production yield for dinaphthylpolyynes under the condition of the C-C reaction and the characterization of the solution containing the molecules by UV-vis absorption spectroscopy combined with DFT-LSDA calculation oh their electronic properties. Furthermore we show the infrared spectrum of the material obtained by depositing some drops of the solution on a Calcium Fluoride (CaF_2) substrate and of the dark precipitate in the solution compared with the infrared spectrum of the reagents. Finally I show differential scanning calorimetry measurements in order to find exothermic reactions providing dinaphthylpolyynes dissociation.

Synthesis, Characterization, and Modeling of Naphthyl-Terminated *sp* Carbon Chains: Dinaphthylpolyynes

*Franco Cataldo** [1,2], *Luca Ravagnan** [3,4], *Eugenio Cinquanta*[4,5], *Ivano Eligio Castelli*[3,6], *Nicola Manini*[3,7], *Giovanni Onida*[3,7], *Paolo Milani*[3,4]

Actinium Chemical Research, Via Casilina 1626/A, I-00133 Rome, Italy,

Istituto Nazionale di Astrofisica. Osservatorio Astrofisica di Catania, Via S. Sofia 78, I-95123 Catania, Italy,

Dipartimento di Fisica, Università degli Studi di Milano, Via Celoria 16, I-20133 Milano, Italy,

CIMAINA, Via Celoria 16, I-20133 Milano, Italy,

Dipartimento di Scienza dei Materiali, Università degli Studi di Milano-Bicocca, Via Cozzi 53, I-20125 Milano, Italy, and

European Theoretical Spectroscopy Facility (ETSF), Via Celoria 16, 20133 Milano, Italy.

* To whom correspondence should be addressed. E-mail: franco.cataldo@fastwebnet.it (F.C.); luca.ravagnan@mi.infn.it (L.R.).

[1] Istituto Nazionale di Astrofisica.

[2] Actinium Chemical Research.

[3] Dipartimento di Fisica, Università degli Studi di Milano.

[4] CIMAINA.

[5] Dipartimento di Scienza dei Materiali, Università degli Studi di Milano-Bicocca.

[6] Present address: Center for Atomic-scale Materials Design (CAMD), Department of Physics, Technical University of Denmark, DK-2800 Kongens Lyngby, Denmark.

ABSTRACT: We report a combined study on the synthesis, spectroscopic characterization and theoretical modelling of a series of α,ω-dinaphthylpolyynes. We synthesized this family of naphtyl-terminated *sp* carbon chains by reacting diiodoacetylene and 1-ethynylnaphthalene under the Cadiot-Chodkiewicz reaction conditions. By means of liquid chromatography (HPLC), we separated the products and recorded their electronic absorption spectra, which enabled us to identify the complete series of dinaphthylpolyynes Ar-C_{2n}-Ar (with Ar = naphthyl group and *n* = number of acetilenic units) with *n* ranging from 2 to 6. The longest wavelength transition (LWT) in the electronic spectra of the dinaphthylpolyynes red shifts linearly with *n* away from the LWT of the bare termination. This result is also supported by DFT-LDA simulations. Finally, we probed the stability of the dinaphthylpolyynes in a solid-state precipitate by Fourier-transform infrared spectroscopy and by differential scanning calorimetry (DSC).

KEYWORDS: Dinaphthylpolyynes; polyynes; *sp*-carbon chains; Cadiot-Chodkiewicz reaction; electronic absorption spectroscopy; FT-IR; DSC.

[7] European Theoretical Spectroscopy Facility.

1. **Introduction**

During the past years the study of *sp* carbon chains (*sp*CCs, also known as acetylenic arrays) has attracted the interest of a number of research group from a multitude of disciplinary areas, ranging from organic chemistry, non linear optics, solid state physics, and astrophysics. Although bare *sp*CCs are extremely unstable and reactive species [1], it has been shown that their stability is remarkably enhanced when their reactive terminations are bond to chemical groups [2-4] or to carbon nanostructures [5,6].

For instance, chemists were able to synthesize *sp*CCs which are stable in solution or even in the solid phase, by terminating the chains with organic group [3,4]. This class of compounds, often referred to as α,ω-diarylpolyynes (DAPs), have interesting and promising physical properties. For instance they exhibit a HOMO-LUMO gap strongly influenced by the number of *sp* carbon atoms constituting the chain [7], and their third-order nonlinear optical properties and their nonresonant molecular second hyperpolarizabilities (γ) have been reported to increase as a function of the chain length [8,9]. Furthermore, it has been shown that the fluorescence, phosphorescence and absorption spectra of DAPs can be modulated by applying an external electric field [10]. Finally, unusual photophysical and spectroscopic properties have been reported for DAPs, and they are considered promising candidates as materials for the fabrication of semiconductive thin film transistor structures [11], as the active semiconductor material in light-emitting diodes in electroluminescent devices [12,13] and in organic solar cells [14].

On the other hand, solid state physicists are studying the possibility to produce carbon solids containing *sp*CCs (*sp*-sp^2 carbon) since the 1960's [15]. Although the feasibility to obtain *sp*-sp^2 carbon solids has been shown for some years [16,17], recent experimental observation by HR-TEM of *sp*CCs forming during the irradiation of graphene planes has strongly increased the interest on this field [18]. *sp*CCs are nowadays considered promising structures for nano-electronic applications [19,20] since they could be used as molecular conductors bridging graphene nanogap devices. First potential applications have been already demonstrated for the realization of non-volatile memories, as their use in two-terminal atomic-scale switches [20]. Furthermore, *sp*CCs are expected to have interesting rectifying

performances [21], to become spin-polarized depending to their axial strain [5], and to be effective as spin-filters and spin-valves [22].

Finally *sp*CCs are of great relevance for astrophysics in the framework of the study of the Diffuse Interstellar Bands (DIBs). DIBs include a large number of absorption lines in the visible-near IR region of the electromagnetic spectrum that are superposed on the interstellar extinction curve and whose identification remains one of the oldest mysteries in stellar spectroscopy [23]. By comparing laboratory spectra of complex molecules with the DIBs lines, several molecules were identified as constituent of the interstellar medium [23,24]. Indeed, both non-terminated *sp*CCs and polycyclic aromatic hydrocarbons (PAHs), as for example naphthalene, have been identified separately [25-27], however *sp*CCs terminated by PAHs (e.g. DAPs) have not been considered to date.

In the present paper we present a combined study on the synthesis, spectroscopic characterization and theoretical modelling of a series of *sp*CCs terminated by naphtyl groups (dinaphthylpolyynes, in short represented as Ar-C_{2n}-Ar, with Ar = naphthyl group and n = number of acetylenic units of the *sp*CC). These molecules, already synthesized in the 1960's and 1970's by the group of M. Nakagawa [28-30], represent a family of chemically stabilized DAPs which are of high interest for several reasons: from one side, they are potentially useful in optoelectronic applications and are promising building blocks for the production of *sp*-sp^2 carbon systems for nano-electronic devices; from the other side, they constitute the simplest examples of *sp*CCs terminated by a PAH that could be identified in the interstellar medium (naphthalene is indeed one of the simpler and most abundant PAHs). Here we present a new route for the synthesis of this class of complexes which enables, by a remarkably simpler chemical approach than in Ref. [28-30], to produce at the same time a solution of dinaphthylpolyynes Ar-C_{2n}-Ar with $2 \leq n \leq 6$.

2. Experimental Section

2.1 Materials and Equipment

All the solvents and reagents (as for instance 1-ethynylnaphthalene) mentioned in the present work were obtained from Sigma Aldrich. Diiodoacetylene was prepared according to the method reported in Ref. [31]. All the equipment and methods for analysis and characterization of the reaction products are reported in Ref. [32].

We performed the HPLC analysis using an Agilent Technologies 1100 station with C_8 column (using acetonitrile/water 80/20 as mobile phase at a flow rate of 1.0 mL/min) and equipped with a diode array detector (used for recording the UV-vis absorption spectra of the separated molecules). UV-vis absorption spectra were also acquired on the solution and thin films by a JASCO-7850 spectrophotometer. FT-IR measurements were carried out on in transmittance mode on an IR300 spectrometer from Thermo-Fisher Corp. The differential scanning calorimetric (DSC) measurements were performed on a DSC-1 Star System from Mettler-Toledo (heating rate of 10°C/min under N_2 flow).

2.2 Synthesis of Dinaphthylpolyynes

We synthesized the dinaphthylpolyynes by reacting copper(I)ethynylnaphthalide with diiodoacetylene under the Cadiot-Chodkiewicz reaction conditions [32,33].

In a first stage we synthesized the copper salt of ethynylnaphthalene by dissolving Cu(I) chloride (1.0 g) in 30 mL of aqueous ammonia (30%) together with 0.5 g of hydroxylamine hydrochloride (NH_2OH•HCl). 1-Ethynylnaphthalene (1.5 mL) was then added to this solution under stirring. We collected a dark yellow precipitate of copper(I)ethynylnaphthalide by filtration in considerable yield (1.8 g).

After that about 6.0 g of I-C≡C-I (Warning! Acetylene diiodide is an irritant and poisonous) was dissolved/suspended in 90 mL of decalin, it was transferred in a 500 mL round bottomed flask and was stirred with 100 mL of distilled water. Copper(I)-ethynylnaphthalide (1.8 g) was then added to the reaction mixture together with 25 mL of tetrahydrofuran, 50 mL aqueous NH_3 30% and 30 mL of N,N',N,N'-tetramethylethylenediamine (TMEDA). The mixture was stirred at room temperature for 2 days and after this process the decalin layer became deep orange. The reaction mixture was filtered with

the aid of an aspirator to separate the black residue formed. The filtered solution consisted of two layers. The organic layer was separated from the aqueous layer by means of a separatory funnel. The resulting crude solution contained dinaphthylpolyynes dissolved in decalin, together with a significant amount of free unreacted ethynylnaphthalene and other by-products. These latter were removed from the crude solution (as a dark red precipitate) by shaking the solution with 4.0 g of CuCl dissolved in 100 mL of aqueous NH_3 30% together with 3.0 g of NH_2OH•HCl.

The resulting orange solution was then characterized by HPLC, UV-vis, FT-IR and DSC.

2.3 DFT Simulations

We simulated the synthesized structures using standard DFT-LSDA (density functional theory in the local spin density approximation), based on a plane-waves basis, and pseudopotentials [34]. We relaxed all atomic positions until the largest residual force was <8 pN. The ensuing structures and electronic Kohn-Shan orbitals are depicted using a standard visualization tool [35].

3. Results and Discussion

3.1 Synthesis and Identification of Dinaphthylpolyynes

Previous work [32] demonstrated the great versatility of diiodoacetylene (C_2I_2) as a building block for the synthesis of symmetrically terminated *sp*CCs through the Cadiot-Chodkiewicz reaction. The synthetic approach adopted previously with copper phenylacetylide and C_2I_2 has been extended here to the case of the copper salt of 1-ethynylnaphthalene. As shown in Scheme 1, the resulting *sp*CCs are thus terminated by the bulkier naphthalene groups.

Figure 1 reports the separation by elution through the HPLC column of the products formed in the Cadiot-Chodkiewicz reaction between diiodoacetylene and 1-ethynylnaphthalene. The presence of well distinct peaks at different retention times demonstrates the formation of products with different molecular weights, in agreement with the formation of dinaphthyl terminated *sp*CCs of different length (according to the Scheme 1). The formation of *sp*CCs having more than three acetylenic units suggests

the formation of the labile asymmetric intermediate Cu-C≡C-I during the coupling reaction [32]. Without the formation of this intermediate, the production of *sp*CCs longer than three acetylenic units would be unjustified.

By using a low flow rate for the mobile phase in the HPLC it was possible to observe the regular elution of all dinaphthylpolyynes, although a very long retention time was observed for the products with higher molecular weight. Figure 1 shows the retention times of the dinaphthylpolyynes in the HPLC column (as a function of the number of acetylenic units) in comparison to the diphenylpolynes ones [32]. The retention times of both series of molecules can be fitted by an exponential law of the type (see inset of Figure 1):

$$R_t = Ae^{B \cdot n} \qquad \text{(eq.1)}$$

where R_t is the retention time in the column, n is the number of acetylenic units of the *sp*CC, and A and B are two parameters whose values are reported in Table 1.

*sp*CCs series	A [min]	B
dinaphthylpolyynes	3.0 ± 0.3	0.53 ± 0.02
diphenylpolyynes	1.4 ± 0.1	0.51 ± 0.02

Table 1. Fitting parameters for the exponential law describing the evolution of R_t with n (eq. 1).

Remarkably, the longer retention times of dinaphthylpolyynes in comparison to those of diphenylpolyynes, (ascribable to their bulkier end groups) seems to affect only the parameter A of the exponential fit, which is almost double in the case of dinaphthylpolyynes in comparison to the value obtained for diphenylpolyynes. In contrast, the exponents B obtained for the two series of chains are comparable.

3.2 Electronic Absorption Spectroscopy

By using the diode array detector interfaced to the column of the HPLC, we could record the electronic absorption spectrum of each molecular species contained in the dinaphthylpolyynes mixture, i.e. for each peak in Figure 1. Figure 2 shows the resulting spectra. The presence of a regular shift for the position of the absorption peaks as the molecular weight of the species increases (i.e., the retention time increases) supports the assignment to diphenylpolyynes of increasing length. Indeed, it is well known that the position of the electronic absorption peaks of *sp*CCs is correlated to the number of acetylene units [28-30,7]. The exact attribution of the different spectra to the corresponding dinaphthylpolyyne is furthermore possible by comparing the absorption spectra with the one obtained by the group of M. Nakagawa [28-30]. Remarkably, the position of the peak at longest wavelength (longest wavelength transition, LWT) of our spectra matches the values in ref. [28-30], corresponding to dinaphthylpolyynes with n=2-6, within a shift of about 3 nm. The presence of this shift has to be ascribed to the different solvent used in our case (decalin) with respect to the one used in the past (tetrahydrofuran) [29].

Considering the different spectra in detail, they are characterized by a complex structure, in which two main regions can be identified. The region at higher wavelength (labeled as Reg. A in Figure 2a) is related to the electronic transitions between the highest occupied molecular orbital (HOMO) and the lowest unoccupied molecular orbital (LUMO); the region at lower wavelength (labeled as Reg. B in Figure 2a) is related to transitions between other molecular orbitals (such as, for instance, the transitions between the HOMO and LUMO+1 or the HOMO-1 and LUMO). In region A in particular, a multipeak structure can be identified that can be fitted as the superposition of several Gaussian components. The presence of several peaks can be attributed to the Franck-Condon shifts of the main HOMO-LUMO transition [28-30,7], i.e. the simultaneous occurrence of the electronic transition and the excitation of vibrational modes of the molecule. In this framework, the LWT peak of the electronic absorption spectrum corresponds to the HOMO-LUMO transition without the excitation of the molecule to a new vibrational level, while the most intense transition (MIT) is the transition for which the starting and final wave functions overlap more significantly (thus, the transition has a higher probability to occur). As shown in Figure 2a dinaphthylpolyynes have MITs that are always distinct by the LWT. This is a

characteristic of *sp*CCs terminated by bulky groups, and indeed has been observed also for diphenylpolyynes [32] and for *sp*CCs terminated by dendridic organic groups [3]. Instead, in the case of simple polyynes, the LWT and the MIT coincide [2].

Figure 2b shows the same spectra as Figure 2a (limited to Reg. A), where the abscissa is expressed as energy shift from the LWT. This means that the wavelength scale of each spectrum in Figure 2a was first converted in energy scale (in cm^{-1} units), and then, the energy of the LWT peak was subtracted from it; as a result, in Figure 2b the LWTs of all spectra are centered at 0 cm^{-1}. Thanks to this representation, it is possible to observe that the energy shift between the peaks in region A is on the order of 1900-2000 cm^{-1}, which is consistent with the typical main vibrational modes of *sp*CCs [36]. Furthermore, the value of this shift decreases as the chain length of the dinaphthylpolyyne increases: this again is consistent with the behavior of the vibrational modes of *sp*CCs that are known to be softer (i.e., characterized by a lower energy) when the chain length is larger [36]. As a matter of fact, this behaviour was also observed in Ref. [29], even if the Franck-Condon shifts measured in our case are slightly lower. Like for the shift of the LWT, this slight deviation can be related to the different solvent.

Figure 3 shows the evolution of the LWT of the electronic absorption spectra of the dinaphthylpolyynes as a function of the number of acetylenic units (*n*) in the chain, compared to the same evolution for diphenylpolyynes [32] and hydrogen-terminated *sp*CCs (i.e., polyynes) [2]. In all cases, a linear relation emerges between the LWT and the number of acetylenic units [7], as described by the following equation:

$$LWT = \alpha \cdot n + LWT_0 \qquad \text{(eq.2)}$$

where LWT_0 is the extrapolated LWT for a chain of "null" length and α is the slope. Although other groups have suggested that LWT for dinaphthylpolyynes evolves as $LWT = \alpha \cdot n^{1/2} + LWT_0$ [28-30] our data are more consistent with a linear dependence with *n*. The fitting parameters of LWT_0 and α obtained for the three series of *sp*CCs in Figure 3 are reported in Table 2.

*sp*CCs series	α	LWT_0

	[nm/C_2 unit]	[nm]
Dinaphthylpolyynes	25.7 ± 0.5	319.8 ± 2.2
Diphenylpolyynes	35.3 ± 0.8	256 ± 3
Polyynes	23.0 ± 0.5	133 ± 3

Table 2. Fitting parameters for the linear relation describing the evolution of LWT with *n* (eq. 2).

Remarkably, the value of LWT_0 for dinaphthylpolyynes at 319.8 is very close to LWT of the the B-band of naphthalene at 313 nm [37-39] as well as to the LWT of binaphthyl at 315 nm [37-39]. Similarly, the value of LWT_0 for diphenylpolyynes at 256 nm is close to LWT of the B band of benzene at 267 nm [37] and is very close to the LWT for biphenyl at about 252 nm [37].

As suggested in Ref. [30], these observations indicate that the intercepts at n=0 correspond to the LWT absorption of the end groups, while the addition of the acetylenic unit causes a red shift in the LWT transition.

In order to better understand the observed behavior, we carried out DFT-LSDA simulations of the geometric and electronic structure of a free-standing naphthalene molecule and of dinaphthylpolyynes with different chain lengths. Naphthalene molecules exibit a HOMO-LUMO gap larger than that of a dinaphthylpolyynes of any length. Figure 4 (left panel) shows the HOMO and LUMO wave functions obtained for Ar-C_4-Ar, Ar-C_8-Ar and Ar-C_{12}-Ar. As can be observed, the HOMO and LUMO orbitals of the *sp*CCs are hybridized with those of the terminations since their wave functions extend out from the *sp*-chain region in the naphthyl region. Nevertheless, as the chain length increases, the HOMO and LUMO orbitals become more and more localized on the sole chain backbone, indicating a diminishing hybridization. At the same time, as the chain length increases, the computed HOMO-LUMO gap decreases, and consequently the theoretical value for the absorption wavelength (LWT_{DFT}, proportional to the inverse of the computed HOMO-LUMO gaps) increases. Figure 4 (right panel) shows the evolution of LWT_{DFT} with n. Although the computed values for the LWT_{DFT} do not match the experimental values for the LWT in Figure 3, the overall trend is in very good agreement. The simulations reproduce the linear relation between LWT_{DFT} and n observed experimentally, and the

intercept at n=0 is not far from to the simulated LWT_{DFT} for naphthalene, given the expected underestimation of the HOMO-LUMO gap of DFT-LSDA.

It is also relevant to note that in the case of polyynes the π and π* orbitals (i.e., the HOMO and LUMO orbitals) are completely localized on the carbon chain axis, and therefore, little or no hybridization of those orbitals occurs with the termination groups. Nevertheless, the same linear relation between LWT and n is observed. This indicates that the slope α of the linear relations in eq. 2 is not simply a measure of the hybridization between the π electron state of the chains and π electron state of the end groups but reflects a gap reduction intrinsic of the carbyne chain. The decrease in chain end-group hybridization seems in fact a direct consequence of this intrinsic gap reduction, with a corresponding movement "off-resonance" of the chain HOMO and LUMO levels relative to those of the end groups.

3.3 Relative Yield of Dinaphthylpolyynes

We compute the relative yield $C(n)$ of dinaphthylpolyynes of different lengths from the intensity of the most intense transition in the electronic absorption spectra (i.e., the MIT in Figure 2). We take advantage of the molar extinction coefficients $\varepsilon(n)$ previously reported [29]. We use the following relation:

$$C(n) = \frac{\frac{I_{MIT}(n)}{\varepsilon(n)} \cdot \frac{A(n,\lambda)}{I(n,\lambda)}}{\sum_{i=2}^{6} \frac{I_{MIT}(i)}{\varepsilon(i)} \cdot \frac{A(i,\lambda)}{I(i,\lambda)}} \qquad \text{(eq.3)}$$

where $I_{MIT}(n)$ is the intensity (i.e., the absorbance) of the MIT of the absorption spectrum for the dinaphthylpolyyne with n acetylenic units (see Figure 2), $I(n,\lambda)$ is the value of absorbance measured in the same spectrum at the wavelength λ and $A(n,\lambda)$ is the time-integrated intensity of the corresponding peak in the HPLC spectrum acquired using the wavelength λ. Table 3 reports the average of the values of $C(n)$ obtained by applying eq. 3 to two different HPLC spectra, acquired at λ=350 nm (see Figure 1a) and λ=250 nm (not shown) respectively.

n	dinaphthylpolyyne formulas	*C(n)*
2	Ar-C_4-Ar	47 ± 4 %
3	Ar-C_6-Ar	19.7 ± 0.6 %
4	Ar-C_8-Ar	18.2 ± 2.2 %
5	Ar-C_{10}-Ar	11.3 ± 1.2 %
6	Ar-C_{12}-Ar	4.1 ± 0.3 %

Table 3. Relative molar concentration of the dinaphthylpolyynes (with $2 \leq n \leq 6$) in the solution.

Figure 5 shows the relative molar concentration of the dinaphthylpolyynes in comparison to relative molar concentration of the diphenylpolyynes series produced using the same synthetic approach [32]. As can be observed, for any chain length larger than $n = 2$ the concentration of dinaphthylpolyynes exceeds that of the diphenylpolyynes. Only at $n = 2$ the concentration of diphenylpolyynes is higher than that of dinaphthylpolyynes. These data suggest that our synthetic approach favors longer chains when bulkier terminations are used as end groups (i.e., naphthyl groups) and shorter chains when the lighter phenyl groups are employed. Nevertheless, in both cases, the shortest chains are predominant, and the abundance of the species with longer chains decreases steadily with the increase of *n*, as normally expected in the synthesis of mixtures of polyynes [2].

In the calculation of the distribution of the dinaphthylpolyynes produced by the Cadiot-Chodkiewicz synthesis, we have neglected the presence of the residual 1-ethynyl-naphthalene which is not detected in the chromatogram shown in Figure 1a that was recorded at 350 nm but was present and detected in the chromatogram recorded at 250 nm (not shown).

3.4 Dinaphthylpolyynes in the solid phase

As previously discussed, *sp*CCs are interesting candidates for the development of a new generation of nanoelectronic devices, where they could be used as molecular conductors or spin filters and spin valves [19,20,22]. In order to produce similar devices, it is necessary to introduce *sp*CCs in solid-state systems and to ensure their stability in time. Unfortunately, *sp*CCs are notoriously unstable structures, and, in

particular, if they are terminated simply by hydrogen or nitrogen atoms, they can be prepared only as very diluted solutions; if they are deposited as thin films, they undergo fast decay [2]. Furthermore, *sp*CCs are known to be highly reactive with oxygen [16,40], making the production of devices containing *sp*CCs quite challenging. Nevertheless, several groups were able to demonstrate that *sp*CCs terminated by bulky end groups have remarkably higher stability [3,4], so that in some cases even their crystallization was achieved [4]. In order to study the possibility to use dinaphthylpolyynes in solid-state systems, we have deposited droplets of the solution of dinaphthylpolyynes in decalin on hard substrates (made by CaF, ZnSe, and KBr depending on the characterization carried out), and we let the solvent evaporate by placing the sample in a dryer. The resulting film was then characterized by UV-vis and FT-IR spectroscopies and by DSC.

In Figure 6, we compare the UV-vis spectra of the whole solution of diphenylpolyynes in decalin (not separated by the HPLC column) and of the film obtained by the same solution after the evaporation of the solvent. As it is possible to observe, the complex structure present in the solution's spectrum (corresponding to the overlap of the separate spectra of Figure 2a) is radically lost in the dried film, where three broad peaks (indicated by arrows in the figure) are still distinguishable on top of an amorphous band. This indicates that during the evaporation of the solvent, the dinaphthylpolyynes undergo chemical reactions that do not completely destroy the molecules, as indicated by the survival of spectral features in the UV-vis spectrum.

To gather more detailed information on the structure of the "polymerized" polyynes, we carried out FT-IR measurements on the samples. Figure 7 shows the FT-IR spectrum of the dried dinaphthylpolyynes film measured in ambient conditions (i.e., the sample has been exposed to air) as compared to the spectrum of pure naphthalene [41] and pure 1-ethynylnaphthalene. The figure also shows the FT-IR spectrum of the dark precipitate depositing on the bottom of the sealed flask containing the dinaphthylpolyynes solution after months of the solution being stored at room temperature.

As can be observed, the FT-IR spectra of both 1-ethynylnaphthalene and of the dried dinaphthylpolyynes exibit the vibrational modes typical of naphthalene (as well as of the naphthyl

group). For instance, we can identify in all the spectra the CH stretching band at about 3060 cm^{-1}, the in-phase –CH– out-of-plane bending band at about 780 cm^{-1} (CH wagging) and a series of C=C stretching bands (at about 1590, 1506 and 1390 cm^{-1}) [42]. 1-ethynilnaphthalene is furthermore characterized by the triple bond ≡C-H stretching band at 3282 cm^{-1} ($\nu_{\equiv C-H}$), by the bending of the ≡C-H at about 600 cm^{-1} ($\delta_{\equiv C-H}$) and by the acetylenic stretching band at 2100 cm^{-1} ($\nu_{C\equiv C}$) [43]. Remarkably, both $\nu_{\equiv C-H}$ and $\delta_{\equiv C-H}$ are no any longer detectable in the spectrum of the dried dinaphthylpolyynes, and the $\nu_{C\equiv C}$ of 1-ethynylnaphthalene at 2100 cm^{-1} is replaced by a complex and relatively more intense band at 2194 cm^{-1} with a series of sub-bands (at 2178, 2153 and 2125 cm^{-1}; see left panel in Figure 7). Indeed, the position of those bands is consistent with the C≡C stretching modes for isolated dinaphthylpolyynes [29].

Thes observations indicates on one hand that the interaction of the dinaphthylpolyynes occurring during their drying (as indicated by the modification of the UV-vis spectrum) is not altering significantly the dinaphthylpolyyne structure. In the FT-IR spectrum, we can indeed identify clearly the vibrational modes of both the naphthyl terminations and the C≡C stretching modes of the *sp*CCs, whose peaks do not show any significant broadening in comparison to the case of naphthalene and 1-ethynilnaphthalene.

On the other side, the complete absence in the dried dinaphthylpolyynes spectrum of the $\nu_{\equiv C-H}$ and $\delta_{\equiv C-H}$ vibrational modes can be interpreted as the indication that the Cadiot-Chodkiewicz reaction of 1-ethynylnaphathalene with diodoacetylene was complete and that the reaction products are essentially constituted by dinaphthylpolyynes. The residual, unreacted 1-ethynylnaphthalene detected in the HPLC analysis of the dinaphthylpolyynes (using the 250 nm wavelength) is thus a minor component not detectable by FT-IR spectroscopy.

Finally, it is significant to consider the FT-IR spectrum of the dark precipitate in Figure 7. The spectrum exibits four main broad bands, whose positions are still consistent with the main vibrational contributions observed for the dried dinaphthylpolyynes. We can distinguish two broad bands at about 3000 cm^{-1} and 750-800 cm^{-1}, consistent with the CH stretching and CH wagging of the dinaphthyl terminations, respectively [42], an intense band in the 1300-1600 cm^{-1} region that can be attributed to C=C stretching modes, and a band in the 2000-2200 cm^{-1} region, related to C≡C stretching modes. This

indicates that the dark precipitate is the result of the polymerization of the dinaphthylpolyynes in the solution. Remarkably anyway, the polymerization process is only capable of inducing a broadening of the vibrational bands, but it does not cause a significant depletion of the *sp*CCs. Furthermore, the obtained spectrum is very similar to the one measured on the black precipitate obtained from the solution of diphenylpolyynes in ref. [32]. The product of the polymerization of *sp*CCs terminated by aromatic groups can then be considered the intermediate step between the isolate *sp*CCs molecules and a solid made by sp-sp^2 carbon [16,5]. Remarkably anyway, both the dried dinaphthylpolyynes and the precipitate do not show any decay evolution during their exposure to air (i.e., to oxygen). This indicates that the high reactivity of the *sp*CCs to oxygen observed in pure sp-sp^2 carbon systems [16,40], is strongly inhibited by the presence of the hydrogen atoms in the aromatic terminal groups.

To gather further information on the stability of dried dinaphthylpolyynes, we repeated the process of vacuum drying of the solution at room temperature, and we recovered the dried dinaphthylpolyynes in the form of a dark orange powder. This powder was then characterized in a DSC, using a heating rate of 10°C/min under a N_2 flow. Figure 8 shows the resulting DSC trace. At 103.5°C can be observed a weak endothermic peak, indicating the onset of melting, probably for the shorter-chain oligomers. The peak is then followed by a broad exothermal transition with an onset temperature at 143°C and a peak at 182°C. The exotherm peak is quite broad, and the released energy is 442 J/g. This suggests the occurrence of a decomposition reaction for the dinaphthylpolyynes, probably initiated by the longer *sp*CCs (that are expected to be more unstable than the shorter ones [5,44]) and then propagating to the shorter ones.

4. Conclusions

In conclusion, we have shown how the Cadiot-Chodkiewicz reaction can be successfully applied to the synthesis of dinaphthylpolyynes. The key innovation in this synthetic approach is the use of diiodoacetylene, which simplifies the synthetic route to long polyyne chains with taylor-made end caps, thus indicating its general applicability in the synthesis of α,ω-diarylpolyynes.

HPLC analysis in conjunction with electronic absorption spectroscopy enabled us to identify the complete series of dinaphthylpolyynes with 2-6 acetylenic units. The length-resolved electronic spectroscopy of the dinaphthylpolyynes indicates, together with the well-known reduction of the HOMO-LUMO gap for increasing chain length, a nontrivial relation to the HOMO-LUMO gap of the end groups. This opens interesting perspectives in the interpretation of DIBs since *sp*CCs terminated by PAHs could give rise (if present in the interstellar medium) to peculiar absorption lines depending both to the chain length of the *sp*CC and to the structure of the PAHs.

By exploiting the observed independence of the molar exctinction coefficient of the sp^2-terminated *sp*CCs by the mass of the terminating organic groups, it was possible to estimate the relative molar concentration of the dinaphthylpolyynes produced. The obtained results indicate that the Cadiot-Chodkiewicz reaction favors the synthesis of longer chains when bulkier terminations are used.

UV-vis and FT-IR spectroscopy show that by evaporating the decalin solvent of the dinaphthylpolyynes solution, a solid film can be deposited where a relevant fraction of *sp*CCs is still present. Although a partial polymerization of the dinaphthylpolyynes has been observed, the obtained film is stable at room temperature even when it is exposed to air (i.e., to oxygen). By DSC, we checked the thermal stability of the dried dinaphthylpolyynes, observing the onset of their decomposition under nitrogen for temperatures higher than about 140°C. This moderately high thermal stability, together with the lack of reactivity at room temperature with oxygen, makes dinaphthylpolyynes promising building blocks for the integration of *sp*CCs in all-carbon electronic systems.

ACKNOWLEDGEMENTS

Franco Cataldo thanks the Italian Space Agency for the support of part of this research (Contract Number I/015/07/0 - Studi di Esplorazione del Sistema Solare). This work was supported by the European Union through the ETSF-I3 project (Grant Agreement No. 211956, user project 164).

REFERENCES

[1] Wakabayashi, T.; Ong, A-L.; Strelnikov, D.; Krätschmer, W. *J. Phys. Chem. B* **2004**, *108*, 3686.

[2] Cataldo, F. (Ed.) *Polyynes: Synthesis, Properties and Applications*: CRC Press: Boca Raton, FL, 2006.

[3] Gibtner, Th.; Hampel, F.; Gisselbrecht, J.P.; Hirsch, A. *Chem. Eur. J.* **2002**, *8*, 408.

[4] Szafert, S.; Gladysz, J.A. *Chem. Rev.* **2003**, *103*, 4175.

[5] Ravagnan, L.; Manini, N.; Cinquanta, E.; Onida, G.; Sangalli, D.; Motta, C.; Devetta, M.; Bordoni, A.; Piseri, P.; Milani, P. *Phys. Rev. Lett.* **2009**, *102*, 245502.

[6] Yamaguchi, Y.; Colombo, L.; Piseri, P.; Ravagnan, L.; Milani, P. *Phys. Rev. B* **2007**, *76*, 134119.

[7] Maier, J. P. *Chem. Soc. Rev.* **1997**, *26*, 21.

[8] Eisler, S.; Slepkov, A.D.; Elliott, E.; Luu, T.; McDonald, R.; Hegmann, F.A.; Tykwinski, R.R. *J. Am. Chem. Soc.* **2005**, *127*, 2666.

[9] Luu, T.; Elliott, E.; Slepkov, A.D.; Eisler, S.; McDonald, R.; Hegmann, F.A.; Tykwinski, R.R. *Org. Lett.* **2005**, *7*, 51.

[10] Wahadoszamen, Md.; Hamada, T.; Iimori, T.: Nakabayashi, T.; Ohta, N. *J. Phys. Chem. A* **2007**, *111*, 9544.

[11] Murphy, A.R.; Fréchet, J.M.J. *Chem. Rev.* **2007**, *107*, 1066.

[12] Friend, R.H.; Gymer, R.W.; Holmes, A.B.; Burroughes, J.H.; Marks, R.N.; Taliani, C.; Bradley, D.D.C.; Dos Santos, D.A.; Brédas, J.L.; Lögdlund, M.; Salaneck, W.R. *Nature* **1999**, *397*, 121.

[13] Wong, W.Y. *Phys. Chem. Chem. Phys*. **2007**, *9*, 4291.

[14] Wang, X.Z.; Wong, W.Y.; Cheung, K.Y.; Fung, M.K.; Djuri A.B.; Chan, W.K. *Chem. Soc. Rev.* **2007**, *36*, 759.

[15] Whittaker, A.G.; Kinter, P.L. *Science* **1969**, *165*, 589.

[16] Ravagnan, L.; Siviero, F.; Lenardi, C.; Piseri, P.; Barborini, E.; Milani, P.; Casari, C.S.; Li Bassi, A.; Bottani, C.E. *Phys. Rev. Lett.* **2002**, *89*, 285506.

[17] Ravagnan, L.; Piseri, P.; Bruzzi, M.; Miglio, S.; Bongiorno, G.; Baserga, A.; Casari, C.S.; Li Bassi, A.; Lenardi, C.; Yamaguchi, Y.; Wakabayashi, T.; Bottani, C.E.; Milani, P. *Phys. Rev. Lett.* **2007**, *98*, 216103.

[18] Jin, C.; Lan, H.; Peng, L.; Suenaga, K., Iijima, S. *Phys. Rev. Lett.* **2009**, *102*, 205501.

[19] Standley, B.; Bao, W.Z.; Zhanh, H.; Bruck, J.; Lau, C.N.; Bockrath, M. *Nano Lett.* **2008**, *8*, 3345.

[20] Li, Y.; Sinitskii, A.; Tour, J.M. *Nature Mater.* **2008**, *7*, 966.

[21] Deng, X.; Zhang, Z.; Zhou, J.; Qiu, M.; Tang, G. *J. Chem. Phys.* **2010**, *132*, 124107.

[22] Zeng, M.G.; Shen, L.; Cai, Y.Q.; Sha, Z.D.; Feng, Y.P. *Appl. Phys. Lett.* **2010**, *96*, 042104.

[23] Herbig, G.H. *Annu. Rev. Astron. Astrophys.* **1995**, *33*, 19.

[24] Snow, T.P. *Spectrochim. Acta, Part A* **2001**, *57*, 615.

[25] Jochnowitz, E. B.; Maier J. P. *Annu. Rev. Phys. Chem.* **2008**, *59*, 519.

[26] Brèchignac, P.; Pino, T.; Boudin, N. *Spectrochim. Acta, Part A* **2001**, *57*, 745.

[27] Allamandola, L.J.; Hudgins, D.M.; Bauschlicher Jr., C.W.; Langhoff, S.R. *Astron. Astrophys.* **1999**, *352*, 659.

[28] Akiyama, S.; Nakasuji, K.; Akashi, K.; Nakagawa, M. *Tetrahedron Lett.* **1968**, *9*, 1121.

[29] Nakasuji, K.; Akiyama, S.; Akashi, K.; Nakagawa, M. *Bull. Chem. Soc. Jpn.* **1970**, *43*, 3567.

[30] Nakagawa, M.; Akiyama, S.; Nakasuji, K.; Nishimoto K. *Tetrahedron* **1971**, *27*, 5401.

[31] Cataldo,F. *Fullerene Sci. Technol.* **2001**, *9*, 525.

[32] Cataldo, F; Angelini, G.; Ursini, O.; Tomassini, M.F.; Casari, C.S. *J. Macromol. Sci. A Pure Appl. Chem.* **2010**, *47*, 739

[33] Cadiot, P.; Chodkiewicz, W. in *Chemistry of Acetylenes*: Viehe, H. G. (Ed.), Marcel Dekker: New York, 1969; pp 597-647.

[34] Giannozzi, P; Baroni, S.; Bonini, N.; Calandra, M.; Car, R.; Cavazzoni, C.; Ceresoli, D.; Chiarotti, G.L.; Cococcioni, M.; Dabo, I.; Dal Corso, A.; de Gironcoli, S.; Fabris, S.; Fratesi, G.; Gebauer, R.; Gerstmann, U.; Gougoussis, C.; Kokalj, A.; Lazzeri, M.; Martin-Samos, L.; Marzari, N.; Mauri, F.; Mazzarello, R.; Paolini, S.; Pasquarello, A.; Paulatto, L.; Sbraccia, C.; Scandolo, S.;

Sclauzero, G.; Seitsonen, A.P.; Smogunov, A.; Umari, P.; Wentzcovitch, R.M. *J. Phys.: Condens. Matter.* **2009**, *21*, 395502. See also http://www.quantum-espresso.org.

[35] Kokalj, A. *Comp. Mater. Sci.* **2003**, *28*, 155. See also http://www.xcrysden.org/.

[36] Tabata, H.; Fujii, M.; Hayashi, S.; Doi, T.; Wakabayashi, T. *Carbon* **2006**, *44*, 3168.

[37] Friedel, A.; Orchin, M. *Ultraviolet Spectra of Aromatic Compounds*: J. Wiley & Sons: New York, 1951. Spectra N°161 and N°303.

[38] Gillam, A.E.; Stern, E.S.; Jones, E.R.H. *An Introduction to Electronic Absorption Spectroscopy in Organic Chemistry*: Edward Arnold Publishers: London, 1954.

[39] Perkampus, H.H. *UV-VIS Atlas of Organic Compounds*: Wiley-VCH: Weinheim, 1992.

[40] Casari, C.S.; Li Bassi, A.; Ravagnan, L.; Siviero, F.; Lenardi, C.; Piseri, P.; Bongiorno, G.; Bottani, C.E.; Milani, P. *Phys. Rev. B* **2004**, *69*, 075422.

[41] NIST Mass Spec Data Center, S.E. Stein, director, "Infrared Spectra" in *NIST Chemistry WebBook, NIST Standard Reference Database Number 69*: Eds. P.J. Linstrom and W.G. Mallard: National Institute of Standards and Technology: Gaithersburg MD 2008, 20899. See also http://webbook.nist.gov.

[42] Srivastava, A.; Singh, V.B. *Ind. J. Pure App. Phys.* **2007**, *45*, 714.

[43] Lin-Vien, D.; Colthup, N.B.; Fateley, W.G.; Grasselli, J.G. *The Handbook of Infrared and Raman Charateristic Frequencies of Organic Molecules*: Academic Press: S. Diego, 1991.

[44] Johnson, T.R.; Walton, D.R.M. *Tetrahedron* **1972**, *28*, 5221.

Scheme 1. Chemical structures of the dinaphthylpolyynes synthesized with the Cadiot Chodkiewicz reaction between copper(I)-ethynylnaphthalide and diiodoacetylene.

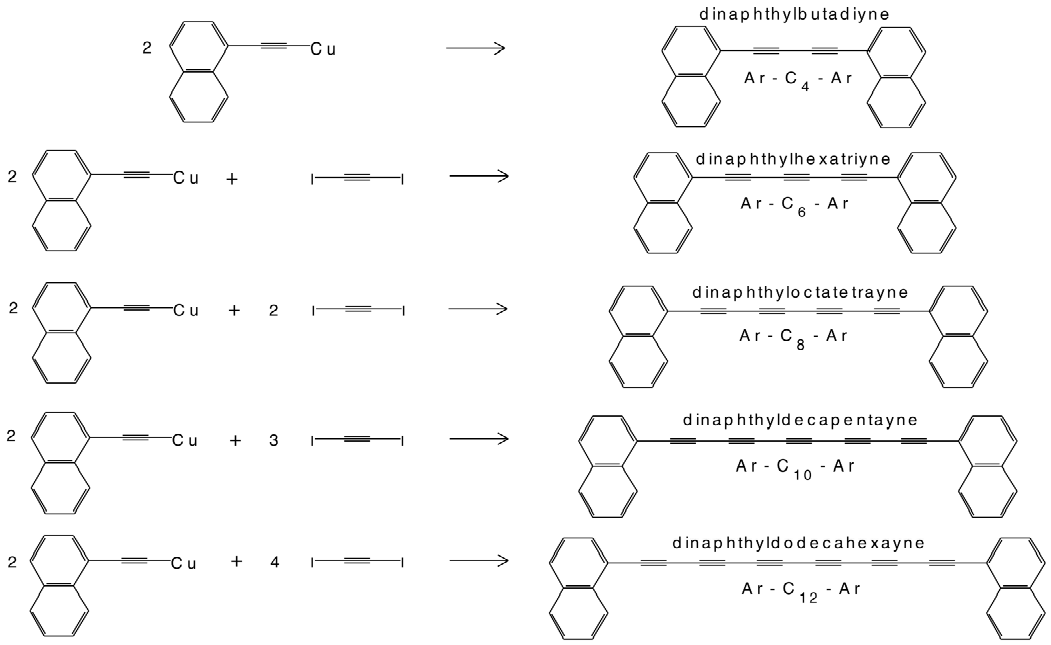

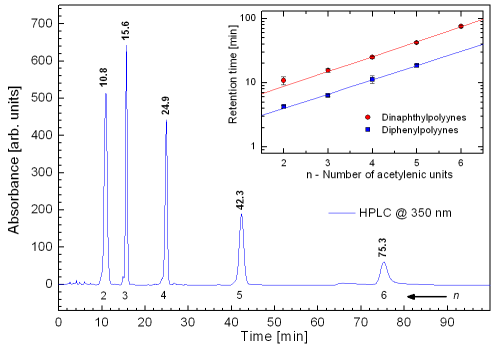

Figure 1. HPLC analysis of the dinaphthylpolyynes recorded at 350 nm. For each observed peak, the retention time and the corresponding number of acetylenic units (*n*) is indicated. Inset: comparison of the retention time of dinaphthylpolyynes and diphenylpolyynes [32] as a function of the number of acetylenic units componing the *sp*CCs. In both cases the mobile phase in the C_8 column was acetonitrile/water 80/20 vol./vol, and the pressure used was 105 bar.

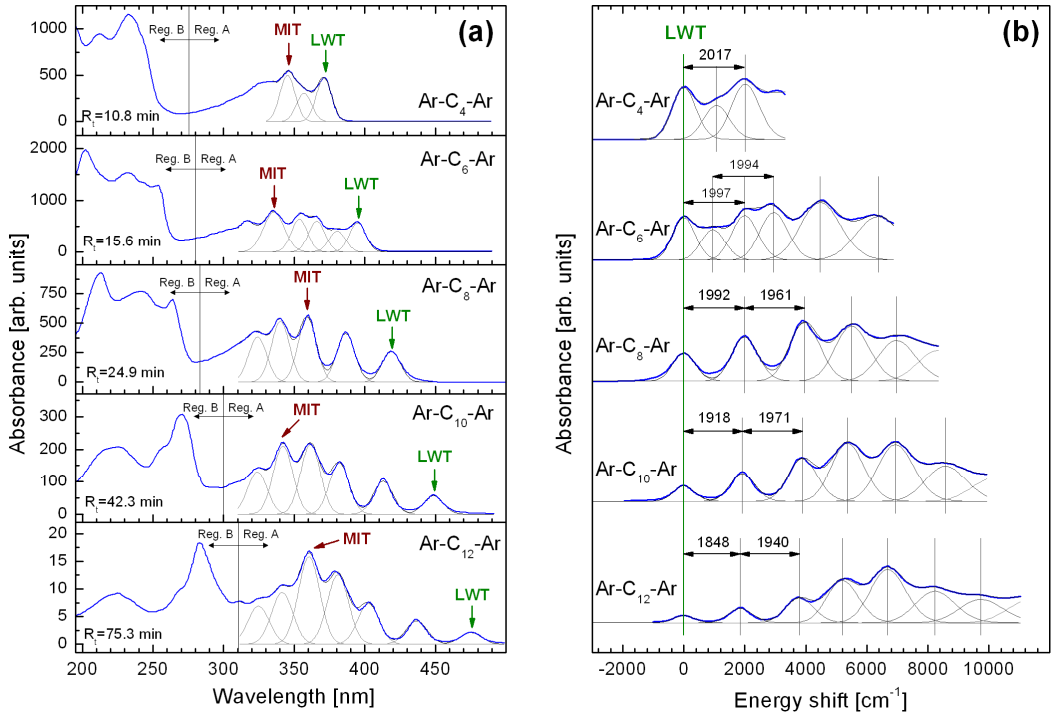

Figure 2. (a) The electronic absorption spectra of the dinaphthylpolyynes series (Ar-C_{2n}-Ar, *n*=2-6) as recorded by the diode array detector of the HPLC. For each spectrum the longest wavelength transition (LWT, inversely related to the HOMO-LUMO gap) and the most intense transition (MIT) are indicated. (b) The electronic absorption spectra of the dinaphthylpolyynes series (Ar-C_{2n}-Ar, *n*=2-6) represented as a function of the energy shift from the LWT (expressed in cm^{-1}). The distance between the peaks in the absorption spectra is consistent with the phonon energy of the optical C-C stretching mode of the *sp*-carbon chain.

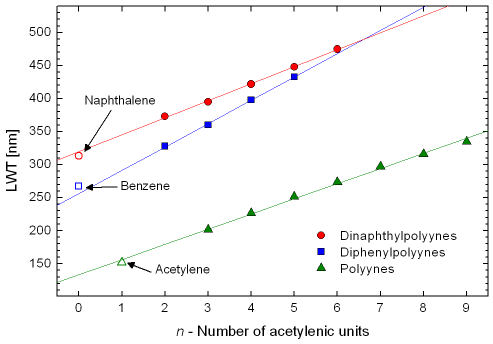

Figure 3. The position of the LWT as a function of the number of acetylenic units composing the carbon chain of three *sp*CCs series: naphthyl-terminated (dinaphthylpolyynes, circles), phenyl-terminates (diphenylpolyynes, squares) [32] and hydrogen-terminated (polyynes, triangles) [2]. The LWT for benzene and naphthalene molecules are indicated at n=0.

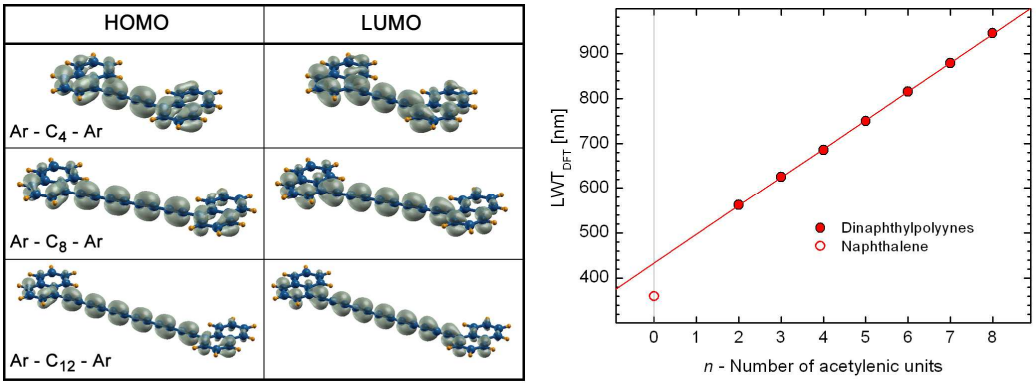

Figure 4. (Left panel) The electron density of HOMO and LUMO states for three different dinaphthylpolyynes: Ar-C_4-Ar, Ar-C_8-Ar, Ar-C_{12}-Ar. As the *sp*-carbon chain is longer, the HOMO and LUMO states become more and more localized on the chain backbone. (Right panel) DFT-LSDA value of LWT_{DFT} (evaluated as the inverse of the HOMO-LUMO Kohn-Sham gap) as a function of the number of acetylenic units composing the carbon chain (*n*) for dinaphthylpolyynes. The evaluated LWT_{DFT} for a single naphthalene molecule is indicated at *n*=0.

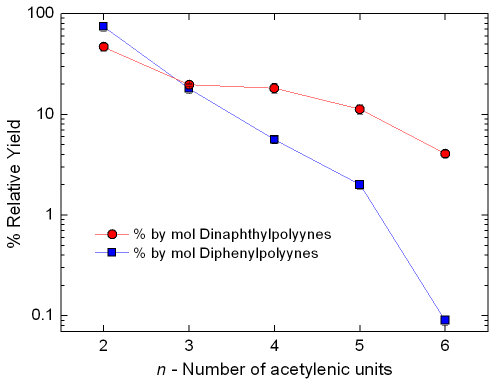

Figure 5. Relative yield of dinaphthylpolyynes and diphenylpolyynes [32] as a function of the number of acetylenic units (*n*). Both series of *sp*CCs are produced by the Cadiot-Chodkiewcz reaction.

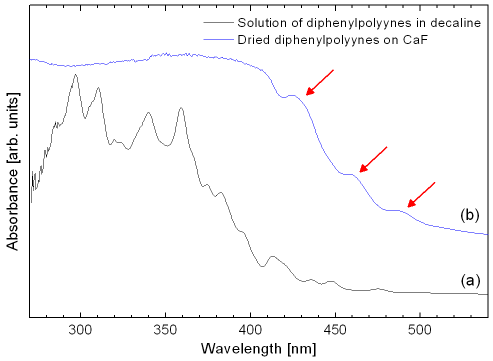

Figure 6. The UVvis spectra of the dinaphthylpolyynes solution (a) and of the dinaphthylpolyynes solution dried on a CaF substrate (b). Spectrum (a) is consistent with the weighted sum of the spectra of the separated dinaphthylpolyynes in Figure 2.

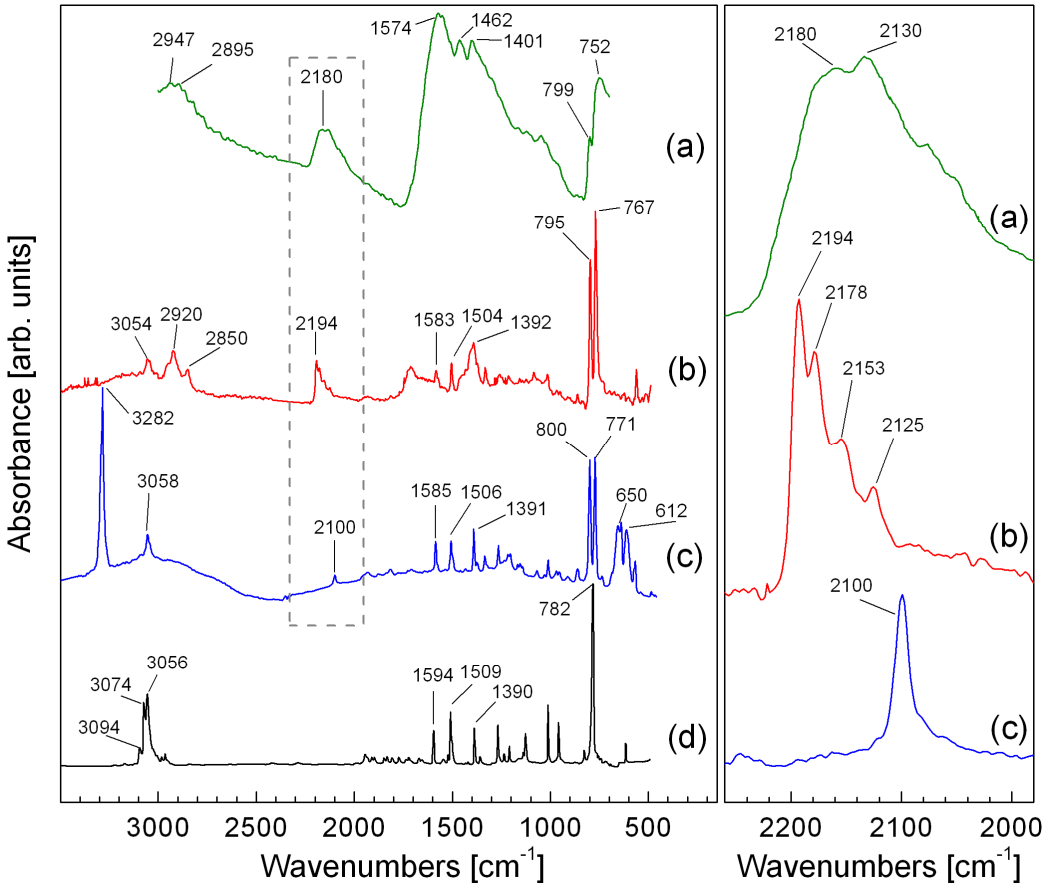

Figure 7. (Left) The FT-IR spectra of the black precipitate produced during storage at room temperature (in closed flasks) of the dinaphthylpolyynes solution (a), of the dried dinaphthylpolyynes solution (b), of pure 1-ethynylnaphthalene (c) and of pure naphthalene (d) (from Ref. [41]). Spectrum (a) has been acquired in reflectance mode depositing the sample on ZnSe, while spectrum (b) has been acquired in transmittance mode after drying the solution on a KBr substrate. (Right) Detail of the triple bonds stretching region of the FT-IR spectra (a), (b) and (c). A linear background has been subtracted to spectra (a) and (c).

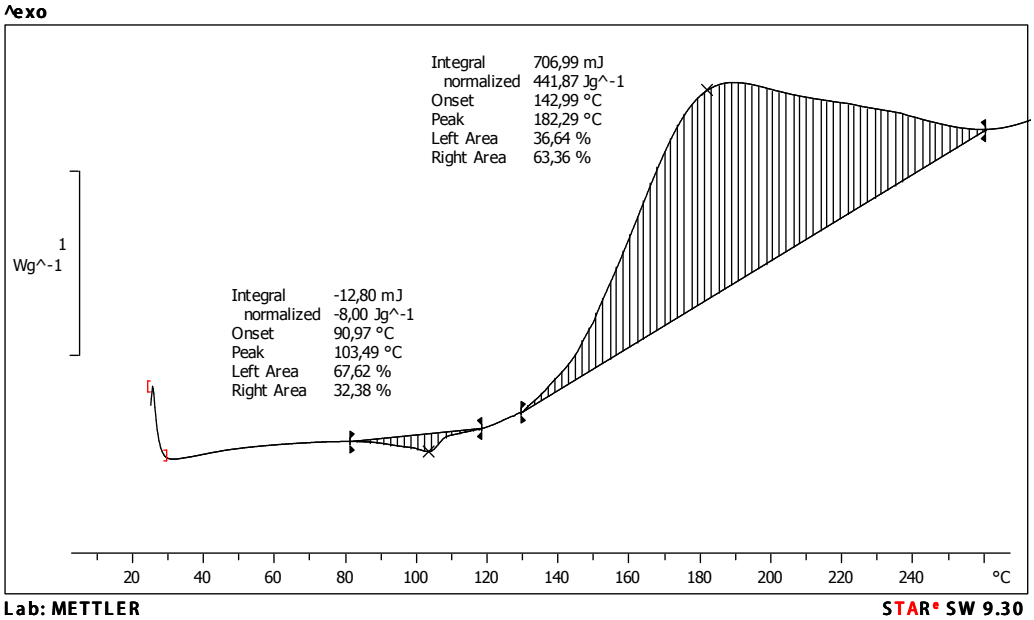

Figure 8. Differential scanning calorimetry (DSC), 10°C/min under N_2, of the dinaphtylpolyynes mixture. The exothermic reaction with onset at 143°C and peak at 182°C can be assigned to the thermal decomposition of the dinaphthylpolyynes.

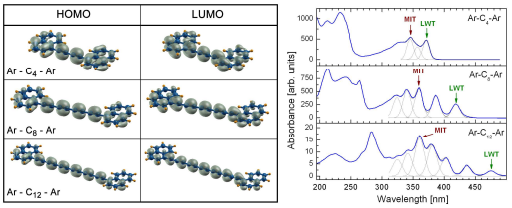

(Left) The electron density of HOMO and LUMO states evaluated by DFT-LSDA simulations for three different dinaphthylpolyynes: Ar-C_4-Ar, Ar-C_8-Ar, Ar-C_{12}-Ar. As the *sp*-carbon chain is longer, the HOMO and LUMO states become more and more localized on the chain backbone. (Right) The experimental electronic absorption spectra of Ar-C_4-Ar, Ar-C_8-Ar and Ar-C_{12}-Ar as recorded by the diode array detector of the HPLC. The observed evolution of the longest wavelength transition (LWT, inversely related to the HOMO-LUMO gap) is in good agreement with the theoretical predictions.

7.2 Combined experimental and theoretical vibrational study of dinaphthylpolyynes

As shown in the previous section, under the C-C reaction conditions, I was able to produce a solution containing dinaphtylpolyynes Ar-C_{2n}-Ar with $n = 2 : 6$. In the following paper I propose a general picture for the study of the vibrational properties of end-capped *sp*CCs based on the results obtained by combining MWRR and infrared spectroscopy with DFT-LSDA calculation of dinaphtylpolyynes. In particular I show how this class of molecules is characterized by a Raman active mode bearing the strongest Raman intensity which shows displacement pattern localized near the chain center. This so called Raman-α mode (R-α) occurs in the range of $1950 - 2300$ cm^{-1} and is characterized by its strong dependence on *sp*CCs length, red-shifting almost uniformly as this length increases. On contrary the most intense IR dipole active modes of the dinaphthylpolyynes involve two main patterns: one (named IR-α) characterized by a displacement distinctly localized at the chain center is present ubiquitously for all dinaphthylpolyynes; another one (named IR-β) with a bilobed pattern occurs from $n > 5$. The IR-α mode vibrates at a frequency almost independent the length of the chains while the IR-β red-shifts uniformly as the chain length increases, such as in the case of the R-α mode. Although the IR-α mode is always present, it carries the main intensity only up to $n = 5$, while it becomes very weak starting from $n = 5$, where the IR-β mode "steals" most of the dipole intensity.

As a consequence I demonstrated how MWRR and IR spectroscopies (complemented by DFT calculations) allows to propose a paradigm for the full identification of general spCCs-containing compounds: MWRR spectroscopy allows the identification of different chain lengths, while IR allows distinguishing families of chains with different terminations (if present).

Vibrational characterization of dinaphthylpolyynes: a model system for the study of end-capped *sp* carbon chains

Eugenio Cinquanta[2,3], *Luca Ravagnan*[*1,2], *Ivano Eligio Castelli*[+1,4], *Franco Cataldo* [5,6]

Nicola Manini[1,4], *Giovanni Onida*[1,4], *Paolo Milani*[1,2]

[1]Dipartimento di Fisica, Università degli Studi di Milano, Via Celoria 16, I-20133 Milano, Italy

[2]CIMAINA, Università degli Studi di Milano, Via Celoria 16, I-20133 Milano, Italy

[3]Dipartimento di Scienza dei Materiali, Università di Milano-Bicocca, Via Cozzi 53, I-20125 Milano, Italy

[4]European Theoretical Spectroscopy Facility (ETSF), Via Celoria 16, 20133 Milano, Italy

[5]Actinium Chemical Research, Via Casilina 1626/A, I-00133 Rome, Italy

[6]Istituto Nazionale di Astrofisica. Osservatorio Astrofisica di Catania,

Via S. Sofia 78, I-95123 Catania, Italy

[*] Corresponding authors. E-mail: luca.ravagnan@mi.infn.it (L.R.)

[+] Present address: Centre for Atomic-scale Materials Design (CAMD), Department of Physics, Technical University of Denmark, DK-2800 Kongens Lyngby, Denmark

ABSTRACT:

We perform a systematic investigation of the resonance and vibrational properties of naphthyl-terminated *sp* carbon chains (dinaphthylpolyynes) by combined multi-wavelength resonant Raman spectroscopy (MWRR), ultraviolet-visible spectroscopy, and Fourier-transform infrared spectroscopy (FT-IR), plus *ab-initio* density functional theory (DFT) calculations. We show that MWWR and FT-IR spectroscopy are particularly suited to identify chains of different lengths and different terminations, respectively. By DFT calculations we further extend those findings to *sp* carbon chains end-capped by other organic structures. The present analysis shows that combined MWRR and FT-IR provide a powerful tool to draw a complete picture of chemically stabilized *sp* carbon chains.

KEYWORDS: *sp*-carbon chains, Raman spectroscopy; Infrared spectroscopy; ab-initio calculations.

1. Introduction

The interest about *sp* carbon chains (*sp*CCs) as building blocks for carbon-based nanoelectronics is very recent [1,2], *sp*CCs have been considered for a long time as objects relevant only for astrochemistry [3-6]: this is due to their high reactivity and instability supporting the opinion that only conditions as those typical of circumstellar and interstellar clouds could allow the presence of large quantities of linear carbon chains acting as intermediates for the formation of either fullerenes or poly-aromatic hydrocarbons (PAHs) [7,8].

In the last decade, an increasing amount of experimental evidences have demonstrated that *sp*CCs can be mass produced in standard laboratory conditions, and, more surprisingly that *sp*CCs can coexist with other carbon allotropic forms [9-10], with *sp*CCs being stabilized by different end-capping groups and in particular by graphene terminations [11-13]. Graphene-terminated *sp*CCs exhibit remarkable magnetic properties, sensitivity to axial strain and rectifying performances potentially enabling their use as spin-filters and spin-valves in magnetic nanodevices [14-17]. End-capped *sp*CCs stabilized by different terminations have also been proposed as building blocks of hydrogen-storage materials [18-19].

Despite the increasing amount of theoretical work dealing with end-capped *sp*CCs, relatively few experimental studies elucidating the structural and functional properties (chain length, bonding nature, electronic structure) are available. Vibrational and optical spectroscopies can provide information about the physical and structural properties of end-capped *sp*CCs, but the identification of the spectroscopic signatures of specific structures is, until now, an open issue.

Recently we demonstrated the possibility to produce efficiently *sp*CCs of different lengths terminated by naphtyl groups (dinaphthylpolyynes) [20]. These compounds represent a family of chemically stabilized α,ω-diarylpolyynes of high interest for several reasons: on one side, they are potentially useful in optoelectronic applications being promising building blocks for the production of *sp*-sp^2 carbon systems for nano-electronic devices; on the other side, they constitute the simplest examples of *sp*CCs terminated by PAHs that could be identified in the interstellar medium

(naphthalene is indeed one of the simplest and most abundant PAHs).

Here we present a full vibrational characterization, both experimental and theoretical, of dinaphthylpolyynes [20]: our approach combines multi-wavelength resonant Raman (MWRR) and Fourier-transform infrared (FT-IR) spectroscopic characterization, with density-functional theory (DFT) modeling. Thanks to the combination of these approaches we obtain an overall description of the vibrational properties of dinaphthylpolyynes thus providing a complete framework for the interpretation of vibrational data of end-capped *sp*CCs.

2. Methods

2.1 Synthesis and chromatographic characterization of dinaphthylpolyynes

The synthesis of a series of dinaphthylpolyynes (in short represented as Ar-C_{2n}-Ar, with Ar = naphthyl group and n = number of acetylenic units of the chain) was obtained, as described in detail in ref. [20], by reacting copper(I)-ethynylnaphthalide with diiodoacetylene under the Cadiot-Chodkiewicz reaction conditions [21,22]. The obtained molecules are dissolved in decahydronaphthalene, and were characterized by high-performance liquid chromatograph (HPLC) analysis using an Agilent Technologies 1100 station with C_8 column (using acetonitrile/water 80/20 as mobile phase at a flow rate of 1.0 ml/min). The HPLC station was also equipped with a diode array detector, allowing recording the ultraviolet-visible (UV-vis) absorption spectra of the separated molecules present in the solution [20]. The UV-vis absorption spectrum of the whole solution was also acquired by using a UV-vis Jasco 7850 spectrometer.

2.2 Multi-wavelength Raman and Infrared characterization

MWRR spectroscopy characterization of the dinaphthylpolyynes solution was performed by using seven different laser wavelengths produced by an Ar ion and a He-Cd laser (Spectra Physics, BeamLok series 2065-7 and Kimmon, IK5352 R-D series, respectively). The wavelengths used were 514.5 nm, 496.5 nm, 488.0 nm, 476.5 nm, 457.9 nm and 363.8 nm for the Ar ion laser, and

441.6 nm for the He-Cd laser. For each wavelength, bandpass clean-up filters (MaxLine filters from Semrock) were used in order to remove spurious plasma lines produced by the lasers.

MWRR spectra were acquired by using a single-grating spectrometer (Acton SP-2558-9N with a 1200 groves/mm grating, blazing 600 nm) equipped with a liquid nitrogen cooled CCD camera (Roper-Princeton Instruments Spec10:400B/LN) and notch filters in order to remove the Rayleigh scattering (StopLine from Semrock). Thanks to this setup the spectra were recorded in a unique acquisition window (typically comprised between 1000 cm^{-1} and 2500 cm^{-1}), repeating 100 times a 60 seconds acquisition. By this approach it was both possible to obtain spectra with high signal to noise ratio (by averaging the different acquisitions) and to detect any possible degradation of the solution induced in time by the laser irradiation. Furthermore, this setup allows us to switch from one laser wavelength to the next in a very short time interval, simply by changing the bandpass and notch filters, and moving the monochromator grating.

Fine calibration of the Raman shift of the acquired spectra was achieved by using the approach proposed by N.C. Craig and I.W. Levin [23]. After each measurement, a spectrum of the plasma lines produced by the lasers was collected by removing the bandpass clean-up filter in the optical system. The accurately tabulated plasma line positions allowed us to correct any possible offset or non linearity of the monochromator and to control the uncertainty on the wave-number axis within 1 cm^{-1} for all excitation wavelengths used (also checked by measuring the G-band position at 1581 cm^{-1} in the spectrum of a highly oriented pyrolytic graphite sample).

The infrared spectrum of the dinaphthylpolyynes solution was acquired in transmission mode by a Perkin Elmer FT-IR/F-FIR (far infrared) Spectrometer “Spectrum 400” with a Universal Attenuated Total Reflectance (UATR) attachment and liquid N_2 cooled Mercury Cadmium Telluride detector operating in the range 750-2500 cm^{-1} with a 2 cm^{-1} resolution. The spectrum of the pure decahydronaphtalene was also acquired and then subtracted from the spectrum of the whole solution in order to remove its infrared features.

2.3 DFT simulations

We simulate isolated (gas phase) dinaphthylpolyynes with n=2-8 acetylenic units within the framework of DFT [24,25] in the local spin-density approximation (LSDA).

We use the QUANTUM ESPRESSO package [26], based on a plane-wave basis (40 Ryd kinetic energy cutoff) and ultra-soft pseudo-potentials [27,28].

We relax the atomic position until the largest residual force and energy difference are smaller than 8 pN and 10^{-5} Ryd, respectively. Starting from the relaxed position, we then compute the molecular vibrational modes, plus their infrared intensities and non resonant-Raman cross-sections, using density-functional perturbation theory [26]. The computational details are similar to those validated and used, e.g., in Refs. [1, 20] for the simulations of the structure and vibrational properties of *sp*CCs terminated by C_{20}, graphene nanoribbons (NR) and CH_2.

3 Results and Discussion

3.1 Raman-active modes

Figure 1a reports the electronic absorption spectrum of each molecular species contained in the dinaphtylpolyynes mixture, measured by using the diode array detector interfaced to the column of the HPLC. Table 1 reports the relative molar concentration *C(n)* of the individual components, as estimated by means of the Lambert-Beer law [20].

n	dinaphthylpolyyne Formulas	*C(n)*
2	Ar-C_4- Ar	47 ± 4 %
3	Ar-C_6-Ar	19.7 ± 0.6 %
4	Ar-C_8-Ar	18.2 ± 2.2 %
5	Ar-C_{10}-Ar	11.3 ± 1.2 %
6	Ar-C_{12}-Ar	4.1 ± 0.3 %
n>6		Not detected

Table 1. Relative molar concentration of the dinaphthylpolyynes (with $2 \leq n \leq 6$) in the solution [20].

One can clearly observe typical multi-peak structure in the optical absorption spectra due to

Franck-Condon satellites of the main electronic transition [20, 29-32]. The wavelength of the purely electronic transition, i.e. the longest-wavelength transition (LWT), shifts linearly with the number of acetylenic units, due to the hybridization of the molecular orbitals of the *sp*CCs with those of the terminations [20].

Figure 1a also reports (as vertical lines) the positions of the individual laser wavelengths used for MWRR spectroscopy. As can be observed, the two laser lines at longer wavelength (514.5 and 496.5 nm) do not match any absorption line of the spectra shown, while from 488.0 nm downwards, at least one absorption peak is crossed. At 363.8 nm, all the dinaphthylpolyynes peaks are crossed.

The matching of the laser wavelength with the energy of an electronic absorption of a molecular species has important consequences for the obtained Raman spectra [33]. Indeed, although Raman scattering occurs for any excitation wavelength, when the energy of the incident photon matches the energy of an optical absorption peak (i.e. an electronic transition) of a species present in the solution, a strong enhancement of the Raman intensity corresponding to this particular species occurs [34]. In contrast, resonance does not affect the position of the Raman peaks (i.e. the vibrational frequency) but only their intensity [32, 34].

Figure 1b shows the Raman spectra obtained on the dinaphthylpolyynes solution using the 7 excitation wavelengths: all the spectra are characterized by a multi-peak structure. In particular, seven of those peaks (indicated as P1-P7 in Figure 1b, and summarized in Table 2) are present in all spectra at the same wavenumber, but with different intensities.

Peak label	Raman shift	Dinaphthylpolyynesassignment
P1	1957 ± 4	
P2	1980 ± 3	
P3	2005 ± 2	Ar-C_{16}-Ar (?)
P4	2029 ± 6	Ar-C_{14}-Ar (?)
P5	2057 ± 6	Ar-C_{12}-Ar
P6	2090 ± 3	Ar-C_{10}-Ar
P7	2129 ±2	Ar-C_8-Ar

Table 2. Assignment of the experimental Raman peaks to dinaphthylpolyynes of different lengths.

Considering for instance the peak P5 in Figure 1b, its intensity remains substantially unchanged when acquired with the 514.5 nm and 496.5 nm laser wavelengths, while it becomes much stronger at 488.0 nm, and reaches its maximum intensity at 476.5 nm. It then drops in intensity at 457.9 nm and increases again at 441.6 and 363.8 nm. The electronic absorption spectra of Figure 1a clarifies that this behavior follows exactly the evolution of the optical absorption of Ar-C_{12}-Ar. It is thus possible to attribute, based on its resonant behavior, the peak P5 to Ar-C_{12}-Ar. Following the same approach, also the peaks P6 and P7 have resonant behaviors that can be clearly attributed to Ar-C_{10}-Ar and Ar-C_8-Ar respectively. Also the peaks P1, P2, P3 and P4 show resonant behaviors, which however do not correspond to any of the dinaphthylpolyynes identified by HPLC. In particular their intensity indicates that they are due to species resonating already at 514.5 nm, and thus at a wavelength exceeding that of the LWT of any of the identified species.

In order to obtain a better understanding, absorption spectroscopy measurements were repeated on the whole solution, before being separated in the HPLC column. Figure 2 shows the resulting spectrum, compared to the sum of the individual spectra, reported in Figure 1a, of the single-*n* Ar-C_{2n}-Ar molecules (weighted with the relative molar concentration of Table 1). The sum of the spectra, although significantly broader, reproduces accurately the spectrum of the whole solution. However as highlighted in the inset of Figure 2, an extra weak peak (between 490 and 530 nm) is

present in the whole-solution spectrum, that is absent in the sum spectrum. This peak must be related to the dinaphthylpolyynes with n>6, as for instance Ar-C_{14}-Ar and Ar-C_{16}-Ar, that are contained in extremely low quantity in the solution and that were thus not identified by HPLC [20]. Indeed, considering the linear evolution of the LWT observed for the dinaphthylpolyynes with n=2-6, one would expect for n=7 a LWT centered at about 500 nm, while for n=8 a value for LWT of about 525 nm [20], consistently with the position of the observed peak. Remarkably, the resonant evolution of P4 for the 514.5 nm, 496.5 nm and 488.0 nm laser lines in Figure 1b follows nicely the evolution of this weak absorption peak. Indications of the presence of dinaphthylpolyynes with n>6 in the solution are furthermore supported by the DFT simulations. Indeed, as typical for *sp* linear carbon chains, the Raman active mode of the dinaphthylpolyynes bearing the strongest Raman intensity shows a displacement pattern localized near the chain center (for more details about the pattern of longitudinal atomic displacements, see figure reported in the supplementary materials [35]). This so-called Raman-α mode (R-α) [1, 36] occurs in the range 1950 ÷ 2300 cm^{-1} and is characterized by its strong dependence on the *sp*CC length, red shifting almost uniformly as this length increases (see Figure 3a). The attribution based on the resonant behavior of P5, P6 and P7 to the alpha mode of dinaphthylpolyynes Ar-C_{2n}-Ar with n = 6, 5 and 4 respectively is also supported by the simulated frequencies, which match the experimental peaks within 15 cm^{-1} (i.e. 1%, see Table 2). Furthermore, the simulations support the attribution of the peaks P1 - P4 at smallest Raman shifts to n>6 dinaphthylpolyynes.

None of the P1-P8 peaks in the Raman spectra can be associated to n = 2 and 3 dinaphthylpolyynes (i.e. Ar-C_4-Ar and Ar-C_6-Ar), even though, altogether, they represent almost 70% of the *sp*CCs present in solution (see Table 1). Only in the Raman spectrum acquired with the 363.8 nm laser line four peaks (P8-P11 in Figure 1b, not present in the other spectra) are clearly identifiable: these peaks have positions compatible with the vibrational *sp*CCs modes of Ar-C_4-Ar and Ar-C_6-Ar. The absence of these peaks in the other spectra can be understood by considering the computed non-resonant Raman cross section for the R-α modes shown in Figure 4a. Indeed, the

Raman cross section grows rapidly with the increasing chain length, being for example 20 times larger for n = 6 than for n = 2. Figure 5 shows the comparison between the experimental Raman spectra recorded using the 514.5 nm laser line (which is non-resonant for the dinaphthylpolyynes with n = 2-6) and the spectrum obtained by summing the simulated non-resonant Raman spectra of the dinaphthylpolyynes weighted by their relative molar concentrations (Table 1). The experimental and simulated spectra display a remarkable agreement. In particular, the simulated spectrum confirms that the Raman peaks from chains with n = 4-6 dominate over those relative to n = 2 and n = 3. The simulations also predict the small spectral features P5' and P6', thus attributed to secondary Raman active modes (weaker than the main α modes).

In the simulated spectrum of Figure 5b we include the contributions of n = 7 and 8 *sp*CCs. Those peaks (indicated as dashed peaks in Figure 5b) were introduced by assuming arbitrary relative molar concentrations of 1% and 0.5% respectively (since n = 7 and 8 were not detected by HPLC). On one hand, their positions are consistent with the positions of P4 and P3, on the other hand their observed intensity is most likely enhanced by resonance: indeed, as previously discussed, Ar-C_{14}-Ar and Ar-C_{16}-Ar are expected to have electronic transitions matching the 514.5 nm laser line (see also Figure 2). Following the same reasoning, P1 and P2 might be related to even longer dinaphthylpolyynes (as for example Ar-C_{18}-Ar and Ar-C_{20}-Ar) that although present in negligible concentrations in the solution (far below the detection limit of the HPLC), appear in the Raman spectrum due to their extremely large Raman cross sections, further enhanced by resonance.

Likewise, we identify the P8-P11 peaks with the simulated vibrational modes of Ar-C_4-Ar and Ar-C_6-Ar because they can be observed only when using the 363.8 nm excitation line (Figure 1b) to match the optical resonance (Figure 1a) and therefore to compensate for the small cross-sections of these short chains.

In summary, by combining electronic absorption spectra recorded during HPLC, MWRR and DFT-LSDA simulations it is possible to fully and coherently describe the mixture of *sp*CCs of several lengths. In particular we can identify the vibrational modes of the different species present

in the system, whose position is strongly dependent on the chain length. Furthermore we demonstrate that Raman spectroscopy with long excitation wavelengths is highly sensitive to long *sp*CCs (rather than to short chains), due to their larger non-resonant cross sections, further enhanced by selective resonant absorption associated to their smaller HOMO-LUMO gaps. As the laser wavelength is shifted toward the UV, shorter *sp*CCs becomes progressively resonant, with their R-α peaks becoming the dominant features of the spectra. This resonance mechanism gives a chance to the R-α peaks of the abundant $n = 2$ and $n = 3$ *sp*CCs to become visible despite their extremely small Raman cross sections.

3.2 Infrared-active modes

Figure 6a shows the FT-IR spectra measured on the dinaphthylpolyynes solution. Similarly to MWRR, a multi-peak structure can be clearly identified, which is distributed on a much narrower wavenumber interval (about 100 cm^{-1} compared to the 250 cm^{-1} interval of Raman).

The peak positions agree well with the IR frequencies of dinaphthylpolyynes with n = 1-6 as measured by K. Nakasuji et al. in ref. [31]. Nevertheless, the small separation between the different peaks in Figure 6a (below 20 cm^{-1}) makes their precise assignment to the dinaphthylpolyynes of specific chain length quite problematic. The DFT-LSDA simulations help us understand the small dispersion of the IR modes. The displacement patterns of the most intense IR-active modes of the dinaphthylpolyynes involve two main patterns: one (named IR-α) characterized by a displacements distinctly localized at the chain center is present ubiquitously for all dinaphthylpolyynes; another one (named IR-β) with a bi-lobed pattern occurs from $n > 5$. As shown in Figure 3b, the IR-α mode vibrates at a frequency almost independent of the length of the dinaphthylpolyynes (with the exception of the $n = 2$ chain), while the IR-β red-shifts uniformly as the chain length increases, like in the case of the R-α mode. Although the IR-α mode is always present, it carries the main intensity only up to $n = 5$, while it becomes very weak starting from n = 6, where the IR-β mode "steals" most of the dipole intensity (see Fig. 4b). Nevertheless, for $n > 6$ the intensity of the IR-α mode

remains relevant, bearing approximately 20% of the intensity of the C=C modes for n = 8. As illustrated in Figure 4b (IR-α for n=6 is less than 10^{-4}), the cross section of the most intense IR mode (the IR-α up to n = 5, and the IR-β for n > 5) increases exponentially like the R-α mode, showing that also IR spectroscopy is much more sensitive to long chains than to short ones. Unfortunately, while Raman spectroscopy, taking advantage of optical resonance, can be tuned to enhance the response of one molecular species, this cannot be done with IR spectroscopy.

Figure 6b shows the simulated IR spectrum obtained, as in the case of Raman in Figure 5b, by summing the simulated IR spectra of the dinaphthylpolyynes weighted by their relative molar concentrations. It must be noted that, in order to match the experimental spectrum in Figure 6a, a global 50 cm^{-1} red-shift of the simulated isolated-molecule spectrum was required. Although shifts of this entity between the simulated frequencies and the experimental one are common (see for example ref. [36,37]), this circumstance becomes surprising when considering the very good agreement of the simulated Raman modes with experiment, with no need of any shift (Figure 5). Nevertheless, one can understand this by considering that, contrary to the R-α mode, the most intense IR modes have wide bond displacement near the chain termination (i.e. at the naphthyl groups). As a consequence, it is likely that the interaction between the dinaphthylpolyynes and the solvent (attenuating the motion of the chain termination) induces the observed softening of the IR active modes much more than the R-α mode, which are localized near the chain center. Similar effects have been observed by many authors also for other systems both in solution and in the solid state [37-41]. Although the solvent-induced shift need not be uniform for dinaphthylpolyyne of different lengths, and also considering the frequent tendency of LDA to overestimate the vibrational frequencies [42-44], the overall agreement between the shifted simulated spectrum in Figure 6b and the experimental one in Figure 6a is good.

In particular, we ascribe the accumulation of the components in the 2150-2200 cm^{-1} interval to the lack of dispersion of the IR-α mode and the weak dispersion of the IR-β as a function of the chain length.

3.3 From dinaphthylpolyynes to general properties of end-capped spCCs

In order to verify the general validity of the observed behavior for the Raman and IR modes on dinaphthylpolyynes, we also carried out DFT-LSDA calculations of *sp*CCs end-capped by other carbon based structures: C_{20}, graphene nanoribbons (NR), and CH_2 [1]. Figure 7 shows the resulting simulated R-α and IR-α frequencies as functions of the number of acetylenic units. Figure 7 also reports the bond-length alternation of the chains (BLA, see definition in ref. [1]) and the length of the first bond between the chain and the terminating structure (FBL).

Figure 7 clarifies that the BLA and FBL values allow to characterize precisely the nature of the different *sp*CCs. Specifically, the BLA measures of the overall degree of dimerization of the *sp*CC. As discussed in Ref. [1], although the BLA is maximum for "ideal" polyynes (having alternating single-triple bonds) and negligibly small for cumulenes (having all double bonds), its value is not only affected by the nature of the chain termination (being inversely related to the order of the bond between the chain and the terminating group), but also by the chain length and, for sp^2-terminated chains, by the chain torsion [1]. Indeed, as shown in Figure 7, for each termination type the BLA decreases progressively with increasing *n*. In contrast, the FBL provides a direct indication of the bond strength between the terminating group and the chain, and its value is almost independent of the chain length.

Consider now the *n*-dispersion of the R-α and IR-α modes: the general validity of the trends of dinaphthylpolyynes discussed in the Sect. 3.1 and 3.2 appears clear. Indeed, the linear *n*-dispersion of the R-α mode and the approximate *n*-independence of the IR-α mode (for $n > 2$) are observed for all kinds of termination. Remarkably, as shown in Figure 7, the evolution of the R-α and IR-α modes follows, respectively, the dispersion of the BLA and FBL values.

Note that the R-α frequency depends only weakly on the nature of the terminating group, but, similar to the BLA, it is dominated by the strong dispersion with *n*. Conversely, the frequency of the IR-α mode (for $n > 2$) correlates to the value of the FBL and, in turn, to the nature of the

chain termination. Those observations strongly indicate that Raman and IR characterization can provide complementary information*: Raman identifies the presence of spCCs of different length within a given family* (i.e. with a specific terminating group), while *IR distinguishes between different families of spCCs compounds regardless their length distribution*.

4. Conclusions

We performed an experimental and theoretical characterization of the vibrational properties of Naphthyl-terminated *sp*CCs, by combining MWRR and FT-IR spectroscopies with theoretical DFT-LSDA modeling. One R-α mode dominates the Raman spectra of dinaphthylpolyynes, while the IR spectrum contains one dominant IR-α dipole-active mode up to n=5, plus a second IR-β from n>5 onwards; both R-α and IR-β red shift as the chain length increases, while IR-α is almost unaffected by the chain length. As a consequence the non-resonant Raman spectrum of a mixture of terminated *sp*CCs of different lengths covers almost uniformly the whole frequency range of *sp* carbon (1900-2300 cm^{-1}), while, due to the length-independence of IR-α, the IR spectrum exhibits an accumulation of components around a single frequency, here 2200 cm^{-1} for dinaphthylpolyynes, with only few weak features far from this frequency.

We demonstrated that resonance effects can be exploited with MWRR spectroscopy for the identification of the detected peaks as R-α modes of dinaphthylpolyynes of specific lengths. Raman spectroscopy is far more sensitive to long chains rather than short ones, due to: (i) the rapid increase of the non-resonant Raman cross section with chain length and (ii) the onset of resonant enhancement already with the long-wavelength (visible) excitation line following the decreasing HOMO-LUMO gap with increasing chain length [20,45].

Due to the weak n-dispersion, no complete assignment of the individual peaks to specific IR-α and IR-β modes was feasible. Nevertheless, DFT calculations indicate that the IR modes, much more than Raman ones, are strongly affected by the chain termination groups, rigidly shifting to lower wavenumbers as the strength of the terminal bonds increases.

The combined characterization of end-capped *sp*CCs by MWRR and IR spectroscopy (complemented by DFT calculations) allowed us to propose a paradigm for the full identification of general *sp*CCs-containing compounds: MWRR spectroscopy allows the identification of different chain lengths, while IR allows distinguishing families of chains with different terminations (if present). The combination of the two techniques represents therefore a very powerful tool for the characterization of complex carbon-based materials [46-49].

Acknowledgments

The authors wish to thank W. R. Browne from the "Stratingh Institute for Chemistry," University of Groningen and O. Ivashenko from the "Zernike Institute for Advanced Materials," University of Groningen for the precious help in the FT-IR measurements.

REFERENCES

[1] L. Ravagnan, N. Manini, E. Cinquanta, G. Onida, D. Sangalli, C. Motta, M. Devetta, A. Bordoni, P. Piseri and P. Milani, *Phys. Rev. Lett.* **102**, 245502 (2009).

[2] B. Akdim, *ACS Nano* **5**, 1769 (2011).

[3] G.H. Herbig, *Annu. Rev. Astron. Astrophys.* **33**, 19 (1995).

[4] L. J. Allamandola, D.M. Hudgins, C.W. Bauschlicher Jr., and S.R. Langhoff, *Astron. Astrophys.* **352**, 659 (1999).

[5] T.P. Snow, *Spectrochim. Acta A* **57**, 615 (2001).

[6] S. Kwok, *Astrophys. Space Sci.* **319**, 5 (2009).

[7] J. Cami, J. Bernard-Salas, E. Peeters and S.E. Malek, *Science* **329**, 1180 (2010).

[8] P. Ehrenfreund, B.H. Foing, *Science* **329**, 1159 (2010).

[9] C.H. Jin, L. Haiping, P. Lianmao, K. Suenaga and S. Iijima, *Phys. Rev. Lett.* **102**, 205501 (2009).

[10] A. Hu, M. Rybachuk, Q.B. Lu and W.W. Duley, *Appl. Phys. Lett.* **91**, 131906 (2007).

[11] L. Ravagnan, F. Siviero, C. Lenardi, P. Piseri, E. Berborini, P. Milani, C.S. Casari, A. Li Bassi and C.E. Bottani, *Phys. Rev. Lett.* **89**, 285506 (2002).

[12] C. S. Casari, A. Li Bassi, L. Ravagnan, F. Siviero, C. Lenardi, P. Piseri, G. Bongiorno, C. E. Bottani and P. Milani, *Phys. Rev. B* **69,** 075422 (2004).

[13] L. Ravagnan, P. Piseri, M. Bruzzi, S. Miglio, G. Bongiorno, A. Barsega, C. S. Casari, A. Li Bassi, C. Lenardi, Y. Yamaguchi, T. Wakabayashi, C. E. Bottani and P. Milani, *Phys. Rev. Lett.* **98,** 216103 (2007).

[14] B. Standley, W.Z. Bao, H. Zhanh, J. Bruck, C.N. Lau and M. Bockrath, *Nano Lett.* **8**, 3345 (2008).

[15] Y. Li, A. Sinitskii and J.M. Tour, *Nature Mater.* **7**, 966 (2008).

[16] X. Deng, Z. Zhang, J. Zhou, M. Qiu and G.J. Tang, *J. Chem. Phys.* **132**, 124107 (2010).

[17] M.G. Zeng, L. Shen, Y.Q. Cai, Z.D. Sha and Y.P. Feng, *Appl. Phys. Lett.,* **96**, 042104 (2010).

[18] C.C.S. Liu, H. An, L.J. Guo, Z. Zeng and X. Ju, *J. of Chem. Phys.* **134**, 024522 (2011).

[19] C.C.S. Liu, H. An and Z. Zeng, *Phys. Chem. Chem. Phys.* **13**, 2323 (2011).

[20] F. Cataldo, L. Ravagnan, E. Cinquanta, I. E. Castelli, N. Manini, G. Onida and Milani P., *J. Phys. Chem B* **114**, 14834 (2010).

[21] F. Cataldo, G. Angelini, O. Ursini, M.F. Tomassini and C.S. Casari, *J. Macromol. Sci. A Pure Appl. Chem.* **47,** 739 (2010).

[22]P. Cadiot, W. Chodkiewicz, In "*Chemistry of Acetylenes*"; Viehe, H. G., Ed.; Marcel Dekker: New York, **1969**; pp 597-647.

[23] N.C. Craig, I. W. Levin, *Applied Spectroscopy* **33**, 475 (1979).

[24] P. Hohenberg and W. Khon, Phys. Rev. **136**, B864 (1964).

[25] W. Kohn and L. J. Sham, Phys. Rev.**140**, A1133 (1965) .

[26] P. Giannozzi, S. Baroni, N. Bonini, M. Calandra, R. Car, C. Cavazzoni, D. Ceresoli, G. L. Chiarotti, M. Cococcioni, I. Dabo, A. Dal Corso, S. de Gironcoli, S. Fabri, G. Fratesi, R. Gebauer, U. Gerstmann, C. Gougoussis, A. Kokalj, M. Lazzeri, L. Martin-Samos, N. Marzari, F. Mauri, R. Mazzarello, S. Paolini, A. Pasquarello, L. Paulatto, C. Sbraccia, S. Scandolo, G. Sclauzero, A. P. Seitsonen, A. Smogunov, P. Umari and R. M. Wentzcovitch, *J. Phys.: Condens. Matter.* **21**, 395502 (2009). See also http://www.quantum-espresso.org.

[27] D. Vanderbilt, *Phys. Rev. B* **41**, 7892 (1999).

[28] F. Favot and A. Dal Corso, *Phys. Rev. B* **60**, 11427 (1999).

[29] J.P. Maier, *Chem. Soc. Rev.* **26**, 21 (1997).

[30] S. Akiyama, K. Nakasuji, K. Akashi and M. Nakagawa, *Tetrahedron Lett.* **9**, 1121 (1968).

[31] K. Nakasuji, S. Akiyama, K. Akashi and M. Nakagawa, *Bull. Chem. Soc. Jpn.* **43**, 3567 (1970).

[32] M. Nakagawa, S. Akiyama, K. Nakasuji and K. Nishimoto, *Tetrahedron* **27**, 5401 (1971).

[33] D.L. Gerrard, W.F. Maddams, *Macromolecules* **8**(1), 4-58 (1975).

[34] Z.L. Wu, S. Dai and S. H. Overbury, *J. Phys. Chem. C* **114**, 412 (2010).

[35] See Supplementary Material Document No. at [link] for the pattern of longitudinal atomic displacements for the main Raman and Infrared active modes of dinaphthylpolyyne, as simulated by DFT-LSDA.

[36] L.M. Malard, D. Nishide, L.G. Dias, R.B. Capaz, A.P. Gomes, A. Jorio, C.A. Achete, R. Saito, Y. Achiba, H. Shinohara and M.A. Pimenta, *Phys. Rev. B* **76**, 233412 (2007).

[37] M. Yildizhan, D. Fazzi, A. Milani, L. Brambilla, M. Del Zoppo, W. A. Chalifoux, R. R. Tykwinski and G. Zerbi, *J. Chem. Phys.* **134**, 124512 (2011).

[38] H. Tabata, M. Fuji, S. Hayashi, T. Doi and T. Wakabayashi, *Carbon* **44**, 3168 (2006).

[39] T. Wakabayashi, T. Murakani, H. Nagayama, D. Nishide, H. Kataura, Y. Achiba, H. Tabata, S. Hayashi and H. Shinohara, *Eur. Phys. J. D* **52**, 79 (2009).

[40] F. Shindo, Y. Bénilan, P. Chaquin, J.C. Guillemin, A. Jolly and Fr. Raulin, *J. Mol. Spectrosc.* **210**, 191 (2001).

[41] A. Lucotti, M. Tommasini, D. Fazzi, M. Del Zoppo, W. A. Chalifoux, M. J. Ferguson, G. Zerbi and R. R. Tykwinski, *J. Am. Chem. Soc.* **131**, 4239 (2009).

[42] F. Favot and Dal Corso A., *Phys. Rev. B* **60**, 11427 (1999).

[43] M. Lazzeri, C. Attaccalite, L. Witz, and F. Mauri, *Phys. Rev. B* **78**, 081406 (2008).

[44] S. Ghosh, *Intermetallics* **17**, 708 (2009).

[45] M. Weimer, W. Hieringer, F. Sala and A. Goerling, *Chem. Phys*. **309**, 77-87 (2005).

[46] M. Bogana, L. Ravagnan, C. S. Casari, A. Zivelonghi, A. Baserga, A. Li Bassi, C.E. Bottani, S. Vinati, E. Salis, P. Piseri, E. Barborini, L. Colombo and P. Milani, *New J. Phys.* **7**, 81 (2005).

[47] Y. Yamaguchi, L. Colombo, P. Piseri, L. Ravagnan and P. Milani, *Phys. Rev. B* **76**, 134119 (2007).

[48] I. E. Castelli, N. Ferri, G. Onida, and N. Manini, "Carbon sp chains in graphene nanoholes", *J. Phys: Condens. Matter*. (in press). "Electronic preprint: arXiv:1109.6591".

[49] C. Jager, H. Mutschke, T. Henning and F. Huisken, *EAS Publications Series* **46**, 293 (2011).

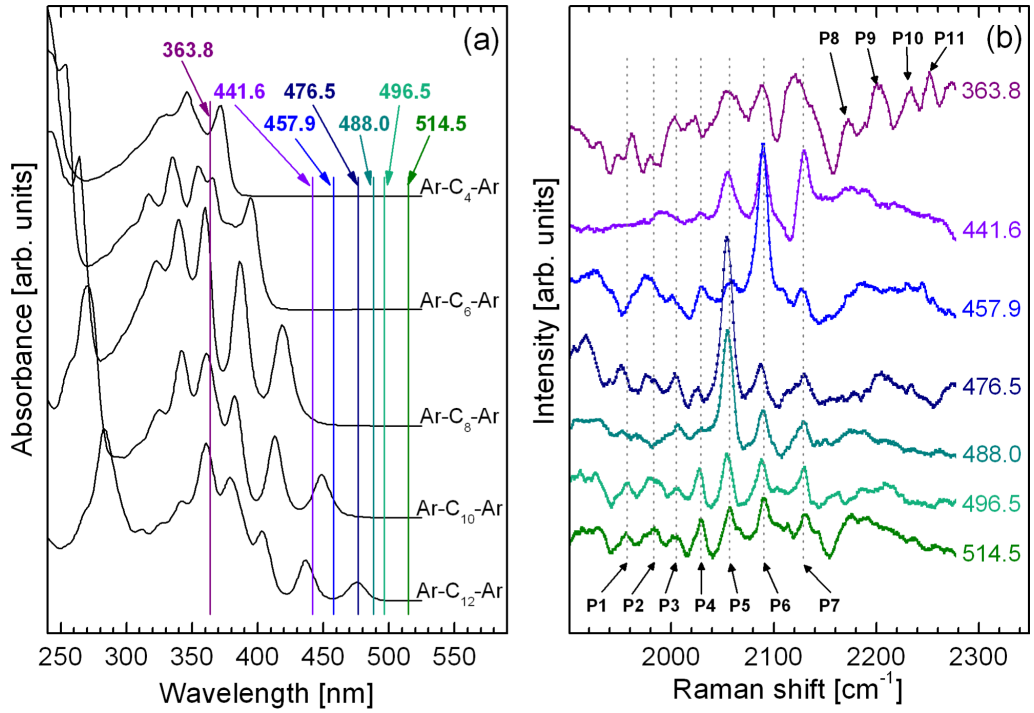

Figure 1 (a) UV-vis absorption spectra of dinaphthylpolyynes of different chain length measured by using the diode array detector interfaced to the column of the HPLC. Vertical lines represent the excitation wavelengths (i.e the laser lines) used for MWRR spectroscopy. (b) MWRR spectra of the whole solution obtained using 7 different excitation wavelengths, whose value in nm is indicated at the right.

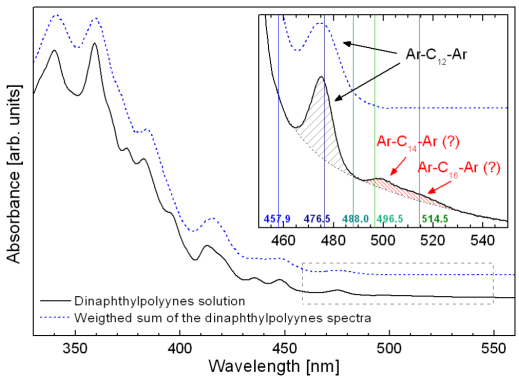

Figure 2 Comparison between the UV-vis spectrum of the solution containing the mixture of dinaphthylpolyynes with different chain length (black solid line) and the weighted sum of the spectra recorded on the individual dinaphthylpolyynes separated by HPLC from the same solution (blue dashed line). Inset: a blowup of the 450-550 nm region, with several excitation lines used for the Raman experiments, and the peak assignments.

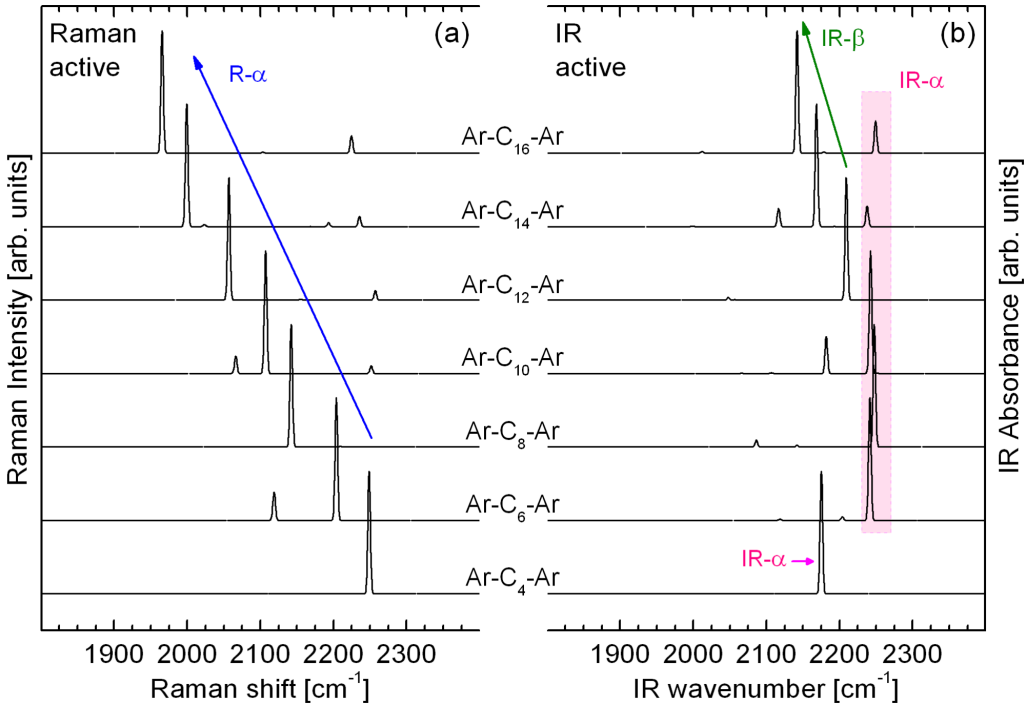

Figure 3: The DFT-simulated frequencies of the (a) Raman and (b) IR active modes of dinaphthylpolyynes. The intensities are normalized to the most intense mode in the 1900-2300 cm^{-1} window.

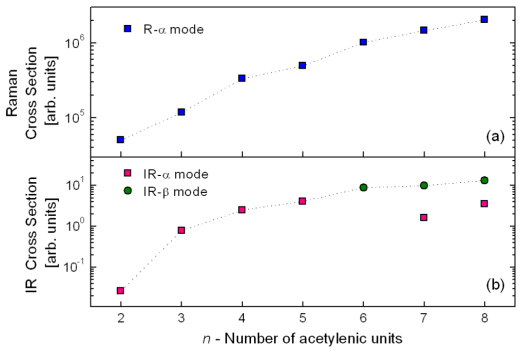

Figure 4: (a) Non-resonant Raman cross sections of the R-α mode of dinaphthylpolyynes as a function of the chain length; (b) the dipole intensity of the IR-α and IR-β modes of dinaphthylpolyynes (IR-α for $n = 6$ is less than 10^{-4}).

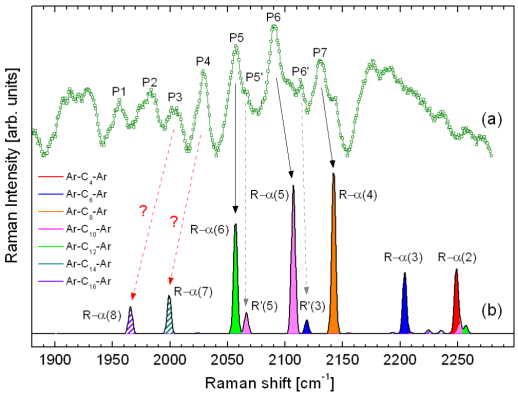

Figure 5: (a) Experimental Raman spectrum measured using the 514.5 nm excitation wavelength. (b) Simulated Raman spectrum obtained by combining the DFT spectra of Fig. 3(a) with the computed non-resonant cross-sections of Fig. 4(a), weighted by the measured concentrations. Arrows indicate the correspondence between experimental and computed peaks.

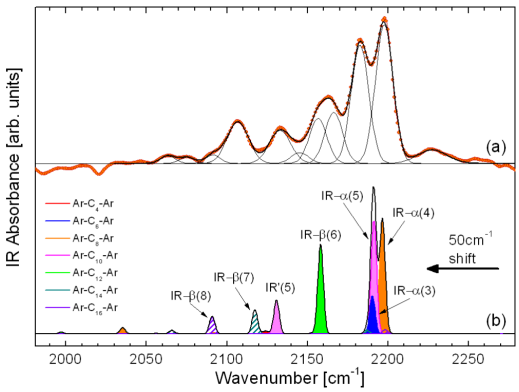

Figure 6: (a) Measured infrared spectrum of the solution containing Ar-C_{2n}-Ar molecules (small circles), with its decomposition into Gaussians (thin solid). (b) Computed infrared spectrum obtained by combining the DFT spectra of Fig. 3(b) (red-shifted by 50 cm^{-1}) and dipole intensities of Fig. 4(b), weighted by the measured concentrations.

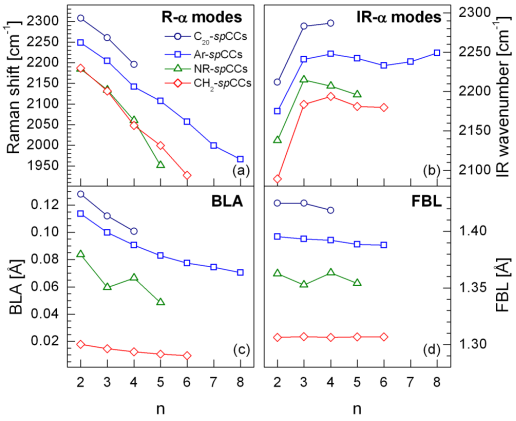

Figure 7: Simulated (a) R-α frequencies, (b) IR-α frequencies, (c) BLA [1], and (d) the length of the first bond between the chain and the terminating structure, as functions of the number of acetylenic units forming the *sp*CC bonded to: C_{20} clusters (circles), naphtil groups (squares), graphene nanoribbons (triangles), and CH_2 groups (diamonds).

Chapter 8

sp-sp^2 pure carbon film

In the recent past the sp-sp^2 pure carbon material has been continuously studied since its identification by L. Ravagnan *et al* in the 2002 [31]. This system can be synthesized, as discussed in details in sec.3.1 and 3.2, by producing pure carbon clusters with a *PMCS* cluster source and depositing them with the *SCBD* technique.

Form the vibrational point of view, Raman spectroscopy provided the first identification of the presence of sp hybridization in the amorphous sp^2 matrix. The first description proposed for the presence of spCCs in this amorphous pure carbon system was based on the identification of two main components constituting the C band in the Raman spectrum of the sp-sp^2 pure carbon material, one related to cumulenic-like chains and the other related to polyynic-like chains.

Beyond the vibrational analysis, reactivity and conductivity measurements have been carried out to better understand the presence and stability of spCCs [70, 71, 59, 86, 60]: polyynic-like and cumulenic-like species are present and stabilized in all-carbon metastable structures and, under He, N_2, and H_2 exposure, the amount of spCCs reduces with an exponential decay with time constants depending upon the type of the gas.

From the transport properties point of view, it has been demonstrated how the presence of sp^2-terminated cumulenic-like chains affect the electrical transport mechanism of the system through a self-doping mechanism by pinning the Fermi level closer to one of the mobility gap edges; cumulenic-like spCCs, stabilized in the sp^2 matrix, and used to tailor the electrical properties of the material by controlling their density, can be thought as building blocks in carbon based nano-electronic devices [19, 20, 21].

Although the huge effort devoted to the study of stabilized spCCs, till now it is not present in the literature a general framework for the interpretation of the physical and chemical properties of end-capped spCCs. The most explored way to fix this lack of comprehension is to try to characterize chains from their spectroscopic signature, nevertheless the assignment of the electronic and vibronic signatures of specific structures is, until now, an open issue.

In this section I present a complete study, both experimental and theoretical, of the vibrational properties of the sp-sp^2 pure carbon films. I apply the model developed for dinaphthylpolyynes to this more complex system in order to provide a complete description of the physical and chemical properties of the carbyne-rich pure carbon film through a clear identification and assignment of the vibrational features presents in the Raman and infrared spectrum related to spCCs with different lengths and terminations .

8.1 Modeling the vibrational properties of sp^2 and sp^3 terminated spCCs

The results obtained for dinaphtylpolyynes suggests that it is possible to provide an exhaustive characterization of *sp*-sp^2 systems by combining different spectroscopical technique with theoretical modeling. *Ab-initio* total-energy and phonon calculations have been performed on a selected range of model structures sampling significantly the infinite variety of 3D arrangements of *sp*CCs bridging graphitic fragments in different hybridization states.

In particular I show that *sp*CCs can be stabilized effectively by termination on graphitic nano-fragments, and that in the resulting structures the carbon chain can be torsionally stiff, due to the broken axial symmetry with staggered π bond. Then has been explored how the structural, vibrational, and electronic properties of such chains are affected by the nature and geometry of the termination. In particular, we show that sp^2 bonding to graphitic fragments and graphene nano-ribbons (NRs) produces remarkably stable structures, with cumulenic-like chains displaying a non-negligible bond-length alternation (BLA), thus making meaningless the traditional categories of polyynes (dimerized chains) and cumulenes (un-dimerized chains).

Theoretical calculation details and technicalities are exhaustively described in the dedicated chapter 6 within the Methods part II.

Effects of axial torsion on sp carbon atomic nanowires

Luca Ravagnan[1,2], Nicola Manini[1,3], Eugenio Cinquanta[1,2*], Giovanni Onida[1,3,†] Davide Sangalli[1,3], Carlo Motta[1,3], Michele Devetta[1,2], Andrea Bordoni[1,2], Paolo Piseri[1,2], and Paolo Milani[1,2‡]

[1] *Physics Department and INFM - University of Milan, Via Celoria 16, 20133 Milano, Italy*

[2] *CIMAINA - Via Celoria 16, 20133 Milano, Italy and*

[3] *European Theoretical Spectroscopy Facility, Via Celoria 16, 20133 Milano, Italy*

(Dated: April 22, 2009)

Abstract

Ab-initio calculations within Density Functional Theory combined with experimental Raman spectra on cluster-beam deposited pure carbon films provide a consistent picture of sp-carbon chains stabilized by sp^3 or sp^2 terminations, the latter being sensitive to torsional strain. This unexplored effect promises many exciting applications since it allows one to modify the conductive states near the Fermi level and to switch on and off the on-chain π-electron magnetism.

PACS numbers: 36.20.Ng, 31.15.A-, 81.07.-b, 61.48.De, 78.30.-j

Keywords: carbyne, Raman spectrum, cumulene, graphene, nanowire

* Present address: Material Science Department - University of Milan Bicocca, Via Cozzi 53, 20125 Milano, Italy

†Electronic address: giovanni.onida@mi.infn.it

‡Electronic address: pmilani@mi.infn.it

Post-silicon electronics has seen the recent opening of entirely new perspectives along the way of carbon-based devices. By proper nanoscale design, entirely carbon-made transistors have been realized [1]. Future applications have been devised, including bio-nanotechnology ones such as devices for fast DNA reading [2]. Even considering only well-demonstrated applications, the potential of carbon-based electronics is undoubtedly enormous, as testified by the realization of non-volatile memories based on two-terminals atomic-scale switches [3] and bistable graphitic memories [4]. Specifically, these structural memory effects have been explained by the formation of carbon chains made by a few aligned sp-hybridized atoms bridging a nanometric gap [3].

In this context, the production of pure carbon nanostructured films with coexisting sp and sp^2 hybridization [5, 6] opens the exciting possibility to tailor complex carbon-based nanostructures with linear chains made of sp-hybridized C atoms connecting graphitic nano-objects. However, despite several theoretical studies devoted to sp carbon nanowires [7, 8, 9, 10] classified either as cumulenes (virtually conducting, characterized by double C-C bonds) or polyynes (large-gap insulators with alternating single and triple bonds), the implications associated with the nanoscale geometrical manipulation of hybrid sp+sp^2 carbon systems are still largely unexplored.

In this Letter we show that sp nanowires can be stabilized effectively by termination on graphitic nanofragments, and that in the resulting structures the $\simeq$ 1 nm-long linear atomic chains can be *torsionally* stiff, due to the broken axial symmetry with staggered π-bonds. This stiffness is rich of consequences. We explore here how the structural, vibrational and electronic properties of such chains are affected by the nature and *geometry* of the termination. In particular, we show that sp^2 bonding to graphitic fragments and graphene nanoribbons (NRs) produces remarkably stable structures, with cumulene-type chains displaying a non-negligible bond length alternation (BLA), so that the traditional categories of polyynes (alternating single-triple bonds, yielding a large BLA) and cumulenes (double bonds, negligible BLA) appear too simplistic for the description of these systems. Torsional deformations are found to affect the BLA, electronic gap, stretching vibrational frequencies and spin magnetization of the chains.

We study these effects in realistic nanostructures, including carbon chains bound to graphitic fragments. We perform all calculations within Density Functional Theory in the Local Spin Density Approximation, using a plane-wave basis as implemented in the

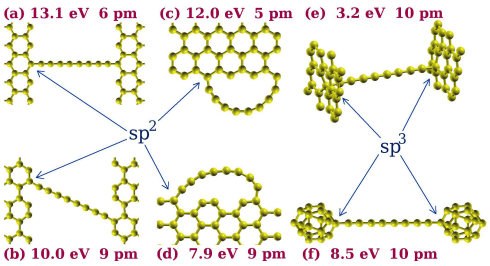

FIG. 1: (Color online) A few representative structures involving an 8-atoms sp-bonded carbon chain terminated on sp^2 carbon fragments [(a-e): NRs; (f): C_{20}]. Either edge termination [(a-d), sp^2-like] or termination on an internal atom of the fragment [(e-f), sp^3-like] is possible. Binding energies (with respect to the uncapped straight chain plus fully relaxed sp^2 fragments) and BLA are reported.

ESPRESSO [11] suite [24].

Figure 1 displays a few of the studied systems involving either sp^2 or sp^3 bonding of a sp nanowire with an sp^2-type fragment. The chosen end-capping nanostructures include planar graphitic fragments and closed-cages clusters (here, C_{20}, the most curved fullerene). These structures are intended to represent typical interfaces present in the nanostructured films produced by cluster-beam deposition [12].

The nature of the terminal bonding turns out to be crucial in determining the structure and electronic properties of the wire. An sp^2-kind termination produces remarkably stable cumulene-type structures (between 7.9 and 13 eV for the formation of the two new bonds), characterized by a BLA between 5 and 9 pm [25]. The computed binding energy should be compared with the energy-per-bond of 2.1 eV that we obtain for a lateral attachment of the same chain to the ribbon edge, and with the formation energy of graphene edges [13, 14]; moreover, it is much larger than the reported binding energies of carbon chains inside nanotubes [15]. Figure 1 also shows that the mere value of the BLA does not allow one to distinguish between carbon chains which would be traditionally classified as cumulenic (a-d) or polyynic (e-f) according to their terminations.

For the sake of comparison we also consider standard cumulenes and polyynes, in the form of isolated carbon chains stabilized by hydrogen terminations. Polyynes, which can be seen conceptually as acetylene molecules with longer alternating triple/single-bond carbon chains

(C_nH_2), have been synthesized up to a considerable length ($n = 20$) [16, 17] in liquid and solid matrices, and also with different stabilizing end-groups. Their electronic and vibrational properties as isolated species have been characterized extensively, mainly by electronic and Raman spectroscopy [17, 18]. On the other hand, cumulenes $C_{n+2}H_4$ can be seen as C_n sp chains terminated by CH_2 groups, yielding all double C=C bonds, and can be ideally thought as ethylene molecules lengthened by extra carbon atoms. Cumulenes are more elusive and less well characterized than polyynes, due to their fragility. Recently, short cumulenic chains have been synthesized in their basic forms, butatriene and hexapentaene [19]. In fact, cumulenic chains are often produced in conjunction with more complex terminations than simple CH_2 units, including CPh_2, i.e. 1,1 diphenyl ethyl (DPE) groups [20], which we also simulate.

As one could infer from elementary valence bond or tight-binding considerations, depending on the number n of carbons being even or odd, sp^2-terminated cumulenes assume a D_{2h} (planar) or a D_{2d} (staggered) ground-state geometry respectively, due to the alternating orientation of the π bonds along the chain [19]. Similarly, chains bonded to sp^2 structures are affected by the relative orientation of their terminations. Indeed, a memory of the orientation of the bonds of the terminating sp^2 carbon propagates along the sp-hybridized chain, so that even-n chains tend to relax to a configuration where the termination sp^2 planes coincide, while odd-n chains tend to keep their terminations at a twist angle $\theta = 90°$. As a consequence, despite their purely one-dimensional nature, sp^2-terminated carbon chains display a non-vanishing torsional stiffness, no matter if they are straight or bent as in Fig. 1c,d. In contrast, ideally polyynic chains (i.e. those terminated at a sp^3 site, with a pure single-triple bond alternation) are almost completely free to rotate around their axis, but suffer from an obvious frustration when the number of atoms is odd since the long-short bond alternation must swap at their middle [21]. Importantly, in nanostructured cluster-assembled carbon characterized by a complex three-dimensional arrangement of graphitic fragments and sp chains [5, 6], a large number of the chains binding to sp^2 structures are not free to relax their terminations to the preferred angular geometry, and must hence be expected to be, in general, strained torsionally.

Since the simulation of carbon-only structures such as graphene NR bridged by chains allow us to investigate few relative angular arrangements only, we extend our study also to chains with simpler saturating ligands, namely CH_2 and DPE. The latter turns out to

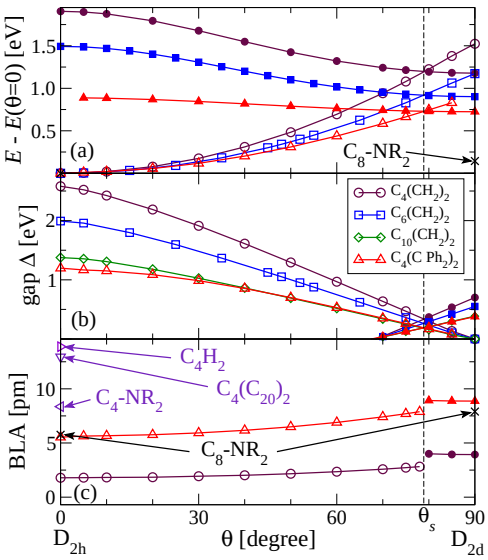

FIG. 2: (Color online) Total torsional energy (a), Kohn-Sham electronic gap (b), and bond-length alternation (c) as a function of the twist angle θ for representative even-numbered sp-carbon chains with different terminations. Open/filled symbols refer to the low/high-spin electronic configurations.

reproduce better the behavior of a large (potentially semi-infinite) graphitic fragment, which, at variance with CH_2, shares with the chain only a fraction of its unsaturated p_z electron, which is partly delocalized over an extended aromatic sp^2 structure.

Figure 2 summarizes the influence of different end groups on the BLA and, for sp^2 termination, the torsional strain energy and the Kohn-Sham electronic gap of even-n chains as a function of θ. Interestingly, largely strained chains undergo a magnetic instability, turning spin polarized. The reason is the quasi-degeneracy of two π-bonding/antibonding electronic levels near the Fermi energy illustrated by the closing of the gap, Fig. 2b. Remarkably, in even-numbered chains of all considered lengths, no matter if CH_2- or DPE-terminated, the switching to a spin-polarized configuration takes place at the same twist angle $\theta_s \simeq 79°$, highlighted in Fig. 2 [26]. This θ_s invariance implies that the energy gap Δ and the exchange splitting of the electrons near the Fermi level scale in the same way.

Calculations show that the BLA of the sp^2-terminated chains varies substantially with

the nature of the termination itself [10]. The length of the extremal bond (i.e. the one connecting the last sp carbon with sp^2/sp^3-hybridized ligand), which correlates with the BLA, is minimal in the case of a simple CH_2 termination, but increases substantially in DPE-terminated chains, assumes even larger values in NR-terminated wires, and is maximum for polyynic-type terminations, see Fig. 1 and Fig. 2c. The torsional barrier is consistently smaller for NR terminations, as indicated by the cross at $\theta = 90°$ in Fig. 2a.

In the light of the above results, chain-termination details are expected to influence the vibrational properties as well. The latter offer an invaluable opportunity to check if the the considered structures are representative of those present in nanostructured cluster-assembled films, for which Raman spectra are the main experimental evidence of the presence of linear carbon chains. In fact, in previous works some of us showed that the Raman fingerprint of carbyne chains in sp-sp^2 carbon is characterized by a broad feature, where 2 components C1 and C2 peaked at 1980 and 2100 cm^{-1} respectively can be recognized [5, 6]. Traditionally these features were attributed generically to cumulenes (C1) and polyynes (C2). We hence calculate the phonon frequencies and eigenvectors of the structures exemplified in Figs. 1a and 1f, plus CH_2- and DPE-terminated carbynes of several lengths, using standard Density-Functional Perturbation Theory [11][27]. As a benchmark, our theoretical C-C streching modes of polyynes C_nH_2 ($n = 8 - 12$) match the experimental frequencies [18] to within 40 cm^{-1}.

Beside several bending and long-wavelength stretching modes, whose low frequency falls in the same range as the vibrations of graphitic and diamond-like carbon material, short linear carbon chains display a few characteristic Raman-active stretching modes in the range $1800 \div 2300$ cm^{-1}. One mode, sometimes named the α-mode in the literature [18], shows a displacement pattern localized near the chain center, and usually bears the strongest Raman intensity [18]. Since the displacements at the chain ends are less than 10% of those of the central atoms, the frequency of the α-mode is almost unaffected by the mass of the termination (e.g. calculations for C_6H_4 and C_8H_4 with 1000-times increased hydrogen mass give frequency shifts of less than 1 cm^{-1}).

The stretching frequencies of sp chains turn out to be influenced by: (i) the type of termination (sp^3 vs. sp^2); (ii) the chain length, with even/odd alternation effects; (iii) for sp^2 termination, the relative orientation of the termination themselves, with effects of torsional strain. The calculated frequencies of the high-energy Raman-active modes display a clear

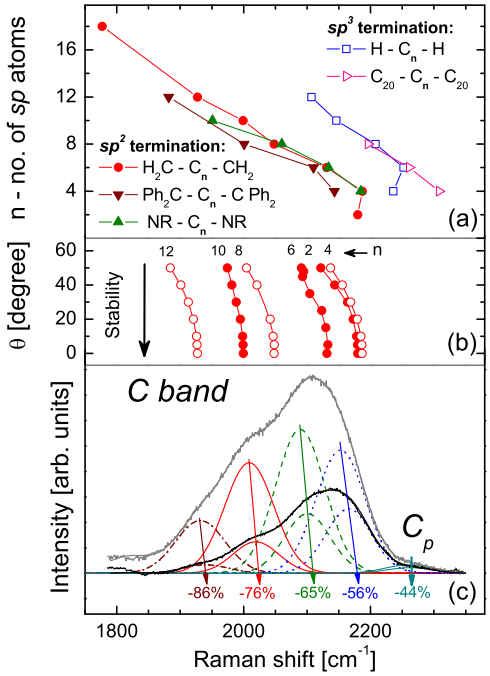

FIG. 3: (Color online) (a) The computed frequency of the Raman α-mode (horizontal scale) for carbon chains of different length n (vertical scale) and with different terminations (b) The softening of this mode for CH_2-terminated chains as a function of the twist angle θ (vertical scale) (c) The experimental Raman spectra of pristine cluster-assembled sp-sp^2 film (grey line) and of the same material after 2 days exposure to He, 100 Torr (black line). The underlying Gaussians report the empirical analysis of both spectra, resulting in 5 components at frequencies separated by approximately 80 cm^{-1}. The individual components display different decays, beside becoming narrower and undergoing a $\sim$ 10 cm^{-1} blueshift.

distinction between sp^2 and sp^3-terminated chains, as shown in Fig. 3. Only even-numbered chains are reported, since odd chains lack α modes, and have in general much smaller Raman cross sections [28].

Figure 3c displays the *in-situ* Raman spectrum of an sp-sp^2 nanostructured-carbon (ns-C) film [5] in the carbyne region, measured using the 488 nm line of an Ar^+ laser and acquired with very high signal-to-noise ratio. The spectrum of the as-deposited material is compared

to that obtained after exposure of the film to He in order to promote sp chain decay [22]. Clearly, a description in terms of two peaks only cannot account for the complex structure and decay observed. In particular, the C_p component at the highest frequency (peaked at 2260 cm^{-1}) can be attributed uniquely to short polyynic chains, as it is higher than any cumulenic α mode (see Fig. 3a), while the other components can be related both to polyynes and cumulenes of different chain length. As illustrated in Fig. 3c, after He exposal, individual components have different evolutions during the C band decay, and in particular the peaks at lower energy, corresponding to longer chains, decay faster than the higher-energy ones (i.e. shorter chains). Furthermore, the C_p peak does not shift during the decay nor change its width, while all lower peaks are blue-shifted by $\sim$ 10 cm^{-1} and narrowed by $\sim$ 7 cm^{-1}. Indeed calculations, summarized in Fig. 3b, show that the high-frequency stretching modes of torsionally-strained CH_2-terminated chains are affected quite strongly by the twist angle, with a redshift up to $\sim$ 100 cm^{-1}. However, since chains with smaller torsional barrier (such as those bound to DPE and nanoribbons) show smaller redshifts, this effect evaluated for CH_2-terminated chains should be considered as an upper limit for realistic pure-carbon nanostructures.

The observed blue shift of the peaks accompanying the decay can then be explained if each peak is related to a particular family of cumulenes, having all the same length but different strain: the more strained chains, having softer Raman modes, decay faster than the others, resulting in a net blue shift and narrowing of the peak. A faster decay of torsionally strained vibrationally red-shifted cumulene-type is indeed to be expected due to their higher total energy (Fig. 2a). On the contrary, no torsional strain applies to polyynes, and this is why the C_p peak does not shift.

In summary, we performed *ab-initio* total-energy and phonon calculations on a selected range of model structures sampling significantly the infinite variety of three-dimensional arrangements of linear carbon chains bridging graphitic fragments in different hybridization states. Theoretical results suggest that sp-carbon chains are stabilized in particular by bonding to the edges of graphitic nanofragments, and allow us to interpret the nontrivial features and decay of experimental Raman spectra of cluster-beam deposited pure carbon films. Moreover, the data for sp^2-terminated chains point towards a rich phenomenology driven by even/odd alternation effects and by the effects of torsional strain. The latter modifies the electronic states near the Fermi level, suggesting the possibility to control the

nanowire conductance[21], optical properties, and spin magnetization, *purely by twisting* its sp^2 termination, e.g. by coupling terminating graphene sheets with micromachined torsional actuators [23]. Linear carbon chains bridging graphene nanogaps, recently proposed as an explanation of the conductance switching in two-terminals graphene devices [3, 4], could hence acquire an important role in future carbon-based electronics.

We acknowledge support by the Italian MIUR through PRIN-2006025747 and by the European Union through the ETSF-I3 project (Grant Agreement No. 211956 / ETSF User Project No. 62).

---

[1] Y.-M. Lin *et al.*, arXiv:0812.1586.

[2] H. W. Ch. Postma, arXiv:0810.3035.

[3] B. Standley *et al.*, Nano Letters **8**, 3345 (2008).

[4] Y. Li, A. Sinitskii, and J. M. Tour, Nature Materials **7**, 966 (2008).

[5] L. Ravagnan *et al.*, Phys. Rev. Lett. **89**, 285506 (2002).

[6] L. Ravagnan *et al.*, Phys. Rev. Lett. **98**, 216103 (2007).

[7] N. D. Lang and Ph. Avouris, Phys. Rev. Lett. **81**, 3515 (1998); Phys. Rev. Lett. **84**, 358 (2000).

[8] Z. Qian *et al.*, Phys. Rev. B **78**, 113301 (2008).

[9] Ž. Crljen and G. Baranović, Phys. Rev. Lett. **98**, 116801 (2007).

[10] M. Weimer *et al.*, Chem. Phys. **309**, 77 (2005).

[11] P. Giannozzi *et al.*, http://www.quantum-espresso.org .

[12] M. P. Bogana and L. Colombo, Appl. Phys. A **86**, 275 (2007).

[13] S. Okada, Phys. Rev. B **77**, 041408(R) (2008).

[14] T. Wassmann *et al.*, Phys. Rev. Lett. **101**, 096402 (2008).

[15] Y. Liu *et al.*, Phys. Rev. B **68**, 125413 (2003).

[16] S. Eisler *et al.*, J. Am. Chem. Soc. **127**, 2666 (2005).

[17] T. Pino *et al.*, J. Chem. Phys. **114**, 2208 (2001).

[18] H. Tabata *et al.*, Carbon **44**, 3168 (2006).

[19] X. Gu, R. I. Kaiser, and A. M. Mebel, ChemPhysChem **9**, 350 (2008).

[20] S. Hino *et al.*, Chem. Phys. Lett. **372**, 59 (2003).

[21] K. H. Khoo *et al.*, Nano Letters **8**, 2900 (2008).

[22] C. S. Casari *et al.*, Phys. Rev. B **69**, 075422 (2004).

[23] J. A. Yeh *et al.*, J. Microelectromechanical Systems, **8**, 456 (1999).

[24] We use the C.pz-rrkjus.UPF ultrasoft pseudopotential from Ref. [11] with a wavefunction/charge cutoff of 30/240 Ry, and relax all atomic positions until the largest residual force is $< 2 \times 10^{-4}$ Ry/a_0 (8 pN). In the case of periodic graphene NRs, we adopt supercells with three hexagonal units along the periodic direction and at least 7 Å of vacuum separating periodic images in the two other directions, optimizing the lattice constant until the stress tensor drops below 2×10^{-5} Ry/a_0^3. We sample the Brillouin zone with at least 13 k-points in each periodic direction and only $k = 0$ in non-periodic directions. Numerical details are similar to those validated and used, e.g., in Ref. [14].

[25] The BLA measures the degree of dimerization and, excluding the terminal bonds, can be defined as $\frac{1}{2}\left[\sum_{j=1}^{n_e}(d_{2j-1} + d_{n-(2j-1)})/n_e - \sum_{j=1}^{n_o}(d_{2j} + d_{n-2j})/n_o\right]$, with $d_i = |\vec{r}_i - \vec{r}_{i+1}|$, $n_e = (n+2)/4$, and $n_o = n/4$ (integer part).

[26] Odd-numbered chains show a reversed behavior, with high-spin states near the energetically unfavorable planar geometry $\theta \simeq 0°$.

[27] All phonon calculations start by fully relaxing all degrees of freedom except, in the case of torsionally strained $C_n(CH_2)_2$ systems, the angular coordinates of the H atoms around the molecular axis.

[28] For the simplest structures (CH_2-terminated chains) we also compute Raman intensities.

physica status solidi, 4 March 2010

Vibrational properties of sp carbon atomic wires in cluster–assembled carbon films

Giovanni Onida[*,1,2], Nicola Manini[1,2], Luca Ravagnan[1,4], Eugenio Cinquanta[3,4] Davide Sangalli[1,2] Paolo Milani[1,4]

[1] Dipartimento di Fisica dell'Università degli Studi di Milano, via Celoria 16, 20133 Milano, Italy
[2] European Theoretical Spectroscopy Facility (ETSF)
[3] Dipartimento di Scienza dei Materiali, Università di Milano Bicocca, Via Cozzi 53, 20125 Milano, Italy
[4] CIMAINA - Via Celoria 16, 20133 Milano, Italy

Received XXXX, revised XXXX, accepted XXXX
Published online XXXX

PACS 81.07.-b Nanoscale materials and structures 73.21.Hb Quantum wires 61.48.De Structure of carbon nanotubes, boron nanotubes, and closely related graphitelike systems 63.22.Gh Nanotubes and nanowires 62.23.Hj Nanowires

[*] Corresponding author: e-mail giovanni.onida@unimi.it, Phone: +39-02-50317407, Fax: +39-02-50317482

Linear chains made by a single row of sp-hybridized carbon are predicted to display fascinating mechano-electronic properties connected with their termination and stabilization inside realistic carbon structures. The present work describes how the computed vibrational properties of cumulenic and polyynic carbon chains allow one to interpret the carbynic features observed in Raman spectra of cluster-assembled $sp - sp^2$ films. The overall picture is consistent with the measured decay of the sp components induced by air or oxygen exposure.

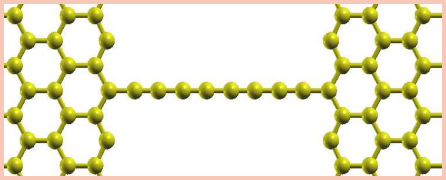

The electronic properties of carbon atomic chains attached to the edges of graphitic fragments can be controlled by a relative twist of the terminating planes.

1 Introduction Fullerenes, nanotubes, and graphene are examples of the wide class of structures based on sp^2-hybridized carbon. Carbon atoms can also show an sp hybridization, and hence form *linear* structures. Linear atomic chains made by a single row of sp-hybridized carbons, known as Carbynes, are indeed the most one-dimensional among all conceivable carbon nanostructures. In the last years, the possibility to use them as conducting bridges between metallic leads, or even between sp^2 or sp^3 carbon fragments, has been suggested [1]. The basic assumption is a possible delocalization of π electrons along the chain, allowing for charge transport.

However, as we show below, this one-dimensional π electron delocalization differs substantially from that observed in aromatic compounds, based on sp^2-hybridized carbons.

Traditionally, finite carbynes are classified as polyynes or cumulenes, according to the nature of their bonding: the first ones display a sequence of single and triple bonds – and acquire a substantial bond length alternation– while the second ones have all double bonds, all of about the same length.

Until recently the "carbyne" scientific community had a small interaction/superposition with the community of people studying sp^2 carbon systems, such as fullerenes and graphene. Works suggesting the relevance of carbynic chains in graphene-based devices appeared very recently [2]; in particular, carbynes were suggested to form bridges across nanometric gaps in graphene. This conjecture was advanced in order to explain the reversible conductance switching observed in two-terminal graphene devices [2, 3]

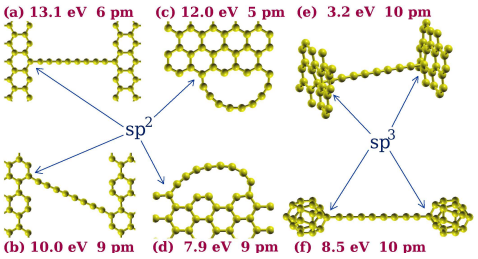

Figure 1 A few representative structures involving an 8-atoms sp-bonded carbon chain terminated on sp^2 carbon fragments [(a-e): NRs; (f): C_{20}]. Either edge termination [(a-d), sp^2-like] or termination on an internal atom of the fragment [(e-f), sp^3-like] is possible. Binding energies (with respect to the uncapped straight chain plus fully relaxed sp^2 fragments) and BLA are reported.

On the other hand, the coexistence of sp^2 and sp hybridization in Carbon has been demonstrated since 2002, based on Raman spectroscopy. In particular, the experimental group of Ref. [4,5] uses supersonic cluster beam deposition to produce nanostructured carbon films with a clear signature of sp-bonded carbon, as demonstrated by measuring in situ the Raman spectra.

The carbynic Raman peak, sometimes identified as "C-band", is due to the stretching of the sp bond and appears around 2000 cm^{-1}, being well separated from the lower structures associated with the stretching of the sp^3 and sp^2 carbon-carbon bonds. The C-band, however, is found to decay with time and with exposure of the sample to oxygen, with the sp component almost disappearing after 3 days [6]. More recent low-noise, high-statistics experiments have allowed one to disentangle, from a purely empirical analysis of the experimental data, the presence of at least five different components building up this carbynic peak, each with a different decay rate [6]. Moreover, 4 out of 5 components also display a blueshift and a narrowing during the decay. Another relevant experimental finding is the reduction of the electrical conductance of the sample associated with the decay of the carbynic Raman peak.

2 Theoretical methods In order to gain more insight in the physics of such $sp+sp^2$ systems, we performed a set of *ab-initio* total energy calculations [1]. We carried out *ab-initio* calculations within the Density-Functional theory in the local-density approximation (DFT-LDA) with a plane-waves package [8] using default ultrasoft pseudopotentials, and wavefunction/charge cutoffs of 15/120 Hartree. We relax the atomic positions until the largest residual force is less than 10^{-4} Hartree/a_0 (8 pN). We compute the vibrational properties within density-functional perturbation theory [9]. Non-resonant Raman intensities were obtained by numerically evaluating second derivatives of the atomic forces with respect to the electric field [10].

[1] These calculations were part of an *user project* of the ETSF [7].

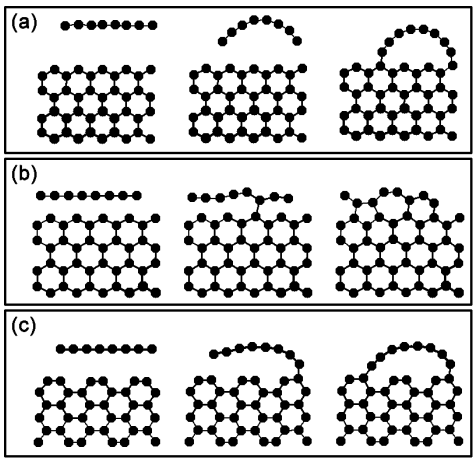

Figure 2 Successive minimization steps for the attachment of a C_8 chain to nanoribbon edges. (a): the chain starts 2.1 Å from the zigzag edge; (b): the chain starts 1.1 Å from the zigzag edge; (c): the chain starts 2.9 Å from the armchair edge.

3 Results In the following we present theoretical and experimental results. The calculations are aimed i) to identify the most stable structures and geometries; and ii) to compute the Raman frequencies and intensities for a selection of realistic structures. Computed Raman spectra are compared with measured spectra of cluster-assembled $sp-sp^2$ carbon films.

3.1 Structure and energetics First of all, we notice that there are essentially two ways to terminate a linear chain on an sp^2 graphitic fragment: either the chain connects perpendicularly to the surface of the fragment (or the surface of a fullerenic cage), by means of an "interface" atom having the sp^3 hybridization, like in the examples shown in Fig. 1e-f, or the chain can be attached to an edge, like in Fig. 1a-d. In the latter case the "interface" atom is also sp^2. The first remarkable result of total energy calculations is the large binding energy which is obtained in this second case, especially for the attachment to a zigzag edge.

Figure 2 shows the result of a geometry optimization for a linear chain put in the vicinity of the edge of a graphene fragment or nanoribbon, ending in different local minima according to the initial conditions. For an 8-atoms long chain, if the initial distance is large enough the chain bends, and attaches its two ends to the edge (Fig. 2); if the distance is smaller, the chain makes multiple bonds

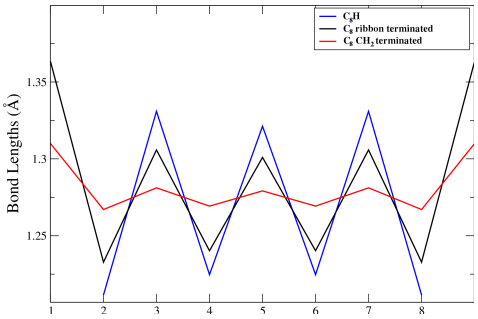

Figure 3 Individual bond length in a C_8 chain with different terminations.

and the nanoribbon grows, possibly incorporating defects. Remarkably, the energy gain *per new bond* is much larger in the first case than in the second.

We made several simulations for systems of this kind, including chains from 4 to 14 atoms, with full geometrical relaxation of the structures. Figure 1 shows a set of typical results for the 8-atoms chain. Besides the binding energies, we also report the bond length alternation (BLA), expressed in picometers.

The BLA should in principle be a criterion to distinguish polyynes (with single and triple bonds) from cumulenes (with double bonds). Naively, one would expect that sp^3-terminated chains are polyynes, while sp^2-terminated ones are cumulenes. As we demonstrate below, the situation is quite more complex and the nature of the bonding along the chains is non trivial.

Recently, nice experimental observation by transmission electron microscopy [11,12] have shown such linear carbon chains attached to graphene edges. The experimental geometries, as shown in figures 1 and 4 of Ref. [12], are very similar to those predicted to be the most stable ones by our DFT calculations, e.g. the straight chain between two zigzag edges and the "handle" structures realized by bent chains. However, present TEM images cannot discriminate between double bonds and single/triple ones, hence theoretical results are necessary to understand if the chains have a polyynic or cumulenic character.

Considering again our prototypical 8-atoms chain attached to the zigzag edges of graphitic nanofragments, we show in Fig. 3 the computed bondlenghts along the chain (black), compared with those of a pure polyyne (blue) and a pure cumulene (red). The alternation is clearly intermediate between the two limiting cases: the chains attached to a graphene edge have hence a mixed polyynic-cumulenic character.

Another intriguing aspect of carbynes terminated on an edge of an sp^2 fragment comes from the breaking of the

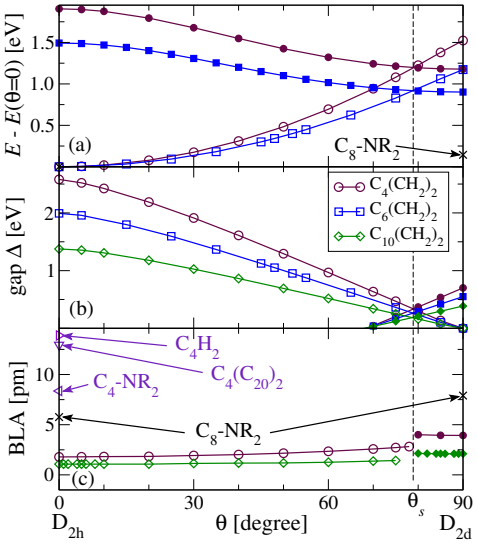

Figure 4 Total torsional energy (a), Kohn-Sham electronic gap (b), and bond-length alternation (c) as a function of the twist angle θ for representative even-numbered sp-carbon chains with different terminations. Open/filled symbols refer to the low/high-spin electronic configurations.

chain axial symmetry, since sp^2 termination defines a specific termination plane.

This point can be clearly illustrated in the case of a purely cumulenic chain. It is well known that the equilibrium geometry of hydrogen-terminated cumulenes (C_nH_4) is either planar or staggered, according to the number of carbons being even or odd. This is simply due to the alternating orientation of π-bonds along the chain. In fact, long cumulenes turn out to be easy to bend, but they are rotationally stiffer.

We can hence expect that sp^3-terminated chains are free to rotate around their axis, and can be classified as polyynic, while chains which are sp^2-terminated on a graphitic edge, instead, are affected by the relative angular orientation of their terminal groups.

In a disordered material a large fraction of the edge-terminated chains will probably be torsionally strained.

3.2 Effects of torsional strain Figure 4 shows the result af explicit calculations of the effects of torsional strain, performed on a representative set of our optimized structures. The latter include pure cumulenes, chains terminated on a double phenilic unit, and chains connecting nanoribbon edges and fullerenic cages. We report total energies, HOMO-LUMO gaps, and bond-length alternation

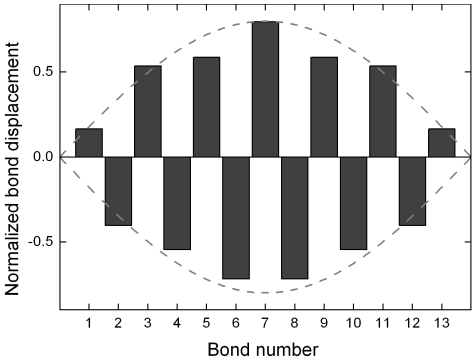

Figure 5 The pattern of longitudinal atomic displacements of the Raman active α mode of an untwisted C_{14} chain.

as a function of the twist angle for a set of even-numbered chains, having then their ground-state geometry in the planar configuration. Full symbols refer to spin polarized configurations, while empty symbols are used for non spin-polarized ones. By forcibly twisting the chain termination, and letting all other degrees of freedom to relax, the total energy undergoes a substantial increase, which is larger for shorter chains and for chains having a more pronounced cumulenic character. The total energy increase is accompanied by a small increase of the BLA and by a substantial reduction of the HOMO-LUMO gap, which would become exactly zero in the D_{2d} configuration due to the degeneracy of the π-bonds oriented in the two orthogonal planes containing the molecular axis. Moreover, beyond a certain angle the system undergoes a magnetic instability, switching to the spin-polarized configuration (which for even numbered chains is favored in the D_{2d} geometry).

3.3 Raman spectra In the light of these results, we expect chain termination details and geometry to influence the vibrational properties of the chains. We focus, in particular, on their Raman signature, associated with the high-frequency sp C-C stretching modes, and perform ab-initio phonon calculations for a set of our optimized structures. We concentrate on the so called "alpha mode", which is known to possess the strongest Raman activity and has a typical displacement pattern as shown in Fig. 5. Since the eigenvector of this mode goes to zero on the chain ends, its frequency does not depend on the mass of the chain termination, and in fact we verified that no changes appear by imposing fixed or free boundary conditions. In fact, the frequency of the alpha mode clearly depends on three factors: the chain lenght, the type of termination (sp^2 or sp^3), and, for sp^2 termination, the relative orientation of the terminating planes.

Figure 6a shows the frequency of the alpha mode as a function of the chain lenght. A first remark is that at

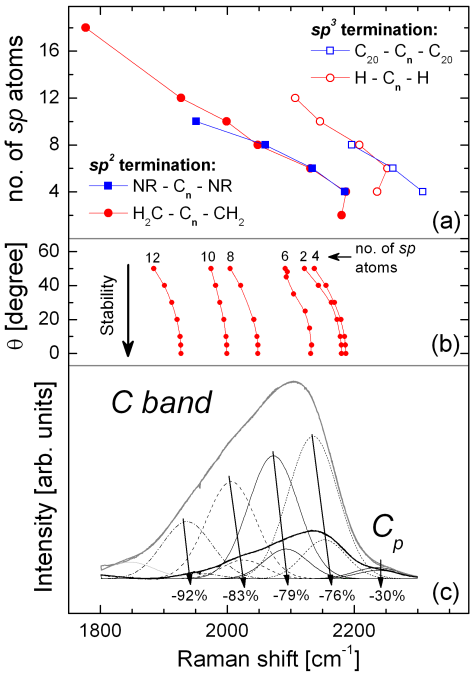

Figure 6 (a) The computed frequency of the Raman α-mode (horizontal scale for carbon chains of different length n (vertical scale) and with different terminations. (b) The softening of this mode for CH_2-terminated chains as a function of twist angle θ (vertical scale). (c) Experimental Raman spectra for pristine cluster-assembled sp-sp^2 film (grey line) and for the same material after 2 days exposure to He, 100 Torr (black line). The underlying Gaussians report the empirical analysis of both spectra, resulting in 5 components at frequencies separated by approximately 80 cm^{-1}. Individual components display different decay rates, beside becoming narrower and undergoing a $\sim$ 10 cm^{-1} blueshift.

fixed lenght the chains with an sp^2 termination are systematically redshifted by about 50 cm^{-1}, with respect to sp^3-termination. From Fig. 6a one can also conclude that any spectral feature above 2200 cm^{-1} must come from sp^3-terminated chains, since the highest mode of sp^2-terminated chains, that is found in the 4-atoms chain, remains below this value. Figure 6b focuses on the effects of the torsional strain: the frequency of the alpha-mode of sp^2-terminated chains is shown as a function of the twist angle. The Raman mode shows a clear *softening* in the torsionally strained configurations. One can hence predict that a system containing a mixture of strained and nonstrained

chains will display broadened peaks, each associated with one family of sp^2-terminated chains.

The picture coming out from the calculations turns out to be consistent with the experimental findings of in-situ Raman characterization of cluster-assembled $sp-sp^2$ carbon films [4,5]. Figure 6c displays the spectra acquired with the 514.5 nm wavelength of a Ar laser[2] on the pristine samples and after 2 days' exposure to He (100 Torr). Several components can be identified in the spectra, behaving consistently with the attribution to sp carbon chains of different lengths. Indeed individual components are characterized, on one side, by faster decays of peaks at lower Raman shift (i.e. longer chains are more reactive), on the other side the redshift and the narrowing of each individual component is consistent with the expected faster decay of the more strained chains (which are also more reactive, as illustrated in Fig. 4a). Remarkably, the absence of shift observed for the highest frequency peak is consistent with the fact that no torsional strain effects applies to the sp^3-terminated chains, which can rotate freely around their axis.

Moreover, the presence of strongly strained, and hence small-gapped chains (here an odd-numbered chain forced to stay in the planar geometry) can explain the higher electrical conductance of the samples immediately after deposition and is consistent with the observed decay. The conductance properties of carbyne-bridged sp^2 structures are being studied actively[13–15].

4 Conclusions In conclusion, we have seen that carbon linear chains can be substantially stabilized by sp^2 termination on the edge of graphitic fragments: this finding is in nice agreement with the structures recently detected by transmission electron microscopy. The nature of the sp bonding along the chain is nontrivial, since in most cases C-C bonds cannot be classified as either purely double or a pure sequence of single-triple bonds. Moreover, when the chains are sp^2-terminated, a memory of the orientation of the termination plane propagates along the chain, through the sequence of π-bonds, making the system sensitive to torsional strain. The theoretical picture coming out from the calculations is consistent with the experimental Raman spectra measured in cluster-deposited carbon films, and with the observed time decay of the sp-related Raman peaks.

Our calculations also suggest that several other properties of sp^2-terminated carbon chains are likely to be influenced by torsional strain, e.g. electrical conductivity, optical spectra, and magnetic properties.

Acknowledgements The research leading to these results has received funding from the European Community's Seventh Framework Programme (FP7/2007-2013) under grant agreement No. 211956 (ETSF-i3). We acknowledge generous supercomputing support from CILEA.

[2] Similar spectra were obtained with the 488 nm excitation Ar laser, and reported in previously published work [6].

References

[1] N. D. Lang and Ph. Avouris, Phys. Rev. Lett. **81**, 3515 (1998); Phys. Rev. Lett. **84**, 358 (2000).
[2] Y. Li, A. Sinitskii, and J. M. Tour, Nature Mat. **7**, 966 (2008).
[3] B. Standley *et al.*, Nano Lett. **8**, 3345 (2008).
[4] L. Ravagnan *et al.*, Phys. Rev. Lett. **89**, 285506 (2002).
[5] C. S. Casari *et al.*, Phys. Rev. B **69**, 075422 (2004).
[6] L. Ravagnan, N. Manini, E. Cinquanta, G. Onida, D. Sangalli, C. Motta, M. Devetta, A. Bordoni, P. Piseri, and P. Milani, Phys. Rev. Lett. **102**, 245502 (2009).
[7] `http://www.etsf.eu/`.
[8] P. Giannozzi *et al.*, J. Phys.: Condens. Matter **21**, 395502 (2009). See `http://www.quantum-espresso.org`.
[9] S. Baroni *et al.*, Rev. Mod. Phys. **73**, 515 (2001).
[10] P. Umari and A. Pasquarello, Phys. Rev. Lett. **95**, 137401 (2005).
[11] C. Jin, H. Lan, L. Peng, K. Suenaga, and S. Iijima, Phys. Rev. Lett. **102**, 205501 (2009).
[12] A. Chuvilin, J. C. Meyer, G. Algara-Siller, and U. Kaiser, New J. Phys. **11**, 083019 (2009).
[13] Z. Qian *et al.*, Phys. Rev. B **78**, 113301 (2008).
[14] M. G. Zeng, L. Shen, Y. Q. Cai, Z. D. Sha, and Y. P. Feng, Appl. Phys. Lett. **96**, 042104 (2010).
[15] J. A. Fürst, M. Brandbyge, and A.-P. Jauho, arXiv:0909.1756.

8.2 Multi-wavelength resonant-Raman and infrared spectroscopy of *sp*-sp^2 pure carbon film

8.2.1 Multi-wavelength resonant-Raman characterization

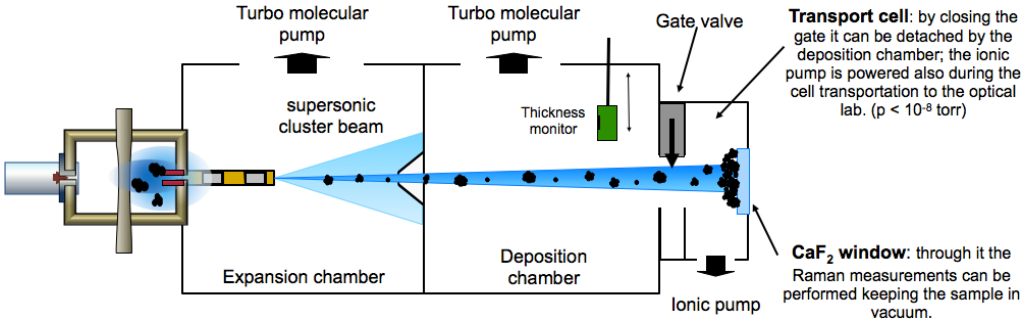

Figure 8.1: Setup used for the in-situ Raman spectroscopy

In-situ Multi Wavelength Resonant Raman (MWRR) spectroscopy measurements have been carried out after the deposition of the pure *sp*-sp^2 carbon cluster, produced by a *PMCS* cluster source, on a Calcium Fluoride (CaF_2) substrate. The setup used for Raman measurements is sketched in fig. 8.1. Once the cluster beam exits from the source and focalized by the aerodynamical focusing system, its central part, selected through a 3 mm skimmer, was then allowed to enter a second differential vacuum chamber (evacuated with a turbo-molecular pump in 10^{-7} mbar) equipped with a translating MakTex thickness monitor, mounted perpendicular to the beam axis. Then the cluster beam apparatus is connected, through a Vaqtec gate valve, with the UHV transportable deposition chamber (evacuated by an Ionic pump in 10^{-8} mbar) equipped with a CaF_2 window on the beam axis which acts as a substrate. After the deposition process it is then possible to close the gate valve, preserving the vacuum in the transportable chamber by means of the ionic pump, and to move the deposition/analysis chamber to the optical laboratory for the Raman measurements.

MWRR spectroscopy was performed by using four different laser wavelengths provided by an Ar ion and a He-Cd laser (Spectra Physics, BeamLok series $2065 - 7$ and Kimmon, IK5352 R-D series, respectively). The wavelengths used were, respectively, 514.5 nm, 488.0 nm and 363.8 nm for the Ar ion laser, and 325 nm for the He-Cd laser. For each wavelength, bandpass clean-up filters (MaxLine filters from Semrock) were used in order to remove spurious plasma lines produced by the lasers.

MWRR spectra were acquired by using a single-grating spectrometer (Acton SP-$2558 - 9N$ with a 1200 groves/mm grating, blazing 600 nm) equipped with a liquid nitrogen cooled CCD camera (Roper-Princeton Instruments Spec10 : 400B/LN) and notch filters in order to remove the Rayleigh scattering (StopLine from Semrock). Thanks to this setup the spectra were recorded in a unique acquisition window (typically comprised between 1000 cm^{-1} and 2500 cm^{-1}), repeating hundreds acquisitions one minute long for the visible laser wavelengths and four minutes long for UV laser wavelengths. Thanks to this approach it was both possible to obtain spectra with high signal to noise ratio (by averaging the different acquisitions) and to monitor any evolution in time of the sample spectra both related to the structural reorganization of the *sp*-sp^2 system and induced

by the laser irradiation.

Fine calibration of the Raman shift of the acquired spectra was achieved by using the approach proposed by N.C. Craig and I.W. Levin [87] and used for the analysis of the MWRR spectra of dinaphthylpolyynes (see sec. 7.2). After each measurement, a spectrum of the plasma lines produced by the lasers was collected by removing the bandpass clean-up filter in the optical system. Since the plasma lines positions are precisely tabulated, this allowed us to correct any possible offset or non linearity of the monochromator and to reach an uncertainty on the wave-numbers axis below 1 cm^{-1} for all stimulating wavelengths used (also checked by measuring the G band position at 1581 cm^{-1} in the spectrum of a highly oriented pyrolytic graphite sample). After this calibration process, the MWRR spectra of the *sp*-sp^2 sample are normalized with the intensity of the G peak.

The Raman spectrum of *sp*-rich amorphous carbon has been deeply studied since the first identification of the vibrational band of *sp* carbon by L. Ravagnan *et. al* [31] in 2002. The spectrum of *sp*-sp^2 is composed by two main components: the well known broad D-G band (1200-1600 cm^{-1}), related to the vibrational frequency of amorphous sp^2 matrix [9], and the C band located in the frequency range of triple and double bonds of *sp* carbon at 1900-2300 cm^{-1}. The first description of the C band was based on the identification of two sub-components, the first one located at $\sim$ 1900 cm^{-1} and the second one at $\sim$ 2100 cm^{-1} [31]. These two features have been attributed to cumulene-like (sp^2 terminated) and polyyne-like (sp^3 terminated) chains respectively. Indeed, polyynics triple bonds are shorter than cumulenics double bonds, thus vibrational modes of sp^3 terminated *sp*CCs are expected to be at higher frequency with respect of those of sp^2 terminated ones. By the way, this picture does not provide any quantitative analysis about the length and termination distributions of *sp*CCs embedded in the *sp*-sp^2 films.

Thus, it is promising to follow the procedure used for the vibrational characterization of dinaphthylpolyynes, that is to perform resonance Raman measurements by using different laser wavelength, both in the visible and in the ultra-violet frequency range. Indeed in [88] I demonstrate that Raman spectroscopy with long excitation wavelengths is highly sensitive to long *sp*CCs (rather than to short chains), due to their larger non-resonant cross sections, further enhanced by selective resonant absorption associated with their smaller HOMO-LUMO gaps [89]. As the laser wavelength is shifted toward the UV, shorter spCCs become progressively resonant, with their R-α peaks becoming the dominant features of the spectra. This resonance mechanism gives a chance to the R-α peaks of most abundant shorter *sp*CCs to become visible despite their extremely small Raman cross sections.

By varying the incident photon energy it is in principle possible to activate the resonance effect of chains with different length, thus paving the way of clearly identify and assign the features present in the Raman spectrum of *sp*-sp^2 pure carbon films. In fig. 8.2 I report resonance Raman spectrum of the *sp*-sp^2 pure carbon film obtained by using the four different laser wavelength. As reported in the left panel of fig. 8.2, the MWRR spectra show the typical features of amorphous carbon. The broad band at $1300 - 1600$ cm^{-1} is due to the sp^2 amorphous matrix vibrations and is composed by two sub-components: the D peak (the small shoulder in fig. 8.2 at $\sim$ 1300 cm^{-1}) is related to normal modes of disordered domains and its blueshift as a function of the excitation energy is due to the double resonance effect [90]. The G band, is related to the bond stretching of all pairs of sp^2 carbon atoms in both rings and chains and follows the same trend of the D peak due to the activation of the resonance of sp^2 structures with different size, whose energy gap is roughly inversely proportional to their dimension

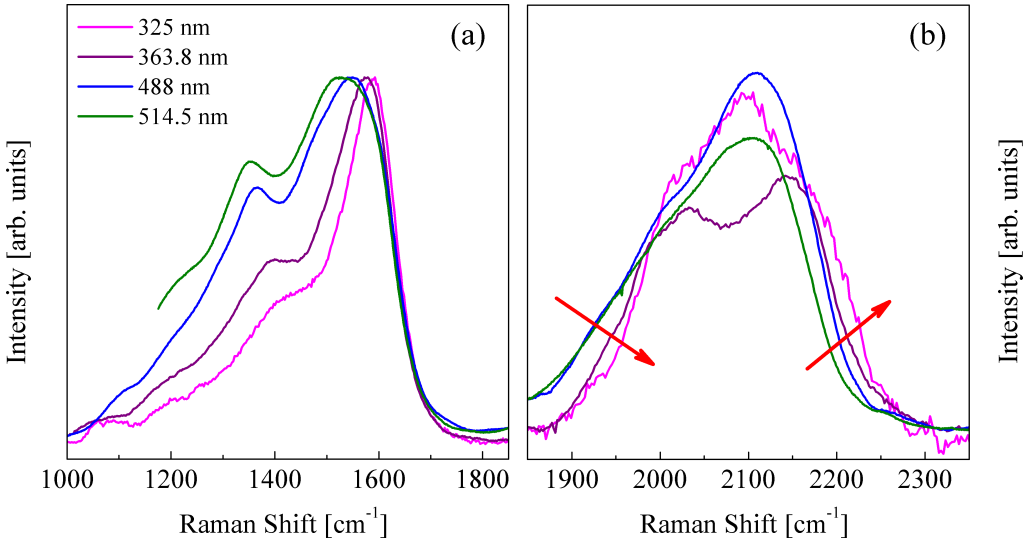

Figure 8.2: superimposed *in-situ* resonant Raman spectra of the *sp*-sp^2 pure carbon film obtained with the four different excitation energy reported in the legend.

($E_g \sim \frac{1}{L_a}$) [91]. The smaller is the structure, the more confined are π and π^* thus leading to the opening of a small gap. On the contrary, the larger is the cluster the more extended is the graphitic structure, thus recovering the half-metallic character of highly ordered graphite. As a consequence, by using photons with increasing energy, the G peak becomes sharper and can shift even beyond its expected value of 1581 cm^{-1} due to the the excitation of those sp^2 configurations with wider gap and stiffer Raman active modes [92].

The C band obtained using the four different wavelengths is reported in the right panel of 8.2. First of all one can note how, by using photons with increasing energy, the C band shifts to higher frequency losing intensity in the region around 1900 cm^{-1} and gaining intensity around 2200 cm^{-1} (as indicate red arrows in fig. 8.2). Furthermore, by switching to UV radiation, it can be clearly observed, in the $1900 - 2200$ cm^{-1} spectral range, the activation of many sub-components, silent in the visible spectra, that don't follow any trend reported for dinaphthylpolyynes. As was oreviously shown for dinaphthylpolyynes, resonance effects can be exploited with MWRR spectroscopy for the identification of the detected peaks as R-α modes of dinaphthylpolyynes of specific lengths due to the matching between the HOMO-LUMO gap of the *sp*CCs and the energy of the laser wavelength (see. sec.7.2 and [88]). Therefore, the dynamics affecting the C band can be interpreted as due to the activation of the resonance effect for chains with decreasing length, increasing energy gap and stiffer Raman active modes.

Having interpreted the blue-shift of C band and the structuring of the UV Raman spectra as a result of the activation of the resonance of *sp*CCs with decreasing length, then it is relevant to fit the C band with different sub-components, each representing an *sp*CCs family with a certain length, as previously done in the case of dinaphthylpolyynes [88].

Despite what happens for crystalline solids where the vibrational features are represented by Lorentzian curves, in the case of amorphous *sp*-sp^2 pure carbon film, gaussian curves are the best choice. Indeed this is a poly-dispersed material in which many dif-

ferent species are present (i.e., chains with different length and termination), each one characterized by small structural and morphological deviations from the most stable isomer. Thus gaussians can take into account the random distribution of the vibrational modes related to spCCs with the same length but, for instance, bended, suffering compressions/elongations and torsions because of the constraints induced by the amorphous nature of the sp^2 matrix.

The fitting procedure is based on the iterative χ^2 minimization setting the same width for all the gaussians (in principles all spCCs families have the same probability of being deformed) leaving their intensities and positions as free parameters. *In-situ* spectra have been fitted together with the spectra acquired both leaving the sample in vacuum conditions and during the gas exposure in order to follow the decay processes of the different sub-components. As previously discussed I was able to collect Raman spectrum during one whole week, thus obtaining a very high signal/noise ratio which allows the precise fitting of the visible Raman spectra. On the contrary, for UV Raman spectra I had to use very low incident laser power in order to prevent samples photo-degradation (because of highly energetics photons), and thus these spectra are characterize by a lower signal/noise ratio. Furthermore, always concerning UV spectra, I had to use a greater number of Gaussian in order to acceptably minimize the χ^2. Unfortunately, the high number of free parameters of such a fitting curve made the minimization procedure poorly consistent.

Let us focus our attention on what happens to the C band when leaving the sample in UHV (10^{-7} mbar) for an entire week. As can be observed in fig. 8.3, the overall decay is not uniform for all the Gaussian sub-components, the width of each curve does not vary and a small blue-shift characterize the first four components lying below 2200 cm^{-1}. These observations suggest that the leading phenomenon responsible for the chains decay is a process based on their cross-linking, leading to the reduction of the overall amount of spCCs, with, nevertheless, a faster decay of longer chains than shorter ones. Indeed, longer chains, which are expected to be characterized by an higher interaction volume and less stability with respect of shorter ones, have Raman features in the low frequency region of the C band, where indeed a faster decay is observed. Because this effect is tightly bonded to the spCCs density, as the latter drops below a certain threshold these cross-linking processes have a very small cross-section (i.e., they will proceed on longer time scale) and, as a consequence, almost the 50% of the spCCs survives. The same trends have been found in the polymer degradation, where polymeric chains covalently interact forming different structures [93, 94]; in the case of spCCs, they graphitize after these cross-linking processes. For more details see [95].

By comparing experimental MWWR spectra of the sp-sp^2 sample, both maintained *in-situ* and during an He exposure, with theoretical modeling it is possible to gain further information about the correlation between the C band behavior and the structures of spCCs. *Ab-initio* DFT-LSDA calculations show that, as already demonstrated for dinaphthylpolyynes (see sec.7.2), the most intense Raman active mode is the R-α one. This mode shows a bond displacements localized near the chain center, and, since the displacement at the chain ends are less than 10% of those of the central atoms, the frequency of the R-α mode is almost unaffected by the mass of the termination [96, 97]. The stretching frequencies of sp chains turn out to be influenced by (i) the type of termination (sp^3 vs sp^2), (ii) the chain length, with even or odd alternating effects, and (iii) for sp^2 termination, the relative orientation of the termination themselves, with effects of torsional strain.

The results summarized in fig. 8.4 show that the calculated frequencies of the high-

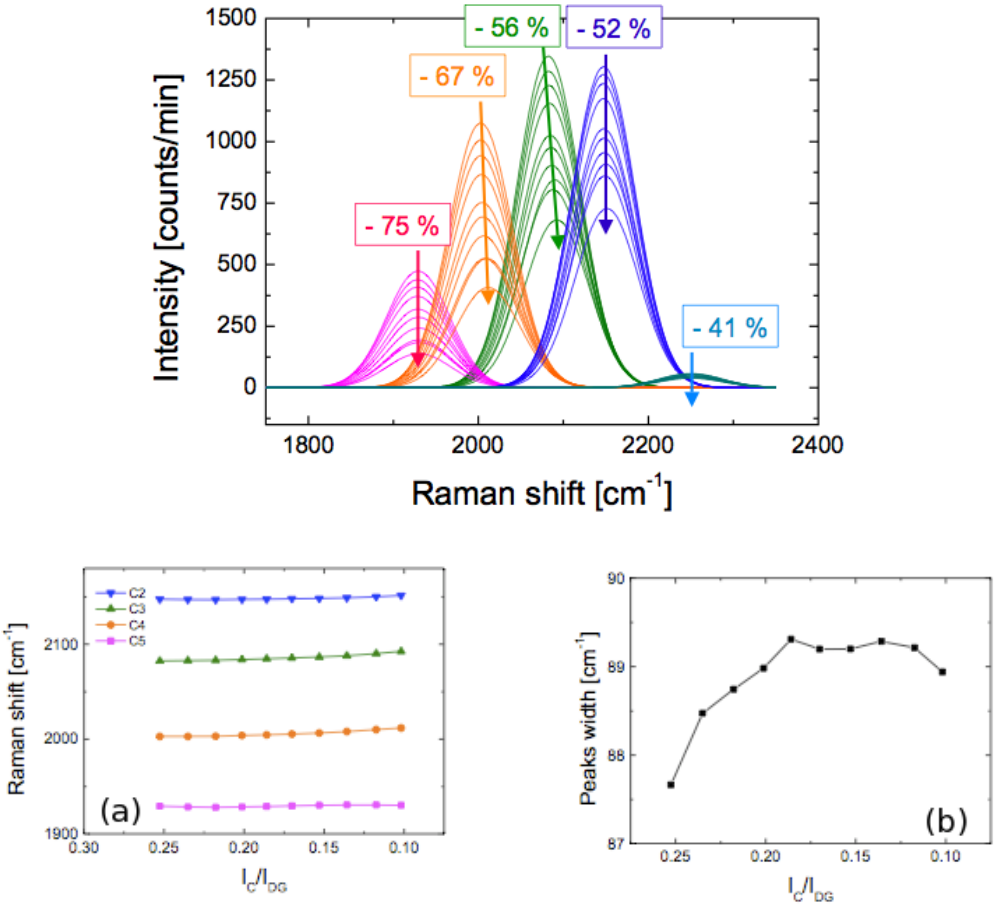

Figure 8.3: (top) evolution of the gaussian components used for the fitting of the Raman spectra during one week long *in-situ*measurements; (bottom) evolution of the position (a) and width (b) of the different gaussian sub-component.

energy Raman-active modes display a clear distinction between sp^2- and sp^3-terminated chains: therefore, the decomposition of the C band in five gaussians sub-components related to different *sp*CCs families is compatible with the one obtained with the fitting of the experimental Raman spectra. Indeed, once fixed the length, the chains with an sp^2 termination are systematically redshifted by about 50 cm^{-1}, with respect to sp^3-termination. In addition, as reported in the right panel of fig. 8.4, one can state that any spectral feature at higher wavenumber than 2200 cm^{-1} must come from sp^3-terminated chains, since the highest mode of sp^2-terminated chains, that is found in the 4-atom chain, remains below this value. In particular, the component at the highest frequency (indicated as C_1 in fig. 8.4, peaked at 2260 cm^{-1}) can be attributed uniquely to short polyynic chains, as it is higher than any cumulenic R-α mode [96, 97]. In table 8.1 I report both experimental and calculated R-α modes for both sp^2- and sp^3-terminated carbon chains with different lengths.

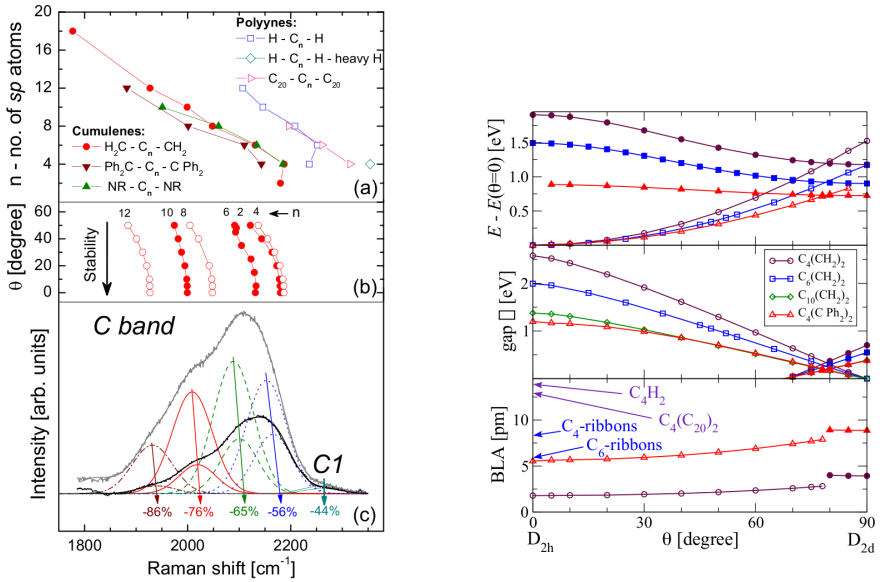

Figure 8.4: (left panel) the computed frequency of the Raman αmode (cm^{-1} (horizontal scale common to all panels) for carbon chains of different length n (vertical scale) and with different terminations. (b) The softening of this mode for CH2-terminated chains as a function of twist angle θ (vertical scale). (c) Experimental Raman spectra for pristine cluster-assembled sp-sp^2 film (gray line) and for the same material after 2 days exposure to He, 100 Torr (black line). The underlying gaussians report the empirical analysis of both spectra, resulting in five components at frequencies separated by approximately 80 cm^{-1}; (right panel) total torsional energy (a), electronic gap (b), and bond-length alternation (c) as a function of the twist angle θ for representative even-numbered sp-carbon chains with different terminations. Open (filled) symbols refer to the low-(high-)spin electronic configurations.

spCCs	fitted peak position [cm^{-1}]	calculated frequency [cm^{-1}]
C_4-NR	2158	2185
C_6-NR	2107	2134
C_8-NR	2058	2060
C_{10}-NR	1931	1950
C_4-C_{20}		2307
C_6-C_{20}	2251	2261
C_8-C_{20}		2240

Table 8.1: center of the experimental fitting gaussian compared with calculated R-α modes

As illustrated in fig. 8.4(c), during He exposure, individual components have different evolutions during the C band decay and, in particular, the four peaks at lower wavenumbers, corresponding to longer chains, decay faster than the higher-energy ones

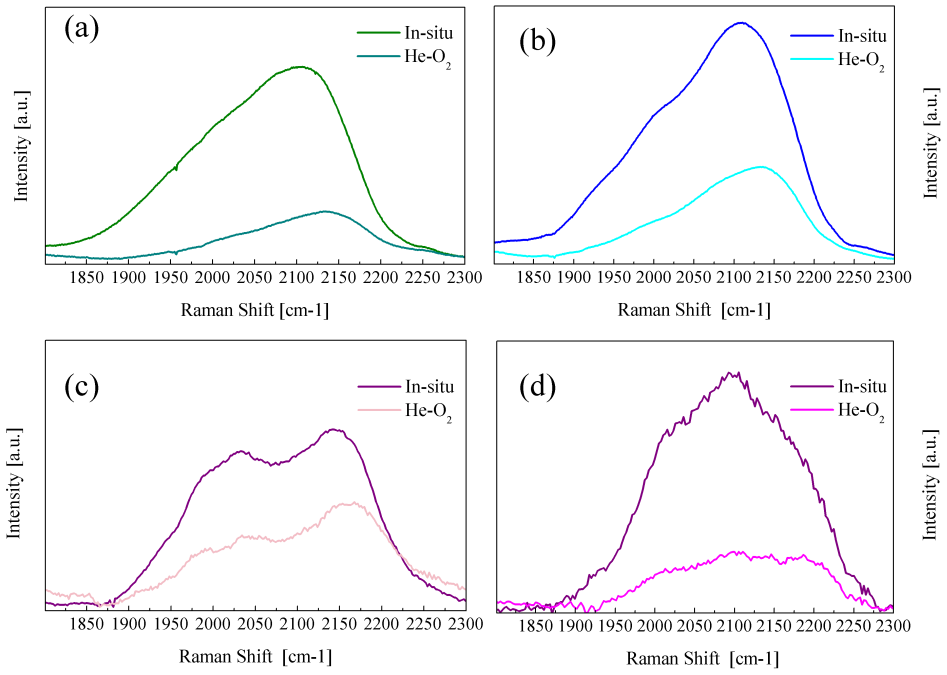

Figure 8.5: "C" band detail of the acquired resonant Raman spectra, both *in-situ* and after an exposure to He-O_2 mixture (20%), by using four different laser wavelength: (a) 514.5 nm, (b) 488.0 nm, (c) 363.8 nm and (d) 325 nm

(i.e., shorter chains). Furthermore, the C_1 peak does not shift during the decay or change its width, while all softer peaks are blue-shifted by 10 cm^{-1} and narrowed by 7 cm^{-1}. By summarizing DFT-LSDA calculation reported in 8.4(b), I can say that the high-frequency stretching modes of torsionally strained CH2-terminated chains are affected quite strongly by the twist angle, with a redshift up to 100 cm^{-1}. However, since chains with smaller torsional barrier (such as those bound to biphenyl groups and nano-ribbons) show smaller redshifts, this effect evaluated for CH2-terminated chains should be considered as an upper limit for realistic pure-carbon nanostructures.

The observed blueshift of the peaks accompanying the decay, very small in the *in-situ* case, quite huge during gases exposure, can then be explained if each component is assigned to a particular family of cumulenes, having all the same length but different strain: the more strained chains, having softer Raman modes, decay faster than the others, resulting in a net blueshift and narrowing of the peak. A faster decay of torsionally strained vibrationally redshifted cumulene-type chains is indeed to be expected due to their higher total energy (right panel of fig. 8.4(a)). On the contrary, no torsional strain applies to polyynes because of their axial symmetry, and this is why the C_p peak does not shift.

It is interesting to notice how He, although it is a non-reactive gas, boosts the decay of *sp*CCs. This indicates that, as previously suggested, if one can wait for long time (namely months or even years) leaving the sample in UHV conditions, can recover the same result

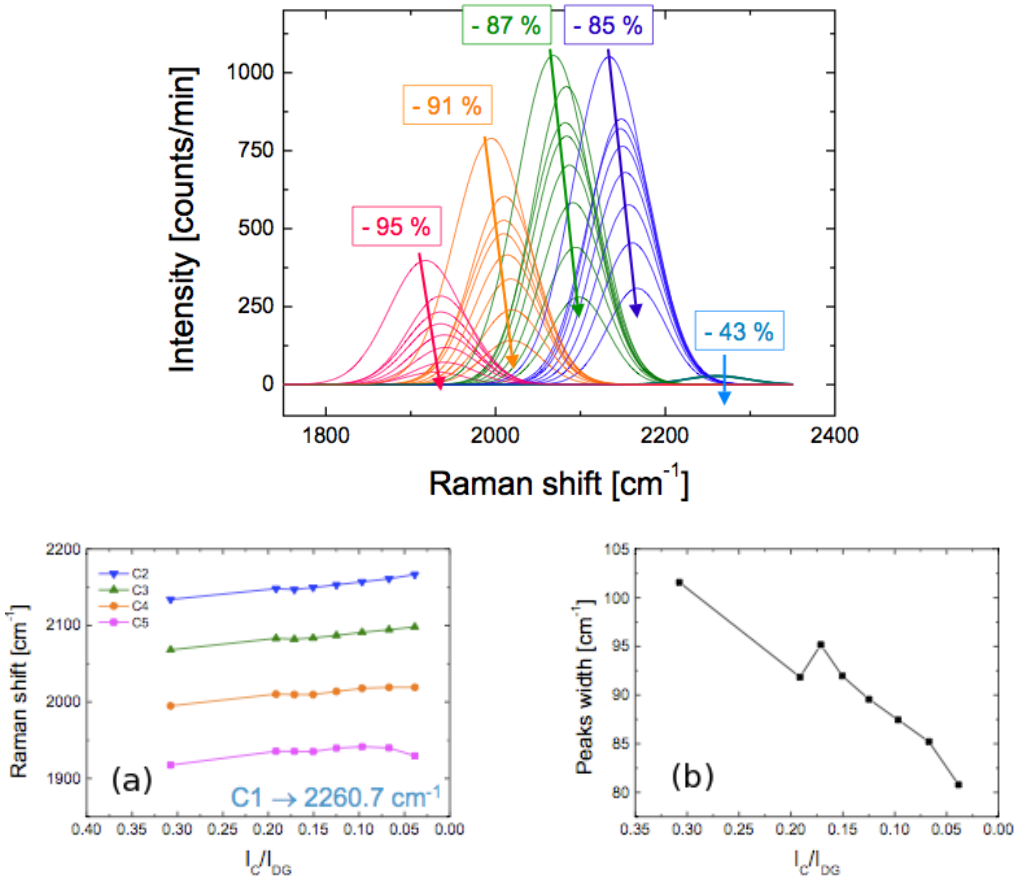

Figure 8.6: (top) decay of the gaussian components used for the fitting of the Raman spectrum during He-O_2 exposure; (bottom) evolution of the position (a) and width (b) of the different gaussian sub-component.

obtained with the He exposure. Remarkably, in the latter, the *sp*CCs decay is accelerated by (i) the compression of the film, resulting in a net diminution of the film volume and the consequent increase of the *sp*CCs density, and (ii) by the gas penetration in porous film which provides, through collisions, enough energy to overcome the potential barrier for the activation of the metastable *sp*CCs decay.

In order to better understand these results and to confirm the proposed picture, it is interesting to consider what happens to the C band if one exposes the samples to reactive gases, as for instance a mixture of He and O_2 at 20% (He-O_2 in the following). As reported fig. 8.5, for all the excitation energy, during the exposure it is the low frequency region $1800 - 2000$ cm^{-1} which suffers the faster decay; furthermore it can be noticed that in the UV Raman spectra of the exposed samples ((c) and (d) in fig. 8.5), some sub-components, almost hided in the *in-situ* spectra, are now more sharply defined.

As reported in fig. 8.6, during oxygen exposures the the four components below 2200

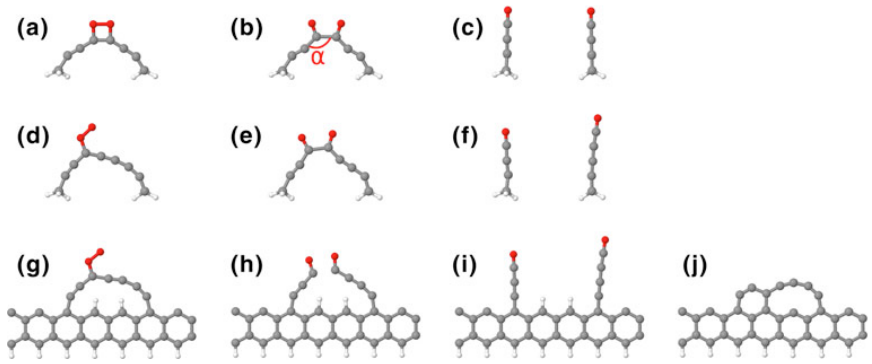

Figure 8.7: structures obtained with nudged elastic band calculation by reacting O_2 molecules with *sp*CCs both sp^2 and sp^3 terminated [98]

sp^2, both the intensity lowering and the blueshift are more prominent than in the *in-situ* and He cases. The component at higher frequency seems to be again the most stable one, since it decays less than the other four, does not shift and preserve its width. I can conclude that although the chemical reactions induced by oxygen is capable of breaking the C-C bond. No matter how long are *sp*CCs, longer and strained chains preserve higher reactivity with respect of shorter ones. Indeed when *sp*CCs react with O_2 molecules, the decays of all the sub-component have different yield: longer chains are less stable than shorter (95% of longest chains decays in contrast of the 85% of the shortest one) but the latest experience the higher increase of their decay as compared to the He exposure case and this can be explained by the chemical nature of the reactions with oxygen (reducing the difference between the decay of long and short chains).

For what concerns oxygen exposure, recently G. Moras *et al.* [98, 99] demonstrated that by exposing *sp*CCs to O_2 molecules one obtains the progressive cleavage of carbon chains due to C-C bond breaking and the following O atoms passivation of the dangling bonds. As shown in fig. 8.7 O_2 molecules undergo chemisorption on the central bonds of the cumulenic-like *sp*CCs: after O_2 adsorption, the reaction proceeds with the concerted breaking of the O-O and C-C bonds thus forming two shorter carbon chains terminated by a graphitic fragment at one side and with an oxygen atom at the other side. This oxygen-induced cleavage of the chains is an exothermic reaction in all the investigated systems in ref. [98,99]: the energy gain ranges between 1.96 and 5.80 eV and, as expected, is larger for the more strained chains. As a consequence, during He-O_2 exposure, the difference between the four sub-components decay rates, can be addressed not only to the different stability of shorter chains in comparison of longer ones, but also to the formation of short chains as a consequence of the long *sp*CCs cleavage. Remarkably, the results obtained by G. Moras *et al.* [98, 99] are consistent with the picture provided by the combined experimental-theorietical study presented in this section.

Despite of what happens with dinaphthylpolyynes, for the *sp*CCs embedded in the *sp*-sp^2 system it is not possible to univocally define an HOMO-LUMO gap, since it is strongly related not only to the chain length but also to the chains distortion. As a consequence, it is not possible to correlate the optical absorption with the enhancement of the Raman signal. Furthermore, it is extremely difficult to theoretically determine to which electronic transitions is correlated the activation of the Raman resonances; indeed,

apart from the very simple case of dinaphthylpolyynes, for an amorphous sp-sp^2 solid it is not obvious what transitions have the best wavefunctions superimposition, i.e. which are the electronic transitions responsible for the activation of the resonance-Raman effect.

Nevertheless by combining MWRR spectroscopy with DFT-LSDA calculations it is possible to provide a quite accurate analysis on the presence and stability of spCCs embedded in the sp-sp^2 pure carbon film. The Raman spectra acquired with different wavelength, both *in-situ* and during gases exposures, show that resonance effects can be exploited with MWRR spectroscopy for the identification and assignment of the peaks whose superimposition give rise to the C band. The observation of the blue-shift of the C band as the photon energy increases, combined with analysis of the decay of its sub-components, allow to assert that each component below 2200 cm^{-1} can be assigned to sp^2-terminated spCCs with different lengths (namely form the C_4 to the C_{12}) while the features at 2260 cm^{-1} is related to sp^3-terminated spCCs.

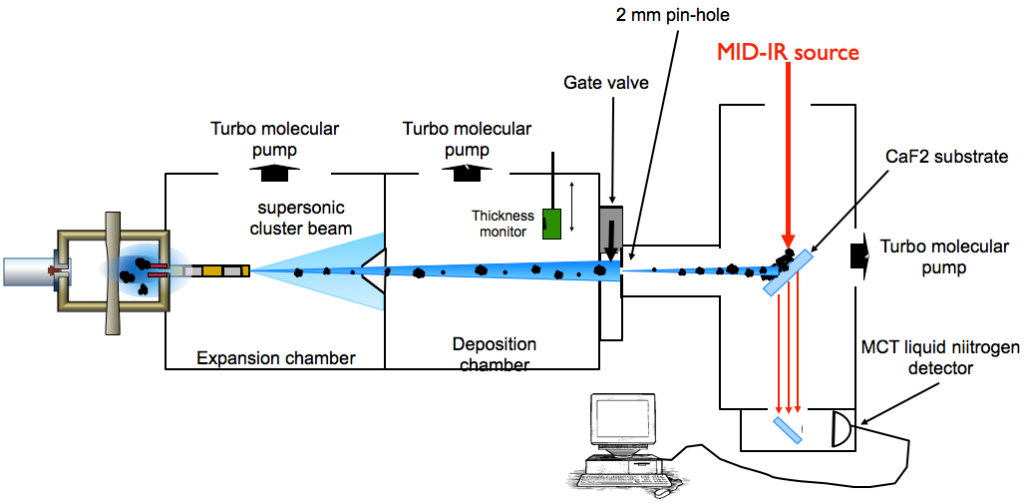

Figure 8.8: Setup used for the in-situ infrared spectroscopy

8.2.2 Infrared characterization

Infrared spectroscopy experiments have been performed within a collaboration between the "Surface and thin films" group, leaded by Professor P. Rudolf ("Zernike Institute of advanced materials" of the University of Groningen), "CIMaINa"(Interdepartmental Center for Nanostructured Materials and Interfaces), leaded by Professor P. Milani (Physics Department of the University of Milan) and the Materials Science Department of the University of Milan-Bicocca. The cluster beam apparatus, previously described in sec.3.1, was moved from Milan to Groningen laboratories and connected, through UHV chambers, to the UHV mid-infrared spectrometer present at the Prof. Rudolf's laboratory. The set-up used for *in-situ* infrared spectroscopy is sketched in fig. 8.8. With respect to the Raman set-up, described in sec.8.2.1, the second chamber is equipped with a 2 mm pin hole mounted on the ending flank on the beam axis, just before the gate valve which connects the cluster beam apparatus with the infrared spectrometer. The in-situ Infrared spectroscopy characterization of the samples was performed in transmission mode by a Brukker IF 66/v FT-IR (Fourier transform infrared/far infrared) spectrometer, equipped with liquid N2 cooled MCT (Mercury Cadmium Telluride) detector operating in the range $700 - 5000$ cm^{-1} with a 2 cm^{-1} resolution. The spectrometer is interfaced with the UHV (10^{-8} mbar) deposition chamber evacuated by a turbo pump. Samples were deposited on a CaF_2 substrate located inside the deposition chamber and mounted with an angle of 45 degree with respect both of the Infrared beam and the cluster beam. As for Raman the measurements, we acquired tens of Infrared spectra for each sample, each of which was obtained by averaging 256 acquisitions (c.ca 4 minutes for a single spectrum) in order to get the highest signal to noise ratio. In the post-processing step I remove the background provided by the sp^2 matrix optical absorption by fitting it with a 3rd order polynomial curve. The background signal is originated by the optical absorption of the sp^2 matrix, thus it increases as a function of the sample thickness and mainly affect the short wavelength part of the infrared spectrum (3.5-1 μm)8.9. In this spectral region, this background has a dependence on the energy typical of the empirical Tauc model [100] for which $\alpha(E) \propto \frac{(E-E_T)^2}{E^2}$, where $\alpha(E)$ is the

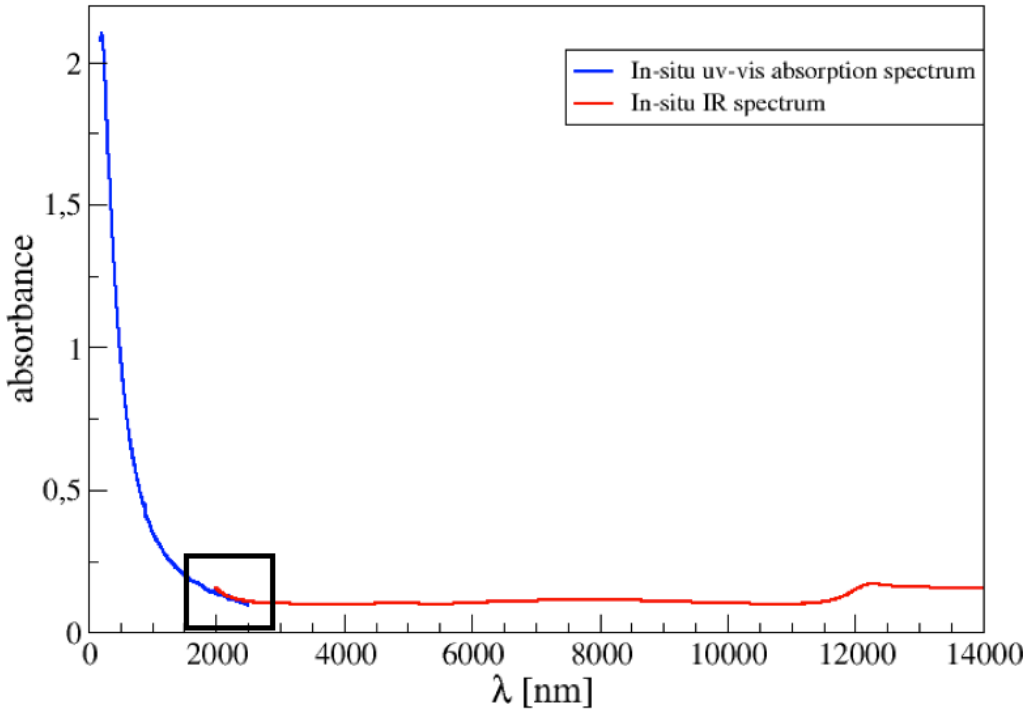

Figure 8.9: *in-situ* infrared spectrum and UV-Vis spectra acquired in transmission mode (here converted in absorption units) by depositing sp-sp^2 pure carbon cluster on a CaF_2 substrate; the black rectangle highlights the fitting region used for the evaluation of the Tauc gap.

the imaginary part of the dielectric function (i.e., absorption coefficient). Within this approximation I was able to extract the optical gap of thesp-sp^2 material, confirming the 0.6 eV value obtained in previous work concerning amorphous carbon [101]. In fig. 8.10 is reported an in-situ IR spectrum of a cluster assembled sp-sp^2 pure carbon film obtained by using the apparatus showed in fig. 8.8. In the frequency range between $1000 - 1600$ cm^{-1} lies the well-known broad component of amorphous sp^2 carbon [102] related to dipole active modes whose carriers are the antisymmetric π C=C stretching frequencies of graphitic domains located at 1238 and 1543 cm^{-1} [103]. With respect to the Raman spectrum, in the infrared one it is not possible to distinguish between vibrational modes related to ordered and disordered structures, thus this broad band can be addressed to the vibrations of the sp^2 structures present in the material, both rings, chains and all the other possible configurations that sp^2 carbon can form.

More interesting is the feature present in the frequency range between $1900 - 2300$ cm^{-1}, which can be addressed to the infrared active modes of spCCs. This is, to our knowledge, the first identification of the infrared features of spCCs embedded in a pure carbon solid. Despite the C band of Raman spectrum reported in the previous section, the infrared one is characterized by the presence of three sharp components between 2150 and 2300 cm^{-1}, and a broader shoulder ranging from 1900 to 2100 cm^{-1}. In order to understand the origin of such sharp vibrational features, I perform the fit of the infrared C band, by using the same procedure proposed in the previous section; then I

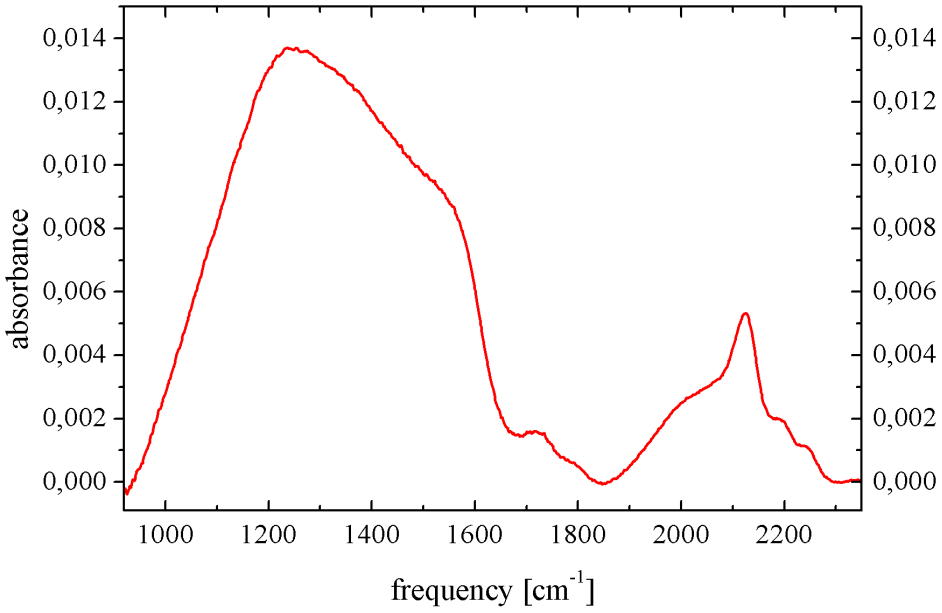

Figure 8.10: *in-situ* infrared spectrum acquired in transmission mode (here converted in absorption units) by depositing *sp*-sp^2 pure carbon cluster on a CaF_2 substrate; (a) the broad band related to the amorphous sp^2 matrix; (b) infrared C band.

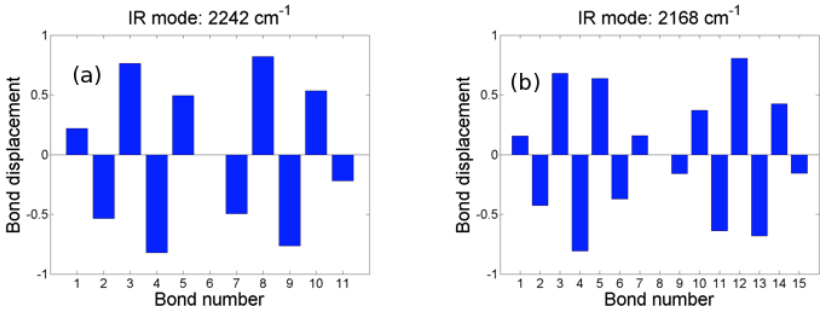

Figure 8.11: longitudinal displacement patterns of most intense dipole active modes. (a) The IR-α modes for the Ar-C_{10}-Ar molecule and (b) the IR-β mode for the Ar-C_{12}-Ar molecule.

compared the parameters of the fitting curves with DFT-LSDA calculated infrared active modes. It is remarkable to underline that the displacement patterns of the infrared active modes preserve their form when ranging from dinaphthylpolyynes to *sp*CCs terminated by graphitic fragments. Thus, since it is not possible to directly calculate infrared cross section for pure carbon *sp*-sp^2 metallic structures (due to the limitation of the used DFT implementation), then I am able to identify the nature of the IR-α modes of the

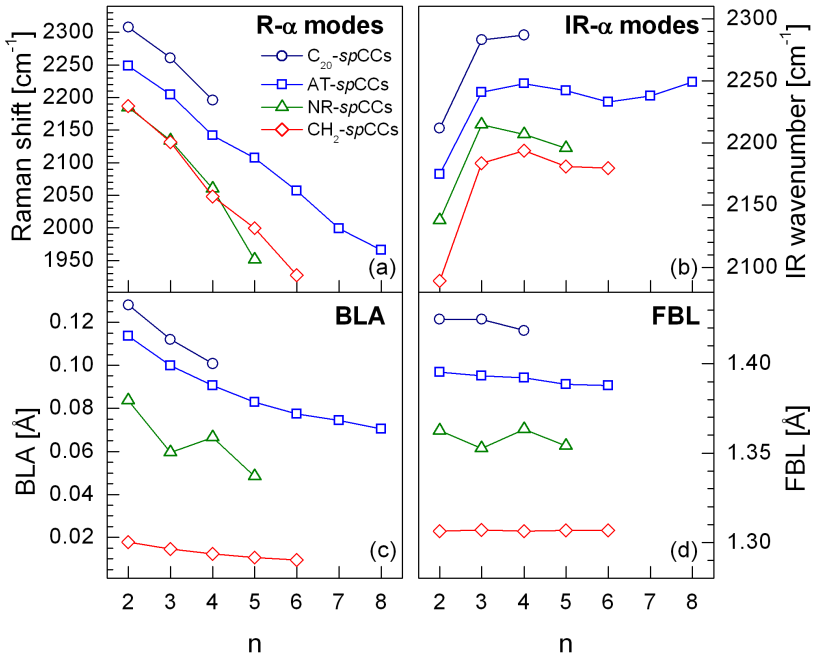

Figure 8.12: (a) - (d) trend of R-α modes, IR-α modes, BLA and FBL as a function of length for different end-capped spCCs

spCCs terminated by graphitic fragments by comparing their longitudinal displacement patterns with the ones of dinaphthylpolyynes. As a reminder, in fig. 8.11 are reported the longitudinal displacement patterns of the IR-α mode of the Ar-C_{10}-Ar and the IR-β of the Ar-C_{10}-Ar dinaphthylpolyynes. By considering the simulations summarized in fig. 8.12, it is clear how the Bond Length Alternation (BLA) and Final Bond Length (FBL) values allow to precisely characterize the nature of the different spCCs. Specifically, the BLA is a measures of the overall degree of dimerization of the spCCs and its value is only weakly affected by the nature of the chain termination, as it is dominated by the chain length and, for sp^2-terminated chains, by the chain torsion. The evolution of the R-α modes with the chains length follows the n-dispersion of the BLA and, as a consequence, the Raman spectrum of both the dinaphthylpolyynes solution and the sp-sp^2 system cover almost uniformly the whole range of sp hybridized carbon atoms $(1800 - 2300)$ cm^{-1}.

In contrast, the FBL provides a direct indication of the bond strength between the terminating group and the chain, thus representing a clear marker of the chains termination; furthermore its value is almost independent of the chain length and therefore, as can be seen in fig. 8.12, once fixed the termination, FBL values have a very weak n-dispersion: by varying the termination, FBL rigidly shifts going from highest value for sp^3-terminated spCCs, sharing strong single σ bond with the end group, to the lowest related to pure cumulenic spCCs, characterized by softer double bonds at their extremes. Remarkably, IR-α modes follow a dispersion similar to the one of FBL (differently than the R-α modes that follow the BLA one), and this confirms those finding obtained for dinaphthylpolyynes [88], that is the accumulation of all the frequency around a fixed

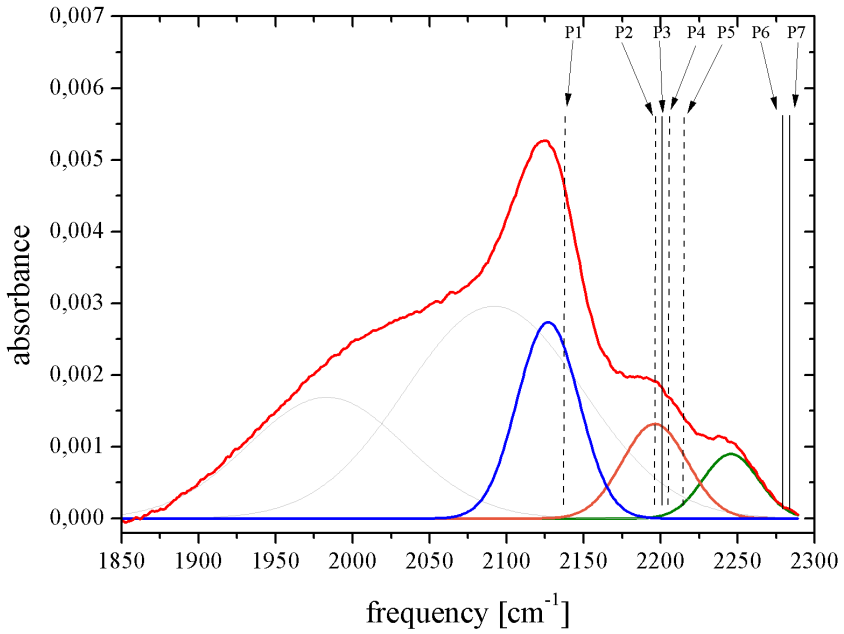

Figure 8.13: matching between the experimental infrared features with calculated ones.

value (in that case induced by naphthalene). From these results I can conclude that the frequency of the IR-α mode correlates to the value of the FBL and, in turn, to the nature of the chain termination.

In fig.8.13 I show the comparison between the experimental infrared C band and calculated IR-α frequencies for two different graphitic terminations (sp^2-terminated *sp*CCs and sp^3-terminated *sp*CCs) and for different chains length (from the C_4 to the C_{10} for sp^2-terminated *sp*CCs and from the C_4 to the C_8 for sp^3-terminated *sp*CCs). The mismatch observed between experimental and simulated modes can be addressed to ten-

*sp*CCs	fitted peak position [cm^{-1}]	calculated frequency [cm^{-1}]
C_4-NR	2127	2138
C_6-NR		2214
C_8-NR	2195	2206
C_{10}-NR		2195
C_4-C_{20}		2211
C_6-C_{20}	2245	2282
C_8-C_{20}		2287

Table 8.2: center of the experimental fitting gaussian compared with calculated IR-α modes

dency of the LSDA to overestimates (up to $\approx$ 20% and more) cohesive energies and bond strengths in molecules and solids. This leads to the undervaluation of the bond lengths with the consequent overvaluation of the vibrational frequencies. As a consequence, since IR-α modes are highly sensitive to the length of the terminating bond, this peculiarity of LSDA reflects in a more important way in evaluating the bond strength and, consequently, the frequencies of infrared active modes.

Remarkably it can be noted that, regardless this systematic error strictly related to the DFT-LSDA framework, it is possible to correlate calculated and measured infrared spectra by assigning the three sharp gaussian component to specific *sp*CCs families. The most intense band peaked at 2127 cm^{-1} is nicely in good agreement with the calculated frequency (reported in table 8.2) of the IR-α mode of the sp^2-terminated-C_4 *sp*CCs (reported as P1 in fig.8.13). Furthermore, the Gaussian peaked at 2195 cm^{-1} can be provided by the superimposition of the IR-α modes of C_6, C_8 and C_{10} sp^2-terminated linear carbon chains (reported in fig.8.13 as P2, P4 and P5). For what concerns the broad shoulder at lower frequency, two possibilities can be considered: first of all Raman inactive modes can turn on and become visible also in the infrared spectrum due to the distortion induced by amorphous matrix *sp*CCs to the relaxed configuration. However, one has to take into account that in order to overcome the complementarity of IR and Raman active mode, it is necessary to break the centro-symmetric nature of sp^2- and sp^3-terminated chains and thus very huge distortions have to be considered. More probably it can occur that some *sp*CCs, in the *sp*-sp^2 cluster assembled film, can present two different terminations, i.e. one sp^2 and the other sp^3, thus breaking the centro-symmetric form and the IR/Raman complementarity. However, to consider this explanation, more theoretical efforts about the nature of *sp*CCs terminated by two different end-group geometry are needed. More concrete at this level of knowledge, although the calculated frequency are not yet available, the broad feature can be tentatively assigned to the superimposition of the red-shifting IR-β active modes of sp^2-terminated C_n-*sp*CCs, with $n \geq 12$ [88].

Then, as can be seen in fig. 8.13 and in table 8.2, the IR-α mode of the sp^3-terminated C_6 C_8 (P6 and P7 peaks) are responsible of the absorption peak at 2245 cm^{-1}. Although this assignment is quite clear, the IR-α mode of the shortest chains of this family (C_4) is far from all the other two frequency; I remark that in the previous section I assigned the highest frequency component in the Raman spectrum of the *sp*-sp^2 film to sp^3-terminated chains, no matter what is the length. This fact suggests that in this material only a few percent of *sp*CCs have an sp^3 terminations and thus, the infrared contribution of the polyynic-like C_4 (P3 peak) is hided by the ones of the more abundant sp^2-terminated chains.

However, as in the case of the Raman spectra, I am aware of the fact that the most important source of inaccuracy in precisely matching such broad experimental features and calculated frequencies is due to the large varieties of different configurations that *sp*CCs can present in the *sp*-sp^2 system and that cannot be simulated. Indeed, for instance, I am considering only even chains and ignoring odd chains, since the latter are expected to be less stable [97], I am neglecting mixed sp^2- sp^3-terminated *sp*CCs and finally I am not taking into account the effect of stress and strain induced by the constraint imposed by the amorphous sp^2 matrix which can affect the infrared active modes by acting on the final bond lengths and thus to the final bond strength.

Remarkably, also considering these clarifications, I can conclude that it is possible to provide an interpretation of the infrared C band by assigning the three sharp component present in the infrared spectrum of the *sp*-sp^2 pure carbon material: the most intense at

2127 cm^{-1} is provided by the IR-α mode of the C_4 sp^2-terminated *sp*CC; the features at 2195 cm^{-1} is the superimposition of the IRα modes of sp^2-terminated chains with a length up to 10 *sp* carbon atoms while the last peak at 2245 cm^{-1} can be assigned to sp^3 terminated *sp*CCs. Finally, by considering the results provided by the vibrational study of dinaphthylpolyynes reported in sec.7.2, it is also possible to tentatively address the broad shoulder to sp^2-terminated chains longer than 12 *sp* carbon atoms.

8.2.2.1 Reactivity of the *sp*-sp^2 pure carbon film

In the recent past the reactivity of the *sp*-sp^2 has been studied by following the evolution of the C band intensity in the Raman spectrum as a function of time and of the D-G band intensity [70, 71]. Since Raman effect is characterized by the resonance effect and it is not sensitive to the products of chemical reactions, these studies could only explain the dynamics of the C band, but it could not provide any information about the chemical reactivity of the film.

On contrary, by using infrared spectroscopy, it is not possible to exploit resonance effect in order to enhance the signal of *sp*CCs with different electronic configurations, but it is rather possible to precisely follow the chemical reactions path and provide informations about the products of such reactions.

I focused the attention on the reactivity of the *sp*-sp^2 films with oxygen. The data were acquired performing infrared absorption spectroscopy of a sample firstly maintained in UHV conditions and then exposed to a mixture of He and Oxygen at 20% (He-O_2 in the following) at a pressure of 500 mbar. The spectra have to be normalized to the intensity of the DG area in order to be compared. Indeed the injection of the gas mixture through the leak valve causes the whole increasing of the intensity of the spectra making them incomparable. As a consequence the reported intensity cannot be used for the quantitative analysis by evaluating the area under the different spectral features. In fig. 8.14 I report the last *in-situ* spectrum acquired few second before the gas exposure is started and the spectrum acquired after the exposure and restored the vacuum. In this way I remove all the volatile species that can give rise to spurious spectral features (CO_2 in particular).

As can be noted, the He-O_2 exposure produce modification both to the DG band and to the C band. For what concerns the amorphous sp^2 features, it occurs the reaction between the graphitic domains and oxygen which mainly induces the graphitization process, as highlighted by the increase of the component at 1550 cm^{-1} and the sharpening of the D shoulder (1200 cm^{-1}), as was already observed in previous work by means of Raman measurement [70, 71]. It is also possible to notice an increase of the feature at 1730 cm^{-1}, whose carriers are the C=O functional groups. As a consequence this effect can be related also to the oxidation of the graphitic matrix [103, 102].

Regarding the infrared C band, it can be noted a remarkable evolution. As shown in details in fig. 8.15, the first effect of He-O_2 exposure is the net diminution of the components at low frequency, i.e. the ones between 1850 and 2100 cm^{-1}. This fact is consistent firstly, with the assignment made in the previous section of this broad shoulder, and then with what I observed in the Raman spectrum during the oxygen exposure (see sec.8.2.1), that is this frequency range arise from the vibrational features of long chains which are characterized by an higher total energy with respect of shorter ones, i.e. they are less stable [96]. I highlight that, by combining calculated infrared active modes with the fitting parameters, I assign these spectral region to *sp*CCs longer than 12 carbon atoms, exactly the same findings I obtained with MWRR spectroscopy.

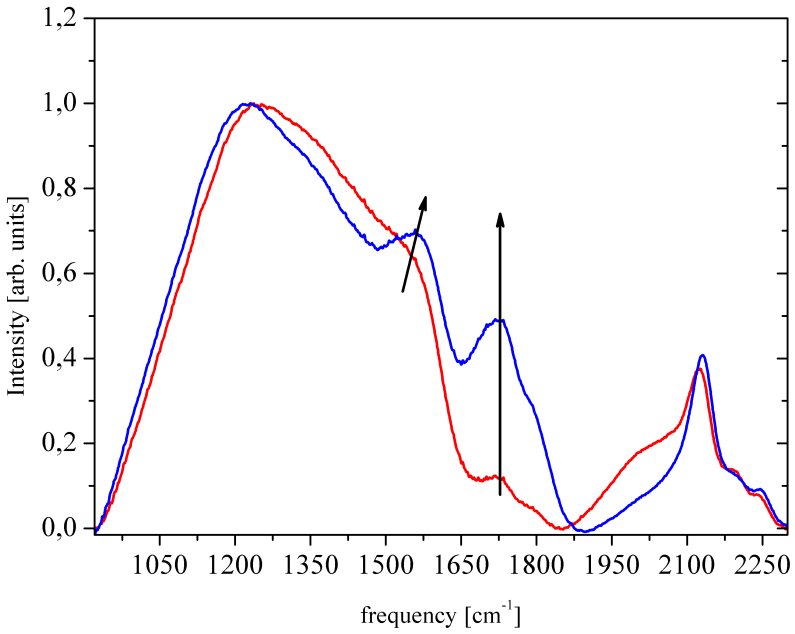

Figure 8.14: *in-situ* infrared spectrum compared with the one acquired after the exposure of the sample to a mixture of He-O_2.

Furthermore it is intriguing what happens to the component peaked at 2127 cm^{-1}: as reported in fig. 8.15 it suffers a weak blue-shift and intensity increase during the He-O_2 exposure. This observation is quite surprising since by Raman measurements it was observed a net diminution of all the components, no matter what is the chains length. In order to understand this behavior it is useful to remind the the results obtained by G. Moras *et al.* regarding the reactivity of linear carbon chains with oxygen: during the He-O_2 exposure O_2 molecules cleave *sp*CCs by breaking the C-C bonds leading to the formation of both shorter and oxidized chains. This process can go on leading to ulterior cleavage steps of the *sp*CCs and then providing the progressive shortening of the chains and the production of CO_2 molecules. These reactions are once again exothermic as the energy gain is, for *sp*CCs composed by $3-5$ carbon atoms, of $4.1-5.9$ eV. In addition, this combustion process can go further as long as the two carbon atoms involved in the reaction are *sp*-hybridized, since the associated energy barrier is about 0.6 eV [98, 99].

As a consequence the blue-shift of the peak at 2127 cm^{-1} towards the IR-α mode of the sp^2-terminated C_4 (2138 cm^{-1}) chains and its growing intensity have to be addressed to the formation of C_4 chains due to the cleavage of longer (less stable) sp^2-terminated *sp*CCs. Then, since in the infrared spectrum of the exposed sample the features of gaseous CO_2 molecules are not present, it means that all these molecules produced during the combustion of progressively shorter chains, are evacuated by the turbo-molecular pump of the deposition/analysis chamber.

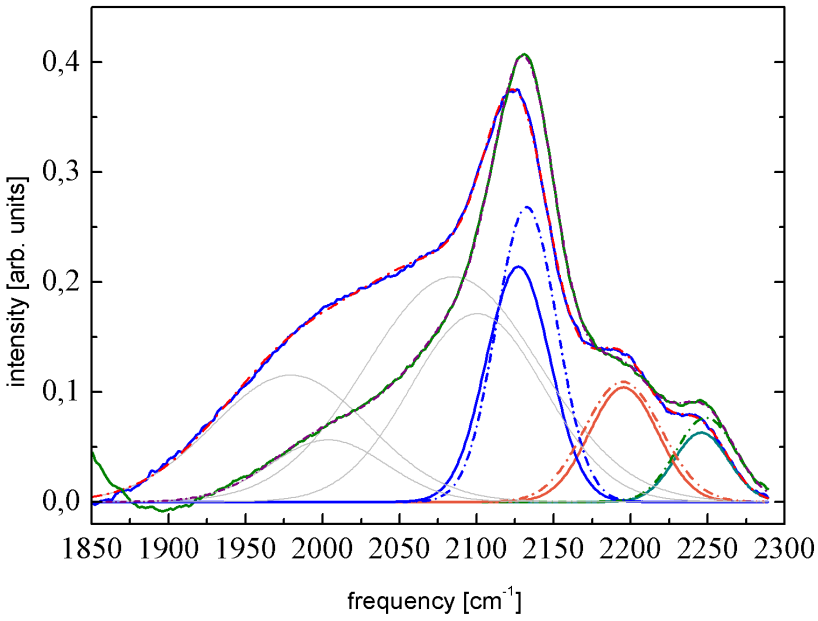

Figure 8.15: fit of the *in-situ* infrared "C" band compared with the fit of the one after the exposure of the sample to a mixture of He-O_2.

Although this picture is quite intriguing, it cannot be exhaustive: as a matter of fact, the weak increasing of the C_4-*sp*CCs is not sufficient to justify the almost complete disappearance of the broad shoulder. It is possible to understand these observations by considering the big difference of the infrared cross-sections, characterizing chains with different length (it grows exponentially with n): the decrease of the intensity accompanying the spectral feature related to long chains is much more evident than the intensity gain provided by the increasing amount of short chains. Unfortunately, as discussed in the section dedicated to the computational methods, I am not yet able to provide infrared intensities for metallic system as the ones under consideration.

On the other hand, it is interesting to consider in details the calculations, as reported in table 8.3, of the vibrational modes of *sp*CCs terminated with a graphene nano-ribbon on one side and with an oxygen atom on the other side. First of all, the centro-simmetry of the system is lost and thus some modes become both Raman and IR active; secondly these *sp*CCs have vibrational modes which have different bond displacement patterns with respect of those of IR-α and IR-β. In particular ν_1 modes, present for both C_4, C_6 and C_8 chains, is characterized by wide displacements for the C=O bond and almost zero displacement for all the other bonds. Remarkably these frequencies match very well with the feature at 1730 cm^{-1}, which experiences the most important increase during the He-O_2 exposure, thus indicating that an oxidations process of *sp* carbon chains is occurring; furthermore, also the highest frequency modes at $\sim$ 2300 cm^{-1} presents a huge displacement for the C=O bond, if compared with all the *C=C sp* bond of the

*sp*CCs	ν_1 [cm^{-1}]	ν_2 [cm^{-1}]	ν_3 [cm^{-1}]	ν_4 [cm^{-1}]	ν_5 [cm^{-1}]
NR-C_4-O	1730	2129	2292	-	-
NR-C_6-O	1747	2081	2142	2304	-
NR-C_8-O	1758	2036	2083	2181	2311

Table 8.3: Calculated vibrational modes of oxidized sp^2-terminated *sp*CCs. A clear distinction between Raman and infrared-active modes is not possible, because cross-sections calculation for metallic sytem is not implemented in the Q-E package. Furthermore, these structures are not centro-symmetric and thus it is not possible to discriminate between Raman and infrared-active modes from their longitudinal displacement patterns.

chains, and their frequency is in good agreement with the experimental features at the highest frequency (2245 cm^{-1}). It is interesting to notice that the latter, during the exposure, also increases its intensity, thus suggesting again the formation of oxidized *sp*CCs.

I can conclude that, by using infrared spectroscopy, I was able to clearly identify *sp*CCs with different terminations by assigning each sharp component to a particular chain family, sp^2- and sp^3-terminated ones. Although further theoretical efforts are required to unambiguously assign the broad shoulder at 2000 cm^{-1}, a tentative assignment can be proposed by extending those findings obtained on the IR-β modes of dinaphtylpolyynes and therefore assign this broad component to the superimposition of most intense IR active modes of C_n-*sp*CCs, with $n \geq 12$.

By exposing the samples to a He-O_2 mixture, I am able to identify the reaction process occurring as O_2 molecules interact with *sp*-sp^2 material: (i) the cleavage of *sp*CCs by the progressively C-C bond breaking, leading to the formation of shorter chains (in particular C_4) (ii) the formation of sp^2-terminated oxidized *sp*CCs, as indicated by the increasing of the features at 1730 cm^{-1} and at 2245 cm $^{-1}$. Finally, at the present knowledge, it is not yet clear who are the carriers of the component at 2195 cm $^{-1}$. The matching of calculated IR-α modes of sp^2-terminated C_n-*sp*CCs, having $6 \leq n \leq 10$, with this spectral feature is quite accurate, nevertheless the very weak effect affecting this component during the O_2 exposure is not compatible with its assignment to sp^2-terminated chains of this length. By following the results provided by G. Moras *et al* [98,99], *sp*CCs composed by 6, 8 and 10 atoms should undergo to chemical reactions with oxygen as longer chains do. In order to address this component, further theoretical efforts are needed, in particular calculations (running while I'm writing this thesis) of infrared intensities of a simplified system, that is oxidized CH_2-terminated *sp*CCs (referred in the literature as "cumulenones" [104]). The patterns of bond displacements will be compared with the one of graphitic-terminated *sp*CCs in order to find which are the most intense infrared active modes of the oxidized sp^2-terminated chains. Then a more accurate assignment of the IR features characterizing the exposed spectrum will be possible.

8.2.3 Summary

In the following I just summarize all the achieved results in this chapter devoted to the study of the vibrational properties of *sp*-sp^2 carbon;

- thanks to the high signal to noise ratio of the Raman spectrum I was able fit the C band with five gaussian sub-components and to precisely follow their *in-situ* decay.

Each sub-components show a peculiar decay rate, in particular the lower frequency components decay the less with respect of higher frequency ones;

- remarkably if the film is exposed to He, then the decay process is accelerated and the first four sub-components, not only loose the great part of their intensity, but also blue-shift and narrow. The highest frequency component, C_p peak at 2250 cm^{-1}, decay the less with respect of all the other and does not shift nor narrow;
- if the film is exposed to an He-O_2 mixture, then all the effects observed with He, the blue-shift and the narrowing of the first four gaussian, are enhanced;
- by comparing *ab-initio* DFT-calculated most intense Raman active modes (R-α) with experimental multi-wavelength resonant Raman spectroscopy both *in-situ* and during gases exposures, I was able to unambiguously assign each component of the C band to *sp*CCs having different length. In particular the four components lying below 2200 cm^{-1} are addressed to sp^2-terminated chains composed by n carbon atoms with $n = 2, 4, 6, 8, 10, 12$. The C_p peak is assigned to sp^3-terminated *sp*CCs;
- remarkably calculations show how sp^2-terminated *sp*CCs are torsionally stiff, thus their properties suffer the distortion imposed by the constraint of the amorphous sp^2 matrix. In particular these *sp*CCs turn spin-polarized if torsionally strained, their total energy increases (they are less stable) their gap tends to an absolute minimum and their R-α modes red-shift as a function of the torsion angle. The latter clearly explain the behavior of the four components below 2200 cm^{-1} observed during gases exposures, that is for each chain length torsionally strained chains (with softer R-α modes) decay faster than relaxed ones providing the centering of the sub-components at the frequency of the relaxed structures and the narrowing, related to the decay of all the unstable isomers. On contrary sp^3-terminated *sp*CCs are not affected by torsional strain due to their cylindrical symmetry and as a consequence the C_p peak does not present any blue-shift and narrowing;
- by characterizing with infrared spectroscopy the *sp*-sp^2 carbon film I observe an intense band, in the spectral region typical of *sp* carbon, composed by three sharp peak and a broad shoulder. This is the first identification of the infrared features of a pure carbon material containing *sp*CCs;
- by comparing *ab-initio* DFT-calculated most intense infrared active modes (IR-α) with experimental infrared spectroscopy of the *sp*-sp^2 carbon film maintained in UHV condition, I was able to tentatively assign each component to *sp*CCs having different terminations, namely sp^2- and sp^3-terminated chains;
- by combining the infrared spectrum of the sample exposed to a mixture of He-O_2 withe theoretical calculation of the *sp*CCs reactivity with oxygen present in the literature [98, 99], I was able to propose a model for the interpretation of the experimental data: O_2 molecules progressively cleave, through exothermic reactions sp^2-terminated chains. As oxygen breaks the central C-C bond, the resulting two shorter chains finds new graphitic fragments or an oxygen atom which saturates their dangling bonds. As a results the cleavage of long chains leads to the formation of both graphitic-stabilized shorter and/or oxidized chains. In order to clarify this point, further theoretical simulations of both infrared-active modes and reaction patterns, are needed.

Chapter 9

Conclusions and prospectives

The most relevant result I obtained in this Thesis is the identification of the different *sp*CCs families embedded in the *sp*-sp^2 pure carbon film by clearly assign their vibrational features.

In order to interpret the broad band of *sp* carbon in the vibrational spectra of the *sp*-sp^2 system, I developed a combinatory approach based on multi-wavelength resonant Raman (MWRR) and infrared (IR) spectroscopy combined with with structural, electronic and vibrational *ab-initio* density-functional theory (DFT) simulations. This approach allowed to obtain a complete vibrational description of a benchmark system, the dinaphtylpolyynes solution, and then to build a general framework for the interpretation of vibrational properties of *sp*CCs embedded in the amorphous sp^2 matrix.

I synthesized dinaphtylpolyynes of different length by reacting Copper(I)-ethynylnaphthalide with diiodoacetylene under Cadiot-Chodkiewicz conditions. The use of diiodoacetylene simplifies the synthetic route to long polyynes chains with taylor-made end caps, thus indicating its general applicability in the synthesis of α,ω-diarylpolyynes.

DFT simulations of dinaphtylpolyynes showed how, for each chain length, there is a Raman active mode (R-α mode) which bears almost the whole intensity, has the longitudinal displacements almost zero at the chains extreme and red-shifts as the chain length increases. This trend of the R-α modes is strictly related to the dispersion of the Bond Length Alternation (BLA), i.e. a measure of the chains dimerization: once fixed the chemical species used as end-group, the BLA decreases as the length increases. For what concerns infrared active modes, simulations show how up to the C_{10} chains the most dipole active mode is the IR-α one which present a node at the chain center. Remarkably this mode follows the trend of the the Final Bond Length (FBL), i.e. the length of the terminating bond and a measure of the bond strength. Indeed, once fixed the chemical species used as termination, the FBL value doesn't shift with chains length. For chains longer than 10 *sp* carbon atoms, the main intensity in the IR spectra is bared by a bi-lobbed mode, the IR-β one, which follows the same trend of the R-α one, that is it red-shifts for progressively longer *sp*CCs.

The resonance effect of dinaphtylpolyynes was exploited by combining Uv-visible absorption with MWWR spectroscopy and, by comparing experimental results with calculated Raman active modes and non-resonant cross sections, I clearly assigned the vibrational features present in the Raman spectrum to dinaphtylpolyynes with different length. Then, regarding infrared spectrum, I observed in the experimental spectrum an accumulation of vibrational features around a central frequency and few weak component

far from the latter, thus reflecting the IR-α and IR-β trends as a function of the chains length.

This novel approach show that, in a poly-dispersed system where different chains families are present, by Raman spectroscopy it is possible to distinguish *sp*CCs with different length, while by infrared spectroscopy it is possible to discriminate *sp*CCs families with different end-groups.

The framework developed for the study of dinaphtylpolyynes was then applied to the characterization of the vibrational properties of the *sp*-sp^2 pure carbon film. This system has been synthesized by producing *sp*-rich sp^2 carbon cluster with the *PMCS* source and depositing them onto a substrate by using the *SCBD* technique.

MWWR experiments were performed on the *sp*-rich pure carbon material both maintaining the sample in UHV conditions and exposing it to gases mixtures. *In-situ* measurements show a blue-shift of the whole C band and, by using Uv excitation wavelength, the pop up of many components silent with visible photons. As for dinaphtylpolyynes, what occurs by increasing the photon energy is the activation of the resonance effect of progressively shorter chains characterized by wider energy gap. By fitting at the same time the C band of the *in-situ* and the gas-exposed visible spectra, I was able to identify five gaussian sub-components and to follow their trend. I found that each component is characterized by a peculiar decay rate, more precisely it is progressively slower for the high frequency sub-components. Furthermore, MWRR spectra of He exposed samples show a blue-shift and the narrowing of all the first four components below 2200 cm^{-1} and these two effect are further enhanced by the exposure to O_2 molecules.

For the assignment of these five sub-components I performed simulation of the structural properties of *sp*CCs end-capped by either sp^2 and sp^3 pure carbon fragments. Those calculations demonstrated that this anchoring sites, which model the stabilization of carbon chains inside an *sp*-sp^2 cluster, induce quite stable structures, that is the binding energy is about $\sim$ 10eV for graphene nano-ribbon and $\sim$ 8 eV for C_{20}.

Surprisingly, while sp^3-terminated chains, as expected, are dimerized as they present an alternation of single and triple bonds (i.e., they are polyynic-like chains with a BLA$\sim$ 12 pm), sp^2-terminated chains, although they are expected to be undimerized with all double bonds with equal length, show a small but finite BLA ($\sim$ 6 pm) . This is a remarkable finding since show that the traditional categories of polyynes (alternating single-triple bonds, yielding a large BLA) and cumulenes (double bonds, negligible BLA) are adequate only if H-terminated chains are considered, while it is too simplistic for the description of *sp*CCs end-capped by bulky groups.

Furthermore, from simulations, I was remarkably able to demonstrate that sp^2-terminated chains present torsional stiffness. As a consequence, if an axial strain is applied, then many effects occur: (i) the energy gap decreases as the torsion angle increases and find an absolute minimum at an angle of 79°, (ii) the ground state turns spin-polarized at the same angle, (iii) the total energy monotonically increases as a function of the torsion angle (torsionally strained cumulenic chains are less stable than relaxed ones) and (iv) the R-α modes red-shifts as the angle increases. On contrary, sp^3-terminated chains are not affected by axial torsion, as they present a cylindrical symmetry due to the single and triple bonds along the chain axis.

By combing experimental spectroscopic data with simulation I demonstrated how it is possible to clearly describe the C band of the Raman spectrum of the *sp*-sp^2 pure carbon film in terms of *sp*CCs families having different length. The four sub-components below 2200 cm^{-1}, emerged from the fitting procedure, were addressed to sp^2-terminated *sp*CCs with different length, indeed: (i) the calculated R-α modes frequencies is system-

atically lower by $\sim$ 50 cm^{-1} than the one of the sp^3-terminated chains, (ii) is always lower than 2200 cm^{-1}, (iii) becomes "softer" if the chains are forcedly twisted. As a consequence the blue-shifting and the narrowing can be explained due to the decay of less stable, torsionally strained C$_n$$-sp^2$-terminated chains, with $n = 2 : 12$, which induce the gaussians sharpening and centering to the frequency of the relaxed (more stable) chains for each length. On contrary, the last features at 2245 cm^{-1} is addressed to sp^3-terminated chains, as the related gaussian doesn't shift and doesn't narrow during the decay, reflecting their insensitivity to axial torsion.

I interpreted the speed up of the sub-components decay noted by exposing the *sp*-sp^2 sample to He both to the compression of the film, induced by the gas injection, and to the gas diffusion in the porous film. In the first case a temporary *sp*CCs density increasing occur providing the enhancement of the cross-linking processes probability. In the second case, the scattering of the He atoms with *sp* chains probably transfers enough energy to activate the graphitization process.

By exposing the film to a mixture of He-O$_2$ I observed that all the components decay almost completely, thus suggesting that oxygen-induced reactions are the responsible of the decay. Remarkably the decay rates of each sub-components preserve some differences, thus indicating that shorter carbon chains somehow are less sensitive to oxygen-induced chemical reactions

Another relevant result I provide in this Thesis is the first identification of the infrared spectrum of a pure *sp*-sp^2 pure carbon material. With respect of the Raman one, the infrared C band present three well-defined features at , 2127 cm^{-1}, 2195 cm^{-1} and 2245 cm^{-1} plus a broader shoulder between 1900 and 2120 cm^{-1}. I explained the presence of such sharp peaks by addressing each component to *sp*CCs having different terminations. Indeed simulations of pure carbon structures confirm those finding bout IR-α obtained for the dinaphtylpolyynes, that is it does depend on the end-group and does not on the length, thus reflecting the trend of the FBL.

By comparing the experimental spectrum with simulated vibrational modes it was possible to address the most intense component at 2127 cm^{-1} to the sp^2-terminated C$_4$ chain, the one at 2195 cm^{-1} to sp^2-terminated C$_n$ (with $n = 6 : 10$) and the last one at 2245 cm^{-1} to sp^3-terminated C$_n$ (with $n > 6$). For what concerns the broad shoulder, I proposed its tentative assignment to the superimposition of the IR-β modes of sp^2-terminated C$_n$ (with $n \geq 12$). Indeed, as shown for the benchmark system, IR-β modes shift as the chains length increases and thus can be responsible of the infrared broad features observed between 1900 and 2120 cm^{-1}.

The component at highest frequency present in the infrared spectrum, the one at 2245 cm^{-1}, is assigned to sp^3-terminated C$_n$ (with $n \geq 6$). The IR-α mode of the C$_4$ chains belonging to this family is in the frequency range of sp^2-terminated chains and it is not detectable as sp^3-terminated chains represent only few percent of the whole *sp* carbon structures embedded in the sp^2 matrix.

Infrared spectrum of the *sp*-sp^2 system exposed to He-O$_2$ mixture show intriguing trends. Firstly I observe an huge decay of the broad shoulder, thus enforcing the assignment of this features to long sp^2-terminated *sp*CCs. Furthermore, the more surprising effect is the blue-shift and the increasing of the component at 2127 cm^{-1}. Thanks to the simulations proposed by G. Moras *et al.*, I explain this two effects with the progressive *sp*CCs cleavage due to exothermic energy-favored reactions with oxygen molecules, which leads to the production of CO_2 molecules, shorter and shorter chains down to the sp^2-terminated C$_4$ chains and also oxidized sp^2-terminated *sp*CCs. As a result the amount of the shortest *sp*CCs increases and consequently increases also the related in-

frared feature. The blue-shift has to be addressed to the progressive approaching of this peak to the IR-α mode of the C_4 chain. The enhancement of the infrared features located at 1730 and 2245 cm^{-1} is tentatively addressed to the formation of oxidated sp^2-terminated *sp*CCs of different length.

The results obtained in my Phd Thesis represent a powerful tool for the description of the presence and stability of *sp*CCs embedded in a pure carbon material by providing an easy way for their identification from their vibrational features. Nevertheless, further efforts are necessary, both theoretical and experimental, for the comprehension of their influence in determining the physical and chemical properties of the macroscopic material, as for instance chemical reactivity, non-linear optical and magnetic properties.

From the theoretical point of view it is necessary to model the chemical reaction between *sp*CCs and reactive gases, in particular with oxygen, atomic hydrogen and atomic nitrogen. Indeed, the comprehension of the oxygen reactivity will help in the interpretation of the related infrared spectrum and provide informations about their instability in ambient conditions, thus clarifying their possible use in actual devices. From the astrochemical point of view the reactivity of *sp*CCs is intriguing because it can open new prospectives in the study if the interstellar medium. As previously discussed, *sp*CCs are supposed to be the building blocks of many different structures already observed in the ISM, as for instance PAHs and amino acids, and therefore it is interesting to study how they interact with the other abundant elements present in the ISM, namely H, N and O. Then recently isolated not-terminated *sp*CCs present in the ISM have been proposed as building blocks also for fullerenes and nanotubes. It is thus clear how fascinating and intriguing are gas-phase infrared measurements of *sp*-sp^2 carbon cluster. Indeed with such experiments it will be possible to get data directly comparable (UHV conditions, diluted and isolated system) with astrophysical ones about the pure carbon structures (very small carbon grains, carbon soot, fullerenes, nanotubes, etc etc) production, presence and stability in the ISM.

For what concerns dinaphthylpolyynes, they represent a very good candidate for being both the building blocks for PAHs and the product of the photo-degradation of larger organic compound due to X-ray and Uv irradiation and thus it would be interesting to study these processes in the laboratory and compare the results with astrophysical ones.

Regarding the more applicative fields, despite the inclusion of *sp*CCs in actual devices is far from being at hand, in the literature many theoretical works have been carried out about the magnetic properties of end-capped carbon chains. In this framework *sp*CCs were proposed as spin-filters, spin-valves and switches in nano-electronics and spintronics devices. Remarkably in the present day and at my knowledge, there are not present in the literature any experimental works about the magnetic properties of *sp*-rich system. By remembering the theoretical results I obtained about the spin-polarization of torsionally strained sp^2-terminated chains and by considering the fact that in the *sp*-rich pure carbon film many *sp*CCs suffer distortions because of the constraints imposed by the amorphous matrix, the characterization of magnetic properties of the *sp*-sp^2 emerges as a fascinating and intriguing step which could pave the way for the inclusion of low-dimensional carbon materials in nano-electronic and spintronic devices.

Appendix A

Spongy Carbon

In MATHEMATICS AND TOPOLOGY OF FULLERENES,
edited by Franco Cataldo, Ante Graovac and Ottorino Ori,
Springer series on CARBON MATERIALS CHEMISTRY AND PHYSICS
(Springer, Heidelberg Berlin 2010), Chap. 12

The Topological Background of Schwarzite Physics

Giorgio Benedek[(1,2)] , Marco Bernasconi[(2)], Eugenio Cinquanta[(2)], Luca D'Alessio[(2,3)], and Marzio De Corato[(2)]

[(1)]Donostia International Physics Centre, P. Manuel de Lardizábal 4,
20018 Donostia-San Sebastián, Spain
[(2)]Dipartimento di Scienza dei Materiali, Universitá di Milano-Bicocca,
Via Roberto Cozzi 53, 20125 Milano, Italy
[(3)]Department of Physics, Boston University, Department of Physics,
590 Commonwealth Avenue, Boston, MA 02215, USA

Abstract

About ten years ago the synthesis of random carbon schwarzites by supersonic cluster beam deposition has endowed the rich sp^2 carbon family with its three-dimensional member. Its reluctance to grow as a three-periodic minimal surface according to topological and physical predictions still prevents schwarzites from being a hot topic, although spongy carbon is already having countless applications. Understanding the links between topology and quantum structure, possibly with the help of large-scale quantum molecular dynamics simulations should trace the route to the synthesis of periodic schwarzites. In this perspective, after a brief account on the growth and characterization of spongy carbon, we review the elementary topology of schwarzites, their stability and growth conditions as derived from pure topological arguments, the electronic structure and the electron-phonon interaction of the smallest periodic schwarzites and what can be learnt by the topological monitoring of quantum molecular dynamics.

You see things and you say "Why?"
But I dream things that never were and I say "Why not?"
(George Bernhard Shaw, Back to Mathusalem)

1. Introduction

The investigation of new sp^2-bonded carbon architectures, marked by the discovery of fullerenes [1] and nanotubes [2], and more recently by the synthesis of spongy carbon [3-5] and the isolation of single graphite layers (graphene) [6-10], is opening fascinating perspectives for nanostructured carbon as a novel all-purpose material [11]. The early observation of superconductivity in alkali metal-doped fullerenes [12], field-emission [13], and supercapacitance [14] from arrays of nanotubes, the extraordinary transport [9,10,15], electrical [16] and electro-mechanical [17,18] properties of graphene, and the unconventional magnetism of spongy carbon [19,20] are just a few examples of the vast areas of application of the most versatile among elemental materials. While fullerenes, nanotubes, and graphite layers aggregate through comparatively weak van der Waals forces, spongy carbon constitutes a fully covalent highly-connected three-dimensional (3D) form of sp^2 carbon, which combines many valuable properties of fullerenes, nanotubes and graphene with a robust 3D architecture. Triply periodic minimal surfaces [21,22] have been theoretically suggested as possible model structures for spongy carbon, which has since termed *schwarzite*, after the name of the mathematician Hermann Schwarz [23] who first investigated that class of surfaces.

Schwarzites synthesized by supersonic cluster beam deposition (SCBD) [4,24] are characterized by a nanometric porosity and, as suggested by numerical simulations of the TEM images [5], by the structure of a *random schwarzite* [21] which grows in the form of a *self-affine minimal surface* [25,26]. Thus, besides offering appealing technological perspectives, this novel material shows intriguing aspects of differential geometry and topology.

It is somewhat surprising that carbon schwarzites, despite their very interesting structural properties and viable applications in efficient supercapacitors [27] and field emitters [28-30], did not receive yet much attention. It is therefore convenient to spend first a few words about the growth method of carbon schwarzites by SCBD (Section 2), also because their growth and structural properties appear to be closely related to their topological features. After introducing some elementary concepts on the topology of sp^2 carbon forms, and illustrating the class of three-periodic P- and D-type schwarzites and the effects of self-affine distortion (Section 3), it is shown (Section 4) that the stability and growth of sp^2 carbon in the form of random schwarzites, rather than as nanotubes or fullerenes, is actually determined by simple initial topological conditions [5]. The surface minimality has direct implications on the growth kinetics, which may present a quasi-deterministic character. It is also shown that, unlike fullerenes where abutting five-fold rings are unfavoured, in schwarzites seven-fold rings tend to aggregate thus preventing the formation of

crystalline three-periodic structures. A calculation of the free energy of schwarzites including the entropic vibrational and configurational contributions allows to estimate the average porosity in thermal equilibrium as a function of the deposition energy (Section 5). The existing calculations of the electronic structure and electron-phonon interaction of the smallest schwarzites, and the possible links between certain topological features and the electronic properties, are discussed in Section 6. Finally the predictions of relevant structural, thermal and electronic properties based on quantum molecular dynamics simulations are briefly discussed in Section 7. The reader should be advised that present review is restricted to the small class of schwarzite structures which are accessible to quantum simulations and ab-initio calculations and may help understanding some features observed in spongy carbon. The vast number of sp^2 forms and fantastic structures which can be generated by complex mathematical algorithms and their intriguing topological aspects, though absolutely relevant for the analysis of the spongy forms of carbon and the future construction of regular architectures, are not discussed here, being found in the other chapters of this volume.

2. The birth of random schwarzites

Nanostructured sp^2 carbon-based solids represent a class of materials where the surface curvature and the structural organization on the nanometric scale, ranging from less than 1 nm to a few hundreds of nanometres, dramatically influence the mechanical, chemical and physical properties [31]. Porous carbon networks are of great importance in many areas of science and technology including catalysis, energy storage, chromatography, gas and liquid purification and molecular sieving [32,33]. The high specific surface area, chemical inertness and large pore volumes are the important parameters for these applications. The complexity of the carbon structure makes the control of the pore size and structure a difficult technological problem. Many synthetic techniques have been proposed for the production of meso- and macroporous carbon [32-35], but more intriguing is the creation of nanoparticles with a specific surface curvature which can be used to control the porosity of the material.

Total energy calculations show that carbon schwarzites are in general more stable than fullerenes with a similar absolute value of the Gaussian curvature [21,22,36]. Nevertheless schwarzite-like materials have not been observed during carbon-arc synthesis of fullerenes and nanotubes, suggesting that a new technique should be implemented for the production of such exotic carbon structures. An effective production technique for *random carbon schwarzites* was found to be a bottom-up approach based on the assembling of sp^2 nanometric clusters. This was achieved by

means of the Supersonic Cluster Beam Deposition (SCBD) of carbon clusters produced by a Pulsed Microplasma Cluster Source (PMCS) [37,38] and assembled onto a substrate.

The source chamber consists of a ceramic cavity hosting along a vertical axis two cylindrical electrodes separated by a gap a few millimeters wide. One of the electrodes, the cathode, is made of graphite and constitutes the target of a pulsed helium beam, which is injected into the source chamber through a solenoid valve along a horizontal axis. On the opposite side of the horizontal axis there is a nozzle which allows for the supersonic molecular beam expansion outside the source chamber into vacuum. The helium pulse directed against the graphite cathode is ionized, after a fixed delay of a few hundreds microseconds, by an intense pulsed discharge (V ~ 750 volts). The helium plasma ablates the cathode surface removing carbon atoms via sputtering; then cluster aggregation occurs at low temperature (T ~ 100 K) in the high pressure region in front of the cathode. These particular thermodynamic conditions allow for the formation of full sp^2 fullerene-like carbon clusters with a mass distribution peaked around 600 atoms/cluster [39]. Since in the supersonic cluster beam the spread in the kinetic energy per atom is much smaller than the atom binding energy, the clusters reach the substrate with their initial morphology and size distribution, thus leading to the synthesis of nanostructured pure sp^2 carbon films under controlled conditions [24,39,3]. It should be noted, however, that the carbon atoms impact the substrate surface with a translational kinetic energy of 0.1 to 0.4 eV/atom.

The film growth via SCBD can be viewed as a random stacking of particles as for ballistic deposition. The resulting material is characterized by a low density as compared to that of films assembled atom by atom and it shows different degrees of order depending on the scale of observation [24,39]. The characteristic length scales are determined by the deposition energy, the cluster dimensions and by their fate after deposition: Carbon cluster beams are characterized by the presence of a finite mass distribution and by the presence of isomers of different stability and reactivity. Once on the substrate, stable clusters can survive almost intact while reactive isomers can coalesce to form a more disordered phase [39,40]. A transmission electron microscope (TEM) analysis of nanostructured carbon films shows that, at this scale, the morphology is reminiscent of the precursor clusters [41,42]. TEM micrographs show the presence of an amorphous matrix with small closed shell particles and bundles of graphene sheets (Fig. 1). Large onion-like and tubular particles have also been observed..

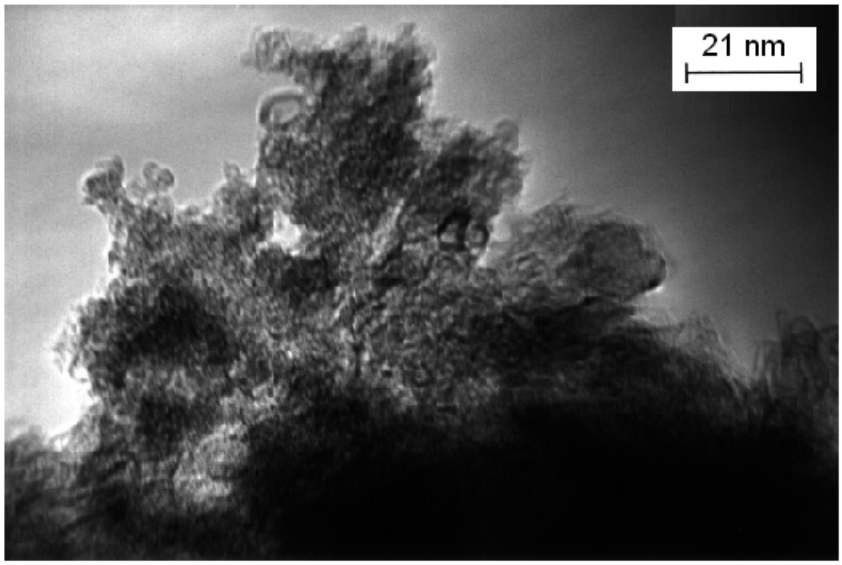

Fig. 1: TEM micrograph showing closed graphitic particles and graphene sheets dispersed among amorphous material (adapted from Ref. [41])

In the case of cluster assembling one should recall that, due to finite cluster mass distribution, relatively large clusters are somehow ‘‘diluted’’ among small particles. Large clusters can act as seeds for the formation of nodular defects, which evolve like isolated structures protruding from the average thin film surface. Depending on the initial density of defects, there is a critical film thickness where the nodular structures start to merge. These defects have a profound influence on the evolution of the surface morphology. Roughness, scale invariance, and spatial correlation of the film surface depend on the cluster precursor size and film thickness.. In general the surface spatial correlation and its dependence on the film thickness show the characters of a fractal self-affine growth [43]. The surface corrugation can be described by a function $h(\mathbf{r},t)$ expressing the height of the surface at position $\mathbf{r}$ with respect to the average surface plane, when the film has a thickness t. For a steady deposition rate, t can be interpreted as a time coordinate. At a given t the height-height correlation function is defined as

$$w(\mathbf{r},t) \equiv \sqrt{\left\langle \left[h(\mathbf{r}+\mathbf{r}',t)-h(\mathbf{r}',t)\right]^2 \right\rangle_{\mathbf{r}'}} \quad , \tag{1}$$

where the average is taken over all the surface positions $\mathbf{r}$’. For an isotropic surface this function

only depends on the distance $r \equiv |\mathbf{r}|$ and grows with r as long as it is smaller than a correlation length ξ, then it saturates to a value $w(\infty,t)$ which defines the *surface roughness* for a thickness t. Self-affinity is characterized by two power-laws [43]

$$w(r,t) \propto r^{\alpha}, \quad r << \xi \ , \tag{2}$$

$$w(\infty,t) \propto t^{\beta} \ , \tag{3}$$

which express a scale invariance in the directions normal and parallel to the growth direction through the *roughness exponent* α and the *growth exponent* β, respectively. The evolution of the roughness during deposition and the extension of spatial correlation on the surface plane turn out to be peculiar of the particular growth mechanism and largely independent of the nature of the physical system. In other words the growth mechanisms can be ascribed to certain universality classes with well defined exponents α and β. In SCBD experiments growing nanostructured carbon described in this chapter the exponents derived with atomic force microscopy (AFM) [44] are

$$\alpha = 0.66 \pm 0.02, \quad \beta = 0.50 \pm 0.03 \, . \tag{4}$$

These exponents can be ascribed to the class of processes described by the Kardar-Parisi-Zhang (KPZ) equation with spatially correlated noise (see [43], Chap. 22). They roughly agree also with the renormalization-group results for the isotropic growth model within the quenched noise regime ([43], Chap. 10).

Scale invariance is seen to extend over up to 3 decades in the thicker films. This allows to compare the results of molecular dynamics simulations, which necessarily are performed on the nanometric scale, to experiments made on a larger length scale. An example is shown in Fig. 3, where the calculated AFM image for a film obtained from a molecular dynamics simulation is compared to the AFM image of a real SCBD carbon film [25]. The morphology of the surface looks very similar in the two images, although the are obtained on length scales which differ by more than two orders of magnitude.

The typical correlation lengths ξ for films assembled by small clusters range from 50 nm to 7 nm. The lowest value refers to film where the density of nodular defects is low and their coalescence has not taken place. These films are very uniform and flat. Apart from isolated nodules, large structures are not present and consequently the correlation length closely reflects the size of the basic morphological units. As long as the morphology develops and larger and larger features appear,

correlation length increases. A similar behavior is seen for films assembled by large clusters and it is observed at considerably lower thickness.

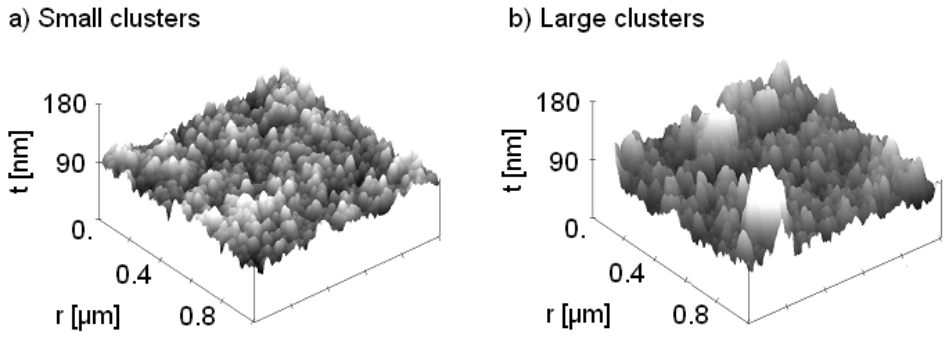

Fig. 2: The surface roughness of SCBD carbon films depends on the average size of the precursor clusters. It is defined by the height-height correlation function $w(r,t)$ which grows with the distance *r* as r^{α} for *r* much smaller than a correlation length ξ, and reaches a saturation value $w(\infty,t)$ for *r* >> ξ. The latter grows with the film thickness *t* as t^{β}. Experiment gives a *roughness exponent* $\alpha = 0.66 \pm 0.02 \cong \frac{2}{3}$ and a *growth exponent* $\beta = 0.50 \pm 0.03 \cong \frac{1}{2}$.

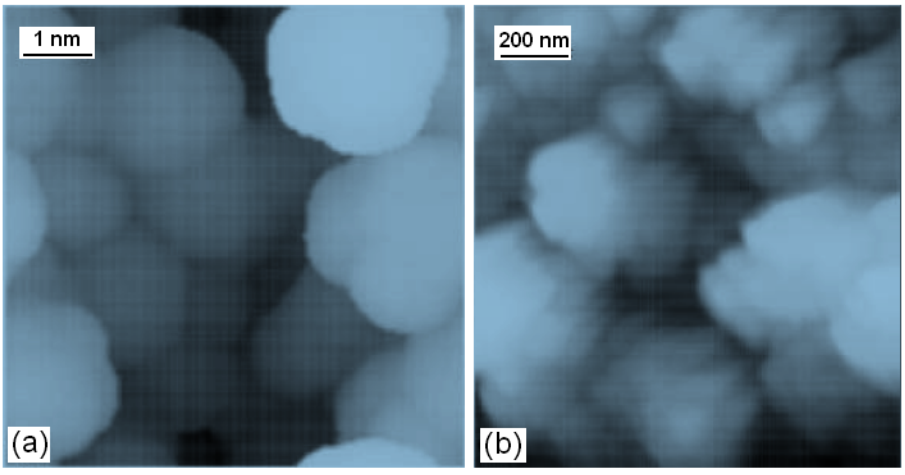

Fig. 3: Visual comparison of the simulated AFM image on the nanometric scale (a) with an experimental AFM image at the scale of 200 nm (b), as reported by Lenardi *et al.* [42] (adapted from Ref. [25]).

By adding a metal catalyst during the cluster formation, either by bubbling the He gas stream with a metallic precursors through a liquid metal-organic compound prior to the injection into the PMCS (Fig. 4(a)) or by using mixed cathodes, it is possible to control to some extent the cluster formation inside the source and the composition of the supersonic beam so as to obtain fairly pure schwarzitic structures (Fig. 4(b)). The metal-organic molecules in the buffer gas are cracked by the electric discharge, thus providing metal atoms and highly reactive radicals to the condensing carbon cloud. By using Molybdenum (V) isopropoxide $Mo(OC_3H_7)_5$ in isopropanol and Cobalt (II) methoxyethoxyde $Co(OCH_2CH_2OCH_3)$ in 2-methoxyethanol as catalysts and PMCS in the standard operational mode, it was possible to obtain spongy schwarzite-like carbon films like the one shown in the TEM picture of Fig.5. The material looks like a free-standing film made by several interconnected undulated foils (fig 1b). In high resolution scanning electron micrograph (fig. 1c), the contrast created by secondary electrons shows that voids are present in the bulk of the sample indicating that the material has a complex three-dimensional porous structure. The structure of spongy carbon consists of thin carbon layers (1-2 nm thick) interconnected to form a network with overall thickness up to micrometers. A crucial role is played by the metal-organic catalyst whose concentration and dispersion seem to determine the final curvature and morphology of the material [16].

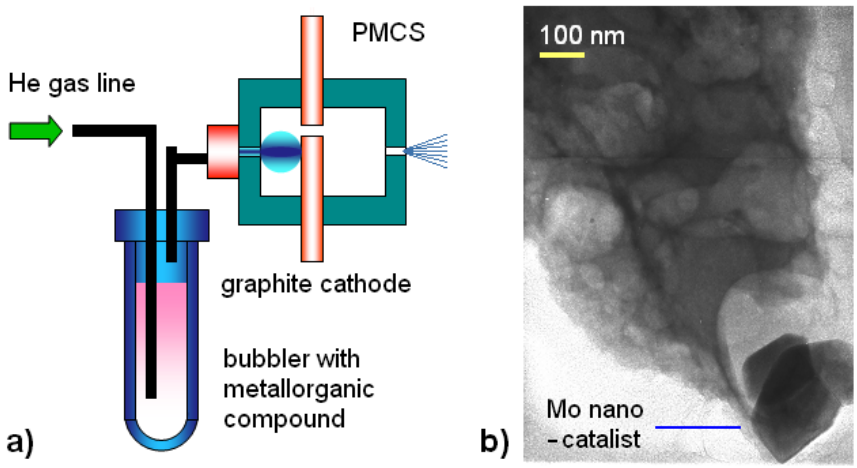

Fig. 4 Catalytic growth of carbon schwarzites can be obtained either by passing the carrier He gas through a bubbler containing a metallorganic compound (a) or by using a mixed electrode containing the needed amount of catalytic metal nanoparticles. (b) A schwarzites grows from a molybdenum catalyst nanoparticle, apparently as a self-affine structure with pore diameters increasing with the distance from the catalyst.

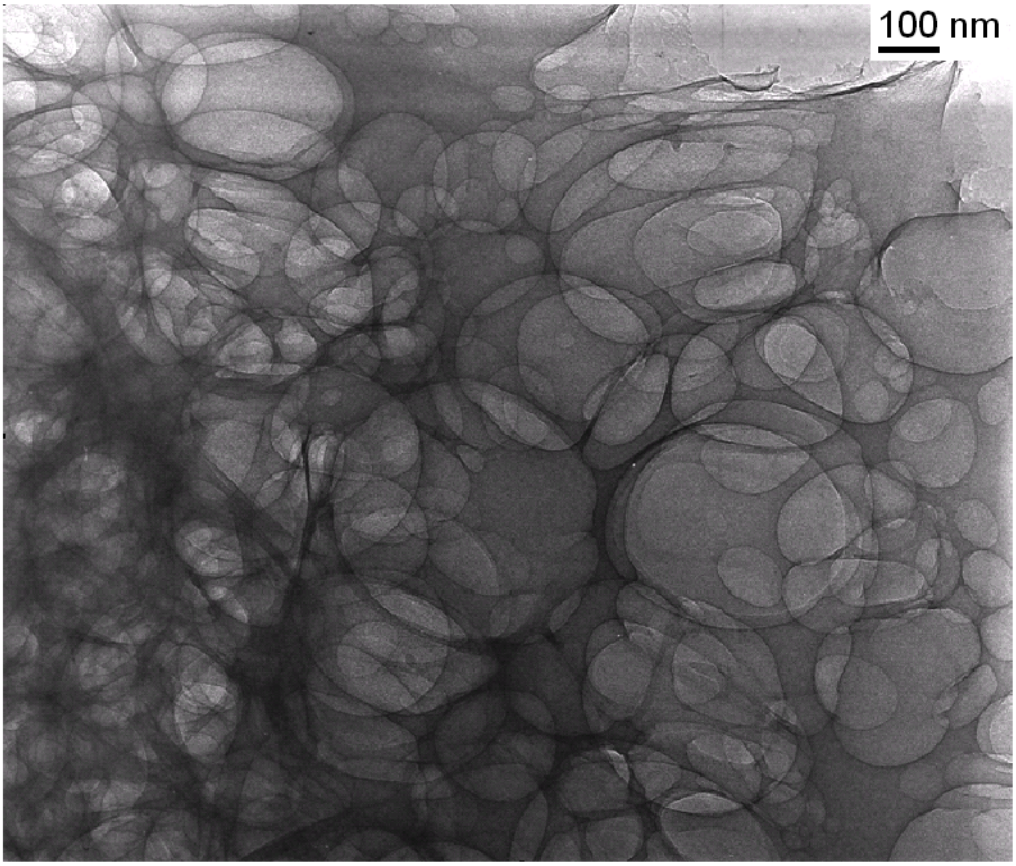

Fig. 5: A transmission electron microscope (TEM) image of a random carbon schwarzite obtained by supersonic cluster beam deposition with a deposition energy of 0.1 eV/atom [4]. Raman and near-edge x-ray absorption fine structure (NEXAFS) spectra indicate a pure sp^2 bonding structure, suggesting a single, highly connected graphene sheet with an average pore diameter in the range of 100 nm.

The formation of the spongy carbon is assisted by the presence of metal catalyst nanoparticles, as clearly appears in Fig. 4(b). The size, concentration and dispersion of catalyst nanoparticles are believed to determine the final morphology and curvature of the material. By comparing the material obtained with mixed cathodes with that obtained with metal-organics, it has been verified that the presence of large catalyst concentrations (several percent) in the form of relatively large clusters favours the production of carbon nanoparticles, whereas a finely dispersed catalyst at a low concentration drives the growth to the formation of spongy networks. Generally, the physical vapour deposition of carbon nanostructures uses mixed cathodes, which gives a high local concentration of catalyst particles. By changing the metallic precursors, it is also possible to control the

porosity of the material. For example, cobalt leads to networks of narrower pores than those formed with molybdenum. The spongy carbon obtained in this way consists of a fully sp^2 three-dimensional structure, as confirmed by Raman and near-edge x-ray absorption fine structure (NEXAFS) spectroscopy [4]. The TEM images (Fig. 5) suggested a topological structure like that of random schwarzites [21], characterized by a porosity in the range of 10^2 nm and by surface minimality.

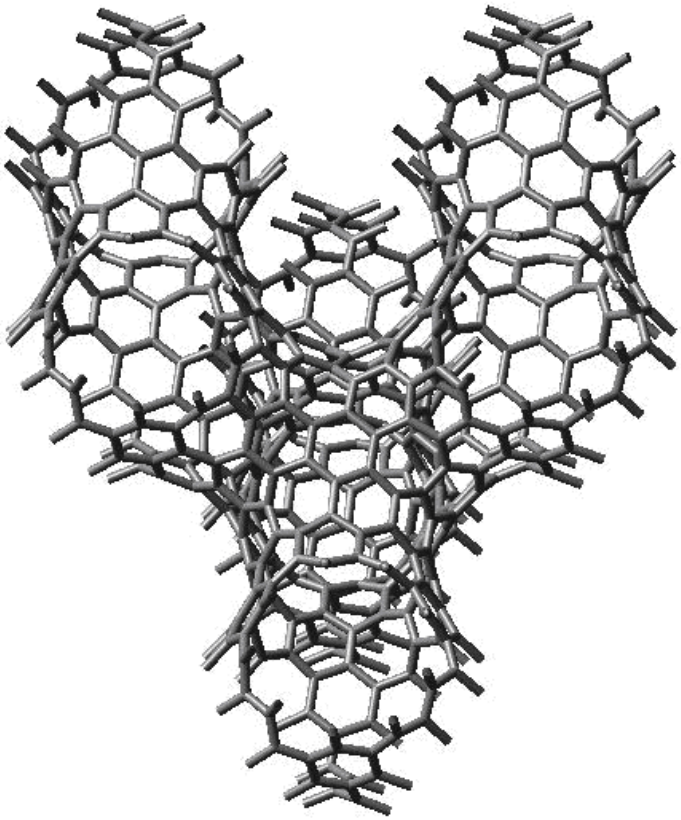

Fig. 6 The carbon schwarzite fcc-$(C_{84})_2$ obtained from a tiling with carbon hexagonal and heptagonal rings of a three-periodic D-type minimal surface [23]. The unit elements of a D-type schwarzite are centred at the sites of a diamond lattice. Each unit cell contains two elements and each element is made of 12 heptagons and any number h ($\neq$ 1) of hexagons. Here h = 28. This is the smallest schwarzite with non-abutting heptagons (equivalent to C_{60} which is the smallest fullerene with non-abutting pentagons and has h = 20). Ab-initio calculations show however that, unlike fullerens where abutting pentagons are less stable, in schwarzites abutting heptagons are more stable, which favours non-periodic schwarzites.

3. Schwarzite topology

The aim of this section is to show how topology alone can help one to predict the structure and some relevant physical properties of sp^2 carbon on the mesoscopic scale from parameters which are supposed to be known on the atomic scale, such as the bond strengths and the surface stiffness constants. A basic question is whether a graphite sheet can be transformed into a surface characterized by a negative Gauss curvature everywhere through the creation of a sufficient number of negative disclinations, which occur wherever a 6-membered ring is replaced by a larger ring. A special case of negative Gauss curvature occurs when the mean curvature is zero everywhere, which corresponds to a minimal surface. The conjecture that a minimal surface is particularly stable has stimulated much theoretical work on hypothetical graphite sheets (graphenes) with the structure of a periodic schwarzite (Fig. 6) [44-46]. Similar theoretical sp^2 carbon structures like polybenzenes [47], hollow graphites [48,49] and plomber's nightmares [36], which have been investigated theoretically, can be assigned to the general family of schwarzites.

From the topological point of view graphenes like fullerenes, graphite sheets, nanotubes and schwarzites are described as a polygonal tiling of the surface, where each vertex corresponds to a carbon atom, each edge to a covalent bond and each polygon to a carbon ring. Moreover each atom has a three-fold coordination. The surface covered by the polygonal tiling of carbon rings is characterized by its *connectivity* or order of connection *k*. According to Hilbert [50] the order of connection is the number plus one of the closed cuts which can be made on the given surface without breaking it apart in two pieces. The surface topology can be alternatively characterized either by the *Euler-Poincaré characteristic* χ or by the *genus g*, which are related each other and to *k* by the equations

$$\chi = 3 - k = 2(1 - g), \quad g = \frac{1}{2}(k - 1) = 1 - \frac{\chi}{2}. \tag{5}$$

For example a sphere, or the equivalent projective plane with one point at infinity, is split into two parts when cut along one single closed line and therefore $k = 1$ ($g = 0$, $\chi = 2$) (Fig. 7(a,b)). A simple (one-hole) torus, or a plane closed by cyclic boundary conditions, can be cut along two closed lines without splitting it in two pieces, whereas a third cut would split it apart, so that $k = 3$ ($\chi = 0$, $g = 1$) (Fig. 7(a,c)). Similarly for an *n*-hole torus $k = 1 + 2n$, $\chi = 2(1-n)$ and $g = n$ (Fig. 7(e)). Thus the genus represents the number of "holes" (or "handles") of a generalized torus. The notion of connectivity includes one-face surfaces, corresponding to even values of *k* (semi-integer *g*, odd χ):

the Möbius ring has $k = 2$ ($g = {}^1/_2$, $\chi = 1$) (Fig. 7(f)), the Klein bottle $k = 4$ ($g = {}^3/_2$, $\chi = -1$) (Fig. f(h)), and so on.

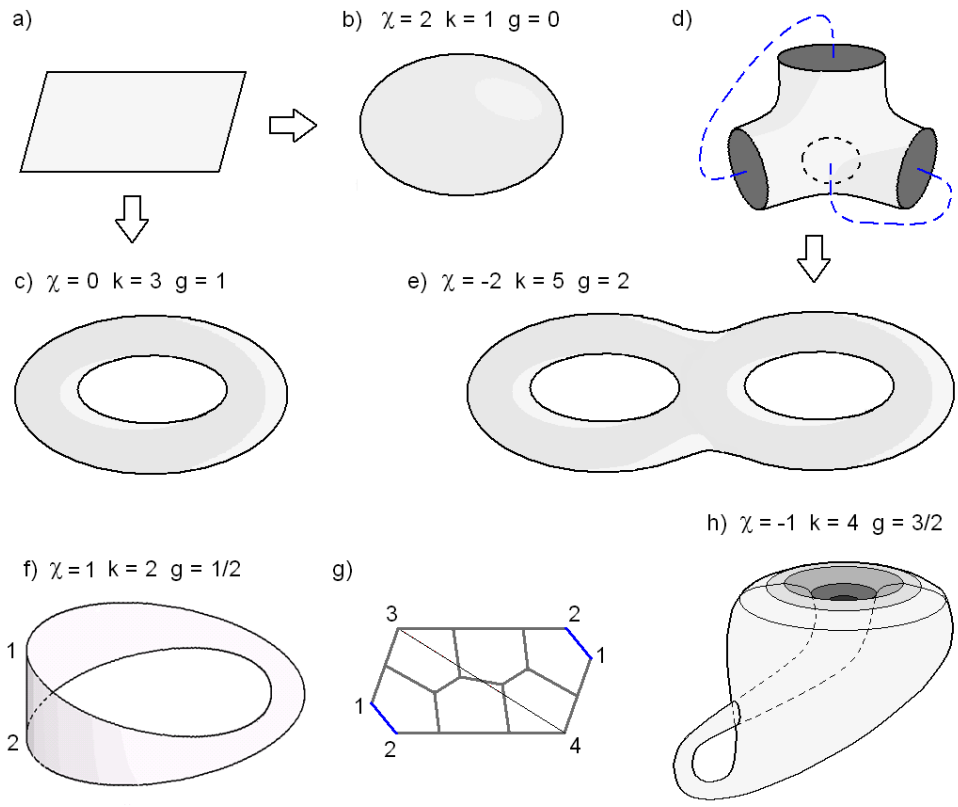

Fig. 7: Surfaces of different topology supporting sp^2 carbon. A graphene sheet (a) can be closed assuming either the topology of a sphere (fullerenes: b) or of a one-hole (-handle) torus (a nanotube with a cyclic boundary condition or a toroidal fullerene: c). The element of D-type schwarzite (d) after being closed on itself (brokel lines) is topologically equivalent to a two-hole (-handle) torus (e). In principle a closed sp^2 carbon form can extend over a one-face surface, like a Möbius ring (f) or a Klein bottle (h). Each form is identified by its Euler-Poincaré characteristic χ or equivalently by the connectivity k or genus g (see text). Within the restricted class of sp^2 carbon with only 6-, 5- and 7-rings, the tiling of these forms require a prevalence of 5- (7-) fold rings for positive (negative) χ. For the Möbius ring the saturation of all bonds implies a minimum tiling with seven 5-rings and one 7-rings (g).

While fullerenes are represented by a closed surface topologically equivalent to a sphere (k = 1), uncapped nanotubes, graphene sheets and schwarzites are open surfaces with an infinite extension in one, two or three dimensions, respectively. However sp^2 surfaces characterized by a periodic atomic structure can be reduced to a closed surface by applying cyclic boundary conditions. In this way uncapped nanotubes and graphene become topological equivalent to an ordinary (one-hole) torus (k = 3) (Fig. 7(a,b,c)). On the other hand periodic infinite surfaces like schwarzites would have an infinite connectivity. However, similarly to the procedure for crystalline lattices in solid state physics, cyclic boundary conditions may be applied on a finite portion of the periodic surface, so as to make k, g and χ finite and linearly dependent on the actual number of unit cells. It is therefore convenient to define the corresponding parameters for the unit cell, k_{cell} , g_{cell} and χ_{cell}. Their values are obtained by closing the portion of surface contained in the unit cell on itself as implied by the cyclic boundary conditions, and the number g_{cell} of handles generated by the closure operation gives $\chi_{cell} = 2(1- g_{cell})$ and $k_{cell} = 2\, g_{cell} + 1$.

For a three-periodic surface having the periodicity of the simple cubic lattice (P-type gyroid [21], Fig. 8(a)) the unit cell contains one element, whereas the one having the structure of the diamond lattice, (D-type gyroid [21], Fig 8(b)) has two elements per unit cell. The two elements may differ just for an inversion operation (as in diamond) or have a different size (as in the sphalerite lattice), but they are topologically identical since they coordinate the same number (four) of neighbor elements. In this case the closure operation may be applied to a single element (Fig. 7(d)), which gives $g_{el} = 2$ ($\chi_{el} = -2$ and $k_{el} = 5$), equivalent to that of a two-handle torus (Fig. 7(e)). Note that for both D- and P-type gyroids $g_{cell} = 3$ ($\chi_{cell} = \chi_{el} = -4$ and $k_{cell} = k_{el} = 7$). It is important to remark that the genus of a cell (e.g., a simulation cell, which may contain several unit cells of the lattice) is always less than the genus per element times the number of elements contained in the cell due to the internal connections.

The polygonal tiling of a surface is subject to Euler's theorem linking the numbers of atoms (v), of bonds (e) and of rings (f) to the connectivity by the equation [50], also known as Poincaré's formula:

$$\begin{aligned} v - e + f &= \chi \\ &= 3 - k = 2(1 - g) \end{aligned} \quad . \tag{6}$$

Note that for the three-fold coordination implied by sp^2 hybridization

$$e = \frac{3}{2} v \tag{7}$$

For periodic schwarzites it may be convenient to refer all quantities in Eq. (6) to the unit cell, or to the unit element, when a comparison is needed to closed sp^2 forms like fullerenes and capped nanotubes, whereas for the statistical arguments of the Sections Eq. (6) shall refer to a large number of unit cells with cyclyc boundary conditions. By calling f_n the number of n-membered rings (hereafter called n-rings) and inserting Eq. (7) into (6) it is found

$$6\chi = \sum_n (6-n) f_n \quad . \tag{8}$$

Note that this conditions on the numbers of different rings is *independent of the number of 6-rings*, which can therefore be any natural number (except 1).

Hereafter we shall restrict to the class of sp^2 structures with only 5-, 6- and 7-rings (5-6-7 class), unless the cases to schwarzites with 8- or 9-rings are explicitly stated. From the pure topological standpoint the extension to other possible structures with larger or smaller rings is indeed straightforward. For 5-6-7 structures it is

$$f_7 - f_5 = -6\chi \, . \tag{8}$$

For fullerenes ($\chi = 2$) with no 7-rings the well known result $f_5 = 12$ is obtained. For open nanotubes and graphene sheets $f_5 = f_7$: in perfect structures this number can be zero, whereas in defective graphene or nanotubes 5- and 7-rings always occurs in pairs, e.g., through the Stone-Wales transformation which converts four adjacent 6-rings into two 5-7 ring pairs. For D- and P-type schwarzites with no 5-rings $f_7 = 24$ in each unit cell ($f_7 = 12$ per element for the D-type schwarzite) (Fig. 8(a,b)) . The smallest D-type schwarzite in this class has twelve 7-rings per element and no 6-ring, which makes 28 atoms per element, to be compared with the smallest fullerene C_{20}. This schwarzite, denoted *fcc*-$(C_{28})_2$, together with the fullerene C_{20}, are examples of *platonic tiling,* made of only one kind of polygons. Larger D-type schwarzites of the 6-7 class are obtained by adding 6-rings and have the formula *fcc*-$(C_m)_2$ where $m = 28 + 2f_6$ ($f_6 \neq 1$) is the number of atoms per element, while the simple-cubic P-type schwarzites of the 6-7 class shall be denoted by *sc*-C_m with $m = 56 + 2f_6$. Schwarzites as well all fullerenes with two kinds of polygons are examples of *archimedean tiling*.

Equation 8 holds also for odd values of χ, i.e., for a steric distribution of bonds and rings lying on a one-face surface, e.g., a Möbius ring ($\chi = 1$, Fig. 7(f)). In this case $f_5 - f_7 = 6$. An

example of tiling is shown in Fig. 7(g), where the two edges 1-2 are supposed to be joined and a bond 3-4 is added. With the rule that adjacent rings have only one edge in common, the bond distribution of Fig. 7(g) yields $f_5 = 7$ and $f_7 = 1$.

D-type schwarzites of the 6-8 class have, according to Eq. (7), six 8-rings per element and the general formula *fcc*-$(C_l)_2$ with $l = 16 + 2f_6$ ($f_6 \neq 1$). The smallest (platonic) form has 16 atoms per element. The polybenzenes studied by O'Keeffe *et al* [47] belong to this class and are obtained by inserting one 6-ring in each plane normal to a three-fold {111} axis. Another example, obtained by the insertion of three 6-rings in each plane normal to a {111} axis – altogether 24 6-rings to give *fcc*-$(C_{64})_2$ – is briefly discussed in Sec. 6. According to Eq. (7), also schwarzites of the 6-9 class can exist, the smallest of which is made of four 9-rings and 12 atoms per element. The general formula is *fcc*-$(C_j)_2$ with $j = 12 + 2f_6$ ($f_6 \neq 1$). To our best knowledge no specific study on the stability of these structures is available.

The minimal gyroid surfaces which support the above schwarzite structures can be analytically described by the Weierstrass-Enneper representation in the complex plane [52,53]. The P- and D-type gyroids are just two special cases, where one can be continuously transformed into the other by the Bonnet transformation [52]. Thus the simulations of TEM images with deformed P- or D-type gyroids, discussed in the next Section, can be easily extended to any intermediate case obtained by a bonnet transformation. The shapes of P- and D-type gyroids (Fig. 8(a,b)) are well approximated by the lowest terms of a Fourier expansion as

$$\cos x + \cos y + \cos z = 0\,, \tag{9}$$

$$\cos x \cos y \cos z + \sin x \sin y \sin z = 1\,, \tag{10}$$

respectively, where the coordinates x, y, z are in units of some conventional length, say $a_0 = 1$ nm.

The spongy carbon structures like those shown in Figs. 4(b) and (5) are examples of random schwarzites, which can be obtained from a numerical simulation, as done, e.g., by Lenosky *et al* [21,22]. Another method to generate images of apparently random schwarzites is to simulate their growth processes by applying to a three-periodic gyroid surface a continuous scale change along the growth direction (z axis), so as to mimic the observed self-affinity. This can be done for a P-type schwarzite by introducing in Eq. (9) a scaling factor z^{β} so as to give a distorted surface obeying the equation

$$\cos(xz^{-\beta}) + \cos(yz^{-\beta}) + \cos(\frac{z^{1-\beta}}{1-\beta}) = 0\,, \tag{11}$$

with $\beta = {}^{1}/_{2}$ taken from experiment. A comparison of a portion of the TEM image of Fig. 5 with a portion of the surface given by Eq. (9) plotted with a contrast and field depth similar to that of the TEM image is shown in Fig. 9; a similar comparison between another portion of the TEM image and a small part of two compenetrating distorted D-type schwarzites is shown in Fig. 10. A visually similar image could be obtained with a single D-type surface with a longer field depth. There is a clear visual resemblance between the experiment and the distorted P-type simulation, whereas the comparison with the image of the compenetrating D-type surfaces is less convincing. The latter, however, shows certain quasi-circular features which are seen in the TEM image but not in the P-type simulation.

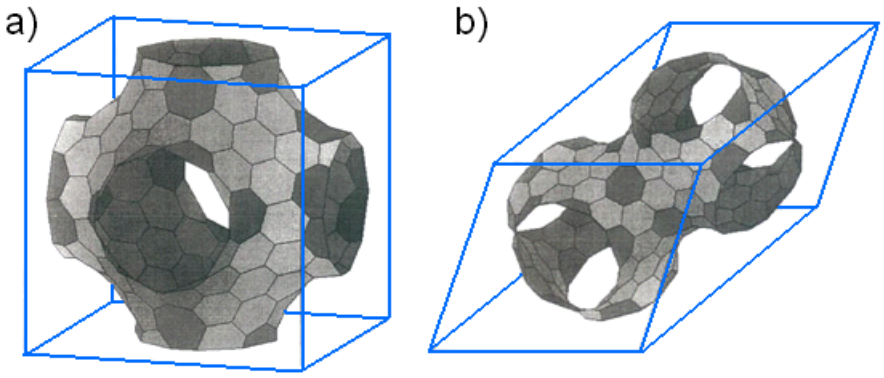

Fig. 8: The tiling with 6- (light grey) and 7- (dark grey) rings of the unit cell of a P-type (a) and D-type (b) schwarzite, both having 216 atoms per unit cell. The 7-rings are 24 per unit cell in both cases. The unit cell of the D-type schwarzite is made of two identical but inequivalent elements, containing twelve 7-rings each, joined in the staggered position as atoms are in the diamond lattice (adapted from Ref. [21]).

A brief discussing on whether the scale distortion preserves minimality is in order. The minimality condition for a surface represented by the equation $x = x(y,z)$ is fulfilled when [51]

$$[1+\left(\frac{\partial x}{\partial z}\right)^2]\frac{\partial^2 x}{\partial y^2} - 2\frac{\partial x}{\partial y}\frac{\partial x}{\partial z}\frac{\partial^2 x}{\partial y \partial z} + [1+\left(\frac{\partial x}{\partial y}\right)^2]\frac{\partial^2 x}{\partial z^2} = 0\,, \qquad (12)$$

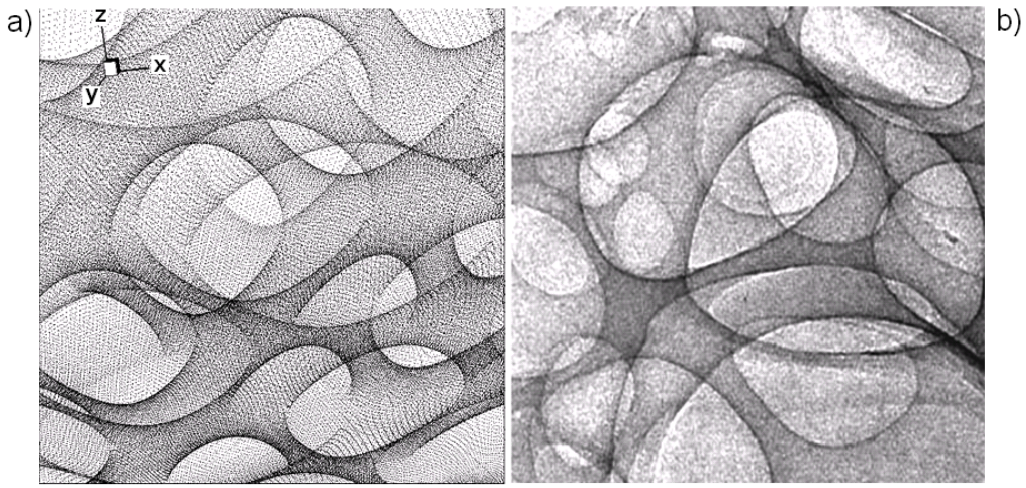

Fig. 9: Comparison between a portion of a distorted ($\beta = {}^{1}/_{2}$) P-type schwarzite, Eq. 11 (a) and of a random carbon schwarzite as observed by TEM (b). The contrast of the simulated image has been chosen so as to give a field depth comparable to that of the TEM image (from Ref. [4]).

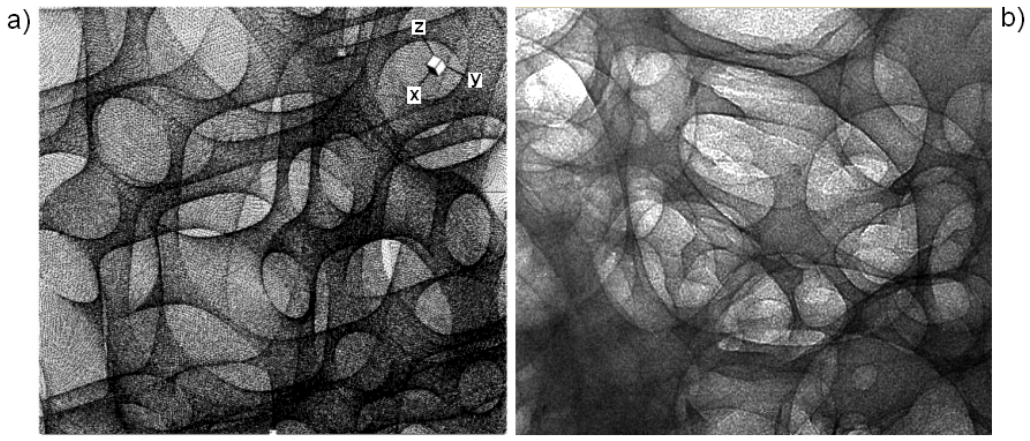

Fig. 10: Comparison between a portion of two compenetrating distorted ($\beta = {}^{1}/_{2}$) D-type schwarzites (a) and another portion of a random carbon schwarzite as observed by TEM (b). The contrast of the simulated image has been chosen so as to give a field depth comparable to that of the TEM image. A similar correspondence would be obtained with a single distorted D-type surface with either longer field depth.

which corresponds to a vanishing mean curvature at any point of the surface. The transformation in Eq. (11), defined by

$$x' = xz^{-\beta}, \quad y' = yz^{-\beta}, \quad z' = z^{1-\beta}/(1-\beta) \tag{13}$$

is seen to violate Eq. (12) by terms of order β/z because

$$\frac{\partial x}{\partial y} = \frac{\partial x'}{\partial y'}, \qquad \frac{\partial x}{\partial z} = \frac{\partial x'}{\partial z'} + o(\beta z^{-1}), \qquad \frac{\partial^2 x}{\partial y^2} = \frac{\partial^2 x'}{\partial y'^2} z^{-\beta}, \tag{14}$$

$$\frac{\partial^2 x}{\partial z^2} = \frac{\partial^2 x'}{\partial z'^2} z^{-\beta} + o(\beta z^{-1}) z^{-\beta}, \quad \frac{\partial^2 x}{\partial y \partial z} = \frac{\partial^2 x'}{\partial y' \partial z'} z^{-\beta} + o(\beta z^{-1}) z^{-\beta}, \tag{15}$$

whereas the principal curvatures decrease like $z^{-\beta}$. Thus for $\beta < 1$ the minimality condition is slowly recovered in the distorted schwarzite model at sufficiently large z.

4. *Schwarzite stability*

Once established the forms of pure sp^2 carbon which are allowed by topology, the second general question is under which conditions schwarzites, rather than to nanotubes or fullerenes, are produced in a catalyzed SCBD experiments. To answer this question one needs first to consider the total energy of a curved single-walled sp^2 carbon as a function of its geometry. In a previous study [5] it has been suggested that a good approximation to the total energy of sp^2 carbon surfaces is provided by the Helfrich's form for membranes and foams [54,55,52]:

$$E = \int_A dA\,(\gamma + \kappa H^2 - \bar{\kappa} K), \tag{16}$$

where A is the (portion of the) surface which the total energy refers to,

$$H = \frac{1}{2}\left(\frac{1}{R_1} + \frac{1}{R_2}\right), \qquad K = \frac{1}{R_1 R_2} \tag{17}$$

are the mean and gaussian curvatures, respectively, with R_1 and R_2 the principal radii of curvature, $\gamma = 2.82$ eV/Å^2 is the energy for unitary *flat* surface (a graphene sheet) [56], κ and $\bar{\kappa}$ are

stiffness constants associated with cylindrical and elliptical/hyperbolic deformations of the surface, respectively.

There is an important link between the topological features of the sp^2 structures and the geometry of the supporting surfaces, established by one of the greatest results of differential geometry, the Gauss-Bonnet theorem [51]. A corollary of this theorem states that *for any closed orientable surface S of genus g for which a representation of class $r \geq 3$ exists the surface integral of the Gaussian curvature K is given by*

$$\int_A K \, dA = 2\pi\chi \, . \tag{18}$$

Minimal surfaces are characterized by $R_1 = -R_2$ at all positions, and therefore the their total energy of a schwarzite is readily obtained from Eq. (18) as

$$E_{schw} = \gamma A + 2\pi\chi\bar{\kappa} \, . \tag{19}$$

Density functional (DF) calculations for single-walled nanotubes of variable radius [56,57], and C_{60} [56] yield for all structures about the same stiffness constants: $\kappa \cong 3.1$ eV and $\bar{\kappa} \cong 1.7$ eV . Other calculations for graphene [17,58] and nanotubes [59] give κ ranging from 2.80 to 2.92 eV. Consistently a value of $\bar{\kappa} = 1.5$ eV can be extracted by means of Eq. (19) from the available calculations of the cohesive energy of schwarzites [21,36,47,60]. This shows that the Helfrich's form for the total energy approximately holds also for all forms of pure sp^2 carbon with universal values of the stiffness constants.

The total energy expressed by Eq. (16) has the important property, if $\bar{\kappa}$ is constant, of having *a stable local minimum for a minimal surface*, since for $\kappa > 0$ the integral on H^2 is always positive unless $H = 0$, while the integral over the Gaussian curvature K is, according to Gauss-Bonnet theorem, independent of any small continuous deformation of the surface. Thus sp^2 carbon taking the shape of a minimal surface like schwarzites are stable forms (up to effects of the contour where $\bar{\kappa}$ may change, as discussed below). If the negative disclinations yielding a negative Gauss curvature are exclusively due to heptagons, the number of disclinations N_d is fixed by the Euler-Poincaré characteristic as $N_d = 6(2-\chi)$ independently of the length scale of the surface [61].

For a free-standing surface the stiffness constants κ and $\bar{\kappa}$ exclusively depend on the electronic structure associated with the sp^2 hybridization, but they can be modified locally at the edges of the carbon surface or along the line where it docks at the substrate or, more significantly, at a catalyst nanoparticle. It is argued that such local values of κ and $\bar{\kappa}$, and the initial values of the

curvature radii as determined by any local geometric constrain may give general indications about whether the growth process of sp^2 carbon will preferentially lead to fullerenes, nanotubes or schwarzites. A local energy minimum implies a relationship between the ratios of the curvature radii and of the stiffness constants:

$$\frac{R_1}{R_2} = \frac{2\bar{\kappa}}{\kappa} - 1 . \tag{20}$$

The surface deformation energy densities for (spherical) fullerenes ($R_1 = R_2 \equiv R$), nanotubes ($R_1 \equiv R$, $R_2 \rightarrow \infty$) and schwarzites ($R_1 = -R_2 \equiv R$) are $(\kappa - \bar{\kappa})/R^2$, $\kappa/4R^2$ and $\bar{\kappa}/R^2$, respectively, and therefore for any given R_1 the values of κ and $\bar{\kappa}$ define three different topological domains: schwarzites are favored for $\bar{\kappa} < \frac{1}{4}\kappa$, nanotubes for $\frac{1}{4}\kappa < \bar{\kappa} < \frac{3}{4}\kappa$ and fullerenes for $\bar{\kappa} > \frac{3}{4}\kappa$ (Fig. 11). In each domain the surface energy minimum lines are $\bar{\kappa} = \kappa$ for spherical fullerenes, $\bar{\kappa} = \kappa/2$ for nanotubes (Fig. 11, broken lines) and $\bar{\kappa} = 0$ for schwarzites. The calculated values of $\bar{\kappa}$ and κ (Fig. 11, red cross) fall in the nanotube/graphene domain close to the surface energy minimum, and are therefore more likely to occur.

It should be remarked that the local values of $\bar{\kappa}$ and κ, either at the surface termination into vacuum, where the growth takes place by cluster addition, or at the contact with a catalyst, are likely to be different from the calculated values for the free-standing structures. One should consider that the local change in the electronic structure, e.g., a π bond-charge depletion or accretion, can substantially modify $\bar{\kappa}$. The charge redistribution produced by a catalyst depends on the actual size of catalyst nanoparticles, which may explain why the growth of schwarzites supersedes that of nanotubes when metallorganic precursors are used. In this case the metallic particles are in general very small and highly dispersed. Another important remark is that once the growth has started in one domain it is very unlikely that the system jumps into another domain since this would require, for *topological reasons*, a prohibitive reshuffling of bonds. For example, jumping from the fullerenes (schwarzite) to the nanotube domain implies the annihilation of twelve 5- (7-) membered rings, which makes the energy hills between valleys rather high.

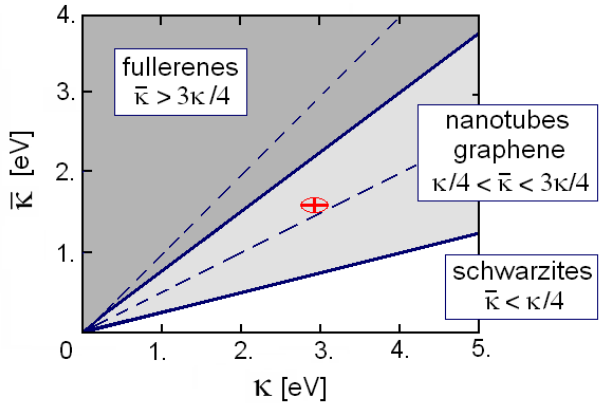

Fig. 11: The stability regions of sp^2 carbon surfaces as functions of the two stiffness constants. The broken lines indicate the minima of the surface energy for quasi-spherical fullerenes and nanotubes. The minimum surface energy for schwarzites would occur at $\bar{\kappa} = 0$.

According to this picture an initial $\bar{\kappa} < ¼\kappa$ at the catalyst-carbon contact line determines the growth of a schwarzite, which continues despite the gradual change of the ratio $\bar{\kappa}/\kappa$. It may be thought that during the sequential addition of fragments to the edge of the growing schwarzite atoms adjust so as to fulfill as much as possible the minimality condition $R_1 = -R_2$, which means to keep as close as possible to the bottom of the surface energy valley. Would the local properties $H = 0$ be exactly fulfilled at each addition of material, the growth could be viewed in this particular case as a deterministic process with the minimum production of entropy. This descends directly from the beautiful Euler theorem linking an extensive property, such as the area of a surface, to an intensive one, the differential conditions $H = 0$ (i.e., Eq. (12)), and may apply to any other physical problem whose total (free) energy minimum can be represented by the area of a minimal surface.

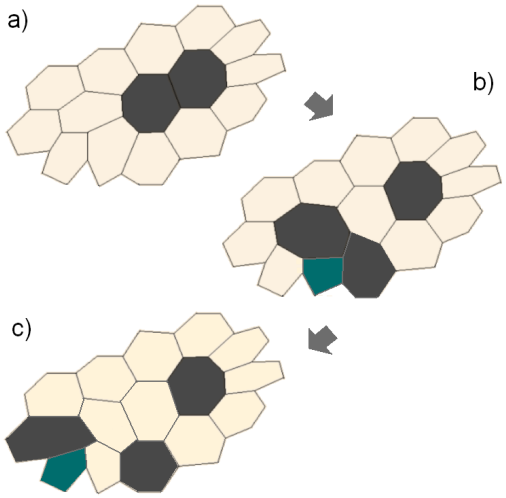

Fig. 12: Two abutting 7-rings (a, dark polygons) are separated by a re-shuffling of bonds at the cost of the creation of a 5-7 ring pair (b,c; dark-green pair of polygons). This occurs within a small schwarzite region with no change of its contour. When two 5-7 ring pairs generated in two different regions get adjacent they can annihilate each other through a Stone-Wales transformation, leaving four 6-rings. The net result is a migration of a 7-ring.

These arguments only tell about the topology of the growing structures with no information about shape, order and symmetries. This requires a thermodynamic approach where the appropriate thermodynamic potential is considered. The ordering depends very much on the mutual interactions between rings of different sizes. In fullerenes abutting 5-rings are not favored; it may be said that they repel each other, which makes the single isomer of C_{60} with no abutting 5-rings particularly stable, beautifully ordered and highly symmetrical. On the other hand total energy calculations on schwarzites [60,62] show that the bond energy between two 7-rings is ε_{77} = -5.107 eV, between a 6- and a 7-ring ε_{67} = -5.181 eV and between two 6-rings ε_{66} = -5.587 eV. Thus the separation of two abutting 7-rings costs 0.332 eV and therefore abutting 7-rings are favored. Figure 12 shows a small region of a schwarzite where some re-shuffling of bonds leads to the separation of two initially abutting 7-fold rings with no change of the contour. This costs the formation of a 5-7 ring pair. However two 5-7 ring pairs formed in two different regions of the sample which become adjacent can annihilate through a Stone-Wales transformation leaving four 6-rings. The net result is a separation of two 7-rings. This process, however, is energetically less favored than the coalescence of two separated 7-rings, which may explain why random schwarzites seem to be more likely than

well ordered three-periodic structures. The bond re-shuffling implies however a change of configurational entropy, which requires some further discussion.

5. Thermodynamics

As a simple example, the configurational entropy associated with all possible distributions of a fixed number f_7 of 7-rings in a schwarzite of given χ can be estimated for a restricted class of schwarzites, for example for the D-type ($\chi_{el} = -2$). The number of possible configurations is given by the number of isomers within this restricted class. The calculation for the smallest D-type schwarzites ($(C_{28})_2$ to $(C_{40})_2$) has been approached in Ref. [62] by adapting to schwarzite elements the spiral sequencing method originally developed for fullerenes by Manolopoulos, Fowler *et al* [63-69] for the enumeration of isomers and spectral analysis. The results for small schwarzites can be extrapolated to larger samples by means of some simple combinatorial argument subject to the further restriction that the D-type elements are connected by six-atom necks, so that an isolated element only contains 6- and 7-rings. This is clearly a crude approximation with retains however a tutorial value and is worth discussing here. For a D-type element of fcc-$(C_m)_2$ with $f_{6,el} \equiv (m-28)/2$ and $f_{7,el} = 12$, the number $W_{el}(f_{6,el})$ of isomers per element grows like the number of combinations of 7- and 6-rings (the latter being $f_{6,el} + 2$ for including one half of the four necks), divided by the number of permutations of the four necks, by the number (3) of possible ways of closing the element on itself (Fig. 7(d)) and by 2, since the distinction between the internal and external surfaces of a schwarzite (extroversion isomery) is irrelevant. This gives

$$W_{el}(f_{6,el}) \approx \frac{1}{144}\binom{14 + f_{6,el}}{12} \tag{21}$$

For example, for $f_{6,el} = 2, 4, 6$ Eq. (21) gives $W_{el}(f_{6,el}) = 12, 128, 874$ which compare fairly well with the exact figures 11, 125 and 893 [62].

Consider now a D-type schwarzite of N elements closed by cyclic boundary conditions. It has has a Euler-Poicaré characteristic $\chi = -2(N-1)$ and a total area $A = N(f_{6,el}A_6 + 12A_7)$, where A_n is the area of an n-ring. The total number of configurations is then $W = (W_{el})^N$, which gives an entropic contribution

$$S_c / k_B = \ln W = (1 + \frac{1}{2}|\chi|)\, \ln W_{el}(f_{6,el})\,. \tag{22}$$

By introducing via the Gauss-Bonnet theorem, Eq. (18), the average Gauss curvature

$$\overline{K} \equiv 2\pi\chi / A \tag{23}$$

and assuming a constant area and temperature T, the corresponding (configurational) Helmholtz free energy per unit area can be written via Eq. (19) as

$$\frac{F_c}{A} = \gamma + \bar{\kappa}\left|\overline{K}\right| - \frac{k_B T}{f_{6,el} A_6 + 12 A_7} \ln W_{el}(f_{6,el}) \ . \tag{24}$$

Since the mean pore radius $\overline{R} = \overline{G}^{-1/2}$ depends on the number of 6-rings, one can obtain $\overline{R}$ at thermal equilibrium by setting $(\partial F_c / \partial f_{6,el})_{A,T} = 0$, which gives for large $f_{6,el}$ and $\beta \equiv 1/k_B T$:

$$f_{6,el} \approx \exp(\beta \pi \bar{\kappa} / 3), \qquad \overline{R} \approx (A_6 / 4\pi)^{1/2} \exp(\beta \pi \bar{\kappa} / 6). \tag{25}$$

These equations show that for increasing temperature $\overline{R}$ decreases which means that the porosity increases. The present equilibrium description can hardly adapt to the SCBD process, unless it is assumed that at the spot hit by the beam there is a defined average temperature proportional to the flux and to the energy per atom. Although the travelling clusters in the supersonic beam are very cold, at the impact on the surface their translational kinetic energy shares among all degrees of freedom. Thus the vibrational contribution to the free energy has to be added. This amounts to [70]

$$\frac{F_v}{A} = \frac{k_B T}{f_{6,el} A_6 + 12 A_7} \sum_{j=1}^{3k} [x_j \coth x_j - \ln(2 \sinh x_j)], \qquad x_j \equiv \tfrac{1}{2} \beta \hbar \omega_j , \tag{26}$$

where $\hbar\omega_j$ are the phonon energies of an element. Since only sums over the whole phonon spectrum are of interest in the present discussion, the same average set of frequencies is used for all elements, and the four elements coordinated by the central one are assumed to be rigid. The last condition ensures a finite energy for all the acoustic modes of the whole schwarzite, whose branches are replaced by the respective top energies. This treatment of the acoustic modes is similar to a Debye approximation, which works quite well in the calculation of thermodynamic functions at comparably high temperatures as in the present case.

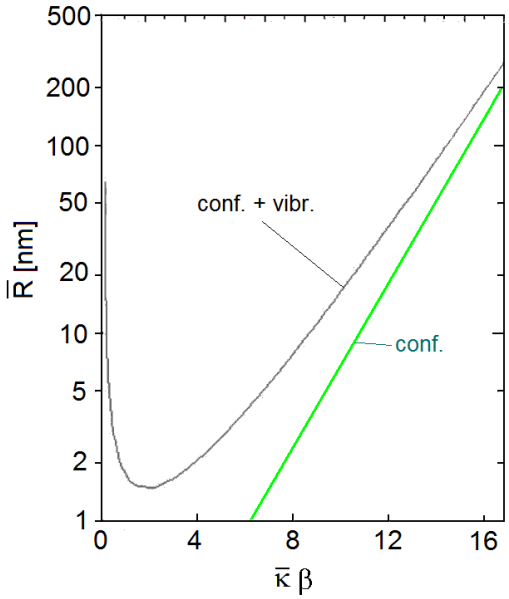

Fig. 13. Mean radius (on a logarithmic scale) of the pores of a d-type schwarzite with a random distribution of the twelve 7-rings per element calculated as a function of the dimensionless parameter $\bar{\kappa}\beta = \bar{\kappa} / k_B T$ temperature from the Helmholtz free energy including both configurational and vibrational contributions (curve) or the configurational contribution only (straight line). When phonon contributions are included the mean radius shows a minimum of about 15 nm for $T \cong \bar{\kappa} / 2k_B$ and a rapid increase above this temperature. According to molecular dynamics simulations this behaviour can be interpreted as due to a rapid graphitization that schwarzite undergoes above 3500 K, before melting. This temperature corresponds to $\bar{\kappa}$ ≅ 0.6 eV which is less than one half of the ab-initio value but falls into the schwarzite domain (Fig.11).

The phonon spectrum has been calculated for the smallest D-type schwarzites with a simple nearest-neighbour force constant model with radial and shear force constants [71], which are taken the same for all bonds and equal to those of graphite [72]. In this case the dynamical matrics can be block-diagonalized into three adjacency matrices [65,66,68,71] whose eigenvalues give the phonon energies for the different polarizations. Model force constants for sp^2 carbon given as functions of the bond length are available for a more precise calculation of the phonon energies [73] This however is not needed at the level of approximation adopted in this discussion.

Figure 13 displays the mean pore radius calculated as a function of the dimensionless parameter $\overline{\kappa}\beta = \overline{\kappa}/k_B T$ from the Helmholtz free energy including both configurational and vibrational contributions (curve) or the configurational contribution only (straight line). When the phonon contributions are included the mean radius shows a minimum for $T \cong \overline{\kappa}/2k_B$ corresponding to about 15 nm, and a rapid increase above this temperature. According to molecular dynamics simulations described below this behaviour can be interpreted as due to a rapid graphitization that schwarzite undergoes above 3500 K, before melting. This temperature corresponds to $\overline{\kappa} \cong 0.6$ eV which is less than one half of the ab-initio value but falls into the schwarzite domain (Fig.11). It is also noted that the experimental schwarzite shown in Fig. 5 has pore radii in the range of 100 nm, which corresponds to a formation temperature of 500 K for $\overline{\kappa} \cong 0.6$ eV or 1170 K for $\overline{\kappa} \cong 1.4$ eV. Both values are reasonable in view of the fact that the incident energy per atom, initially associated with one translational degree of freedom, is subsequently distributed over the three vibrational degrees of freedom of each atom. For the present example the vibrational contribution was calculated for a single element size corresponding to $m = 36$ [71]; for consistency a larger element should have been used so as to have a mean curvature radius corresponding to the minimum $\overline{R}$. Nevertheless the molecular dynamics simulations of the thermal evolution of a three-periodic schwarzite qualitatively confirm the present analysis.

In principle the present model can be extended to the case of self-affinity It si found [26] that mean Gauss curvature decreases for increasing thickness t as [26]

$$\left|\overline{K}\right| = \left|\overline{K}_o\right| \frac{1+\beta}{1-\beta} t^{-2\beta} \quad , \tag{27}$$

and $\overline{K}_o$ is the average initial Gauss curvature. Thus for the quasi-equilibrium growth regime discussed above the mean pore radius from the pure configurational part, Eq. (25), is corrected by a factor $\sqrt{(1-\beta)/(1+\beta)}t^{\beta} \approx t^{\beta}/\sqrt{3}$.

6. Electronic structure and electron-phonon interaction

Like nanotubes, schwarzites are either metals or insulators, depending on the topological structure and element size. Tight-binding calculations of the band structure have been performed for the smallest D-type schwarzites *fcc*-$(C_m)_2$ of tetrahedral symmetry (m = 28, 36 and 40) [60,74,75].

More recent *ab-initio* calculations of the electronic band structure of *fcc*-$(C_{28})_2$ are also available [76]. The structure of *fcc*-$(C_{28})_2$ exists in two enantiomers of opposite chirality (Fig. 14(a,b)), having however the same band structure (Fig. 14(c)). As also seen in the density of electron states (DOS) (Fig. 14(d)), rather large gaps occur between the valence as well as between the conduction bands. The Fermi level (E_F) crosses the lowest conduction band, which confers to fcc-$(C_{28})_2$ a metallic character. The DOS's of the next tetrahedral schwarzites *fcc*-$(C_{36})_2$ and *fcc*-$(C_{40})_2$ as obtained by tight-binding calculations [60] are displayed in Fig. 15. The occurrence of many sharp peaks in the DOS of both schwarzites is indicative of rather flat bands due to the existence of localized electronic states within each element, notably at the 7-rings.

Table I: Cohesive energy per atom (E_{coh}), density, bulk modulus (B), bond strength (b) and conductive property for the smallest D-type schwarzites with tetrahedral symmetry, as compared to fullerite and diamond [60,74,75].

D-type schwarzite	E_{coh} (eV/atom)	Density (g/cm^3)	B (Mbar)	b (Mbar Å^3)	
fcc-$(C_{28})_2$	-7.66	1.33	1.58	16.12	metal
fcc-$(C_{36})_2$	-7.71	1.05	1.26	16.20	insulator
fcc-$(C_{40})_2$	-7.92	1.60	1.92	16.25	metal
fullerite	-7.99	1.71	0.14	-	insulator
diamond	-8.36	3.52	4.42	16.71	insulator

There is an interesting alternation in the conducting properties: while *fcc*-$(C_{28})_2$ is metallic, the next one, *fcc*-$(C_{36})_2$, having four 6-rings per element, is an insulator and *fcc*-$(C_{40})_2$, with six 6-rings per elements, is metallic. For increasing m larger and larger portions of the surface acquire a graphene-like structure with, however, a slight negative Gaussian curvature, similar to graphene subject to a shear strain. The effects of a shear strain on the electronic structure of graphene have been theoretically investigated in a recent paper by Cocco *et al* [77], who show that a shear strain

opens a gap at the Dirac points, with the intriguing consequence that a band-gap engineering based on the application of suitable stress field would be possible [77]. The data of Table I show that schwarzites are particularly stable, with a cohesive energy per atom which rapidly increases in absolute value, tending for large m to that of diamond and graphite. The density is comparatively low and oscillating with m, but must tend to zero for $m \rightarrow \infty$ as expected for a two-dimensional surface filling a three-dimensional space.

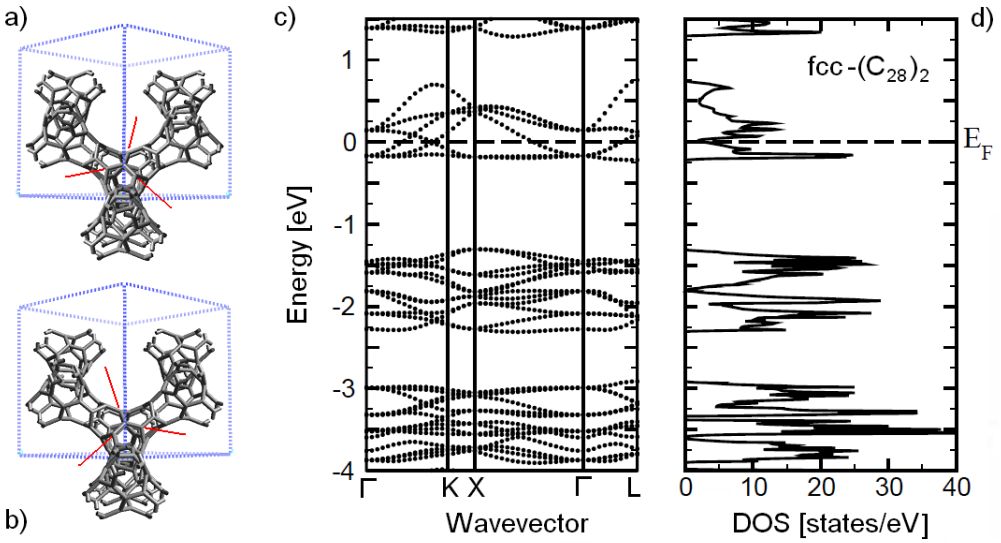

Fig. 14: (a,b) The two enantiomers of the D-type schwarzite fcc-$(C_{28})_2$ made of only 7-rings,here shown in the conventional cubic cell with four formula units. The chirality is evidenced by the directions of three bonds and the lack of mirror symmetry with respect to the (110) plane. The two enantiomers have the same electronic band structure (c) obtained from an ab-initio calculation [76]. Comparatively large gaps occur between valence as well between conduction bands, as also seen in the density of electron states (DOS). The Fermi level (E_F) cuts the lowest conduction band, which confers to fcc-$(C_{28})_2$ a metallic character.

The search of superconductivity in exotic carbon forms, e.g., in clathrates [78], has stimulated an *ab-initio* study of the vibrational structure and of the electron-phonon coupling in *fcc*-$(C_{28})_2$ of the 6-7 class and *fcc*-$(C_{64})_2$ of the 6-8 class [76]. Figure 16 shows the calculated phonon density of states at the Γ-point of *fcc*-$(C_{28})_2$ with indications of the even-symmetry optical modes which mostly contribute to the electron-phonon interaction. Their electron-phonon coupling is

explicitly indicated in meV units (if larger than 2 meV). It appears that the largest contribution comes from phonons which deform the narrow necks joining two neighbour elements. Here the Gauss curvature is the largest, which support the conjecture made for clathrates [78] that a larger Gauss curvature should favour superconductivity. The calculation yields however a discouraging $\lambda = 0.116$ for the overall electron-phonon coupling parameter, which is quite smaller that that of doped fullerenes. Nevertheless it is conjectured that doping, by shifting E_F to regions of much higher density of states, could increase λ up to a factor five [76]. For comparison a similar analysis has been carried out for the schwarzite *fcc*-$(C_{64})_2$ of the 6-8 class, which has larger and much less curved necks due to the insertion of 6-rings. The structure and the *ab-initio* electronic bands are shown in Fig 17(a,b) [76]. The first important difference with respect to the schwarzites of the 6-7 class is the disappearance of gaps. This is attributed to the appreciable conjugation which is allowed by the even-ring structure and removes the localization effects seen in 6-7 class schwarzites. The resulting metallic solid has however a comparatively low density at the Fermi level (E_F), and the resulting electron-phonon interaction is even smaller than in *fcc*-$(C_{28})_2$.

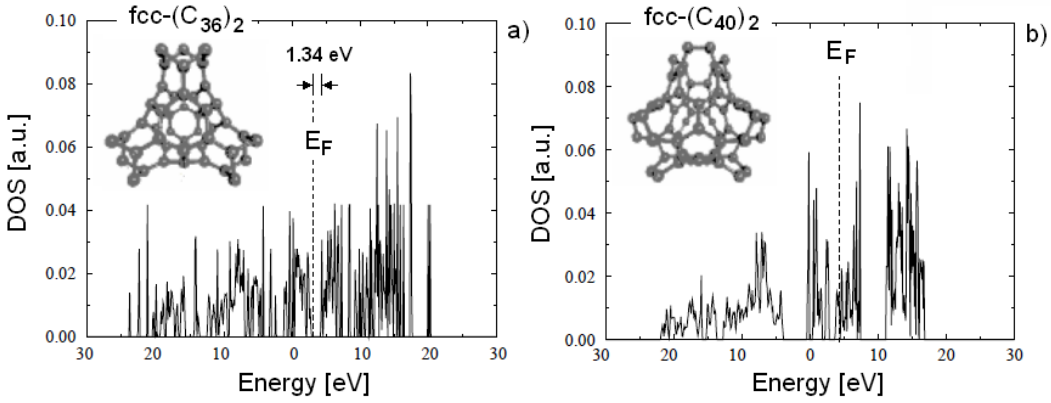

Fig. 15: Density of the electronic states (DOS) of the D-type schwarzites fcc-$(C_{36})_2$ (a) and fcc-$(C_{36})_2$ (b) a tight-binding calculation [60]. As seen from the position of the Fermi level (E_F), the former schwarzite is an insulator with a gap of 1.34 eV, the latter is a metal. The presence of many sharp peaks in the DOS is indicative of bands of states strongly localized within each element. The insets show the element atomic structures.

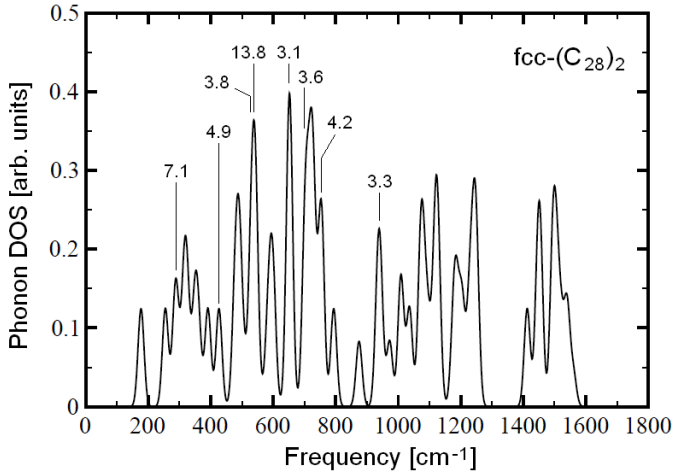

Fig. 16: The *ab-initio* density of phonon states at the Γ-point (zone center) of *fcc*-$(C_{28})_2$. Some of the phonon peaks are labelled by the corresponding calculated values of the electron-phonon coupling (in meV units), if larger that 2 meV (adapted from [76]).

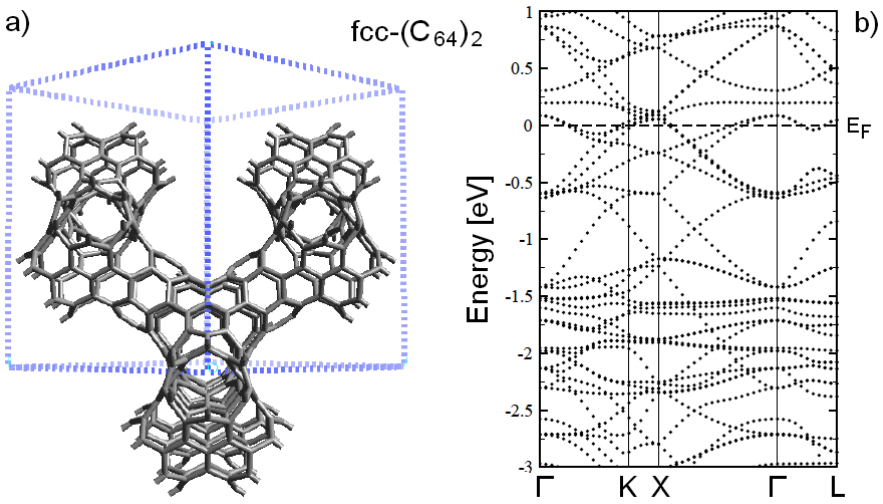

Fig. 17: The fcc-$(C_{64})_2$ belongs to the class of schwarzites made of 8- and 6-rings and has, according to Eq. (8), six 8-rings per element (a). The appreciable conjugation which is allowed by the even-ring structure removes the localization effects seen in schwarzites of the 6-7 class: no gap is found in the band structure (b), the resulting solid is metallic with a comparatively low density at the Fermi level (E_F), and the electron-phonon interaction is small.

7. Quantum molecular dynamics simulations

Thanks to the development of efficient tight-binding molecular dynamics (TBMD) methods [79], there have been also a few TBMD simulations of the growth and temperature evolution of low-coordinated carbon structures from cluster assembling, aiming at clarifying the conditions for schwarzite formation [80-85,3]. In particular it has been investigated how the size distribution of clusters, their density and kinetic energy are effective in the growth of sp^2 schwarzitic material rather than mixed sp^2-sp^3 carbon or less-coordinated forms like carbynes [85-87]. Here we briefly discuss just one particular simulation which shows the useful information which topology can provide in the molecular dynamics of a complex structure.

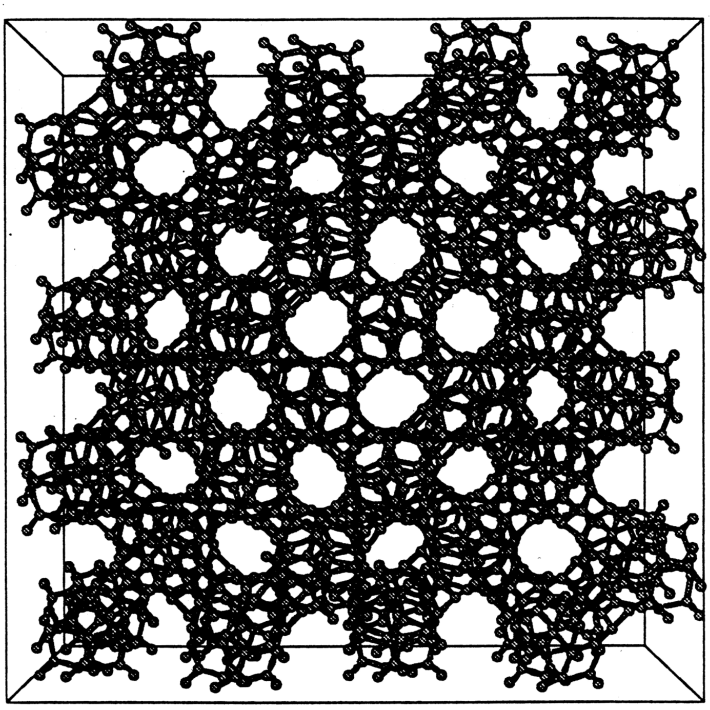

Fig. 18: The cell with periodic boundary conditions made of 32 unit cells of the D-type schwarzite *fcc*-$(C_{36})_2$ for a tight-binding molecular dynamics simulation [84,85].

A D-type *fcc*-$(C_{36})_2$, represented in Fig. 18 inside a simulation cell of 32 unit cells (64 elements) with cyclic boundary conditions, is gradually heated from room temperature to 4250 K. The evolution is monitored through the topological connectivity (Fig. 19(a)), evaluated over a

subunit of five unit cells (10 elements). As shown in Fig. 19(b), the initial connectivity of the subunit is $k = 19$ and is slowly reduced by increasing the temperature down to 16 due to some bond breaking and reshuffling. Just above 3800 K the connectivity drops to 3, thus signalling a rapid graphitization of the schwarzite. It would be quite hard to visualize what looks to be a topological phase transition by just examining the simulation snapshots. On the contrary the change of connectivity, as derived from Eq. (6) by counting at each time the numbers of bonds and rings, constitutes a sort of topological order parameter which allows to monitor the phase change from an ordered schwarzite to a disordered graphite-like material.

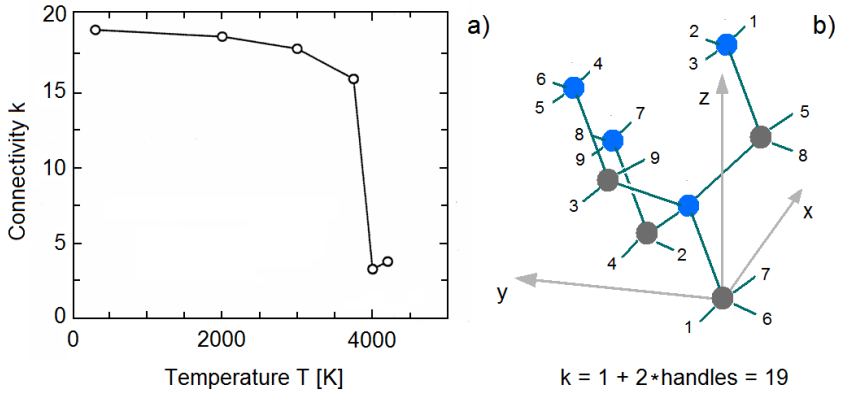

Fig. 19: (a) Tight-binding molecular dynamics simulation of the graphitization of the schwarzite fcc-$(C_{36})_2$ (Fig. 14). The evolution for increasing temperature is monitored by the connectivity of a subunit of 8 elements (4 molecules) (b). Since 9 handles are required to close the 8-element subunit on itself (by joining the corresponding numbers in b)), the low-temperature connectivity is 19. The graphitization occurs slightly below 4000 K, where the connectivity suddenly drops from k =16 to the graphene value k = 3, thus depicting a topological phase transition (adapted from [84,85])

Further examples of TBMD simulations illustrating the dependence of the output on the temperature variation protocol can be found in Refs. [80,81]. A mixture of large clusters (C_{39} fragments) dispersed in a gas of C_2 dimers, under a gradual increase of temperature from 1500 to 3500 K starts coalescing until they form a single connected cluster. The structure, reminding a random schwarzite, shows the formation of some 7-ring associated with a negative Gaussian curvature. For comparison the cluster coalescence a constant temperature of 3500K leads instead to a graphite-like structure dominated by 6-membered rings. Other simulations starting from a gas of

only carbon dimers yield open tubular structures with the corresponding connectivity $k = 3$. It is hoped that larger and larger-scale quantum simulations will help finding a viable route to the new world of crystalline schwarzites.

8. Conclusion

Although schwarzitic carbon sponges did not know the glamour of the ordered forms of sp^2 carbon, they have nevertheless led to important applications, some of which have been mentioned in the introduction. Countless examples may be found in the literature, ranging from the engineering of SCBD carbon-based composites [86] to biological applications, one for all the recent demonstration of interfacing live cells with nanocarbon substrates [87]. The path towards low-dimensional carbon for nanotechnologies has now reached the still poorly known world of pure carbon chains, carbynes, which were looked for since the time of fullerene discovery [1]. The recent production of carbynes by SCBD [88,89] and from graphene [90] is calling for new theoretical investigations [91]. However the real challenge for possible developments on more fundamental questions is, in our opinion, the synthesis of ordered three-periodic schwarzites or even supported planar architectures formed by two-periodic schwarzites, eventually obtained by joining nanotubes, as it would be made by a nano-plomber. Such a new class of ordered sp^2 carbons would represent a natural extension to curved highly connected two-dimensional spaces of what has been learnt from and about graphene [6-10]. The fascinating mutual implications linking graphene and Dirac fermion physics would be greatly enriched by the exploration of periodic curved carbon surfaces once their topology can be designed and controlled.

Another intriguing aspect related with the growth of minimal surfaces is the one-to-one correspondence between global and local minimal conditions which may allow for a deterministic growth along the valley floor of the energy landscape. In principle any global thermodynamic potential which can be represented as a surface integral has minima which can be determined from local conditions, and allows for a deterministic growth process.

Carbon, as the most versatile element of the periodic table, keeps stimulating the ingenuity of versatile scientists. The invention of new *possible* sp^2 structures by means of powerful mathematical tools, like, e.g., those recently investigated by Diudea [92] (Fig. 20), as well as the great excitement started with the isolation of a single graphene sheet [6-10], now raised to the rank of paradigm linking distant areas of physics, suggest that fantasy joined to the rigorous thought are the lifeblood of science.

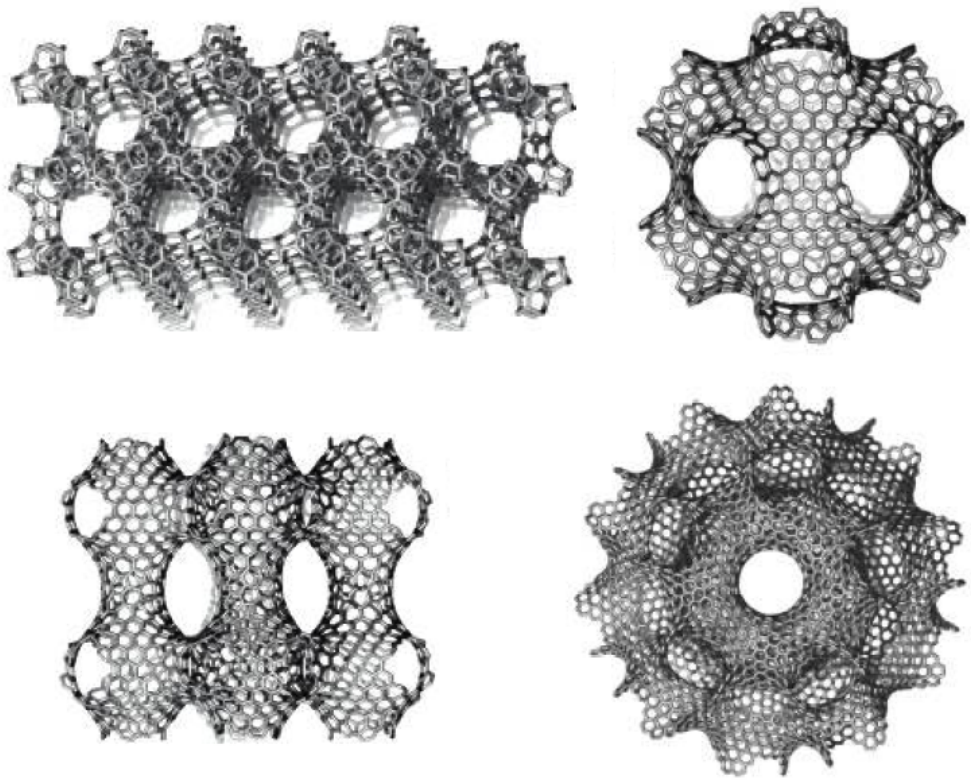

Fig. 20: A few examples of nanoporous carbon allotropes designed by Mircea Diudea [92] by septupling map operations

Acknowledgement: one of us (GB) gratefully acknowledges the Ikerbasque Foundation for support within the project ABSIDES. We acknowledge many stimulating discussions with Prof. Paolo Milani (University of Milano).

REFERENCES

[1] H. W. Kroto, J. R. Heath, S. C. O'Brien, R. F. Curl and R. E. Smalley, *Nature* **318**, 162 (1985).

[2] S. Iijima, *Nature* **324**, 56 (1991).

[3] D. Donadio, L. Colombo, P. Milani and G. Benedek, *Phys. Rev. Lett.*, **84,** 776 (1999).

[4] E. Barborini, P. Piseri, P. Milani, G. Benedek, C. Ducati and J. Robertson, *Appl. Phys. Lett.* **81**, 3359 (2002); see also E. Gerstner, *Nature*, *Materials Update*, 7 Nov 2002 (http://www.nature.com/materials/news/ news/021107/portal/m021107-1.html)

[5] G. Benedek, H. Vahedi-Tafreshi, E. Barborini, P. Piseri, P. Milani, C. Ducati and J. Robertson, *Diamond and Rel. Mater.* **12**, 768 (2003).

[6] K. S. Novoselov, A. K. Geim, S. V. Morozov, D. Jiang, Y. Zhang, S. V. Dubonos, I. V. Grigorieva, A. A. Firsov, *Science* **30**, 666 (2004).

[7] K. S. Novoselov, D. Jiang, T. Booth, V. V. Khotkevich, S. M. Morozov, and A. K. Geim, *Proc. Natl. Acad. Sci. U.S.A*. **102**, 10451 (2005).

[8] K. S. Novoselov, A. K. Geim, S. V. Morozov, D. Jiang1, M. I. Katsnelson, I. V. Grigorieva, S. V. Dubonos, and A. Firsov, *Nature,* **438**, 197 (2005)

[9] A. K. Geim and K. S. Novoselov*, Nature Mater*. **6**, 183 (2007).

[10] A. H. Castro Neto, F. Guinea, N. M. R. Peres, K. S. Novoselov, and A. K. Geim, *Rev. Mod. Phys*. **81**,109 (2009).

[11] G. Benedek and M. Bernasconi, in *Encyclopaedia of Nanoscience and Nanotechnology* (Marcel Dekker, Inc., New York 2004) p. 1235.

[12] L. D. Rotter, Z. Schlesinger, J. P. McCauley, N. Coustel, J. E. Fisher and A. B. Smith, *Nature* **355**, 532 (1992).

[13] H. Wang, A. A. Setlur, J. M. Lauerhaas, J. W. Dai, E. W. Seelig and R. P. H. Chang, *Appl. Phys. Lett.* **72**, 2912 (1998).

[14] C. Niu, E. K. Sichel, R. Hoch, D. Moy and H. Tennent, *Appl. Phys. Lett*. **70**, 1480 (1997).

[15] J. H. Seol, I. Jo, A. L. Moore, L. Lindsay, Z. H. Aitken, M. T. Pettes, X. Li, Z. Yao, R. Huang, D. Broido, N. Mingo, R. S. Ruoff, and L. Shi, *Science* **328**, 231 (2010).

[16] M. D. Stoller, S. Park, Y. Zhu, J. An, and R. S. Ruoff, *Nanoletters* **8**, 3498 (2008).

[17] E. Cadelano, P. L. Palla, S. Giordano, and L. Colombo, *Phys. Rev. Lett*. **102**, 235502 (2009)

[18] G. Li, A. Luican, J. M. B. Lopes des Santos, A. H. Castro Neto, A Reina, J. Kong, and E. Y. Andrei, *Nature Phys*. **6**, 109 (2010).

[19] A. V. Rode, E. G. Gamaly, A. G. Christy, J. G. Fitz Gerald, S. T. Hyde, R. G.Elliman, B. Luther-Davies, A. I. Veinger, J. Androulakis, and J. Giapintzakis, *Phys. Rev. B* **70**, 054407 (2004); highlighted by R. F. Service*, Science* **304**, 42 (2004).

[20] D. Arčon, Z. Jagličič, A. Zorko, A. V. Rode, A. G. Christy, N. R. Madsen, E. G. Gamaly, and B. Luther-Davies, *Phys. Rev. B* **74**, 014438 (2006).

[21] T. Lenosky, X. Gonze, M. Teter and V. Elser, *Nature*, **355,** 333 (1992).

[22] S. J. Townsend,T. Lenosky, D.A. Muller, C.S. Nichols and V. Elser, Phys. Rev. Lett. 69, 921 (1992).

[23] K. H. A. Schwarz, *Gesammelte Mathematische Abhandlungen* (Springer, Berlin 1890).

[24] P. Milani e S. Iannotta, *Cluster Beam Synthesis of Nanostructured Materials* (Springer, Berlin 1999).

[25] M. Bogana, D. Donadio, G. Benedek and L. Colombo, *Europhys. Lett.,* **54**, 72 (2001).

[26] G. Benedek, H. Vahedi-Tafreshi, P. Milani and A. Podestà, "Fractal Growth of Carbon Schwarzites" in *Complexity, Metastability and Non-Extensivity*, edited by C. Beck et al. (World Scientific, Singapore 2005), p. 146-155.

[27] L. Diederich, E. Barborini, P. Piseri, A. Podestà, P. Milani, A. Scheuwli, and R. Gallay, *Appl. Phys. Lett.* **75**, 2662 (1999).

[28] I. Boscolo, P. Milani, M. Parisotto, G. Benedek, and F. Tazzioli, *J. Appl. Phys.* **87,** 4005 (2000)

[29] G. Benedek, P. Milani, and V. G. Ralchenko, Eds., *Nanostructured Carbon for Advanced Applications* ((Kluver, Dordrecht 2001) and papers therein.

[30] A.C. Ferrari, B. S. Satyanarayana, J. Robertson, W. I. Milne, E. Barborini, P. Piseri, and P.Milani, *Europhys. Lett.*, **46**, 245 (1999).

[31] A. M. Rao and M.S. Dresselhaus, in *Nanostructured Carbon for Advanced Applications*, NATO Science Series II, Vol. 24, edited by G. Benedek, P. Milani, V.G. Ralchenko (Kluwer, Dordrecht, 2001), p.3.

[32] W. Lu and D. D. L. Chung, *Carbon* **35**, 427 (1997).

[33] T. Kyotani, *Carbon* **38**, 269 (2001).

[34] P. Ryoo, S. H. Joo, M. Kruk and M. Jaroniek, *Adv. Mater*. **13**, 677 (2001).

[35] H. Kajii, Y. Kawagishi, H. Take, K. Yoshino, A. A. Zakhidov and R. H. Baughman, *J. Appl. Phys*. **88**, 758 (2000).

[36] D. Vanderbilt and J. Tersoff, *Phys. Rev. Lett.* **68**, 511 (1992).

[37] E. Barborini, P. Piseri and P. Milani, *J. Phys. D* **32**, L105 (1999).

[38] P. Piseri, A. Podesta`, E. Berborini and P. Milani*, Rev. Sci. Instrum.* **72**, 2261 (2001).

[39] E. Barborini, F. Siviero, S. Vinati, C. Lenardi, P. Piseri, P. Milani, *Rev. of Sci. Instrum*. **73**, 2060 (2002).

[40] P. Milani, M. Ferretti, P. Piseri, C.E. Bottani, A. Ferrari, A Li Bassi, G. Guizzetti and M. Patrini*, J. Appl. Phys*. **82**, 5793 (1997)

[41] P. Milani, E. Barborini, P. Piseri, C.E. Bottani and A. Li Bassi , *Eur. Phys. J. D* **9**, 63 (1999)

[42] C. Lenardi, P. Piseri, V. Briois, A. Li Bassi, C.E. Bottani and P. Milani, *J. of Appl. Phys*. **85**, 7159 (1999).

[43] A.-L. Barabàsi and H. E. Stanley, *Fractal concepts in surface growth* (Cambridge University Press, Cambridge 1995)

[44] A. L. McKay, *Nature* **314**, 604 (1985).

[45] A. L. McKay and H. Terrones, *Nature* **352**, 762 (1991).

[46] H. Terrones and A. L. McKay, in *The Fullerenes*, H. W. Kroto, J. E. Fisher and D. E. Cox, Eds. (Pergamon Press, Oxford 1993) p. 113.

[47] M. O'Keeffe, G. B. Adams and O. F. Sankey, *Phys. Rev. Lett.* **68**, 2325 (1992).

[48] G. Benedek, L. Colombo, S. Gaito, E. Galvani and S. Serra, *J. Chem. Phys.* **106**, 2311 (1997).

[49] M. Coté, J. C. Grossman, M. L. Cohen and S. G. Louie, *Phys. Rev*. **B58**, 664 (1998).

[50] D. Hilbert and S. Cohn-Vossen, *Anschauliche Geometrie* (Springer, Berlin 1932).

[51] R. Osserman, *A Survey of Minimal Surfaces* (Dover, New York 1986).

[52] S. T. Hyde, in *Foams and Emulsions,* J. F. Sadoc and N. Rivier, Eds. (Kluver, Dordrecht 1999) p. 437

[53] D. Hoffman, *Nature* **384**, 28 (1996).

[54] W. Helfrich, *Z. Naturforsch.* **28**, 768 (1973).

[55] C. Oguey, in *Foams and Emulsions,* J. F. Sadoc and N. Rivier (Kluwer, Dordrecht, 1999) p. 471.

[56] J. M. Sullivan, in *Foams and Emulsions,* J. F. Sadoc and N. Rivier (Kluwer, Dordrecht, 1999) p. 379.

[57] C. T. White *et al*, in *Buckminsterfullerenes,* W. E. Billups and M. A. Ciufolini (VCH, New York, 1993) p. 125.

[58] Q. Lu, M. Arroyo, and R. Huang, *J. Phys. D: Appl. Phys*. **42**, 102002 (2009).

[59] K. N. Kudin, G. E. Scuseria, and B. I. Yakobson, *Phys. Rev. B* **64**, 235406 (2001).

[60] S. Gaito, L. Colombo and G. Benedek, Europhys. Lett. **44**, 525 (1998); *erratum*: **81**, 559 (2001).

[61] J. F. Sadoc, in *Foams and Emulsions,* J. F. Sadoc and N. Rivier, Eds. (Kluver, Dordrecht 1997) p. 511

[62] L. D'Alessio, *Thesis*, University of Milano-Bicocca (2007, unpublished).

[63] D. E. Manolopoulos, J. C. May, and S. E. Down, *Chem. Phys. Lett*. **181**, 105 (1991).

[64] M. Yoshida and P. W. Fowler, *J. Chem. Phys*. **96**, 7603 (1992).

[65] D. E. Manolopoulos and P. W. Fowler, *J. Chem. Phys.* **96**, 7603 (1992).

[66] P. W. Fowler, D. E. Manolopoulos, G.Orlandi, and F. Zerbetto*, J.Chem. Soc.Faraday Trans*. **91**, 1421 (1995).

[67] D. E. Manolopoulos and P. W. Fowler, *J. Chem. Soc. Faraday Trans*. **93**, 3289 (1997).

[68] Y. Achida, P. W. Fowler, D. Mitchell, and F. Zerbetto, J. Phys. Chem.A 102, 6835 (1998).

[69] I. Làszlò, A. Rassat, P. W. Fowler, and A. Graovac*, Chem. Phys. Lett*. **342**, 369 (2001).

[70] G. K. Horton and A. A. Maradudin, *Dynamical Properties of Solids - Vol 2: Crystalline solids* (North Holland, 1975) p.33.

[71] M. Di Corato, E. Cinquanta, and G. Benedek, to be published.

[72] G. Benedek and G. Onida, *Phys. Rev. B* **47**, 16471 (1993).

[73] G. Benedek, G. Onida, M. Righetti and S. Sanguinetti, *Nuovo Cim.* **15D**, 565 (1993); see also in *Perspectives in Many-Particle Physics,* ed. by P.F. Bortignon, R.A. Broglia and J. R. Schrieffer (North-Holland, Amsterdam 1994).

[74] G. Benedek, L. Colombo, S. Gaito and S. Serra, in *The Physics of Diamond*, A. Paoletti and A. Tucciarone Eds. (IOS Press, Amsterdam 1997) p.575-598.

[75] G. Benedek, M. Bernasconi, D. Donadio and L. Colombo, in *Nanostructured Carbon for Advanced Applications* edited by G. Benedek, P. Milani and V. G. Ralchenko (Kluver, Dordrecht 2001) p. 89.

[76] I. Spagnolatti, M. Bernasconi and G. Benedek, Eur. Phys. J. B **32**, 181 (2003).

[77] G. Cocco, E. Cadelano, and L. Colombo, *Phys. Rev. B* **81**, 241412 (**R**) (2010).

[78] X. Blase, G. Benedek, and M. Bernasconi, "Structural, Mechanical, and Superconducting Properties of Clathates", in *Computer-Based Modeling of Novel Carbon Systems and Their Properties*, Carbon Materials: Chemistry and Physics 3, edited by L. Colombo and A.L. Fasolino (Springer, Berlin Heidelberg 2010) Chap. 6.

[79] L. Colombo, Riv. Nuovo Cimento **28**, 1 (2005).

[80] S. Spadoni, L. Colombo, P. Milani and G. Benedek, *Europhysics Lett*. **39** (1997) 269.

[81] G. Benedek, L. Colombo, S. Spadoni, S. Gaito and P. Milani, in *Tight-Binding Approach to Computational Materials Science*, ed. by P. E. A. Turchi, A. Gonbis and L. Colombo, *MRS Symp. Proc.* Vol 491 (MRS, Warrendale 1998) p. 529.

[82] Y. Yamaguchi, L. Colombo, P. Piseri, L. Ravagnan, and P. Milani, *Phys. Rev. B* **76**, 134119 (2007).76]

[83] M. Bogana and L. Colombo, *Appl. Phys. A* **86**, 275 (2007).

[84] V. Rosato, M. Celino, G. Benedek and S. Gaito, *Phys. Rev. B* **60**, 16928 (1999).

[85] V. Rosato, M. Celino, S. Gaito and G. Benedek, *Comp. Mater. Sci.* **20** (2001) 387.

[86] G. Bongiorno, C. Lenardi, C. Ducati, R.G. Agostino, T. Caruso, M. Amati, M. Blomqvist, E. Barborini, P. Piseri, S. La Rosa, E. Colavita and P. Milani, J. Nanosci. Nanotechnol. **10**, 1 (2005).

[87] S. Agarwal, X. Zhou, F. Ye, Q. He, G. C. K. Chen, J. Soo, F. Boey, H. Zhang, and P. Chen, *Langmuir Lett*. **26**, 2244 (2010).

[88] L. Ravagnan, F. Siviero, C. Lenardi, P. Piseri, E. Barborini, P. Milani, C. S. Casari, A. Li Bassi, and C. E. Bottani, *Phys. Rev. Lett.* **89**, 285506 (2002)

[89] L. Ravagnan, P. Piseri, M. Bruzzi, S. Miglio, G. Bongiorno, A. Baserga, C. S. Casari, A. Li Bassi, C. Lenardi, Y. Yamaguchi, T. Wakabayashi, C. E. Bottani, and P. Milani, *Phys. Rev. Lett.* **98**, 216103 (2007).

[90] C. Jin, H. Lan, L. Peng, K. Suenaga, and S. Iijima, *Phys. Rev. Lett.* **102**, 205501 (2009)

[91] L. Ravagnan, N. Manini, E. Cinquanta, G. Onida, D. Sangalli, C. Motta, M. Devetta, A. Bordoni, P. Piseri, and P. Milani. *Phys. Rev. Lett*. **102**, 245502 (2009).

[92] M. V. Diudea, *J. Chem. Inf. Model.* **45**, 1002 (2005); see also A. E. Vizitiu and M. V. Diudea, Chap. 3 of the present volume.

Bibliography

[1] S. Iijima. Helical microtubules of graphitic carbon. *Nature*, 354:56, 1991.

[2] H. W. Kroto *et al.* C60: Buckminsterfullerene. *Nature*, 318(6042):162–163, 1985.

[3] K. S. Novoselov *et al.* Electric filed effect in atomically thin carbon film. *Science*, 306(5696):666–669, 2004.

[4] T. Lenosky *et al.* Energetic of negatively curved graphitic carbon. *Nature*, 355(6358):333–335, 1992.

[5] S. Townsend *et al.* Negatively curved graphitic sheet model of amorphous carbon. *Phys. Rev. Lett.*, 69(6):921–924, 1992.

[6] K. H. A. Schwarz. *Gesammelte Mathematische Abhandlungen*. Springer, Berlin, 1999.

[7] D. Donadio *et al.* Growth of nanostructured carbon films by cluster assembly. *Phys. Rev. Lett.*, 83:776, 1999.

[8] G. Benedek *et al.* *"The Topological Background of Schwarzite Physics" in Mathematics and Topology of Fullerenes*. Springer series on CARBON MATERIALS CHEMISTRY AND PHYSICS, Heidelberg, Berlin, 20010.

[9] A. C. Ferrari and J. Robertson. Interpretation of Raman spectra of disordered and amorphous carbon. *Phys. Rev. B*, 61(20):14095–14107, 2000.

[10] F. Piazza *et al.* Interpretation of raman spectra of disordered and amorphous carbon. *Diam. Relat. Mater.*, 13(4-8):1505–1510, 2000.

[11] A. Ilie *et al.* Effect of sp(2)-phase nanostructure on field emission from amorphous carbons. *Appl. Phys. Lett.*, 76(18):2627–2629, 2000.

[12] N. Boutroy *et al.* Hydrogenated amorphous carbon film coating of pet bottles for gas diffusion barriers. *Diam. Relat. Mater.*, 15(4-8):921–927, 2006.

[13] M. Weimer *et al.* Electronic and optical properties of functionalized carbon chains with the localized hartree-fock and conventional kohn-sham methods. *Chem. Phys.*, 309(1):77–87, 2005.

[14] S. Eisler *et al.* Polyynes as a model for carbyne: Synthesis, physical properties, and nonlinear optical response. *J. Am. Chem. Soc.*, 127(8):2666–2676, 2005.

[15] M.D. Wahadoszamen *et al.* External electric field effects on absorption, fluorescence, and phosphorescence spectra of diphenylpolyynes in a polymer film. *The Journal of Physical Chemistry A*, 111(38):9544–9552, 2007.

[16] A.R. Murphy *et al.* Organic semiconducting oligomers for use in thin film transistors. *Chemical Reviews*, 107(4):1066–1096, 2007.

[17] R.H. Friend *et al.* Electroluminescence in conjugated polymers. *Nature*, 397(6715):1121–128, 1999.

[18] W.Y. Wong *et al.* Tuning the absorption, charge transport properties, and solar cell efficiency with the number of thienyl rings in platinum-containing poly(aryleneethynylene). *Journal of the American Chemical Society*, 129(46):14372–14380, 2007.

[19] B.B. Standley *et al.* Graphene-based atomic-scale switches. *Nano Letters*, 8(10):3345–3349, 2008.

[20] Y. Li *et al.* Graphene-based atomic-scale switches. *Nature Materials*, 7(12):966–971, 2008.

[21] M. G. Zeng *et al.* Perfect spin-filter and spin-valve in carbon atomic chains. *Appl. Phys. Lett.*, 96(4):042104, 2010.

[22] C. S. Li *et al.* Theoretical realization of cluster-assembled hydrogen storage materials based on terminated carbon atomic chains. *J. of Chem. Phys.*, 134(2):024522, 2011.

[23] C. S. Li *et al.* Titanium-capped carbon chains as promising new hydrogen storage media. *Phys. Chem. Chem. Phys.*, 13(6):2323–2327, 2011.

[24] S. Kwok. Organic matter in space: from star dust to the solar system. *Astrophys. Space Sci.*, 319(1):5–21, 2009.

[25] G. H. Herbig. The diffuse interstellar bands. *Annual Review of Astronomy and Astrophysics*, 33(1):19–73, 1995.

[26] T. Snow. The unidentified diffuse interstellar bands as evidence for large organic molecules in the interstellar medium. *Annual Review of Astronomy and Astrophysics*, 57(4):615–626, 2001.

[27] L. J. Allamandola *et al.* Carbon chain abundance in the diffuse interstellar medium. *Astron. and Astrophys.*, 352(2):659–664, 1999.

[28] J. Cami *et al.* Detection of c60 and c70 in a young planetary nebula. *Science*, 329(5996):1180–1182, 2010.

[29] P. Ehrenfreund and B.H. Foing. Fullerenes and cosmic carbon. *Science*, 329(5996):1159–1160, 2010.

[30] K. Wegner *et al.* Cluster beam deposition: a tool for nanoscale science and technology. *J. Phys. D: Appl. Phys.*, 39(22):1159–1160, 2006.

[31] L. Ravagnan *et al.* Cluster-beam deposition and *in situ*characterization of carbyne-rich carbon films. *Phys. Rev. Lett.*, 89(28):285506, 2002.

[32] A. Lucotti *et al.* Raman and sers investigation of isolated sp carbon chains. *Chem. Phys. Lett.*, 417(1-3):78–82, 2006.

[33] C.S. Casari *et al.* Stabilization of linear carbon structures in a solid ag nanoparticle assembly. *Appl. Phys. Lett.*, 90(1):013111, 2007.

[34] A. Lucotti *et al.* Evidence for solution-state nonlinearity of sp-carbon chains based on ir and raman spectroscopy: Violation of mutual exclusion. *J. Am. Chem. Soc.*, 131(12):4239–4244, 2009.

[35] R. Matzutani *et al.* Wavelength dependence of polyyne preparation by liquid-phase laser ablation using pellet targets. *Chem. Comm.*, 47(20):5840–5842, 2011.

[36] K. Inoue *et al.* Preparation of long-chain polyynes of c(24)h(2) and c(26)h(2) by liquid-phase laser ablation in decalin. *Carbon*, 48(14):4209–4211, 2010.

[37] M. Tsuji *et al.* Formation of hydrogen-capped polyynes by laser ablation of c-60 particles suspended in solution. *Carbon*, 41(11):2141–2148, 2003.

[38] S. K. Shin *et al.* Preparation of polyynes by laser ablation of graphite in aqueous media. *Appl. Surf. Sci*, 257(12):5156–5158, 2011.

[39] S. Akiyama *et al.* On the electronic spectra of some α-ω-diarylpoly-yne. *Tetrahedron Lett.*, 9:1121, 1968.

[40] K. Nakasuji *et al.* Linear conjugated systems bearing aromatic terminal groups. iii. the synthesis and the electronic spectra of 1,1'-dinaphthyl- and 2,2'-dinaphthylpoly-ynes. *Bull. Chem. Soc. Jpn.*, 43:3567, 1970.

[41] M. Nakagawa *et al.* Novel linear relation in the electronic spectra of α-ω-diarylpoly-ynes. *Tetrahedron*, 27:5401, 1971.

[42] W. Chodkiewicz. Synthesis of acetylenic compounds. *W. Ann. Chim.*, 2:819–869, 1957.

[43] W. Chodkiewicz and P. Cadiot. New synthesis of symmetrical and asymmetrical conjugated polyacetylenes. *Hebd. Seances Acad. Sci.*, 241:1055, 1955.

[44] P. Cadiot and W. Chodkiewicz. *Chemistry of Acetylenes, pp* $597-647$. New York, 1969.

[45] J. P. Marino and H.N. Nguyen. Bulky trialkylsilyl acetylenes in the cadiot-chodkiewicz cross-coupling reaction. *The Journal of Organic Chemistry*, 67(19):6841–6844, 2002.

[46] N.J. Matovic*et al.* Polyunsaturated alkyl amides from echinacea: Synthesis of diynes, enynes, and dienes. *The Journal of Organic Chemistry*, 76(11):4467–4481, 2011.

[47] F. Cataldo *et al.* Simple synthesis of α,ω-diarylpolyynes part 1: Diphenylpolyynes. *Journal of macromolecular science. Pure and applied chemistry*, 47(8):739–746, 2010.

[48] C. Jin *et al.* Deriving carbon atomic chains from graphene. *Phys. Rev. Lett.*, 102:205501, 2009.

[49] A. Chuvilin *et al.* From graphene constrictions to single carbon chains. *New J. Phys.*, 11:083019, 2009.

[50] A. Hu *et al.* Spectroscopic characterization of carbon chains in nanostructured tetrahedral carbon films synthesized by femtosecond pulsed laser deposition. *J. Chem. Phys.*, 126:154705, 2007.

[51] M. Rybachuk *et al.* Direct synthesis of sp-bonded carbon chains on graphite surface by femtosecond laser irradiation. *Appl. Phys. Lett.*, 91:131906, 2007.

[52] A. Shvartsburg *et al.* Ball-and-chain dimers from a hot fullerene plasma. *The Journal of Physical Chemistry A*, 103(27):5275–5284, 1999.

[53] A. Shvartsburg *et al.* Observation of "stick" and "handle" intermediates along the fullerene road. *Phys. Rev. Lett.*, 84:2421–2424, 2000.

[54] T. G. Dietz *et al.* Laser production of supersonic metal cluster beams. *J. Chem. Phys.*, 74:6511–6512, 1981.

[55] G. Gantef́or *et al.* Pure metal and metal-doped rare-gas clusters grown in a pulsed-arc cluster ion-source. *Chem. Phys. Lett.*, 165:293–296, 1990.

[56] E.A. Rohlfing *et al.* Production and characterization of supersonic carbon cluster beams. *J. Chem. Phys.*, 81:3322–3330, 1984.

[57] R.F. Bunshah. *Handbook of deposition technologies for films and coating.* Noyes Publications, 1994.

[58] G. Scoles. *Atomic and Molecular Beam Methods. Science, Technology and Applications.* Oxford University Press., New York, 1988.

[59] M. Bogana *et al.* Leaving the fullerene road: presence and stability of sp chains in sp2 carbon clusters and cluster-assembled solids. *New J. Phys.*, 81(7), 2005.

[60] Y. Yamaguchi *et al.* Growth of sp-sp(2) nanostructures in a carbon plasma. *Phys. Rev. B*, 76(13):1098–0121, 2008.

[61] C. Lenardi *et al.* Preliminary results with cesyra (cluster experiments with synchrotron radiation). *Elettra Highlights* 03-04, page 92, 2004.

[62] P. Milani and S. Iannotta. *Cluster Beam Synthesis of Nanostructured Materials.* Springer, Berlin, 1999.

[63] P. Milani *et al.* Nanostructured carbon films from supersonic cluster beam deposition: structure and morphology. *Eur. Phys. J. D*, 9:63–68, 1999.

[64] L. Ravagnan *et al.* sp hybridization in free carbon nanoparticles–presence and stability observed by near edge x-ray absorption fine structure spectroscopy. *Chem. Commun.*, 47:2952–2954, 2011.

[65] E.H. Haberland *et al.* Molecular-dynamics simulation of thin-film growth by energetic cluster impact. *Phys. Rev. B*, 51:11061–11067, 1995.

[66] E Barborini *et al.* Synthesis of carbon films with controlled nanostructure by separation of neutral clusters in supersonic beams. *Chem. Phys. Lett.*, 300(5-6):633 – 638, 1999.

[67] E Barborini *et al.* Cluster beam microfabrication of patterns of three-dimensional nanostructured objects. *Appl. Phys. Lett.*, 77:1059, 2000.

[68] P. Piseri *et al.* Production and characterization of highly intense and collimated cluster beams by inertial focusing in supersonic expansions. *Rev. Sci. Instrum.*, 72(5):2261, 2001.

[69] D. Donadio *et al.* Growth of nanostructured carbon films by cluster assembly. *Phys. Rev. Lett.*, 83(4):776–779, 1999.

[70] C.S. Casari *et al.* Gas exposure and thermal stability of linear carbon chains in nanostructured carbon films investigated by in situ raman spectroscopy. *Carbon*, 5-6(42):1103–1106, 2004.

[71] C.S. Casari *et al.* Chemical and thermal stability of carbyne-like structures in cluster-assembled carbon films. *Phys. Rev. B*, 7(69):075422, 2004.

[72] A. C. Albrecht. On the theory of raman intensities. *J. Chem. Phys.*, 34:2476, 1961.

[73] P. R. Griffiths and J. A. de Haseth. *Fourier Transform Infrared Spectrometry, 2nd edition.* Wiley-Interscience, New York, 2007.

[74] P. Hohenberg and W. Khon. Inhomogeneous electron gas. *Phys. Rev.*, 136(3B):B864–B871, 1964.

[75] W. Kohn and L. J. Sham. Self-consistent equations including exchange and correlation effects. *Phys. Rev.*, 140:A1133–A1138, 1965.

[76] G. Seifert *et al.* Calculations of molecules, clusters, and solids with a simplified lcao-dft-lda scheme. *Int. J. of Quantum Chemistry*, 58:185, 1995.

[77] A. J. Cohen *et al.* Insights into current limitations of density functional theory. *Science*, 321:792, 2008.

[78] P. Mori-Sanchez *et al.* Localization and delocalization errors in density functional theory and implications for band-gap prediction. *Phys. Rev. Lett.*, 100:146401, 2008.

[79] A. J. Cohen *et al. et al.* Fractional charge perspective on the band gap in density-functional theory. *Phys. Rev. B*, 77:115123, 2008.

[80] D. Vanderbilt. Soft self-consistent pseudopotentials in a generalized eigenvalue formalism. *Phys. Rev. B*, 41:7892, 1990.

[81] P. Giannozzi *et al.* Quantum espresso: a modular and open-source software project for quantum simulations of materials. *J. Phys.: Condens. Matter*, 21:395502, 2009.

[82] A. Kokalj. Xcrysden-a new program for displaying crystalline structures and electron densities. *J. Phys.: Condens. Matter*, 17:176–179, 1999.

[83] T. Wassmann *et al.* Structure, stability, edge states, and aromaticity of graphene ribbons. *Phys. Rev. Lett.*, 101:096402, 2008.

[84] G. Placzek. *in: Handbuch der Radiologie 2nd ed.*, volume 6, part II. E. Marx, ed. (Akademische Verlagsgesellschaft, Leipzig, Germany, 1934.

[85] C. Jäger *et al.* From pahs to solid carbon. *EAS Publications Series*, 46:293, 2011.

[86] L. Ravagnan *et al.* Influence of cumulenic chains on the vibrational and electronic properties of *sp*-sp^2 amorphous carbon. *Phys. Rev. Lett.*, 98(21):216103, 2007.

[87] Norman C. Craig and Ira W. Levin. Calibrating raman spectrometers with plasma lines from the argon ion laser. *Appl. Spectrosc.*, 33(5):475–476, 1979.

[88] E. Cinquanta *et al.* Vibrational characterization of dinaphthylpolyynes: A model system for the study of end-capped sp carbon chains. *J. Chem. Phys*, 135:194501, 2011.

[89] F. Cataldo *et al.* Synthesis, characterization, and modeling of naphthyl-terminated sp carbon chains: Dinaphthylpolyynes. *J. Phys. Chem. B*, 114:14834–14841, 2010.

[90] C. Thomsen and S. Reich. Double resonant raman scattering in graphite. *J. Phys. Chem. B*, 85(24):5214–5217, 2000.

[91] J. Robertson and E. P. O'Reilly. Electronic and atomic structure of amorphous carbon. *Phys. Rev. B*, 35:2946–2957, 1987.

[92] A. C. Ferrari and J. Robertson. Resonant raman spectroscopy of disordered, amorphous, and diamondlike carbon. *Phys. Rev. B*, 64:075414, 2001.

[93] J. Hlavat *et al.*. Polymerisation of 1-iodohexa-1,3,5-triyne and hexa-1,3,5-triyne: a new synthesis of carbon nanotubes at low temperatures. *Chem. Commun.*, pages 737–738, 2000.

[94] L. Kavan. Electrochemical carbon. *Chem. Rev.*,, 97(8):3061–3082, 1997.

[95] O. Nicoletti. Caratterizzazione della stabilitá di catene lineari di carbonio mediante spettroscopia raman. private communication, 2008.

[96] L. Ravagnan *et al.* Effect of axial torsion on *sp* carbon atomic wires. *Phys. Rev. Lett.*, 102(24):245502, 2009.

[97] G. Onida *et al.* Vibrational properties of *sp* carbon atomic wires in cluster-assembled carbon films. *Phys. Status Solidi B*, 247:2017–2021, 2010.

[98] G. Moras *et al.* Formation and oxidation of linear carbon chains and their role in the wear of carbon materials. *Tribol. Lett.*, 44:355–365, 2011.

[99] G. Moras *et al.* Progressive shortening of *sp*-hybridized carbon chains through oxygen-induced cleavage. *J. Phys. Chem. C*, 115:24653–24661, 2011.

[100] J. Tauc. *Amorphous and Liquid Semiconductors.* Plenum, London, 1974.

[101] P. Milani *et al.* Synthesis and characterization of cluster-assembled carbon thin films. *J. Appl. Phys.*, 82(11):5793–5798, 1997.

[102] S. E. Rodil A. C. Ferrari and J. Robertson. Interpretation of infrared and raman spectra of amorphous carbon nitrides. *Phys. Rev. B*, 67:155306, 2003.

[103] R. A. Friedel and G. L. Carlson. Infrared spectra of ground graphite. *J. Phys. Chem.*, 8, 1971.

[104] L. Radom A.P. Scott. Are cumulenones kinked? a systematic high-level ab initio study. *J. Mol. Struc.*, 556:253–261, 2000.

Acknowledgments

At the end of my Ph. D. thesis, I would like to turn my mind to all those people who shared this experience with me over these three years.

First of all I want to thank again Federica for the life we are living together, for all the support and for all the patience she ever had. Then, a sweat though to my little son Enea who completely changed my world; it's incredible how you made my life better, now everything is in the right place. Nowadays it is not easy to decide to begin the scientific career and, to be honest, I have to say that without the encouragement and support of my parents, I would have not be able to carry out my job. Thanks mom and thanks dad.

During these years I had the opportunity to work with very smart colleagues. I want to than Luca for the time he dedicated to me and to my formation as a physicist, for the successful research we did together and for the method you taught me. I want also to thank Gabriele for these three years made of discussions, ideas and thoughts; good luck. So say we all. Then I also want to thank all the other LGMers, Michele, Giorgio B., Marco, Simone, Christian, Ajay, Luca B., Claudio and Cristina for all the time and experiences we shared by the CIMaINa labs. I spent six months of my PhD by the "Surface and Thin Films" laboratories of the Zernike Institute for Advanced Materials of the University of Groeningen and I want to thank all the people for the kind time we had. I want in particular to thank Professor Petra Rudolf for the kind welcome and for all the support she provided and Luc for the precious help in experimental and technical issues.

Furthermore I want also to mention Giovanni Onida, Nicola Manini and Ivano Castelli for the tight collaboration we had and for all the results we obtained by working together.

I am mostly beholden to Paolo Milani and Giorgio Benedek for the great opportunity they gave me, for the incessant support and stimulus and, above all, for making me an open minded scientist.

I gratefully acknowledge Fondazione Cariplo for the financial support provided for my research.